

UNIVERSITÉ DU QUÉBEC

THÈSE
PRÉSENTÉE À
L'UNIVERSITÉ DU QUÉBEC À CHICOUTIMI
ET
L'INSTITUT DE GÉOTECTONIQUE À CHANGSHA,
L'ACADÉMIE CHINOISE DES SCIENCES
POUR L'OBTENTION
DU DOCTORAT EN RESSOURCES MINÉRALES

PAR
GUOXIANG CHI

CONTRÔLE POLYGÉNÉTIQUE SUR LA LOCALISATION DES GISEMENTS
PROXIMAUX ET DISTAUX DANS LE CHAMP POLYMÉTALLIQUE-
STANNIFÈRE À XINLU, GUANGXI, CHINE MÉRIDIIONALE

MAI 1992



Mise en garde/Advice

Afin de rendre accessible au plus grand nombre le résultat des travaux de recherche menés par ses étudiants gradués et dans l'esprit des règles qui régissent le dépôt et la diffusion des mémoires et thèses produits dans cette Institution, **l'Université du Québec à Chicoutimi (UQAC)** est fière de rendre accessible une version complète et gratuite de cette œuvre.

Motivated by a desire to make the results of its graduate students' research accessible to all, and in accordance with the rules governing the acceptance and diffusion of dissertations and theses in this Institution, the **Université du Québec à Chicoutimi (UQAC)** is proud to make a complete version of this work available at no cost to the reader.

L'auteur conserve néanmoins la propriété du droit d'auteur qui protège ce mémoire ou cette thèse. Ni le mémoire ou la thèse ni des extraits substantiels de ceux-ci ne peuvent être imprimés ou autrement reproduits sans son autorisation.

The author retains ownership of the copyright of this dissertation or thesis. Neither the dissertation or thesis, nor substantial extracts from it, may be printed or otherwise reproduced without the author's permission.

**Polygenetic Control of the Localization of Proximal versus Distal Deposits in the
Xinlu Tin-Polymetallic Ore Field, Guangxi, Southern China**

By

Guoxiang Chi

A thesis submitted in partial fulfillment of the requirements for the degree of Doctor of Philosophy at l'Université du Québec à Chicoutimi, Chicoutimi, Québec, Canada, and the Changsha Institute of Geotectonics, the Chinese Academy of Sciences, Changsha, P. R. China.

May 1992

ABSTRACT

The Xinlu tin-polymetallic ore field in the Guangxi Autonomous Region of the Zhuang Nationality of southern China is associated with the Mesozoic Guposhan granitic batholith. The batholith consisting of at least three phases of intrusion intrudes Pre-Devonian meta-sedimentary rocks and Late Paleozoic sedimentary rocks including large amounts of carbonates. The ore field is situated at the southern margin of the batholith, where sedimentary rocks are surrounded by granites on three sides (west, north and east) and underlain by unexposed granites, exhibiting a concave intrusion surface. Dykes of intermediate to granitic compositions similar in age to the granites are widespread. Five tin-polymetallic deposits occur in the ore field; among them two (the Dachong and Liuhe'ao deposits) are located at the contact zone between the granitic intrusions and the Devonian sedimentary rocks and are considered as proximal deposits. The Baimianshan and Shimen deposits, classified as distal deposits, are located in the Devonian sedimentary rocks relatively far above the intrusions and are spatially related to dykes and/or fractures. The Muqiaomian deposit is situated in the sedimentary rocks not far from the contact zone, forming a transitional type between proximal and distal deposits. This study is an attempt to understand the mechanism of emplacement of proximal versus distal deposits, through factors such as ore-forming sources, migration and deposition processes.

The proximal and distal deposits in the Xinlu ore field are mainly composed of sulfides, with pyrrhotite and sphalerite being the major components coexisting with cassiterite. A major difference between proximal and distal deposits is that the proximal deposits are associated with ore skarns superimposed on preore skarns, whereas the distal deposits are hosted by carbonates with relatively weak and restricted alterations. Both types have been considered to be related to late-stage intrusions of the Guposhan batholith. The localization of the ore deposits do not appear to be controlled by a specific sedimentary bed at the ore field scale. A correlation between the vertical distance from ore bodies to intrusion surface and the depth of emplacement of the intrusions can be established: proximal deposits are developed in the northern part of the ore field, where the granites were emplaced at higher levels; on the contrary distal deposits are developed in the southern part of the ore field where the granites were emplaced deeper. The transitional type of deposit (Muqiaomian), on the other hand, is developed in the western part of the ore field where the depth of emplacement of the intrusions is intermediate.

The geochemical characteristics of the host rocks (granites, dykes and sedimentary rocks), including their major elements, trace elements, REE patterns, and Sr isotopes have been examined. It

is indicated that the second and third phases of the Guposhan batholith belong to S-type granites, and fractional crystallization is most likely to be the process responsible for the differentiation between phase II and III and within each phase. Phase I intrusion is derived from a S-I transitional source (closer to I type). The dykes are probably comagmatic with the intrusions of the Guposhan batholith; their compositional deviation from the granites may be due to contamination with the sediments. Comparison of various criteria distinguishing Sn-generating granites and barren granites shows that the late-stage granites of the batholith have high ore-forming potential, whereas the early-stage granites and dykes have relatively low ore-forming potential. Sedimentary rocks in general have low ability to provide ore-forming fluids and metals. The S, O, Pb isotope compositions of the ore minerals from proximal and distal deposits are similar, and indicate that the majority of the ore-forming fluids and metals was derived from the granite intrusions. Thus the separation of proximal and distal deposits does not appear to be due to non-magmatic ore-forming sources of the distal deposits.

The fluid inclusions in cassiterite from proximal and distal ores and in quartz from granites associated with the proximal deposits have been studied systematically. The chemical system of the ore-forming fluids can be circumscribed by $\text{H}_2\text{O}-\text{CO}_2-\text{NaCl}-\text{CaCl}_2$ components. The common coexistence of relatively CO_2 -rich gas inclusions and relatively saline liquid inclusions indicates that fluid phase separation is probably an important mechanism of the deposition of both proximal and distal deposits. Homogenization temperatures of fluid inclusions are similar between proximal and distal deposits, being mainly between 280 and 460 °C for the Baimianshan deposit, 320 and 460 °C for the Shimen deposit, 320 and 500 °C for the Liuhe'ao deposit. This indicates a rather small temperature gradient in the conduits of the ore-forming fluids. Fluid pressures estimated from isochores of fluid inclusions range from 469 to 630 bars for the Baimianshan deposit, from 446 to 792 bars for the Shimen deposit, from 148 to 404 bars for the Liuhe'ao deposit, and from 124 to 2303 bars for the granites at Liuhe'ao. The thickness of the cover over the ore deposits at the time of mineralization is estimated to be 3900 m according to stratigraphic data, the corresponding hydrostatic and lithostatic pressures being 382 bars and 1032 bars respectively, thus the fluid pressure data derived from fluid inclusion study indicate that there was probably a fairly high pressure contrast between the source area of the fluids within the intrusions (approximated by lithostatic pressure) and the contact zone and conduits (approximated by hydrostatic pressure).

An analysis of the conduit systems in the Xinlu ore field indicates that structures, especially those which controlled the intrusion of the dykes or those which were reactivated by the force of granite intrusion, played an important role in the migration of the ore-forming fluids. The dyke-controlling

structures are generally consistent with the principal compressive stress generated by granite intrusions, which greatly promotes the extension of the structures.

A numerical modelling has been carried out to simulate the temperature gradient distribution patterns associated with the granite intrusions. It is indicated that in a concave intrusion environment like the Xinlu ore field, the temperature gradient is lowest at the contact zone, and increases away from the intrusion, which is opposite to a convex intrusion environment. Since hydrothermal deposits tend to occur where the temperature of the ore-forming fluid drops in a localized area, namely in the high-temperature segment of the environment, proximal deposits are more difficult to form in a concave intrusion environment.

Based on all the above findings, a general model is proposed to explain the separation of proximal and distal deposits. It has been shown that the migration capacity and phase separation fields of the ore-forming fluids are associated with the change from lithostatic pressure system within the intrusions to hydrostatic pressure system outside the intrusions and in turn are related to the depth of emplacement of the intrusions. Therefore, when the intrusion is emplaced at high levels, mineralization tends to take place near the contact zone, forming proximal deposits, whereas when the intrusion is emplaced at deeper levels, mineralization is more likely to occur in some distance from the intrusion, forming distal deposits. This is consistent with the temperature gradient patterns because in a given region, a convex shape of intrusion surface favouring shallow intrusion environment has highest temperature gradient at the contact zone and promotes the formation of proximal deposits; a concave shape of intrusion surface having lowest temperature gradient at the contact zone is more likely to be related to deep intrusion environment, and therefore is unfavourable for the formation of proximal deposits.

A preliminary survey of the literature indicates that the models established in the Xinlu ore field may be applied to a variety of intrusion-associated hydrothermal deposits in other regions in the world, although specific geological settings may distort the models to variable extents. It is believed that these models, in addition to those studied by previous authors (e.g. metal zoning models), have added some new constraints on the localization of hydrothermal deposits, and may be useful in selecting prospecting targets and planning the depth of drilling.

CONTRÔLE POLYGÉNÉTIQUE SUR LA LOCALISATION DES GISEMENTS PROXIMAUX ET DISTAUX DANS LE CHAMP POLYMÉTALLIQUE- STANNIFÈRE À XINLU, GUANGXI, CHINE MÉRIDIIONALE

Résumé Prolongé

La plupart des gisements d'étain primaires sont associés avec des intrusions granitiques. Pourtant, les relations spatiales entre eux ne sont pas toujours évidentes, celles-ci montrant plusieurs variantes. Certains gisements sont situés dans ou près de la zone de contact entre l'intrusion et les roches environnantes: ce sont les gisements proximaux. D'autres sont localisés dans des roches relativement éloignées de l'intrusion: ce sont les gisements distaux. Quel est le mécanisme de la séparation spatiale des gisements d'étain? Sous quelles conditions se forment les gisements proximaux? Sous quelles conditions se forment les gisements distaux? Ces questions sont liées de près avec l'exploration minérale. Vu que la zone de contact entre l'intrusion et les roches environnantes est une frontière géologique et géophysique, elle est donc une référence utile pour étudier la localisation des gisements et choisir les cibles d'exploration, et surtout pour établir la profondeur des forages d'exploration. Ces problèmes n'ont pas été étudiés systématiquement jusqu'à maintenant. La localisation des gisements d'étain a été généralement attribuée aux environnements locaux de déposition des minerais, ex.: "des couches sédimentaires favorables" ou "des positions structurales favorables", etc.. Par conséquent, il semble que la localisation des gisements d'étain est indépendante des intrusions elles-mêmes et est principalement déterminée par les conditions locales. Etant donné que la plupart des composantes de la minéralisation et la capacité de mouvement des fluides minéralisateurs originent des intrusions granitiques, on peut quand même affirmer que la localisation des gisements d'étain associés avec des intrusions est contrôlée principalement par les intrusions elles-mêmes. Pourquoi certains gisements d'étain sont-ils localisés au contact entre les intrusions et les roches environnantes, alors que d'autres sont localisés dans des roches relativement éloignées des intrusions? Cette localisation des gisements est probablement plus déterminée par les intrusions elles-mêmes que par les conditions locales. Les modèles de zonation métallique ont expliqué la distribution spatiale régulière des différents éléments ou des assemblages d'éléments par

rapport aux intrusions, mais n'ont pas examiné la différenciation d'une zone spécifique de minéralisation par rapport aux intrusions.

Le champ de minéralisation polymétallique-stannifère de Xinlu, Guangxi, Chine méridionale, où des gisements d'étain proximaux et distaux se sont développés, constitue une excellente région pour examiner certains des problèmes mentionnés ci-dessus. Ce champ fait partie du district minéralifère de Ping-Gui, lequel est un des plus importants producteurs d'étain de la Chine. La minéralisation polymétallique-stannifère dans cette région, comme dans les autres parties de la Chine, est associée avec des intrusions granitiques formées dans les environnements tectoniques de "diwa" ou d'activation de plateforme, ce qui est typique des provinces métallogéniques en Chine et ailleurs.

Le champ de minéralisation de Xinlu a une histoire tectonique compliquée, qui se divise en trois étapes: l'étape géosynclinale (du Protérozoïque à la fin du Silurien), l'étape de plateforme (du Dévonien au début du Triassique), et l'étape de diwa (du milieu du Triassique au récent). La minéralisation polymétallique-stannifère est reliée aux intrusions granitiques du Batholithe de Guposhan, qui s'est formé lors de l'étape de diwa. Le champ de minéralisation de Xinlu se trouve à la marge sud du batholithe. Il y a trois phases d'intrusion dans le batholithe. La première phase est située du côté est de Xinlu, la deuxième phase se trouve à l'ouest; ces deux phases se chevauchent au nord de Xinlu, et la troisième phase est située dans le milieu du champ de minéralisation sous forme de petits stocks. Les roches sédimentaires à Xinlu sont des carbonates et des roches clastiques déposées lors de l'étape de plateforme. Elles sont entourées par les granites du Batholithe de Guposhan sur trois côtés (est, nord et ouest) et à la base. Par conséquent, le champ de minéralisation est en fait situé dans un profil concave de la surface des intrusions. Plusieurs dykes, principalement de composition intermédiaire, injectent les roches sédimentaires.

Cinq gisements polymétalliques-stannifères ont été découverts à Xinlu. Les gisements Dachong et Liuhe'ao sont situés au nord du champ de minéralisation, là où les intrusions granitiques recoupent les niveaux plus élevés. Les corps minéralisés se superposent sur les skarns et les hornfels développés dans la zone de contact entre les intrusions et les roches encaissantes. Les gisements Baimianshan et Shimen se trouvent dans la partie sud du champ de minéralisation, là où les granites sont plus profonds. Les corps minéralisés se sont développés dans les carbonates situés entre quelque cents et mille mètres au-dessus des intrusions granitiques. Il y a une relation serrée entre les corps minéralisés, les dykes et les failles remobilisées par les intrusions granitiques. Le gisement

Mouqiaomian est situé à l'ouest de Xinlu, là où les carbonates sont entourés par les granites sur tous les côtés et à la base, et les corps minéralisés sont développés dans les carbonates au-dessus des skarns dans la zone de contact entre les granites et les roches encaissantes. La plupart des corps minéralisés distaux sont du type veine escarpée, excepté les deux corps minéralisés stratiformes à Baimianshan. Les assemblages des minéraux métalliques sont similaires, composés principalement de pyrrhotite et sphalerite, avec la présence de cassitérite dans le minerai.

L'étude des caractéristiques géochimiques des granites du Batholithe de Guposhan indique que la troisième phase d'intrusion a évolué à partir du magma de la deuxième phase, les deux étant des granites de type S. La première phase a une source similaire aux granites de type I. La troisième phase intrusive a le plus haut potentiel de minéralisation, ce qui est supporté par son association spatiale avec les gisements, par son plus haut degré de différenciation, et ses plus hauts contenus en éléments minéralisateurs que les granites "stériles". La déficience en ETR, Sn et F dans les granites de la troisième phase par rapport à ceux de la deuxième phase peut être expliquée par le partage des éléments dans les fluides hydrothermaux qui lui sont associés, ce qui est supporté par leur caractère hyperalumineux. Les contenus en éléments de minéralisation dans les granites de la deuxième phase et dans le membre le plus felsique de la première phase sont assez élevés, mais ces magmas granitiques ont retenu les éléments de minéralisation plutôt que de les relâcher dans les fluides hydrothermaux, réduisant ainsi leur potentiel de minéralisation. Les dykes sont génétiquement reliés aux granites du Batholithe de Guposhan, comme le démontre leur rapport spatial et temporel. Un modèle de contamination sédimentaire est proposé pour expliquer la composition moins riche en silice des dykes en comparaison avec les granites, ce qui est supporté par les observations pétrologiques et les études géochimiques. Le potentiel de minéralisation des dykes est généralement bas à cause de leur petite taille et de leur potentiel de rétention des éléments de minéralisation. Les roches sédimentaires ont en général un plus faible potentiel de minéralisation que les granites, parce que leurs contenus en éléments de minéralisation sont généralement faibles, et que la remobilisation des éléments requiert des conditions plus spécifiques.

Les caractéristiques géochimiques des minéraux métalliques ont été étudiées. Les compositions isotopiques de S, O et Pb des minéraux métalliques des gisements proximaux et distaux sont similaires, et indiquent que la majorité des fluides minéralisateurs sont dérivés des magmas granitiques, quoique une certaine partie des éléments et fluides

minéralisateurs soient dérivés des roches sédimentaires et de l'eau météorique. Il est clair que la formation des gisements distaux n'est pas déterminée par une source non-magmatique des éléments minéralisateurs. Les gisements proximaux et distaux dans le champ polymétallique-stannifère de Xinlu sont formés dans un système hydrothermal contrôlé par les intrusions granitiques.

Les inclusions fluides dans la cassitérite des gîtes proximaux et distaux et dans le quartz des granites associés avec les gisements proximaux ont été systématiquement étudiées. Les températures des fluides minéralisateurs sont estimées à l'aide des températures d'homogénéisation et indiquent que le gradient de température dans les conduits est faible. Les pressions des fluides sont estimées à partir des isochores des inclusions individuelles. Dans les gisements, les valeurs se situent entre celles des pressions lithostatique et hydrostatique (plus près de hydrostatique). Pour ce qui est des intrusions, la pression des fluides se rapproche de la pression lithostatique vers l'intérieur des intrusions. Il est possible que le contraste des pressions des fluides entre l'intérieur et l'extérieur des intrusions soit à l'origine de la dynamique de mouvement des fluides. L'étude des inclusions fluides indique aussi que la séparation des phases fluides est un mécanisme important pour la déposition des gisements proximaux et distaux. Ce point est démontré par la coexistence générale des inclusions fluides homogénéisées à l'état liquide et à l'état vapeur à des températures similaires.

Une analyse du système des conduits à Xinlu indique la présence de systèmes sub-verticaux et d'autres sub-horizontaux. Le premier est représenté par des failles et fractures, et le second est représenté par les litages et fractures interstratifiées dans les roches sédimentaires. Les conduits les plus efficaces pour les courants des fluides de minéralisation à Xinlu sont les failles et fractures contrôlant l'intrusion des dykes et/ou remobilisées par l'intrusion granitique. Puisque les dykes sont génétiquement associés avec les granites, les structures contrôlant les dykes sont plus probablement reliées aux sources des fluides de minéralisation. L'association temporelle entre les dykes et les granites fait en sorte que ces structures peuvent mieux conserver leur forte perméabilité pendant l'activité des fluides de minéralisation. Le caractère géomécanique d'extension des structures indique que les fluides à l'intérieur de celles-ci approchent un état hydrostatique. Ceci contraste avec l'état lithostatique à l'intérieur des intrusions. Le système sub-horizontale a peut-être joué un rôle pour fournir de l'eau souterraine et des solutions à partir des roches sédimentaires aux fluides de minéralisation dans les conduits, mais les quantités incorporées sont limitées.

Des modélisations sont effectuées pour simuler la distribution des gradients de température dans un environnement d'intrusion concave comme celui de Xinlu. Il est démontré que le gradient de température est le plus bas à la zone de contact et augmente loin de l'intrusion. Ceci est à l'opposé d'un environnement d'intrusion convexe. Les gisements hydrothermaux ayant tendance à être localisés là où la température des fluides de minéralisation baisse brusquement, il s'en suit que les gisements proximaux se forment plus difficilement dans un environnement d'intrusion concave.

Fondé sur les études ci-dessus, un modèle général est établi pour expliquer la localisation des gisements proximaux et distaux à Xinlu. Ce modèle tient compte des conduits, de la dynamique de migration, de la séparation de phase et de la baisse de température des fluides de minéralisation. La dynamique de migration des fluides de minéralisation est principalement déterminée par le gradient de pression entre les régions sources et les conduits, ce qui est associé de près avec la profondeur d'emplacement des intrusions granitiques. L'étude des inclusions fluides de Xinlu et les conclusions d'autres auteurs dans la littérature indiquent que la pression des fluides à l'intérieur d'une intrusion est égale ou supérieure à la pression lithostatique, alors que la pression des fluides dans les conduits s'approche plutôt de la pression hydrostatique. Puisque la pression lithostatique augmente avec la profondeur plus rapidement que la pression hydrostatique, le contraste entre les deux augmente avec la profondeur. Par conséquent, plus l'intrusion est profonde, plus la dynamique de migration des fluides sera élevée et plus ceux-ci pourront migrer sur de grande distance avant de déposer les minerais. Ceci est supporté par le fait que les gisements proximaux sont mieux développés au nord de Xinlu, là où les intrusions sont moins profondes, alors que les gisements distaux sont mieux développés au sud de Xinlu, là où les intrusions sont plus profondes. La distance verticale entre les gisements et les intrusions est proportionnelle à la profondeur d'emplacement des intrusions. Ce point est aussi supporté par les caractéristiques géochimiques des minéraux métalliques qui indiquent que les fluides de minéralisation sont principalement dérivés des intrusions granitiques, et par l'étude des inclusions fluides qui indique un faible gradient de température dans le système des conduits, ce qui implique une haute vitesse de courant des fluides de minéralisation. La séparation de phase, qui est un des mécanismes les plus importants pour la déposition des minerais, a joué un rôle très important pour la localisation des minerais. Le fait que la séparation de phase se fasse dans un lieu proximal ou distal, et la distance de migration des fluides de minéralisation avant la séparation de phase, sont déterminés par la

composition, la température et la pression des fluides et la profondeur d'emplacement des intrusions. Au nord de Xinlu, la profondeur des intrusions est assez faible et les fluides de minéralisation sont transférés du champ à une phase à celui à deux phases dans la zone de contact immédiate en sortant des intrusions. Au sud de Xinlu, la profondeur d'emplacement des intrusions est assez grande et les fluides de minéralisation restent dans le champ à une phase même sous la pression hydrostatique au niveau de la zone de contact. La séparation de phase ne se produit donc pas immédiatement à la sortie des intrusions, mais à plusieurs centaines de mètres au-dessus de celle-ci. La baisse de température est un autre mécanisme très important pour la déposition des minerais. Ceci est compatible avec le modèle, vu que les environnements moins profonds des intrusions sont généralement associés aux intrusions convexes. Celles-ci, avec un gradient de température plus élevée à la zone de contact, favorisent la formation des gisements proximaux. Inversement, les intrusions plus profondes sont plus probablement concaves et avec un gradient de température moins élevée à la zone de contact, ce qui est défavorable à la formation des gisements proximaux.

En résumé, les gisements hydrothermaux associés avec les intrusions magmatiques se forment plutôt dans la zone de contact entre l'intrusion et les roches environnantes lorsque l'intrusion est placée à des niveaux élevés et est convexe. Ils sont plutôt localisés à des emplacements distaux quand l'intrusion est située à des niveaux plus profonds et est concave. Le niveau de déposition des minerais dépend en grande partie du développement du système de conduits et de la composition, la température et la pression des fluides de minéralisation. Une revue de la littérature indique que les modèles établis à Xinlu peuvent être appliqués sur une variété de gisements hydrothermaux associés avec les intrusions granitiques dans d'autres régions du monde, bien que les conditions géologiques spécifiques peuvent influencer les modèles. Les connaissances de la géologie locale, de la distribution spatiale des intrusions, de la source, la composition, la température et la pression des fluides de minéralisation, des données P-V-T-X correspondantes, de la distribution des conduits et des diverses unités lithologiques favorables pour la déposition des minerais influencent l'application des modèles. Ces modèles peuvent servir à choisir les cibles d'exploration minérale et à établir la profondeur des forages.

广西新路锡多金属矿田 近岩体矿床与远岩体矿床定位的多成因控制

论文摘要

世界上的原生锡矿床绝大部分与花岗岩有关，但是，矿床与侵入体的空间关系有一定的变化范围。有些锡矿床产在岩体接触带附近，称为近岩体矿床，有些则产在远离岩体的围岩中，称为远岩体矿床。是什么原因造成锡矿床定位的空间分异，在什么条件下形成近岩体矿床，在什么条件下形成远岩体矿床，这些问题与找矿勘探有密切关系，因为岩体与围岩的接触面是一个明显的地球物理界面，以此界面为参照系来探讨矿床的定位，对于选择勘探靶区和设计钻孔深度有着很大的意义。但是，至今为止尚未有人对其作过系统的研究。在很多情况下，锡矿床的定位被归因于与矿质沉淀直接有关的局部环境，如有利构造部位，有利交代层位等。但是，这些因素与矿床定位对岩体的远近没有直接的联系。金属分带模式虽然解释了不同元素或元素组合在空间上相对于岩体的分布规律，但是没有说明为什么同一元素或元素组合相对于岩体的空间分布会发生变化以及这种变化的规律性。

在广西新路锡多金属矿田，与花岗岩侵入体有关的近岩体矿床和远离岩体矿床都很发育，这为我们研究锡矿床与侵入体的空间关系的规律性提供了一个很好的例子。该矿田属中国主要产锡区之一——平桂锡多金属成矿区的一个组成部分，该成矿区又是世界上著名的南岭多金属成矿带的一部分。因此，以新路矿田为例子有一定的代表性。

新路矿田的大地构造演化史可分为三个阶段，即地槽阶段（元古代至志留纪末），地台阶段（泥盆纪至早三叠世），和地洼阶段（中三叠世至现在）。锡多金属成矿作用与地洼阶段（主要为燕山期）形成的姑婆山花岗岩基有关。该岩基至少由三次侵入体组成。新路矿田位于该岩基的南部接触带，其东面是该岩基的第一次侵入体，西面是第二次侵入体，北面是这两次侵入体的接触处，下部为隐伏岩体，岩体接触面呈内凹状。矿田中部有几个小花岗质侵入体，属姑婆山岩基的第三次侵入体。矿田内的地层为地台阶段形成的碳酸盐岩和碎屑岩，其东、北、西三面为花岗岩所包围。矿田内有大量岩脉，其成分主要为中性和中酸性。地层中发育印支期和燕山期的构造。

矿田内已发现五个锡多金属矿床，其中大冲和六合凹矿床位于矿田北部，产于岩体接触带，岩体定位深度相对较小。白面山和石门矿床位于矿田南部，产于远离岩体的碳酸盐

岩地层中, 岩体定位深度相对较大。木桥面矿床位于矿田西部, 其四周及底部为花岗岩所包围, 矿床产于碳酸盐岩地层中, 而在岩体接触带的夕卡岩中矿化很弱, 矿体与隐伏岩体的距离大于大冲和六合凹, 而小于白面山和石门; 岩体定位深度比大冲和六合凹大, 而比白面山和石门小。除了白面山的两个似层状矿体外, 绝大部分远岩体矿体呈陡脉状。不同矿床的矿石矿物组合很相似, 以磁黄铁矿为主, 次为闪锌矿和黄铁矿, 锡石与之共生。

本文对围岩, 包括花岗岩, 脉岩和沉积岩的地球化学特征作了系统的研究。研究表明, 姑婆山岩基的第三次侵入体是由第二次侵入体的岩浆经结晶分异演化而成, 二者均属S-型花岗岩。第一次侵入体接近I-型花岗岩。第三次侵入体的成矿能力最强, 体现在其成矿元素含量及分异程度比世界上的‘无矿花岗岩’高, 世界上的成矿花岗岩一般也是晚期侵入体。第三次侵入体的稀土, 锡及氟的含量相对于第二次侵入体有所降低, 是因为这些元素在晚岩浆阶段大量分配到热液中的缘故。第三次侵入体的过铝质特征有利于这种分配。第二次侵入体和第一次侵入体边缘相的分异程度及成矿元素含量也较高, 但它们的融体性质倾向于使成矿元素残留于岩浆中而不是使之分配到热液中, 从而降低了其成矿能力。岩脉与花岗岩基有成因联系, 体现在它们在时间, 空间及地球化学特征上的相关性。根据岩石学与地球化学的研究, 岩脉被认为主要来源于姑婆山岩基的花岗质岩浆, 其成分偏基性是因为受到沉积岩组分的混染的缘故。岩脉的成矿能力总的来说较低, 因为它们的规模比花岗岩体要小得多, 而且其融体性质倾向于使成矿元素残留于岩浆中而不是使之分配到热液中。沉积岩的成矿能力总的来说比花岗岩低得多, 因为其成矿元素含量较低, 而且这些元素的活化要求更多的条件。

远岩体矿床与近岩体矿床矿石矿物的硫, 氧同位素特征相似; 硫, 氧, 铅同位素和稀土元素特征指示成矿热液主要来源于花岗岩, 地层只提供了少量成矿物质, 雨水也少量地进入成矿热液。显然远岩体矿床的形成并非由非岩浆来源物质所控制。远岩体矿床和近岩体矿床都受控于与花岗岩有关的热液系统。

对远岩体矿床与近岩体矿床的锡石及成矿花岗岩的石英中的流体包裹体的研究表明, 远岩体与近岩体矿床的成矿热液温度相差较小, 反映了导矿系统的温度梯度很小。成矿热液的压力介于静岩压力与静水压力之间, 但更接近静水压力。岩体内的岩浆热液压力变化范围从低于静水压力到高于静岩压力。流体包裹体的研究还表明, 流体相分离是矿质沉淀的主要因素之一, 体现在具有相似均一温度的两种包裹体(一种为均一成液相的盐度更高的包裹体, 另一种为均一成气相的更富二氧化碳的包裹体)共存于同一锡石颗粒中, 二者相距仅几微米或沿锡石中同一生长带排列。

热液传导系统可分为两大类, 一类为近直立系统, 另一类为近水平系统。前者以断层和断裂为代表, 后者主要是层理和层间破碎带。对成矿热液的传导最起作用的是控制岩脉

侵入的断裂以及受岩浆侵入动力改造的构造, 因为这些构造最可能与成矿热液源相连, 而且最可能在成矿热液活动期间保持高的张性和渗透性, 并使容于其中的热液接近静水压力状态. 近水平传导系统对于提供地下水及地层中的成矿物质到成矿热液中起一定的作用, 但这种掺合作用的量是有限的.

数值模拟实验表明, 在象新路矿田这种内凹型的岩浆侵入环境中, 温度梯度在岩体接触带最小, 而远离岩体逐渐增大, 与外凸型岩浆侵入环境正相反. 由于热液矿床倾向于产在热液温度在局部突降的地方, 即环境中温度梯度最大处, 因此在内凹型的岩浆侵入环境中形成近岩体矿床的难度更大.

基于以上认识, 本文提出一个解释新路矿田远岩体矿床与近岩体矿床分离的综合模式. 该模式在成矿热液主要来源于花岗岩的前提下, 考虑了热液的传导系统, 迁移动力, 相分离及温度梯度变化. 这些因素都与花岗质侵入体的定位深度有关. 成矿流体的迁移动力主要由流体源与传导系统的压力差所决定. 这个压力差主要取决于岩体定位深度. 新路矿田的流体包裹体研究及其它作者的研究表明, 花岗质侵入体内的成矿流体在与外界沟通之前所受的压力等于或大于静岩压力, 而在近直立传导系统中的热液较接近静水压力. 由于静岩压力随深度增大的速度远大于静水压力, 所以二者的差值也随深度而增大. 因此, 岩体定位深度越大, 从岩体内排出的成矿热液的迁移能力越强, 成矿物质被迁离岩体的距离越远. 这与在新路矿田观察到的矿床与岩体的垂直距离与岩体的定位深度呈正相关关系的现象是一致的, 并与流体包裹体及矿石矿物地球化学特征所指示的流体快速流动特征相符. 流体相分离作为矿质沉淀的重要因速之一, 对于矿床的定位起着重要的作用. 研究表明, 相分离作用是发生在岩体接触带还是在远离岩体的围岩中以及离接触带的远近, 取决于流体的成分, 温度, 压力及岩体的定位深度. 在新路矿田的北部, 岩体定位深度小, 当成矿流体从岩体中进入接触带时, 流体从静岩压力状态下的一相区变成静水压力状态下的两相区, 相分离作用立即发生. 相反, 在新路矿田的南部, 岩体定位深度较大, 当成矿流体从岩体中进入接触带时, 流体在静水压力状态下仍然处在一相区, 因此在接触带没有发生相分离作用; 相分离作用发生在距接触带一定距离的围岩中, 该距离与岩体的定位深度呈正相关关系. 温度降低作为矿质沉淀的另一因素, 其对矿床定位所起的作用与岩体定位深度的作用正好吻合, 因为具凸起形状的岩体更可能具小的定位深度, 此时岩体接触带既是温度梯度最大的地方, 又可能是成矿流体相分离的地方, 易于形成近岩体矿床; 而具内凹形状的岩体更可能具大的定位深度, 此时岩体接触带既是温度梯度最小的地方, 又较不可能发生流体相分离, 因此不易形成近岩体矿床.

总之, 与侵入体有关的热液矿床的定位在很大程度上受控于岩体定位的深度和形态. 当岩体定位深度小且具凸起形状时, 矿体倾向于产在岩体接触带附近; 当岩体定位深度大

且具内凹形状时, 矿体倾向于产在远离岩体的围岩中. 矿床定位处与岩体接触带的垂直距离与热液传导系统的发育程度, 成矿热液的成分, 温度及压力有关. 初步的文献调查表明, 在新路矿田所建立矿床定位模式可以应用到世界上许多与花岗质侵入体有关的矿床或矿田中, 尽管由于各个地区的具体地质条件不同而与理想模式有不同程度的偏离. 对所应用地区地质环境, 侵入体的空间分布, 成矿流体的来源, 成分, 温度, 压力以及相应流体的 P-V-T-X (压力, 密度, 温度, 成分) 实验资料的了解, 是模式应用的基础. 合理地运用这一模式, 将有助于选择勘探靶区和设计钻孔深度.

ACKNOWLEDGEMENTS

I would like to thank the following individuals and organizations for their contributions and help in the preparation of this thesis.

The graduate studies and the preparation of the thesis were supervised by Prof. Jayanta Guha, Prof. Huan-Zhang Lu and Prof. Jacques Carignan on the part of l'Université du Québec à Chicoutimi, and by Prof. Academician Guo-Da Chen, Prof. Han-Hui Yin and Prof. Ho-Yan Hu on the part of the Changsha Institute of Geotectonics, the Chinese Academy of Sciences. I have greatly benefited from direction of all these professors and the discussions with them.

Scholarships were provided by the Chinese Academy of Sciences for the first one and half years and by the Ministère de l'Enseignement Supérieur et de la Science du Québec (Programme Action Structurante) for the last two years of the graduate studies.

The Ping-Gui Mining Bureau and the Xinlu Mine have provided all the convenience for me during the field work. The help of the following staffs from these two organizations, Mr. Zhi-Cheng Dong, Mr. Gui-Yuan Huang, Mr. Tao-Yu Chen, Mr. Huan-Wen Wang, Mr. Zhe-Zhong Li, Mr. Xiong Ouyang, are especially acknowledged.

A number of professors and colleagues of mine, both in the Changsha Institute of Geotectonics and l'Université du Québec à Chicoutimi, have helped me in a variety of ways. A complete list of them is difficult, but I would like to express my sincere thanks to: Dr. Gérard Woussen and Ms Xiu-Juan Wang for their various support for the graduate study program; Prof. Xin-Yi Yang for his critical examination of the research proposal; Dr. Alain Rouleau for his good suggestions and critical review of the numerical models; Mr. Guo-Yuan Xie, Mr. Liang-Bin Qiu, Mr. Hao-Ming Li, Mr. Xiang-Zhao Hu and Mr. Jian-Sheng You for their help in the field work; Mr. Paul Bédard and Michel Hervet for their help in neutron activation analysis; Prof. Ci-Mei Yu and Ms Jeannette See for their help in fluid inclusion studies; Mr. Jean-Yves Labbé, Mr. Denis Côté, Mr. Claude Dion, and Ms Danielle Giovenazzo for their help in using computers; Prof. Da-Kang Chen, Ms Man-Xia Zhong, Mr. Richard Lechasseur for their work and help in chemical analyses; Mr. Raymond Blanchette for developing photographs; Mr. Claude Dallaire for making

computer-scanning copies of diagrams; Mr. En-Tao Yin, Ms Jian-Ping Liu and Mr. Yvon Boudreault for making thin sections.

The detailed and patient correction of the first draft of this thesis by Dr. Edward Chown of l'Université du Québec à Chicoutimi and by Dr. A. James Macdonald of the University of British Columbia is especially appreciated. The final version has benefitted from the critical and constructive review by Dr. M. Zentili of the Dalhousie University. The French abstract has been improved by corrections of Dr. Jacques Carignan and M. Réjean Gérard, for which I am thankful. Finally, I have benefitted from the critical review and constructive comments by Dr. A.E. Williams-Jones of the McGill University of a manuscript drawn from a part of the thesis.

TABLE OF CONTENTS

ABSTRACT	i
RÉSUMÉ PROLONGÉ.....	iv
ABSTRACT IN CHINESE.....	x
ACKNOWLEDGEMENTS	xiv
TABLE OF CONTENTS	xvi
LIST OF FIGURES	xx
LIST OF TABLES	xxviii
LIST OF PLATES.....	xxx
CHAPTER I INTRODUCTION.....	1
CHAPTER II REGIONAL GEOLOGICAL SETTING.....	9
2.1 Introduction.....	9
2.2 Tectonic Evolution.....	9
2.3 Stratigraphy.....	13
2.4 Structures.....	16
2.5 Intrusives.....	18
CHAPTER III CHARACTERISTICS OF THE XINLU ORE FIELD.....	21
3.1 Geological Features of the Ore Field.....	21
3.1.1 Sedimentary rocks.....	21
3.1.2 Granites.....	24
3.1.3 Dykes.....	27
3.1.4 Structures.....	27
3.2 Geological Features of Ore Deposits.....	28
3.2.1 Dachong deposit.....	28
3.2.2 Liuhe'ao deposit.....	29
3.2.3 Muqiaomian deposit.....	31
3.2.4 Baimianshan deposit.....	33
3.2.5 Shimen deposit.....	35
3.2.6 Dongjia'ao deposit.....	36
3.3 Temporal and Spatial Relationship of Ore Deposits with Host Rocks.....	38

3.3.1 Temporal relationship.....	38
3.3.2 Spatial relationship.....	38
CHAPTER IV GEOCHEMICAL CHARACTERISTICS OF THE HOST	
ROCKS AND THEIR ORE-FORMING POTENTIAL	42
4.1 Introduction.....	42
4.2 The Sedimentary Rocks.....	42
4.2.1 Major elements.....	42
4.2.2 Trace elements.....	45
4.2.3 REE contents.....	45
4.2.4 The ore-forming potential.....	50
4.3 The Granites.....	50
4.3.1 Major elements.....	51
4.3.2 Trace elements.....	59
4.3.3 REE patterns.....	63
4.3.4 Isotopic characteristics.....	63
4.3.5 Genesis.....	68
4.3.6 The ore-forming potential.....	78
4.4 The Dykes.....	84
4.4.1 Major elements.....	84
4.4.2 Trace elements.....	87
4.4.3 REE patterns.....	93
4.4.4 Sr isotopes.....	93
4.4.5 Genesis.....	93
4.4.6 The ore-forming potential.....	100
CHAPTER V GEOCHEMICAL CHARACTERISTICS OF THE ORES AND	
THE SOURCES OF THE ORE-FORMING FLUIDS.....	104
5.1 Introduction.....	104
5.2 Geochemical Characteristics of the Ores	104
5.2.1 S isotopes.....	104
5.2.2 O isotopes.....	108
5.2.3 Pb isotopes.....	111
5.2.4 REE patterns.....	114
5.3 Fluid Inclusions.....	117

5.3.1 Selection of fluid inclusion samples.....	117
5.3.2 Types and microthermometric features of fluid inclusions.....	118
5.3.3 Association of fluid inclusions and phase separation.....	124
5.3.4 Systematics of composition, temperature and pressure of proximal versus distal fluids.....	125
5.4 The Generation Processes of the Ore-forming Fluids.....	129
CHAPTER VI DYNAMICS OF THE MIGRATION OF THE ORE-FORMING FLUIDS.....	133
6.1 Introduction.....	133
6.2 The system of Conduits.....	133
6.3 Fluid Flow Dynamics.....	137
CHAPTER VII MODELLING OF DEPOSITIONAL THERMAL CONDITIONS.....	146
7.1 Introduction.....	146
7.2 Analytical Models.....	147
7.3 Two-dimension Steady-state Numerical Models.....	151
7.4 Two-dimension Transient Numerical Model.....	156
7.5 Implication for the Localization of Proximal vs. Distal Deposits.....	158
CHAPTER VIII DISCUSSIONS ON THE APPLICATION OF THE INTRUSION DEPTH-FLUID FLOW AND THERMAL FIELD MODELS.....	161
8.1 Introduction.....	161
8.2 Geological Examples from Other Regions.....	161
8.2.1 Examples of relationship of ore localization and intrusion depth..	161
8.2.2 Examples of concave intrusion environments.....	166
8.3 Lithostatic vs. Hydrostatic Systems.....	168
8.4 Phase Separation Fields of the Most Common Fluid Systems.....	171
8.5 Forced Venting vs. Convective Fluid Flow.....	177
8.6 Possible Application of the Models in Ore Prospecting.....	180
CHAPTER IX CONCLUSIONS.....	184
REFERENCES	187
PLATES.....	204
APPENDIX A Petrographic Characteristics of Samples of Granites, Dykes,	

Sedimentary Rocks and Ores.....	211
APPENDIX B Calculation of REE Parameters for Analysis by INAA.....	226
APPENDIX C Description of the Methods Used in Chemical Analyses.....	229
APPENDIX D Description of the Methods used in Fluid Inclusion Study.....	234
APPENDIX E Computer Programs of Modelling of Temperature Gradient Patterns.....	240

LIST OF FIGURES

- Fig. 1 Schematic diagram showing spatial zones within a space of the intrusion-country rock system (not to scale). (1) the interior of the intrusion; (2) the transitional zone between the intrusion and the country rocks, referred to as "proximal area" in the text; (3) the country rocks relatively far from the intrusion, referred to as "distal area" in the text.....2
- Fig. 2 A map showing the extent of the Xinlu tin-polymetallic ore field, the distribution of ore deposits and diamond drill holes (compiled after the unpublished data of No.204 Geol. Team of Guangxi, 1986 and Ping-Gui Mining Bureau, 1986). The insert map shows the position of Xinlu in Guangxi, China.....5
- Fig. 3 A schematic diagram showing the various factors considered in the model of ore localization in the Xinlu ore field.....8
- Fig. 4 Geological map of the Ping-Gui mineralization district, and an insert map showing its position in the tectonic framework of China (modified from Hu, 1986)10
- Fig. 5 Schematic diagrams illustrating the tectonic evolution of the Ping-Gui district (not to scale).....12
- Fig. 6 Strata, tectonic episodes and geotectonic stages of the Ping-Gui district (compiled from unpublished data of No.204 Geol. Team of Guangxi, 1986).....14
- Fig. 7 A Sketch diagram showing the evolution of the stress field in the Ping-Gui district. The thick shaded arrows indicate the regional compressive stress in southern China, and the solid arrows indicate the local stress field in the Pin-Gui district.17
- Fig. 8 Geological map of the Guposhan batholith (modified from unpublished map of No.8 Geol. Team of Guangxi, 1981). $\gamma\delta 3$ - Caledonian granodiorite; $\gamma 5^1$ - Indo-China granite; $\gamma 5^2$ - Yanshanian granite (I-phase I; II-phase-II; III-phase-III; Ic-central part of phase I; It-transitional part of phase I; Im-marginal part of phase I).....19
- Fig. 9 Histogram of isotopic ages of the Guposhan batholith (compiled after

	the data collected by Ping-Gui Mining Bureau, 1986).....	19
Fig.10	Geological map of the Xinlu ore field (modified from unpublished map of No.204 Geol. Team of Guangxi, 1986 and No.8 Geol. Team of Guangxi, 1981). Open circle-placer deposit; black circle-primary deposit; III-phase III; II-phase II; Im-marginal part of phase I; It-transitional part of phase I.	22
Fig.11	A WNW-ESE geological profile of the Xinlu ore field, showing the attitude of the strata, the structures and the extent of the granite intrusions (III-phase III; II-phase II; Im-marginal part of phase I).....	23
Fig.12	A map showing the distribution of granites (including unexposed granites) and dykes as well as their ages in the Xinlu ore field. I, II and III are the same as Fig. 10. The contours indicate the elevation of the surface of the unexposed granites.....	25
Fig.13	No.0 geological cross-section of the Liuhe'ao deposit (after Ping-Gui Mining Bureau, 1986).....	30
Fig.14	Geological map of Muqiaomian deposit (after Ping-Gui Mining Bureau, 1986).....	32
Fig.15	No.5 geological cross-section of Muqiaomian deposit (after Ping-Gui Mining Bureau, 1986).....	32
Fig.16	A geological cross-section of the Baimianshan deposit (after Ping-Gui Mining Bureau, 1986).....	34
Fig.17	A geological cross-section of the Shimen deposit (after Ping-Gui Mining Bureau, 1986).....	37
Fig.18	A NNW-SSE synthetic geological cross-section of the Xinlu ore field, showing the correlation between the location of deposits and the depth of intrusions. The numbers on the vertical scale are referenced to sea level. The sizes of ore bodies and dykes are expanded because of the small scale of the diagram. Not all the drill holes are shown for clarity.....	40
Fig.19	Comparison of Na ₂ O/K ₂ O ratios of sedimentary rocks from the Ping-Gui district with granites from the Guposhan batholith.....	44
Fig.20	Comparison of trace element contents in sedimentary rocks and the average from granites of the Guposhan batholith.....	47
Fig.21	REE patterns of sedimentary rocks from Xinlu and adjoining regions (data from Table 4).....	49

- Fig.22 Plots of Qz, Af and Pl data of the Guposhan batholith on the IUGS (1972) classification. Qz-quartz; Af-alkaline feldspar; Pl-plagioclase. Af and Pl are calculated from the CIPW Ab, Or and An data according to the method proposed by Rittmann (1973); Qz is CIPW normative value. a-alkali-feldspar granite; b-granite; c-adamellite; d-granodiorite; e-tonalite; f-alkali-feldspar quartz syenite; g-quartz syenite; h-quartz monzonite; i-quartz monzodiorite/quartz monzogabbro; j-quartz diorite/quartz gabbro; k-alkali-feldspar syenite; l-syenite; m-monzonite; n-monzodiorite/monzogabbro; o-diorite/gabbro.....56
- Fig.23 Histograms of (a) normative corundum (cm in table 6) and (b) differentiation index (DI in table 6) of granites of the Guposhan batholith....57
- Fig.24 Variation of major element contents and related parameters in different phases of the Guposhan batholith. δ (Rittmann index) = $(\text{Na}_2\text{O} + \text{K}_2\text{O})^2 / (\text{SiO}_2 - 43)$; A/NKC = molecular $\text{Al}_2\text{O}_3 / (\text{Na}_2\text{O} + \text{K}_2\text{O} + \text{CaO})$58
- Fig.25 Variation of trace element concentrations and magma differentiation-related parameters between different phases of the Guposhan batholith (data from table 8).....62
- Fig.26 Comparison of average REE pattern of each phase of the Guposhan batholith.....65
- Fig.27 Rb-Sr isotope whole-rock isochrons for different phases of the Guposhan batholith (data from table 10).....67
- Fig.28 Harker diagrams of phase III and II of the Guposhan batholith.71
- Fig.29 Harker diagrams of phase I granite of the Guposhan batholith.....72
- Fig.30 A Rb-Sr variation diagram of phase II and III granites of the Guposhan batholith, in comparison with the curves of partial melting and fractional crystallization models (both with Rb=300 ppm and Sr=155 ppm at F=0.99, where F is the weight fraction of melt relative to original parent).....74
- Fig.31 Sr-Lu (a) and Eu-Lu (b) variation diagrams of phase I granites of the Guposhan batholith, in comparison with the curves of partial melting and fractional crystallization models (both Sr=181 ppm, Eu=1.33 ppm and Lu=0.48 ppm in the original parent) and lines of restite unmixing and sedimentary contamination models (sedimentary end member represented by a half of clastic rocks and a half of carbonate rocks,

- with Sr=185 ppm, Eu=0.752 ppm, Lu=0.288 ppm).....77
- Fig.32 Different phases of the Guposhan batholith plotted on (a) Rb-Cs-Ba diagram (Neiva, 1984) and (b) Rb-Sr-Ba diagram (Biste, 1982). In (a), area A--muscovite granite, greisenized granite, aplites and pegmatite related to Sn-W mineralization; area B--muscovite and biotite granite and hybrid granodiorite associated with Sn-W mineralization; area C--granites without related Sn-W mineralization. In (b), the shaded area is granites associated with Sn, W and Mo deposits. Data are from table 7.....81
- Fig.33 Plots of Qz, Pl and Af data of dykes from the Xinlu ore field on the IUGS (1972) classification. Af and Pl are calculated from CIPW Ab, Or and An data according to the method proposed by Rittmann (1973), Qz is CIPW normative values. a-granite; b-adamellite; c-granodiorite; d-quartz monzonite; e-quartz monzodiorite.....86
- Fig.34 Harker diagrams of major elements for dykes from the Xinlu ore field.....88
- Fig.35 SiO₂-CO₂ (a) and SiO₂-K₂O/Na₂O (b) variation diagrams for dykes from the Xinlu ore field.....89
- Fig.36 SiO₂-trace element variation diagrams for dykes from the Xinlu ore field...91
- Fig.37 SiO₂-element ratio variation diagrams for dykes from the Xinlu ore field...92
- Fig.38 REE patterns of representative dykes from the Xinlu ore field.....95
- Fig.39 SiO₂-REE parameter variation diagrams for dykes from the Xinlu ore field.....96
- Fig.40 Rb-Sr isotope whole-rock isochron for intermediate dykes from Shuiyanba (a) and single-sample Rb-Sr isotope points and inferred (⁸⁷Sr/⁸⁶Sr)_i values for dykes from Xinlu (b) with Rb-Sr whole-rock ages approximated by K-Ar ages98
- Fig.41 Samples of dykes from the Xinlu ore field plotted on (a) Rb-Cs-Ba diagram (Neiva, 1984) and (b) Rb-Sr-Ba diagram (Biste, 1982). In (a), area A--muscovite granite, greisenized granite, aplites and pegmatite related to Sn-W mineralization; area B--muscovite and biotite granite and hybrid granodiorite associated with Sn-W mineralization; area C--granites without related Sn-W mineralization. In (b), the shaded area is granites associated with Sn, W and Mo deposits. Data are from table 14...102
- Fig.42 Histograms of S isotope composition of ore minerals from

- different ore deposits in the Xinlu ore field.....106
- Fig.43 Comparison of S isotope composition between different types of ore body (a) and between different levels of the Baimianshan deposit.....107
- Fig.44 Pb isotope data of ore minerals from the Xinlu ore field plotted on $^{207}\text{Pb}/^{204}\text{Pb}$ - $^{206}\text{Pb}/^{204}\text{Pb}$ (a) and $^{208}\text{Pb}/^{204}\text{Pb}$ - $^{206}\text{Pb}/^{204}\text{Pb}$ (b) diagrams, in comparison with the single-stage growth curves. The parameters of the curve in (a) are: $T_o=4.43$ b.y., $(^{206}\text{Pb}/^{204}\text{Pb})_o=9.307$, $(^{207}\text{Pb}/^{204}\text{Pb})_o=10.294$; $(^{238}\text{U}/^{204}\text{Pb})_o=9.58$; the parameters of the curve in (b) are: $T_o=4.57$ b.y., $(^{208}\text{Pb}/^{204}\text{Pb})_o=29.476$, $(^{206}\text{Pb}/^{204}\text{Pb})_o=9.307$; $(^{232}\text{Th}/^{204}\text{Pb})_o=36.50$, $(^{238}\text{U}/^{204}\text{Pb})_o=9.1743$ (from Doe and Stacey, 1974).....113
- Fig.45 REE patterns of ores (a), cassiterite from Liuhe'ao (b), cassiterite from Shimen (c) and cassiterite from Baimianshan (d).....116
- Fig.46 Histograms of homogenization temperatures of fluid inclusions in cassiterite from proximal and distal deposits and in quartz from granite associated with the proximal deposit in the Xinlu ore field. The types of fluid inclusions shown on the figure are the same as explained in the text.....120
- Fig.47 Histograms of density of fluid inclusions in cassiterite from proximal and distal deposits. The types shown on the figure are the same as explained in the text.....121
- Fig.48 Composition of fluid inclusions from proximal deposits, granites and distal deposits plotted on a H_2O - NaCl - CaCl_2 diagram. The isotherms are compiled from Sheets et al. (1990), Oakes et al. (1990) and Vanco et al. (1988).....126
- Fig.49 Isochores of fluid inclusions from: (a) the proximal deposit at Liuhe'ao, (b) the distal deposit at Baimianshan, (c) the distal deposit at Shimen, and (d) the granite associated with the proximal deposit at Liuhe'ao. Solid lines represent the isochores within the calculated values by the program FLINCOR, and dash lines represent the isochores inferred from the calculated values. Black points are H_2O - NaCl system, black squares are H_2O - CO_2 system, and open squares indicate temperature and pressure at homogenization temperature.....128

- Fig.50 Comparison of REE patterns between altered and unaltered granites (a), dykes (b) and limestone (c) from the Xinlu ore field (data from table 23)..132
- Fig.51 Rose diagram showing the radial orientation of the dykes in the four dyke intrusion centres which correspond to the four tin-polymetallic ore fields surrounding the Guposhan batholith (the dykes in the central and northern part of the Xinlu ore field are not included)135
- Fig.52 Rose diagrams showing the orientation of dykes in the central and southern parts of the Xinlu ore field in relation to the local geometry of the granite intrusions136
- Fig.53 (a) the position of fault F2 with respect to the granite intrusion in the Baimianshan deposit; (b) variation of displacement of F2 along the strike (data from Xie, 1989); (c) block diagram showing the rotation of F2 caused by magmatic intrusion.....138
- Fig.54 Depth-pressure diagram showing that the contrast between hydrostatic and lithostatic pressures increases with depth.....141
- Fig.55 A schematic model showing how the depth of emplacement of the intrusion controls the sites of phase separation with respect to the intrusion. A-B and C-D represent the flow paths of the ore-forming fluids. For more detailed explanation see the text.....143
- Fig.56 Analytical models of heat conduction in concave (a) and convex (b) environments148
- Fig.57 Isotherms of the concave (a) and convex (b) models illustrated in Fig. 56....150
- Fig.58 Two-dimension steady state heat conduction models simulating concave (a) and convex (b) magma intrusion environments. Explanations see the text....152
- Fig.59 Isotherms of concave (a) and convex (b) models of steady state heat conduction illustrated in Fig. 58.....154
- Fig.60 Calculation results of steady state heat conduction models in concave (upper) and convex (lower) environments (Fig. 58).....155
- Fig.61 Unsteady state heat conduction model simulating a concave magma intrusion environment. Explanations see the text.....157
- Fig.62 Isotherms of the unsteady state model illustrated in Fig. 61, showing the thermal patterns of 90,000 years (a), 900,000 years (b), 1,800,000 years (c) and 2,700,000 years (d) after magmatic intrusion.....159

- Fig.63 Examples showing the relationship between the depth of emplacement of intrusions and the localization of associated mineralization.
 a--Schematic cross section of Xihuashan-Dangping-Piaotang tungsten mineralization district (after Tanelli, 1982); b--Cross section from Longxianggai to Changpo in the Dachang Sn-polymetallic ore field (simplified from Zheng, 1987 and Chen et al., 1987); c--Schematic section from Cornwall Sn-polymetallic ore field (after Charoy, 1979); d--Cross section of Deputaskoye Sn-polymetallic deposit (after Rundqvist, 1982); e--Cross section depicting the distribution of W grades in the Lake George Sb-W-Mo deposit (after Seal et al., 1987); f--Schematic section of the Sn-Pb-Zn-Ag mineralization district in the Zeehan-Renison Bell area (after Laznicka, 1985). For explanations see the text.....163
- Fig.64 (a) Geological map of the Camsell River Area, N.W.T. Canada; (b) Sketch section of a-a' line shown in (a); (c) sketch section illustrating the most suitable sites for the late magmatic hydrothermal mineralization in the Camsell River Area (simplified from Badham, 1975)....167
- Fig.65 Diagrammatic relationship between the fluid pressure in a fracture and the lithostatic and hydrostatic pressures in relation to depth, showing the deviation of fluid pressure from the hydrostatic pressure. Points A, B and C are explained in the text.....170
- Fig.66 Diagrammatic demonstration of the relationship between the phase separation boundary and the geometry of the magmatic intrusion for a given composition of fluid (here H₂O-salt system) and T-P condition.....173
- Fig.67 Phase boundaries plotted on a temperature-depth diagram, showing the phase separation domains for various fluid systems. (a) H₂O, P-T data from Raznjevic (1975); (b)H₂O-NaCl (30 wt%), P-T data from Sourirajan and Kennedy (1962), Haas (1976) and Bodnar et al. (1985); (c) H₂O-KCl (20 wt%), P-T data from Bodnar and Sterner (1985); (d) H₂O-CaCl₂ (5.3 wt%), P-T data from Zhang and Frantz (1989) for T>500 °C and estimated from the equation by Khaibullin and Borisov (1966) for T <500 °C (the equation is for 2.0 molal NaCl-H₂O fluid, but it can be used for other salts and other concentrations, because at T<500 °C, the variation of P with composition on the phase boundary

	is relatively small, see Zhang and Frantz, 1987); (e) H ₂ O-CO ₂ (4 mole%), P-T data from Gehrig et al. (1979); (f) H ₂ O-CO ₂ (9.7 mole%)-NaCl (1.7 mole%), P-T data from Gehrig et al. (1979); (g) H ₂ O-CO ₂ (16 wt%)-CaCl ₂ (4.7 wt%), P-T data from Zhang and Frantz (1989). Density=1.0 g/cm ³ for the hydrostatic system; =2.7 g/cm ³ for the lithostatic system	176
Fig.68	Schematic diagram showing the fluid convection patterns in convex and concave intrusion environments.....	179
Fig.69	A schematic diagram showing possible locations (A, B, C, ..., J) of mineralization with respect to the magmatic intrusion. See the text for explanation.....	182
Fig.70	A diagram showing the method of calculation of unanalysed REEs from analysed ones.....	227
Fig.71	Correlation between measured and calibrated temperatures for the U.S.G.S. Gas-Flow Heating-Freezing System.....	238

LIST OF TABLES

Table 1	Isotopic ages of granites and dykes in the Xinlu ore field.....	26
Table 2	Contents of major elements in the sedimentary rocks from Ping-Gui and adjoining regions (wt%).....	43
Table 3	Contents of some trace elements in sedimentary rocks from Xinlu and adjoining regions (ppm).....	46
Table 4	REE contents in sedimentary rocks (ppm) and some parameters.....	48
Table 5	Major element contents in granites of the Guposhan batholith (wt%).....	52
Table 6	CIPW norms of granites of the Guposhan batholith.....	54
Table 7	Contents of trace elements in granites of the Guposhan batholith (ppm).....	60
Table 8	Average content (ppm) of trace elements and some parameters in different phases of the Guposhan batholith.....	61
Table 9	REE contents and some parameters for granites of different phases of the Guposhan batholith.....	64
Table 10	Sr isotopic compositions of granites of the Guposhan batholith.....	66
Table 11	Comparison of some geochemical parameters of various phases of the Guposhan batholith with S- and I-type granites.....	69
Table 12	Some geochemical parameters for distinguishing tin-generating granites and barren or normal granites, in comparison with the average data of each phase of the Guposhan batholith.....	80
Table 13	Major element contents and CIPW norms for dykes from the Xinlu ore field.....	85
Table 14	Contents of trace elements in dykes from the Xinlu ore field (ppm).....	90
Table 15	REE contents (ppm) and parameters for dykes from the Xinlu ore filed....	94
Table 16	Sr isotope compositions of dykes from Xinlu and Shuiyanba.....	97
Table 17	Some geochemical parameters for distinguishing tin-generating granites and barren or normal granites, in comparison with dykes from the Xinlu ore filed.....	101
Table 18	Sulfur isotope compositions of ore minerals from the Xinlu ore field.....	105

Table 19	Oxygen isotope compositions of quartz, garnet and cassiterite in granites, skarns and ores from the Xinlu ore field as well as the calculated values of associated water.....	109
Table 20	Pb isotope composition of ore minerals from the Baimianshan and Shimen deposits in the Xinlu ore field.....	112
Table 21	REE contents (ppm) and some parameters in cassiterite and ores from the Xinlu ore field.....	115
Table 22	Microthermometric measurements of some fluid inclusions in cassiterite and granites from the Xinlu ore field and Dongjia'ao deposit.....	119
Table 23	Comparison of REE and some ore element contents in altered and unaltered rock pairs (ppm)from the Xinlu ore field.....	131

LIST OF PLATES

Plate 1-A	"Dark enclaves" of intermediate composition developed in the central part of the phase I granite of the Guposhan batholith.....	204
Plate 1-B	Oligoclase "envelope" around K-feldspar megacrysts in the central part of the phase I granite of the Guposhan batholith.....	204
Plate 1-C	Branches of an intermediate dyke intruding phase III granite at Liuhe'ao, also showing a xenolith of the dyke in the granite.....	204
Plate 1-D	Stratiform skarns developed near the contact zone at Liuhe'ao.....	204
Plate 1-E	Wrigglite skarn composed of rhythmic opaque mineral and fluorite layers from Liuhe'ao.....	204
Plate 1-F	Biotite replaced by muscovite in granite from Liuhe'ao.....	204
Plate 2-A	A proximal ore composed of sulfides, cassiterite, chlorite and actinolite from Liuhe'ao.....	205
Plate 2-B	Cassiterite-bearing quartz-fluorite veinlets superimposed on skarns at Liuhe'ao.....	205
Plate 2-C	Cassiterite-quartz veinlets developed at the margin of the granite intrusion at Liuhe'ao.....	205
Plate 2-D	A cassiterite-bearing sulfide vein developed in the marble at the Muqiaomian deposit.....	205
Plate 2-E	A branch of a stratiform ore body cutting the sedimentary beds at the Baimianshan deposit.....	205
Plate 2-F	A distal ore composed mainly of cassiterite and some sulfides, calcite and quartz at Baimianshan.....	205
Plate 3-A	Lens-like bedding structures developed in a stratiform ore body at Baimianshan.....	206
Plate 3-B	Bleached (white) and unbleached limestone near an ore body at Baimianshan.....	206
Plate 3-C	Bleached (white) and unbleached limestone near an ore body at Baimianshan.....	206
Plate 3-D	Cassiterite-bearing sulfide veins developed in the marble at the Shimen deposit.....	206

Plate 3-E Dolomite breccia pipe which hosts the cassiterite mineralization at Dongjia'ao deposit.....	206
Plate 3-F Cassiterite occurring in the dolomite near the breccia pipe at the Dongjia'ao deposit.....	206
Plate 4-A Calcite in an intermediate dyke.....	207
Plate 4-B Carbonate in an intermediate dyke.....	207
Plate 4-C An argillaceous fragment in an intermediate dyke.....	207
Plate 4-D Oscillatory zoning in plagioclase from an intermediate dyke.....	207
Plate 4-E Titanite in an intermediate dyke.....	207
Plate 4-F Apatite in an intermediate dyke.....	207
Plate 5-A Type-I fluid inclusion in cassiterite from the Liuhe'ao deposit.....	208
Plate 5-B Type-II fluid inclusions in cassiterite from the Dongjia'ao deposit.....	208
Plate 5-C Type-II fluid inclusion in cassiterite from the Baimianshan deposit.....	208
Plate 5-D Type-III fluid inclusion in cassiterite from the Liuhe'ao deposit.....	208
Plate 5-E Type-IV fluid inclusion in cassiterite from the Liuhe'ao deposit.....	208
Plate 5-F Type-V fluid inclusion in cassiterite from the Shimen deposit.....	208
Plate 6-A A melt inclusion with associated fluid inclusions in the granite at the Liuhe'ao deposit.....	209
Plate 6-B A melt inclusion with associated fluid inclusions in the granite at the Liuhe'ao deposit.....	209
Plate 6-C Co-existence of type-II and -V fluid inclusions in the same growth zone in cassiterite from the Shimen deposit.....	209
Plate 6-D Co-existence of type-I and II fluid inclusions in the close proximity in cassiterite from the Liuhe'ao deposit.....	209
Plate 6-E Co-existence of type-I and II fluid inclusions in cassiterite from the Liuhe'ao deposit.....	209
Plate 6-F Co-existence of type-II, -III and IV fluid inclusions in quartz in the granite from the Liuhe'ao deposit.....	209

CHAPTER I

INTRODUCTION

The extent of mineral exploration on the earth surface has been increasing rapidly. Accordingly, the difficulty of finding new mineral resources increases. One of the tasks of economic geologists is to establish ore deposit models based on the data from known deposits and apply these models to the exploration and prospecting of unknown deposits or regions. For exploration and prospecting geologists, the most important point of a model is the demonstration of the factors that control the localization of mineral deposits, because it directly influences the strategy and technique of exploration and prospecting of hidden deposits.

For intrusion-associated hydrothermal deposits, the focus of ore localization is the spatial distribution of ore deposits with respect to the intrusion. The space of the intrusion-country rock system can be divided into three parts: (1) the interior of the intrusion; (2) the contact zone which consists of the marginal part of the intrusion and the adjacent country rocks, and (3) the country rocks relatively far from the intrusion (Fig. 1). Most intrusion-associated hydrothermal deposits are located in part 2 and 3 (Strong, 1988). Rundkvist (1977) estimated that of more than 800 rare-metal deposits related to granites worldwide, 41.3% are from the endocontact, 27.5% from the exocontact, and 31.2% from the exo- and endocontact. His "endocontact" and most of the "exo- and endocontact" are probably in part 2, and "exocontact" mainly in part 3. Ginzburg et al. (1974) divided the intrusion-country rock system into three parts: intra-intrusive, exocontact, and over-intrusive. His "intra-intrusive" and "exocontact" correspond to part 2 in Fig. 1, and "over-intrusive" to part 3. Since part 2 stands for the transitional zone between the intrusion and the country rocks and host most of the deposits, while part 3 stands for another condition and host the rest of the deposits, the problem of the localization of intrusion-associated hydrothermal deposits is in fact a problem of ore deposition in part 2 vs. part 3. In the following text, the term "proximal" is used to refer to the space of part 2, and "distal" to the space of part 3. Accordingly, the deposits which are located in part 2 are defined as "proximal deposits", and those which are located in part 3 are defined as "distal deposits". This division is of

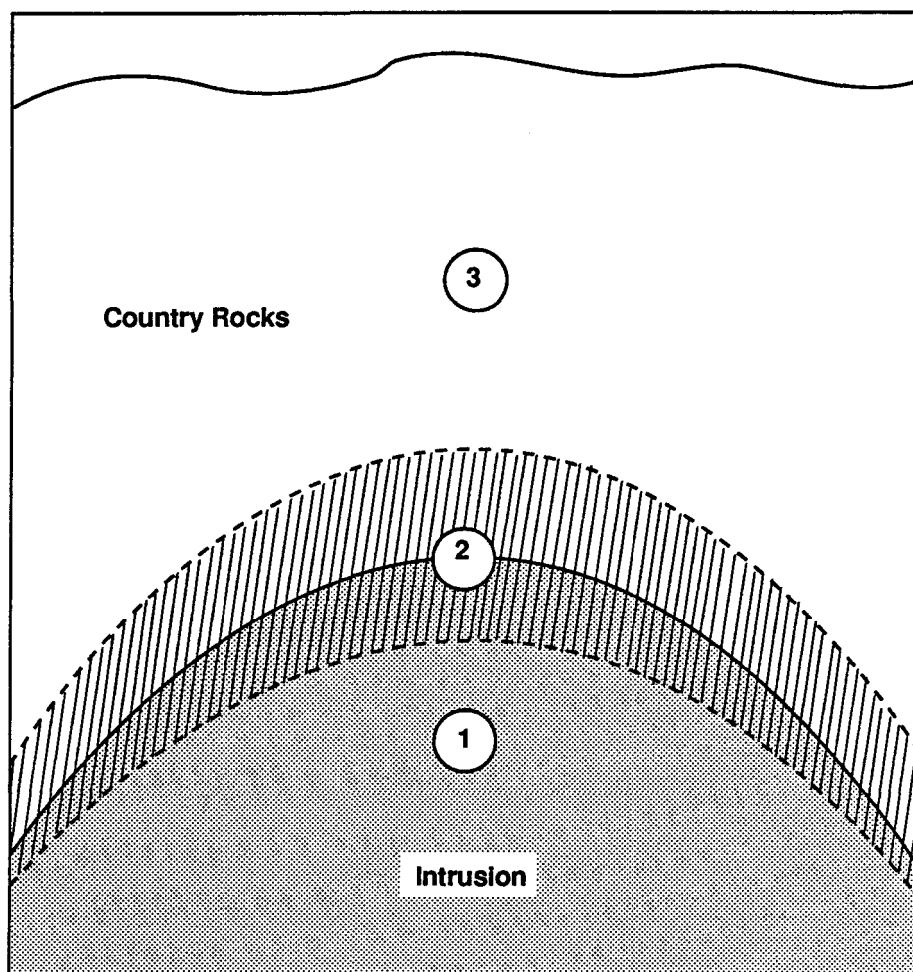


Fig. 1 Schematic diagram showing spatial zones within a space of the intrusion-country rock system (not to scale). (1) the interior of the intrusion; (2) the transitional zone between the intrusion and the country rocks, referred to as "proximal area" in the text; (3) the country rocks relatively far away from the intrusion, referred to as "distal area" in the text.

practical significance for prospecting geologists, because it differentiates two regions which are apparently distinct as prospecting targets.

What is the mechanism that controls the separation of proximal and distal deposits? In other words, why are some deposits situated near the intrusion-country rock boundary, while others occur relatively far away from the intrusion? This is largely dependent on specific kinds of deposits and geological conditions. Traditionally, the spatial arrangement of ore deposits with respect to the intrusion is mainly referred to metal zoning, e.g. in the sequence of Sn and Cu at depth giving way to Pb, Zn and eventually Fe, Sb and Mn at the highest levels in the Cornubian ore field (Willis-Richards and Jackson, 1989), or from W through Sn to Cu and Pb zones in Herberton tinfield of Australia (Blake and Smith, 1970), although some zones may be absent in individual mineralization centres (Taylor and Steveson, 1972), or from Sn, W, As and U through U, Ni and Co to Cu to Pb-Zn-Ag to Fe and Sb sulfides as a general model for granophile deposits (Strong, 1981).

The zoning patterns reflect the spatial differentiation of different elements or element assemblages, and can serve as a useful exploration guide in searching for hidden deposits (Strong, 1988). However, they do not account for the phenomenon that the concentration of the same element (e.g. Sn) or element assemblage (e.g. Sn+W) can be spatially differentiated with respect to the intrusion; in other words, the same metal or metal assemblage can form proximal deposits in some cases and distal deposits in other cases. For instance, Sn skarns can occur at the contact between the intrusion and the country rocks (proximal tin skarns) or more than 500 metres from the intrusion (distal tin skarns) (Kwak, 1987). Although these two types of Sn skarns have different mineral assemblages (Kwak, 1987), both of them are tin ores, and their localization does not seem to be simply the effect of metal zonation. Many examples showing the spatial separation of proximal vs. distal rare-metal hydrothermal deposits with respect to the intrusion can be found (Chi et al., 1991), e.g. the Xinlu (this study) and Dachang (Zheng, 1987) tin-polymetallic ore fields in southern China, tin-polymetallic deposits in Cornwall (Charoy, 1979), Pb-Zn-Ag-Sn deposits in Zeehan-Renison Bell area of west Tasmania (Laznicka, 1985), Lake George W-Mo deposits in southern New Brunswick (Seal et al., 1987), Panasqueira W-Cu (Ag)-Sn deposits in Portugal (Polya, 1989), etc. In all these examples, both proximal and distal deposits exist, and the localization of the ore bodies does not seem to be simply the effect of metal zonation, because the mineralization of the same metal (e.g. Sn) or metal assemblage (e.g. Sn+Zn) can be greatly separated spatially with respect to the intrusion. A question arises, are there

certain factors other than metal zonation that control the separation of proximal and distal deposits?

The object of this thesis is an attempt to answer this question by studying the ore localization in the Xinlu tin-polymetallic ore field, Guangxi Autonomous Region of the Zhuang Nationality, southern China. This is a highly explored ore field. Five tin-polymetallic deposits and a number of ore occurrences have been found within the 90 km² area. Since most of the reserve has been used up, searching for new reserve has been an urgent task for the geologists working in the mine. More than 280 bore holes have been drilled (Fig. 2). However, with the increase in the extent of prospecting, the economic efficiency of diamond drilling becomes a major factor. Two problems face the prospecting geologists: where should the drilling be targeted? How deep should the holes be drilled? The latter cannot be too strongly emphasized, since the idea that the contact zone between the granites and the country rocks is a potential site of mineralization might drive people to drill as deep as possible to reach the unexposed granites, which is not necessary in many cases. Therefore, the study of the factors controlling ore localization is of practical significance for the Xinlu ore field.

Both proximal and distal tin-polymetallic deposits exist in the Xinlu ore field, exhibiting a variable spatial distribution of the deposits with respect to the granite intrusions. The obvious difference between proximal and distal tin deposits as to their distance from the intrusions and their similarity in mineral and metal assemblages exclude metal zonation as the major mechanism of the separation of proximal and distal tin deposits. There must be other factors which are more effective than metal zonation in controlling the tin ore localization.

In order to understand the mechanism of the ore localization, particularly of the separation of proximal and distal deposits in the Xinlu ore field, the following aspects have to be considered.

First of all, the sources of the ore-forming fluids must be determined, as different sources have different influence on ore localization. The deposits in the Xinlu ore field show evident affiliation with the granite intrusions, as is indicated by the spatial and temporal relationship with the granites, and by the geochemical features of the ores and granites (Qin, 1985; Deng, 1984, 1985; Yang, 1986; Shan, 1987; Liu and Yuan, 1989). However, the observation that most of the distal ore bodies are hosted directly by sedimentary rocks instead of granites and that a few ore bodies are stratabound and are in conformity with the

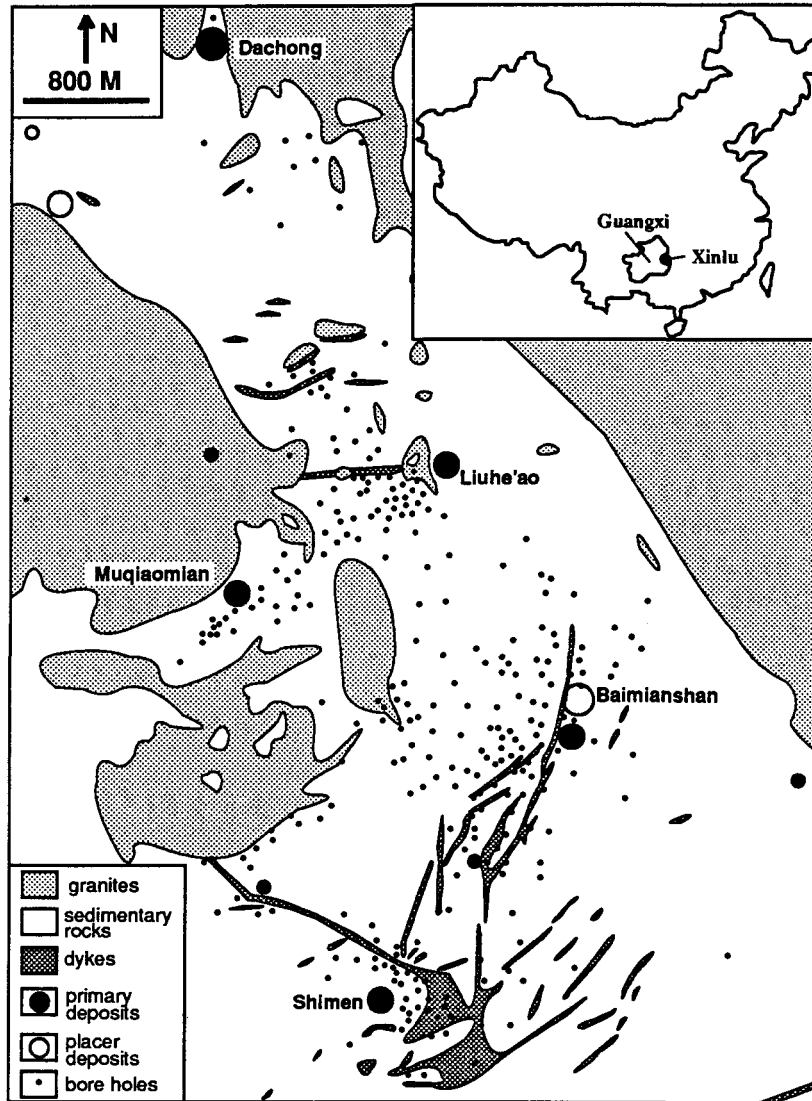


Fig. 2 A map showing the extent of the Xinlu tin-polymetallic ore field, the distribution of ore deposits and diamond drill holes (compiled after the unpublished data of No.204 Geol. Team of Guangxi, 1986, and Ping-Gui Mining Bureau, 1986). The insert map shows the position of Xinlu in Guangxi, China.

sedimentary beds has encouraged some authors (e.g. Zheng, 1987; Li, 1985; Li, 1986; Qiu, 1989) to suggest that certain sedimentary beds have provided most of the ore-forming components in the ore-forming fluids. Besides, the obvious spatial correlation between mineralization and dykes (Chi, 1989a) suggests a possibility that the dykes may have also contributed some ore-forming components to the mineralization. The question is: is the granite the major source of the ore-forming fluids? If there are some contribution from other sources, do they greatly influence the localization of ore deposits? This requires a study of the geochemical characteristics of the ores and the ore-forming potential of the host rocks.

Secondly, a study of the migration processes of the ore-forming fluids is necessary, since they determine where the ore-forming fluids go. The migration of ore-forming fluids is mainly related to the system of conduits and the flow dynamics of the ore-forming fluids. The conduit system consists of a series of channels which have higher permeability than the neighbouring segments during the period of mineralization and are connected to the sources of the ore-forming fluids. The structures (faults and fractures) developed in the host rocks before and during the period of mineralization are likely to be used as conduits. However, not all faults and fractures are linked to the sources of the ore-forming fluids, and they do not always have high permeability as they can be sealed if they stop being active, especially in carbonate rocks; only the fractures produced, and the faults reactivated, by granite intrusion can meet the demand of a conduit. This requires a study of the identification of intrusion-produced or -reactivated structures. Since it is observed that most of the deposits in the Xinlu ore field and adjoining ore fields are spatially close to dykes, it is possible that the structures that control the intrusion of the dykes have been preferentially used as conduits of the ore-forming fluids. This requires a study of the temporal and genetic relationship between the dykes and the major sources of the ore-forming fluids.

The flow dynamics of the ore-forming fluids directly influences the localization of the deposits. Since the contact zone between the intrusions and the country rocks represents a potential trap of ore-forming components due to its position as a pressure transition zone (Cunningham, 1978) and the highly unusual depositional environment provided by the skarns which are often developed at the contact (Kwak, 1987), the spatial separation of proximal and distal deposits is actually determined by the contrast of the ability of the contact zone to trap the ore-forming components vs. the ability of the ore-forming fluids to break through the contact zone. Both aspects are closely related to the dynamic behavior of the ore-forming fluids. Since the flow dynamics of the ore-forming fluids is related to their

properties such as composition, temperature, density, pressure and phase status, which can be observed or inferred from fluid inclusion study, a study of fluid inclusions in ores and source rocks is necessary.

Thirdly, the conditions of deposition must be studied, because they directly determine the precipitation of ore-forming components. The formation of a deposit requires favourable conditions of deposition, which lead to the accumulation of the ore-forming materials in a limited area. It has been noticed by various authors that hydrothermal deposits occur where the highest temperature gradients exist (e.g., Sams and Thomas-Betts, 1988). Since the Xinlu ore field has an intrusion shape (concave) which is somewhat different from usual cases, and the thermal field of which have not been specially studied, a study of the temperature gradient in this kind of intrusion environment is needed.

In brief, the objective of this thesis is to establish a model which deals with the mechanism of the localization of the tin deposits with respect to the granite intrusions in the Xinlu ore field. The various factors to be considered in the model are illustrated in Fig. 3. The model should explain why some tin deposits are located at the contact zone, while others are situated in the country rocks far from the granites. The results are believed to be of practical significance for the further prospecting in the Xinlu ore field, and some of the rules concerning the localization of hydrothermal deposits as revealed in this study may be of more general application in ore prediction.

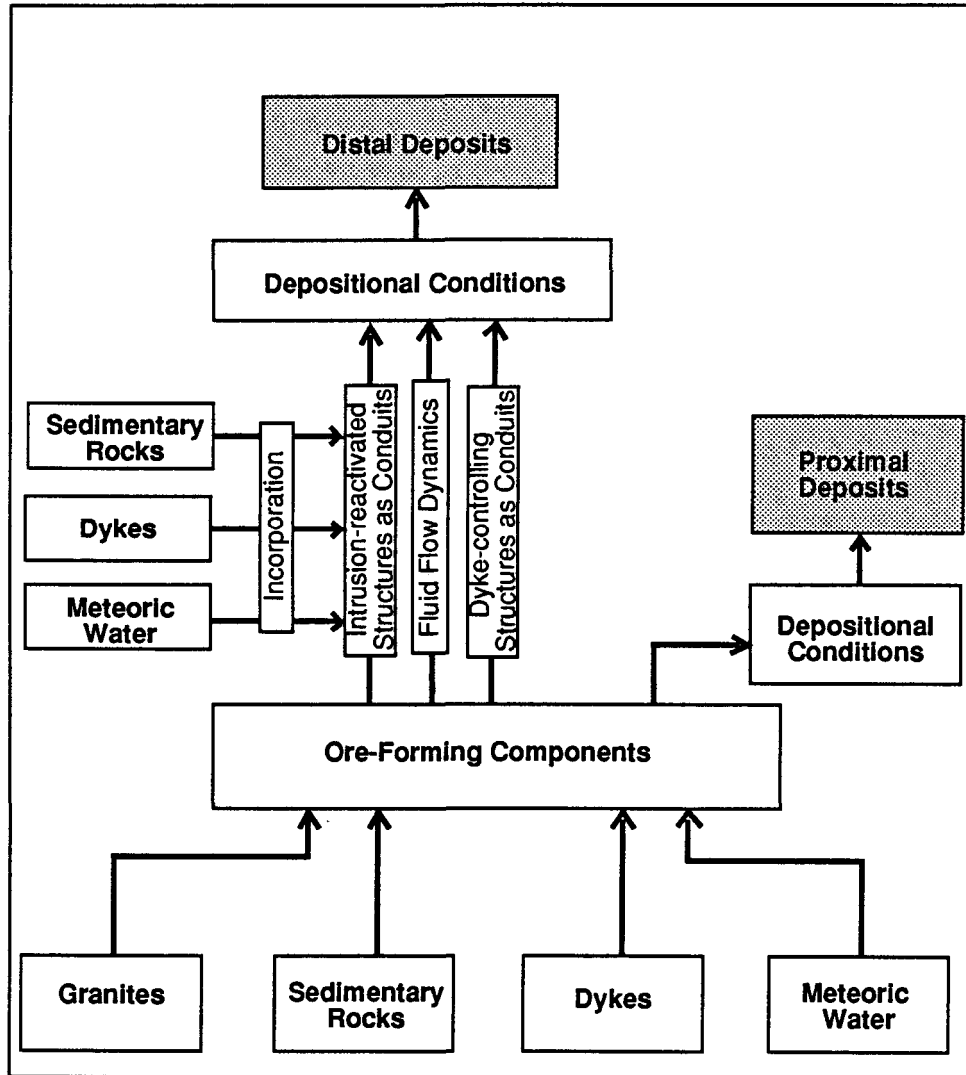


Fig. 3 A schematic diagram showing the various factors considered in the model of ore localization in the Xinlu ore field.

CHAPTER II

REGIONAL GEOLOGICAL SETTING

2.1 Introduction

The Xinlu ore field is located in eastern Guangxi Autonomous Region of the Zhuang Nationality, southern China. It is an important part of the Ping-Gui tin-polymetallic mineralization district which, with an area of about 6000 km² and comprising several ore fields, is one of the major tin ore-producing camps in China.

In regional tectonic framework, the Ping-Gui mineralization district belongs to the Southeast China Diwa Region (Fig. 4), which is the result of the reactivation of a mainly Late Paleozoic platform in Mesozoic time. The Diwa region stands for a new type of geotectonic element apart from the better-known geosynclinal and platform regions, and is the result of platform activation, characterized by block-faulting and intense magmatic (esp. granitic) activity as well as the formation of a large number of continental basins (Chen, 1959, 1965, 1988). Much of China is composed of this type of geotectonic element (Chen, 1988; Fig. 4). The Southeast China Diwa Region is a typical platform activation region, and is held to be the classic model for comparison with other regions having similar character both in China and abroad (e.g. Sheglov, 1968; Laznicka, 1986; Chi, 1989b). A large number of granite intrusions were emplaced in the SE China Diwa region during the Diwa geotectonic stage (mainly Mesozoic), and gave rise to many rare-metal deposits, which make this region known as "hometown of rare metals (principally W, Sn, Nb and Ta)". The Guposhan and Hushan granite batholiths, to which most of the tin-polymetallic deposits in the Ping-Gui district are related, are among these diwa-stage granites (Chi, 1989a).

2.2 Tectonic Evolution

The tectonic history of the Ping-Gui mineralization district can be divided into three stages, namely, the geosynclinal stage, the platform stage and the Diwa (platform activation) stage.

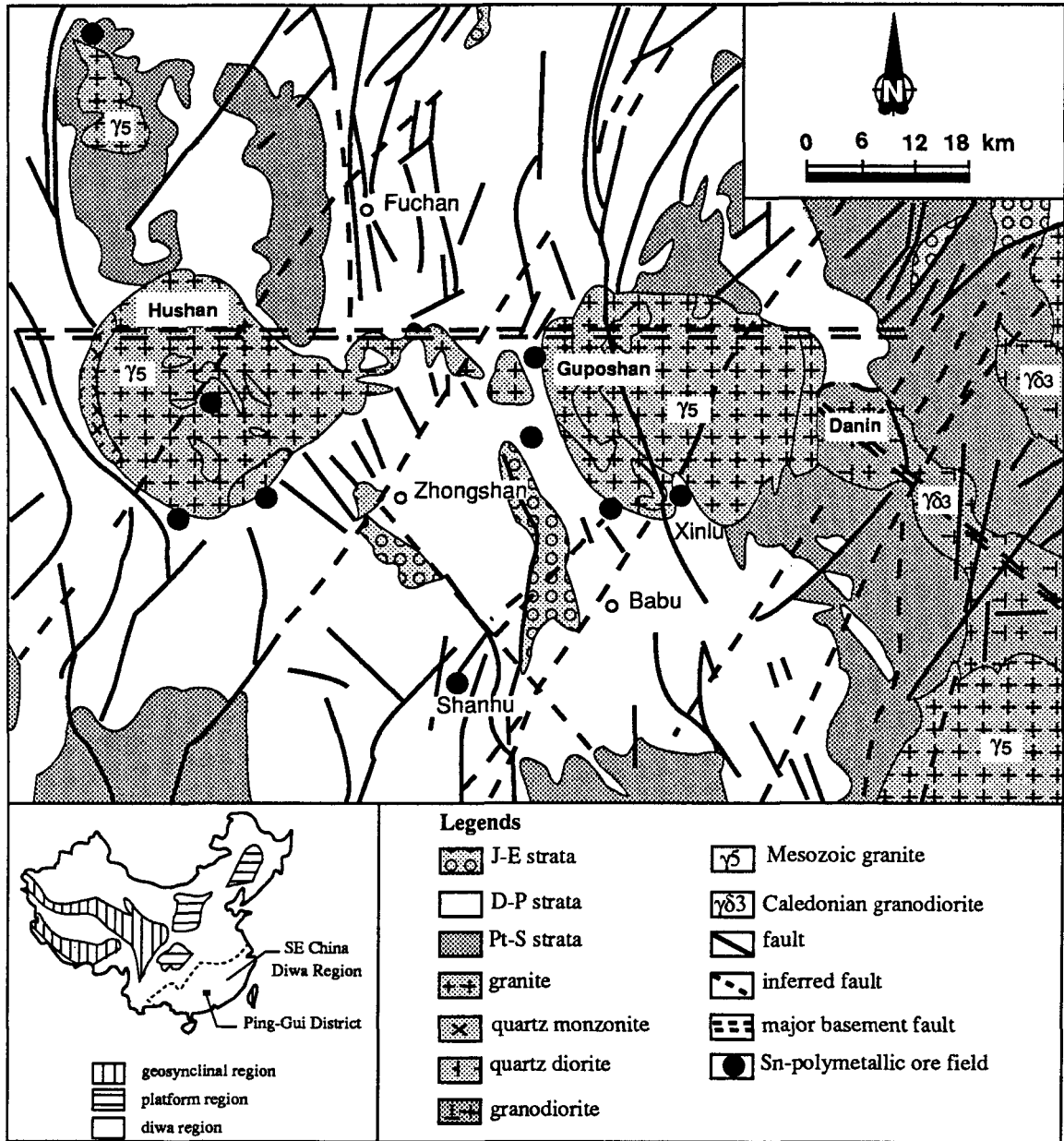


Fig. 4 Geological map of the Ping-Gui mineralization district, and an insert map showing its position in the tectonic framework of China (modified from Hu, 1986)

The geosynclinal stage began in the Proterozoic and ended at the end of Silurian. In this stage, marine flysch formations more than 8000 metres thick were formed in the geosyncline, a part of the Caledonian Southern China geosynclinal region. The Caledonian Movement which took place at the end of Silurian terminated the geosynclinal regime and deformed the sedimentary rocks and metamorphosed them slightly, accompanied by intrusion of granodiorite magma. After a short period of erosion of the folded belt, the region attained a relatively stable stage--the platform stage --which began in Devonian and ended after Early Triassic. This stage is characterized by the development of widespread carbonate and shale-sandstone formations similar to the other parts of the Southern China region.

Following the Early Triassic, a strong tectonic movement, the Indo-China Movement, took place and broke up the platform, starting the Diwa stage, which ranges from Middle Triassic to the Cenozoic. The Diwa stage is divided into three periods: the "initial-mobility period" (T₂-T₃), the "maximum-mobility period" (J-K) and the "residual-mobility period" (E-Q) (see Chen, 1988). In the initial-mobility period, the strata which were formed in the platform stage were folded and faulted as a result of the Indo-China movement, and some granite magma intruded the sedimentary rocks of the platform and the geosynclinal stages. In the maximum-mobility period, which began in the Jurassic, tectonic movements (Yanshanian) took place frequently and intensively, which further deformed the pre-existent strata and structures; large quantities of granite magma were emplaced in the upper crust, forming the large Guposhan and Hushan granite batholiths (Fig. 4). Most of the Sn-polymetallic deposits in the Ping-Gui mineralization district were formed in this period.

The tectonic evolution of this region is illustrated in Fig. 5. It is shown that in the geosynclinal stage, the sedimentation, magmatism, metamorphism and tectonism took place in a plate subduction environment, while in the Diwa stage, tectonomagmatism took place in an intra-continental environment. It is also shown that the structure of the crust is more complex in the Diwa stage than in the previous stages.

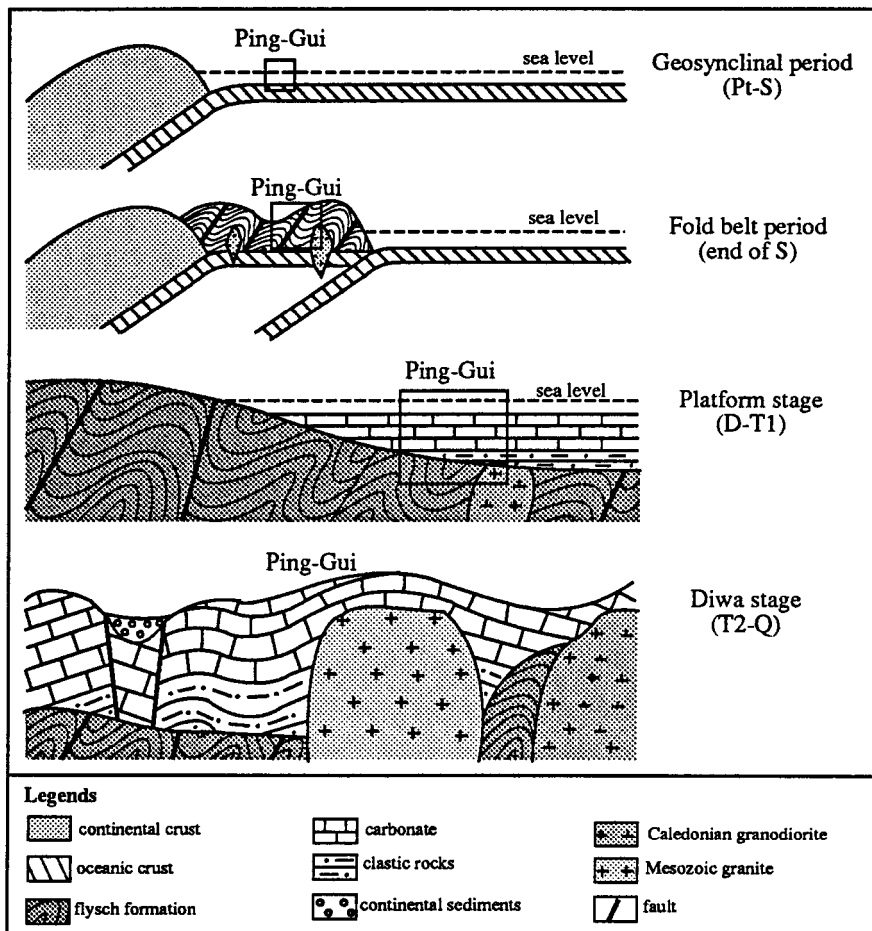


Fig. 5 Schematic diagrams illustrating the tectonic evolution of the Ping-Gui district (not to scale)

2.3 Stratigraphy

The strata in the Ping-Gui district range from the Proterozoic to the Quaternary. They belong to three "structural layers" (see Chen, 1988) according to their tectonic stages, namely the geosynclinal, platform and Diwa structural layers (Fig. 6).

The geosynclinal strata (Proterozoic to Cambrian), with a thickness of 8153-9997 metres (see Fig.6), consist of unmetamorphosed and slightly metamorphosed sedimentary rocks, including feldspar-quartz sandstone, shale, silty sericite shale, quartz sandstone, siltstone, phyllitic slate, silty phyllite, sericite phyllite, chlorite phyllite and tuffaceous phyllite. The following rocks are commonly found in the form of intercalated beds: carbonaceous shale, phosphatic rocks, pyrite-rich beds, banded magnetite, hematite, specularite deposits, marble, dolomite, spilite and keratophyre. The lowest part consists of biotite-quartz schist and biotite-plagioclase schist.

The platform strata (D-T₁) are characterized by the development of carbonate, although clastic rocks are also important components. The lower part of this structural layer (D_{2y}-D₁₁), with a thickness of 1183-2168 metres, consists mainly of clastic rocks, including fine-grained sandstone, siltstone, sandy shale and shale, and small amounts of limestone, dolomite, argillaceous limestone, argillaceous dolomite, conglomerate and iron deposits. The middle part of the platform structural layer (D_{2d}-P₁), with a thickness of 2127-3156 metres, is mainly composed of carbonate, including limestone, dolomite, argillaceous limestone and dolomitic limestone, and small amounts of siliceous shale, chert, carbonaceous shale, silty shale and siltstone. The upper part of the platform structural layer (P₂-T₁), with a thickness of 568-756 metres, consists mainly of clastic rocks (argillaceous siltstone, carbonaceous shale, shale, sandstone) and minor amounts of siliceous rocks and limestone, with a few intercalated beds of intermediate tuff, coal beds, dolomite, siderite and manganese concretions. The platform strata are widely distributed in the central, northern and western parts of the Ping-Gui district, and is the major host rocks of the Sn-polymetallic mineralization.

The Diwa strata (T₃-Q), with a total thickness up to 1733 metres, consist of shale, feldspar-quartz sandstone, siltstone and silty shale, with a small number of intercalated beds of coal, carbonaceous clastic rocks, siliceous rocks, acidic and intermediate-acidic volcanics. The strata from J to E are mainly restricted to several small continental basins, while the Quaternary deposits are scattered everywhere. The Diwa strata are not related to

Erathem or System	Units of Strata	Column	Thickness (metres)	Major Components	Tectonic Episodes	Geotectonic Stages
Q	(Q)		0-100	sands & pebbles	Himalayan	Diwa Stage
E	(E)		137	siltstone & conglomerate	Yanshanian V	
K	(k2)		190	acidic volcanics	Yanshanian IV	
	(K1)		89-420	shale, sandstone	Yanshanian III Yanshanian II Yanshanian I	
J1	Shiti Formation (J1s)		265-520	shale, sandstone		
	Daling Formation (J1d)		60-192	sandstone, sandy shale, limestone		
	Tiantang Formation (J1t)		0-174	shale, siltstone, breccia	Indo-China II	
T1	(T1)		>146	limestone, shale	Indo-China I	Platform Stage
P	Dalong Formation (P2d)		22	siliceous rock		
	Heshan Formation (P2h)		400-588	siltstone, shale sandstone	Hercynian	
	Gufeng Formation (P1g)		143	siliceous rock, limestone		
	Qixia Formation (P1q)		66-79	limestone		
C	Hutian Group (C2+3h)		>180	dolomite, limestone		
	Locheng Member (C1l)		280	limestone dolomite		
	Shimen Member (C1s)		110	siliceous rock		
	Huangjin Member (C1h)		430	limestone		
	Yanguan Stage (C1y)		200-230	limestone, dolomite		
D	Rongxian Formation (D3r)		137-417	limestone dolomite		
	Guilin Formation (D3k)		150-250	limestone dolomite		
	Donggangling Formation (D2d)		431-1037	limestone dolomite		
	Yujiang Formation (D2y)		568-865	sandstone shale		
	Nagaoling Formation (D1n)		73-440	shale, siltstone, limestone		
	Lianhuashan Formation (D1l)		542-863	sandstone, shale limestone, conglomerate		

Fig. 6 (to be continued next page)

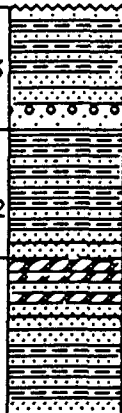
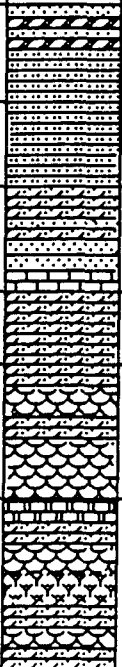
					Caledonian		
	Shuikou Group (€sh)	sh3		>1971	quartz sandstone feldspar sandstone, shale	Geosynclinal Stage	
		sh2		1344-1485	sericite shale, quartz sandstone feldspar sandstone		
		sh1		>1373	quartz sandstone feldspar sandstone, sericite shale, siliceous rocks		
Z	zb			184	feldspar sandstone, siliceous rocks		
	za			400	feldspar sandstone		
Pt	Banxi Group (P _{tb})	P _{tb} 4		730-1100	phyllite, quartz-feldspar sandstone, marble		
		P _{tb} 3		790-860	phyllite, silty phyllite, schist		
		P _{tb} 2		495-1335	phyllite, tuffaceous phyllite, breccia tuff, spilite		
				866->1289	tuffaceous phyllite, breccia tuff, spilite, keratophyre, schist, dolomite		

Fig. 6 Strata, tectonic episodes and geotectonic stages of the Ping-Gui district (compiled from unpublished data of No. 204 Geol. Team of Guangxi, 1986).

primary Sn mineralization, although the Quaternary deposits around the granite intrusives and near primary Sn mineralization are the main sources of Sn placers.

2.4 Structures

The structures in the Ping-Gui mineralization district are divided into two systems: the basement structures which were formed in the geosynclinal stage and developed mainly in the geosynclinal structural layer and the cover structures which were formed in the Diwa stage and developed in both platform and geosynclinal structural layers.

The basement structures were formed during the Caledonian orogeny. They are mainly developed in the geosynclinal structural layer, but may be reactivated and penetrated into the cover strata during the diwa stage. NW-trending (south of the Guposhan batholith), NE-trending (north of the Guposhan batholith) and EW-trending folds and faults are exposed in basement outcrops. A major EW-trending basement fault is inferred from the distribution of Huashan and Guposhan granite batholiths of Mesozoic age (Hu, 1986) and from analysis of terrane tectonics (Yuan and Yang, 1988). A major NW-trending fault is inferred along the NW-trending Danin granodiorite batholith of Caledonian age. EW-trending structures and NS compression stress seem to be dominant during the Caledonian orogeny in this region (Hu, 1986). However, if taking southern China as a whole, NE-trending folds and accompanying reverse faults are dominant in the geosynclinal structural layer, indicating the NW-SE compression stress field (Fig. 7). The somewhat abnormal Caledonian structures in Ping-Gui district may be the result of distortion of the regional NW-SE compression stress due to the influence of local boundary conditions. It is also possible that the basement of the Ping-Gui district belongs to a terrane which originated differently from the rest of the southern China. It is proposed that the Huashan-Guposhan basement fault is part of the suture zone of this proposed terrane (Yuan and Yang, 1988).

The cover structures were formed during the Indo-China and Yanshanian orogenies in the Diwa stage. The Indo-China orogeny is the first tectonic orogeny of the Diwa stage. The folds and reverse faults in the platform structural layer were mainly formed during this orogeny. In the Ping-Gui district, they are mainly NS-trending (Fig. 4), which belongs to a NS-trending structural belt, indicating E-W compression. Although there are several other NS-trending structural belts of this age, most of the folds and reverse faults of Indo-China age are NE trending in southern China, indicating NW-SE compression. The NS-trending

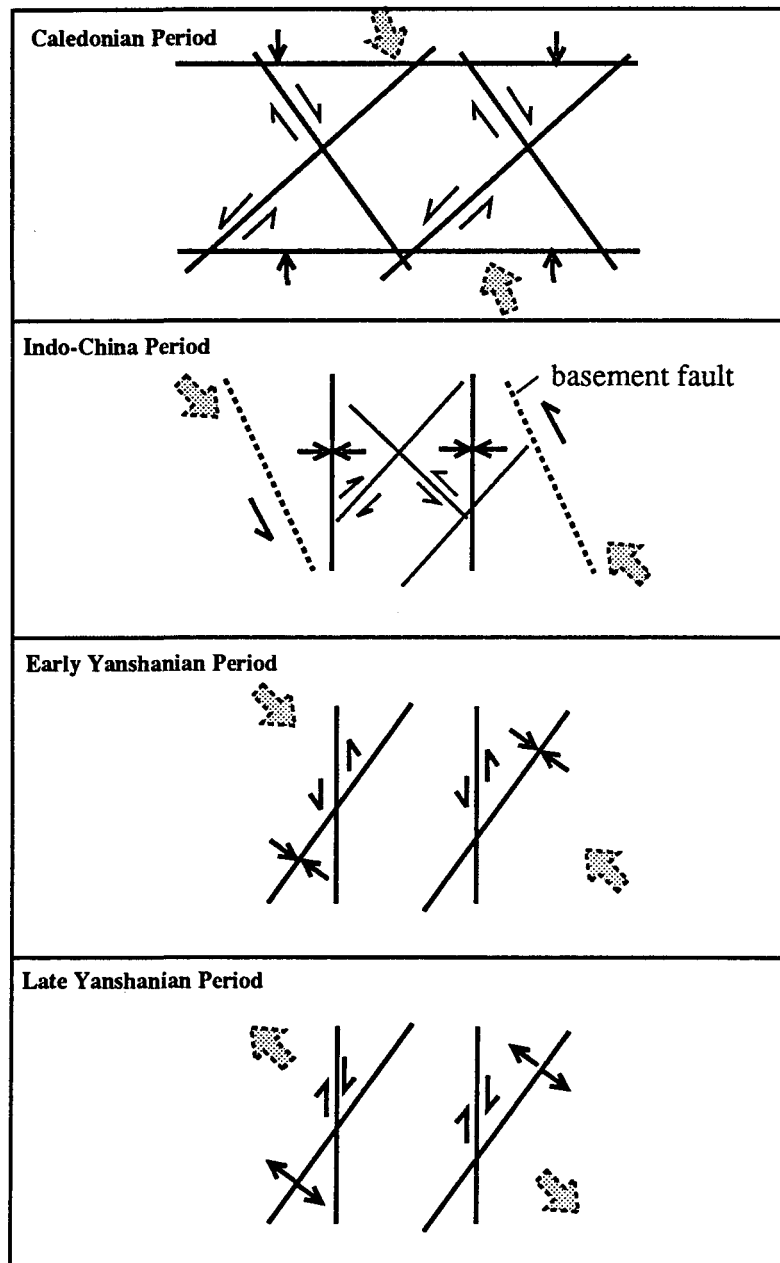


Fig. 7 A sketch diagram showing the evolution of the stress field in the Ping-Gui district. The thick shaded arrows indicate the regional compressive stress in southern China, and the solid arrows indicate the local stress field in the Pin-Gui district.

fold-fault belts are probably the result of sinistral shearing of NW-trending basement faults in the stress field of NW-SE compression (Fig. 7; Chi, 1989c). The locally NW-trending Indo-Sinian folds (southwest of Guposhan batholith) are probably the results of sinistral shearing of the EW-trending basement faults in the E-W compression stress field (Hu, 1986).

Apart from the structures formed in the Indo-China orogeny, a number of structures (mainly fractures) were formed during the Yanshanian orogeny, which is the most important tectonic event in eastern China in Mesozoic time. It consists of five episodes, and at least three of them are recognizable in the Ping-Gui district. The Early Yanshanian movements (Episode I, II, III) are shown by the unconformity between J₁ and K₁ (Fig. 6). As in the rest of southern China, the NW-SE compression stress field prevailed in the Ping-Gui district. Since the platform structural layer had undergone deformation related to the Indo-China orogeny, fracturing prevailed over folding. The well-developed NE-trending fractures were mainly formed in this period. At the same time, pre-existent faults were subject to different kinds of reactivation. The NS-trending faults were likely to undergo sinistral shearing (Fig.7). In the Late Yanshanian period (episode IV, V), with the development of the NE-trending Eastern Hunan rift system (Chi, 1989c), the stress field changed radically. NW-SE extensional stress became dominant. As a result, the pre-existent NE faults became tensional, and NS faults underwent dextral shearing (Fig. 7).

2.5 Intrusives

There are several granitic, granodioritic and dioritic intrusions in the Ping-Gui district. Among them the Danin granodiorite batholith was formed in the geosynclinal stage (Caledonian), and the others were formed in the Diwa stage (mainly in the Yanshanian period, partly in the Indo-China period). The Danin granodiorite batholith is situated at the eastern margin of the Ping-Gui district (Fig. 4). It was emplaced into the geosynclinal structural layer. No tin-polymetallic mineralization is observed to be directly related to this intrusion. The Guposhan and Hushan granite batholiths are the major intrusions which are related to the tin-polymetallic mineralization in the Ping-Gui district. Both show multiple episodes of intrusion, and have several ore deposits around them (Fig. 4). The Xinlu ore field is spatially related to the Guposhan batholith.

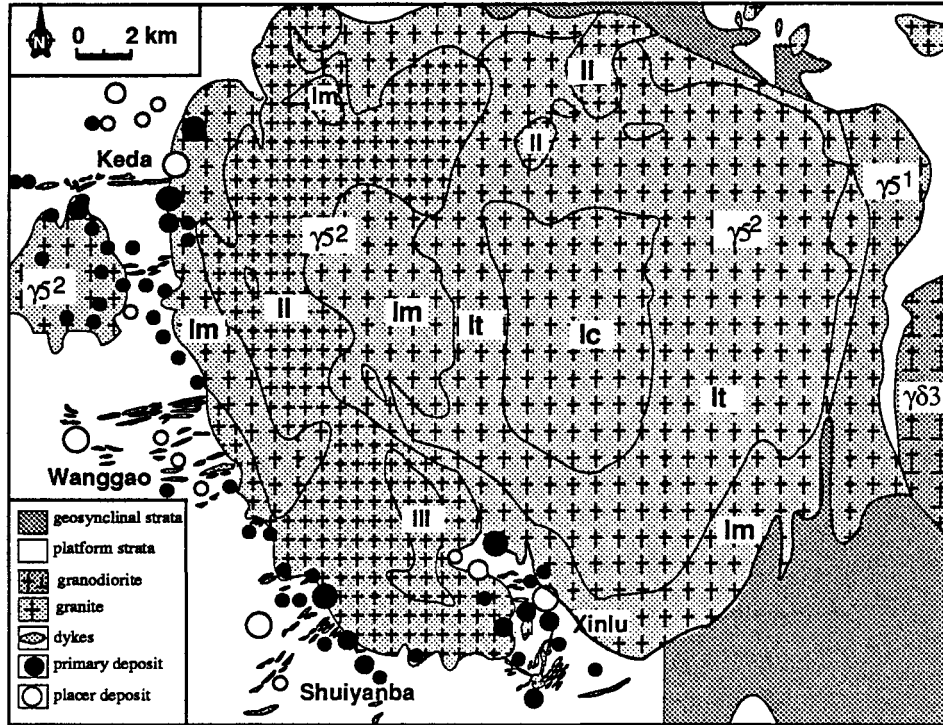


Fig. 8 Geological map of the Guposhan batholith (modified from unpublished map of No.8 Geological Team of Guangxi, 1981). $\gamma 3$ - Caledonian granodiorite; $\gamma 1$ -Indo-China granite; $\gamma 2$ -Yanshanian granite (I-phase I; II-phase II; III-phase III; Ic-central part of phase I; It-transitional part of phase I; Im-marginal part of phase I).

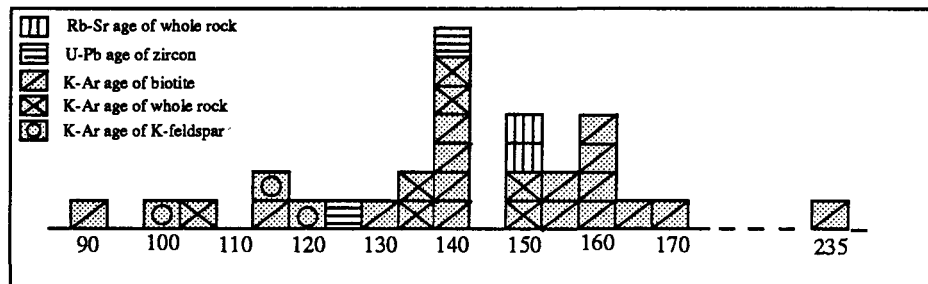


Fig. 9 Histogram of isotopic ages of the Guposhan batholith (compiled from the data collected by Ping-Gui Mining Bureau, 1986).

The Guposhan granite batholith is composed of intrusive phases of Indo-China (T2–T3) and Yanshanian (J-K) ages (Fig. 8) according to the geological mapping (unpublished data of No.8 Geological Team of Guangxi, 1981). The Yanshanian age intrusions, which are the major components of the batholith, consist of at least three phases: I, II and III, corresponding to three episodes of intrusion. Clear intrusion contacts are observed: phase I is cut by phase II, and phase II is cut by phase III (Qin, 1985). Isotopic ages (K-Ar, Rb-Sr and U-Pb ages of biotite, K-feldspar, zircon and whole rocks) cover a range from 90 to 235 Ma, mainly between 100 and 170 Ma (Fig. 9). Phase I occupies about 3/4 of the area of the Guposhan batholith. It is composed of three zoning parts (Ic, It and Im, see Fig. 8) with transitional boundaries. The central part (Ic) is composed of median- to fine-grained porphyritic hornblende biotite granite, which contains numerous dark enclaves (E) of intermediate composition with microlitic and porphyritic texture (Plate 1-A). The transitional part (It) is composed of median- to coarse-grained porphyritic biotite granite, and the marginal part (Im) is composed of coarse- to extremely coarse-grained (locally median- or fine-grained) biotite granite. Phase II occurs in irregular bands within phase I, mainly in the western part of the batholith. It is composed of median- to fine-grained porphyritic biotite granite. Phase III consists of small stocks, which are scattered in phase I and II as well as in the country rocks surrounding the batholith. It is composed of fine-grained or fine-grained porphyritic biotite granites. The composition tends to be more and more felsic from phase I through II to III and from Ic through It to Im in phase I.

Apart from the granite batholiths, a number of dykes were formed in the Yanshanian period. There are four groups of dykes surrounding the W-SW-S contact zone of the Guposhan granite batholith, distributed in Keda, Wanggao, Shuiyanba and Xinlu respectively (Fig. 8; Chi, 1989a). Each group consists of tens of dykes. In Keda and Wanggao, most of the dykes are quartz porphyry or granitic porphyry, while in Shuiyanba and Xinlu, intermediate dykes are dominant. All the dykes are arranged radially around the Guposhan batholith, trending in EW direction in Keda, EW to ENE in Wanggao, NE in Shuiyanba and N-S to NNE in Xinlu (Fig. 8).

CHAPTER III

CHARACTERISTICS OF THE XINLU ORE FIELD

3.1 Geological Features of the Ore Field

The Xinlu ore field, comprising five tin-polymetallic deposits and several ore occurrences and with an area of 90 km², is situated at the southern margin of the Guposhan granite batholith, and is one of the four tin-polymetallic ore fields surrounding the Guposhan batholith (Fig. 4 and 8). It is covered by platform-stage sedimentary rocks which are underlain by unexposed granites, and is bordered on three sides by the granites of the Guposhan batholith. Dykes of various compositions are widespread, and structures are well developed (Fig. 10). All these geological factors are related to the tin mineralization to varying extents, and are described in this section.

3.1.1 Sedimentary rocks

The sedimentary rocks in the Xinlu ore field are mainly Devonian and Lower Carboniferous carbonate and clastic rocks, including (from lower to upper) the Nagaoling (D_{1n}), Yujiang (D_{2y}), Donggangling (D_{2d}), Guilin (D_{3k}) and Rongxian (D_{3r}) Formations. The lower formations (D_{1n}, D_{2y}) are mainly clastic rocks, while the upper formations (D_{2d}, D_{3k} and D_{3r}) are mainly carbonate rocks. Petrography of selected samples of these formations are described in appendix A. The clastic formations include fine-grained sandstone, siltstone, argillaceous sandstone and shale, with intercalated beds of argillaceous limestone and lens-like limestone. The carbonate formations are mainly composed of limestone, argillaceous limestone, dolomitic limestone, dolomite, bioclastic limestone and lens-like limestone.

The sedimentary rocks strike in NNW direction, and dip toward SSW, with the lower formations exposed in the eastern part of the ore field, and the upper formations in the west (Fig. 11). In the northern part of the ore field, the granite magmas intruded the sedimentary rocks up to the level of the Rongxian Formation (D_{3r}), while in the southern part the Nagaoling Formation (D_{1n}) or lower Formations are preserved and in contact with

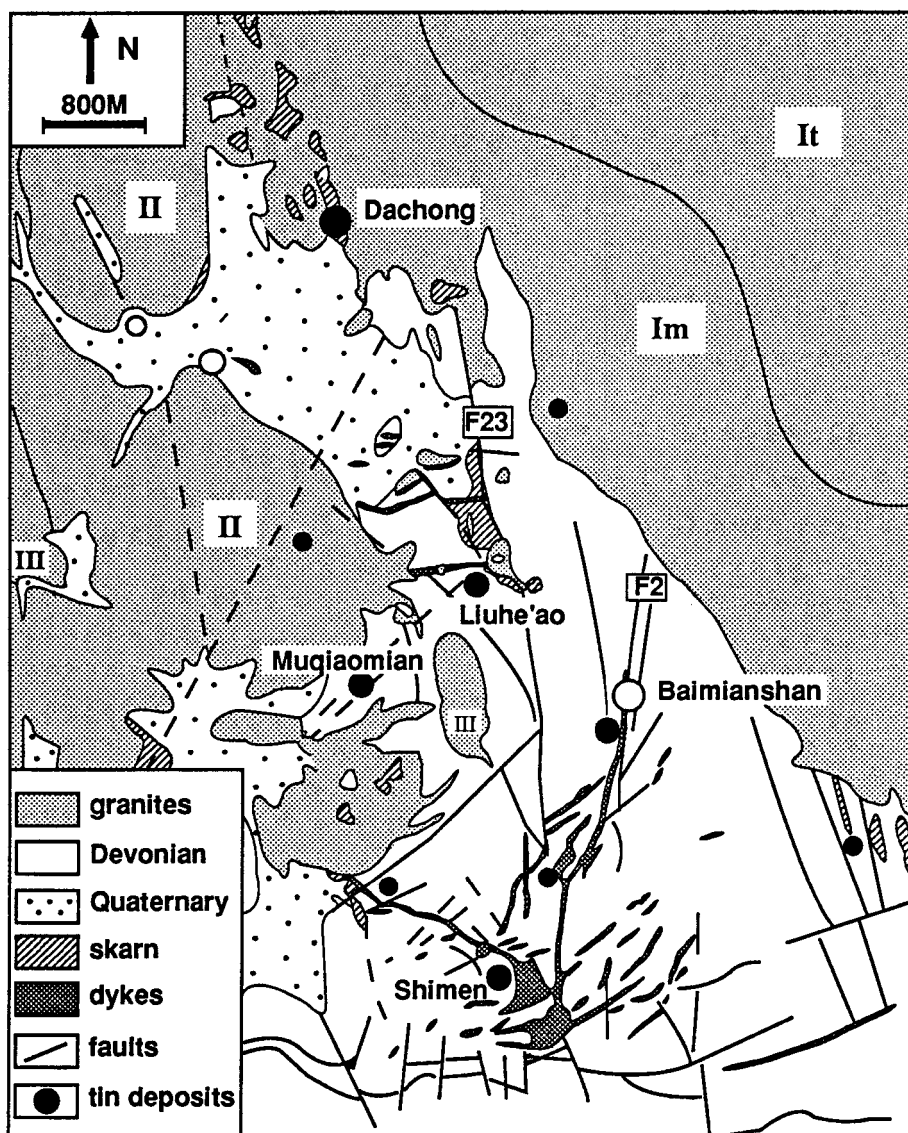


Fig. 10 Geological map of the Xinlu ore field (modified from unpublished map of No.204 Geol. Team of Guangxi, 1986, and No.8 Geol. Team of Guangxi, 1981).
 Open circle-placer deposit; black circle-primary deposit; III-phase III; II-phase II, Im-marginal part of phase I; It-transitional part of phase I.

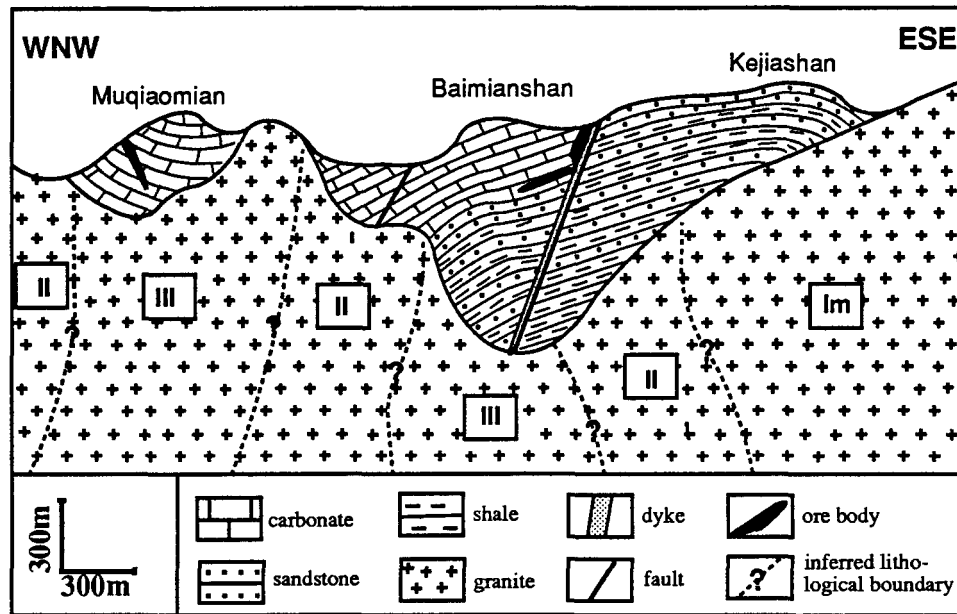


Fig. 11 A WNW-ESE geological profile of the Xinlu ore field, showing the attitude of the strata, the structures and the extent of the granite intrusions (III--phase III; II--phase II; Im--marginal part of phase I).

the unexposed granites.

3.1.2 Granites

Granites are exposed on the eastern, northern and western sides of the Xinlu ore field. According to geological mapping (No.8 Geol. Team of Guangxi, 1981), the granites on the eastern side of the ore field belong to the marginal part of phase I of the Guposhan batholith (Im), those on the western side belong to phase II, and the Fuchuanling and Bojiling stocks in the central part of the ore field correspond to phase III of the Guposhan batholith (Fig. 10). The northern part of the ore field is underlain by unexposed granites, which have been reached by diamond drill holes (Fig. 12). From the attitude of the intrusion surface of the exposed granites and unexposed granites which have been encountered by drilling (Fig. 12), and from the occurrence of felsic dykes (including quartz porphyry and fine-grained granite), it is inferred that unexposed granites also exist in the southern part of the ore field. From the distribution of exposed granites, it may be inferred that part of the unexposed granites belong to phase II, part to phase I, and some to phase III. The abundance of each phase is uncertain.

All the granites in the Xinlu ore field (Im, II, III) are biotite granites, but a difference in the average contents of major minerals in different phases is noticed (Pu, 1986): the average content of quartz is 30.8% in Im, 35% in II, 40% in III; the average content of K-feldspar is 39.8% in Im, 36.5% in II, 33.5% in III; the average content of plagioclase is 25.7% (An=17-36) in Im, 23% (An=16-36) in II, 17.5% (An=15-28) in III; the average content of biotite is 3.6% in Im, 4.4% in II and 3.1% in III.

Several K-Ar ages have been reported for the granites in the Xinlu ore field (Table 1), with a range from 107 to 167 Ma. The ages for which sampling data (locality, mineral and phase) exist are shown in Fig. 12. Three K-Ar ages of phase I are 130, 140 and 167 Ma. No K-Ar ages are reported for the exposed granites of phase II in Xinlu. The K-Ar ages of hidden granites are: 160, 148, 135, 120, 107 Ma. These K-Ar age data indicate an overlap between phase I and II, which is also true for the whole Guposhan batholith (Pu, 1986). This may indicate the lasting, continuity and temporal proximity between the two episodes of intrusion and the complexity of thermal and erosion history.

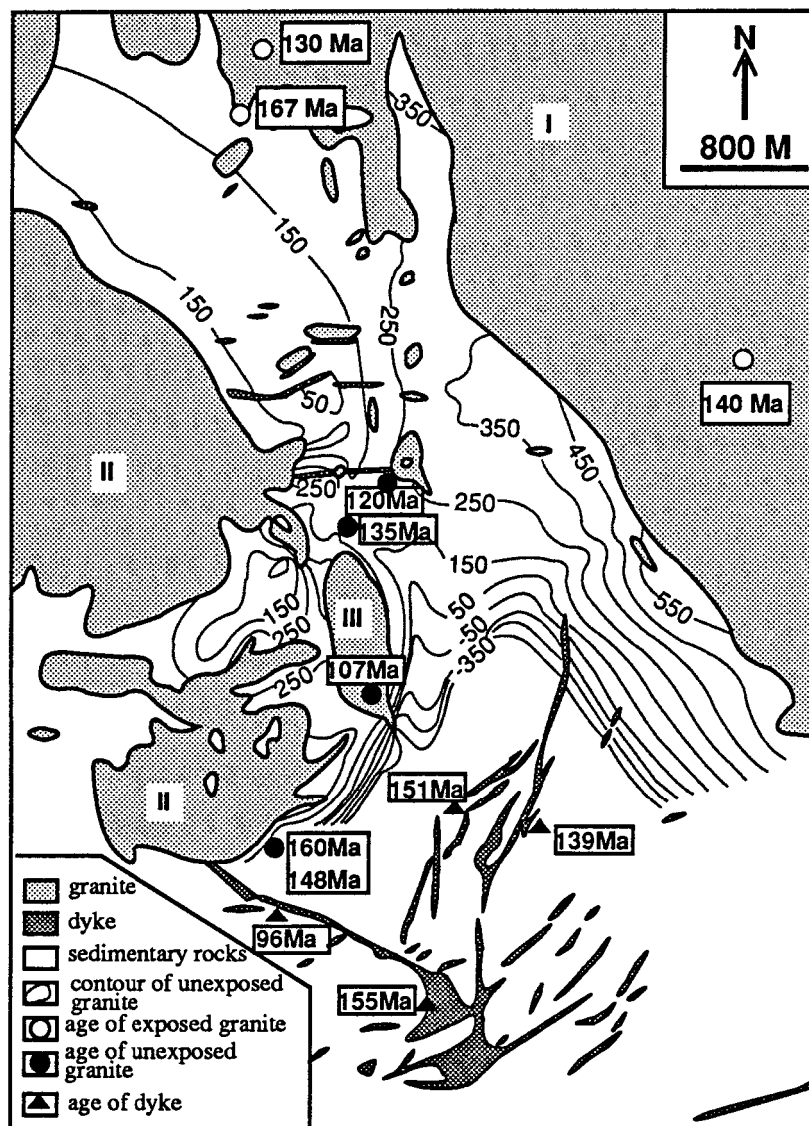


Fig. 12 A map showing the distribution of granites (including unexposed granites) and dykes as well as their ages in the Xinlu ore field. I, II and III are the same as Fig. 10. The contours indicate the elevation of the surface of the unexposed granites.

Table 1 Isotopic ages of granites and dykes in the Xinlu ore field

sample No	phase	locality	rock type	object	method	age (Ma)	data sources
No.20	Im	Guo'ershan	biotite granite	biotite	K-Ar	140	Geochem. Inst. of Chinese Acad. Sci., 1975*
63-2a	Im	1 km north of Xinlu	biotite granite	biotite	K-Ar	130	Zhang et al., 1985
No.26	Im	Xinlu	biotite granite	whole rock	K-Ar	135	No.204 Geol.Team of Guangxi, 1986*
No.6	Im	quarter of the mine	biotite granite	whole rock	K-Ar	167	Yichang Inst. of Miner. Resour. & Geol., 1982*
No.9	hidden granite (I,II,III)	Shuijingshan drill ZK1	biotite granite	biotite	K-Ar	160	No.204 Geol.Team of Guangxi, 1979*
No.17		Shuijingshan drill ZK1	biotite granite	whole rock	K-Ar	148	
No.27		Qiongsan drill ZK302	biotite granite	whole rock	K-Ar	135	
L84		Liuhe'ao Level 208	biotite granite	whole rock	K-Ar	120	You, 1990
No.28		Fuchuanling drill ZK310	biotite granite	whole rock	K-Ar	107	No.204 Geol.Team of Guangxi, 1979*
No.22		Xinlu	biotite granite	biotite	K-Ar	140	Geol. Inst. of Chinese Acad. Sci., 1964*
	I	east Guposhan batholith	granite	whole rock	Rb-Sr isochron	148	see table 10
	II	west Guposhan batholith	biotite granite	whole rock	Rb-Sr isochron	148	see table 10
V22-1	dyke	Maobeiling	quartz diorite	whole rock	K-Ar	155	this study, analysed by No.3 Inst. of Geol. Beijing
V14-1-1		west Shimen	quartz porphyry	whole rock	K-Ar	96	this study, analysed by No.3 Inst. of Geol. Beijing
V11-3		south Baimianshan	dioritic porphyry	whole rock	K-Ar	139	this study, analysed by No.3 Inst. of Geol. Beijing
No.30		south Shanbahe	dioritic porphyry	whole rock	Rb-Sr isochron	151	Guiling Inst. of Miner. Resour. & Geol., 1986*

* cited from Hu et al.,1989 (the sample number in this table corresponds to their serial number).

Note: All the K-Ar ages are analysed by conventional K-Ar method, and are calculated by using the following parameters. Ages analysed before 1977 have been recalculated (Dai, 1992, personal communication).

$$K^{40}=1.193 * 10^{-4} K; \lambda_K=0.581 * 10^{-10}/y; \lambda_\beta=4.962 * 10^{-10}/y.$$

3.1.3 Dykes

There are more than 50 dykes in the Xinlu ore field (Fig. 10, 12), with a wide range of compositions. The main rock types are dioritic porphyry and quartz dioritic porphyry, while a variety of other rock types also exist, including fine-grained granite, granitic porphyry, quartz porphyry, granodioritic porphyry, quartz monzonite, quartz diorite, granodiorite and diopside gabbro. The petrography of some dyke samples from the Xinlu ore field is described in appendix A.

Most of the dykes are distributed relatively far from the granites (mainly in Shimen deposit); some of them are located in the contact zone of the granitic intrusions (mainly in Liuhe'ao deposit). In the former case, the relationship between the dykes and the granite is not observed. In the latter case (in the Liuhe'ao deposit), veins of granite have been observed to cut through intermediate dykes and some xenoliths of the dyke are included in the granite (plate1-C). It is clear that the intermediate dykes in the Liuhe'ao deposit crystallized earlier than the granite belonging to phase III of the Guposhan batholith. The relationship between acidic dykes and granites has not yet been observed, and the relationship between dykes of different compositions is not completely clear, although it is reported that a quartz porphyry dyke is cut by a quartz dioritic porphyry dyke in Shimen deposit (Qin, 1985).

The K-Ar ages of three samples of dykes from the Xinlu ore field are as follows: 155 Ma for the quartz diorite from Shimen, 139 Ma for the quartz dioritic porphyry from South Baimianshan and 96 Ma for the quartz porphyry from West Shimen (Table 1; Fig. 12). A Rb-Sr whole rock isochron age of 151 Ma for dioritic dykes at South Baimianshan was reported by the Guilin Institute of Mineral Resources and Geology (1986), and a Rb-Sr whole rock isochron age of 149 Ma for the dioritic dykes from the adjoining Shuiyanba ore field was reported by the Yichang Institute of Mineral Resources and Geology (1985). The ages of the dykes are comparable to those of the granites: the K-Ar ages of granites in Xinlu range from 107 to 167 Ma, and those of dykes from 96 to 155 Ma. The Rb-Sr whole rock isochron ages of the dykes are very close to those of the phase I and II granites of the Guposhan batholith.

3.1.4 Structures

The structures in the Xinlu ore field include folds and faults in the sedimentary rocks.

The folds are relatively simple and are normal folds. The attitudes of the sedimentary rocks in the ore field are mainly controlled by a single NNW-trending anticline--the Kejiashan anticline (Fig. 11); only those at the southern margin of the ore field are controlled by a NEE-trending syncline--the Siliangchong syncline. The Kejiashan anticline is an open fold, with its axial plane vertical and its two limbs symmetric (Xie, 1989). Most of the sedimentary rocks in the ore field belong to the western limb of this fold. A number of second order folds with similar attitudes as the major fold are developed on both limbs of the major fold.

Faults are rather complex in the Xinlu ore field, and trend NNW, NNE, WE, NE and NW. The NNW-trending Guanyingshan-Nanzhudou fault (F23) and the NNE-trending Kejiashan fault (F2) are the major faults in the ore field. Both are normal faults. Structural analysis indicates that these two faults can not be separated from the formation of the Kejiashan anticline, which should have resulted in reverse or strike-slipping reverse displacement, so the normal fault effect of these two faults may be caused by later tectonic movements or magmatic intrusion. Faults of other orientations may have formed in the same stress field as the NW-trending folds and faults, but superimposition and reworking by later tectonic movements must have contributed to the development of these faults, since the stress field in the region experienced a change from W-E compression (Indo-China period) through NW-SE compression (Early Yanshanian period) to NW-SE stretching (Late Yanshanian period). Many NE- (northern Xinlu) and WE-trending (southern Xinlu) faults are filled by dykes (Fig. 10).

3.2 Geological Features of Ore Deposits

There are five main tin-polymetallic deposits in the Xinlu ore field: Dachong, Liuheao, Muqiaomian, Baimianshan and Shimen (Fig. 10). The geological features of these deposits will be described in this section. A deposit from the adjoining Shuiyanba ore field, the Donjia'ao deposit has also been studied.

3.2.1 Dachong deposit

This deposit is situated in the north of the ore field (Fig. 10). The ore bodies are subhorizontal veins superimposed on the skarn which occurs in the contact zone of the

granite intrusion. The intrusion surface is about 200 to 250 metres above sea level. Metallic minerals include magnetite, cassiterite, scheelite, galena, sphalerite, pyrrhotite, pyrite, chalcopyrite, arsenopyrite, jamesonite and marcasite. Gangue minerals include garnet, diopside, hedenbergite, andradite, vesuvianite, actinolite, epidote, fluorite, plagioclase, mica, calcite and quartz. Sn grade is generally low (0.2-0.3%).

The ore bodies and unmineralized skarns are exposed on the surface or directly overlain by Quaternary sediments which contain large amounts of placer tin. Most primary ores are oxidized.

3.2.2 Liuhe'ao deposit

This deposit is situated in the central part of the Xinlu ore field (Fig.10). It is spatially close to the Gongposhan granite in the west and the Bojiling granite stock in the east. A dioritic porphyry dyke occur at the contact zone of the granite intrusions and extends up along fractures in the sedimentary rocks. The intrusion surface is mainly between 150 and 250 metres above sea level.

The two main ore bodies, No.1 and No.2, of the Liuhe'ao deposit belong to proximal type. The No. 1 ore body occurs in the contact zone between D_{2d} carbonate and the Bojiling granite in an arc-like shape (Fig. 13). The No. 2 ore body is situated in the contact zone between D_{2d} carbonate and the Gongposhan granite. The direct host rocks of the ore bodies are mainly skarn and hornfels, developed mainly in the carbonates of the Donggangling Formation (D_{2d}) and partly in the shale or argillaceous limestone of the Yujiang Formation (D_{2y}). Minor amounts of skarn were formed in granite (endoskarn). The exoskarn and hornfels generally retain the stratiform features of the original sedimentary rocks (Plate 1-D). Dioritic porphyry dykes, although not the main host rock of the ore bodies, very often occur nearby and are cut by small sulfide veins. Wrigglite skarn composed of rhythmic opaque mineral layer and fluorite layer, which is typical of Sn-skarn (Kwak, 1987), is often observed (Plate 1-E). Granites which are not transformed to skarns are unevenly altered, showing potash feldspathization, albitization, greisenization and tourmalinization. Biotite is partially altered to muscovite (Plate 1-F).

Ore minerals of No.1 and No.2 ore bodies are mainly composed of pyrrhotite, pyrite, sphalerite, arsenopyrite, chalcopyrite, magnetite, cassiterite and scheelite, and non-metallic minerals include actinolite, garnet, diopside, vesuvianite, epidote, chlorite, quartz,

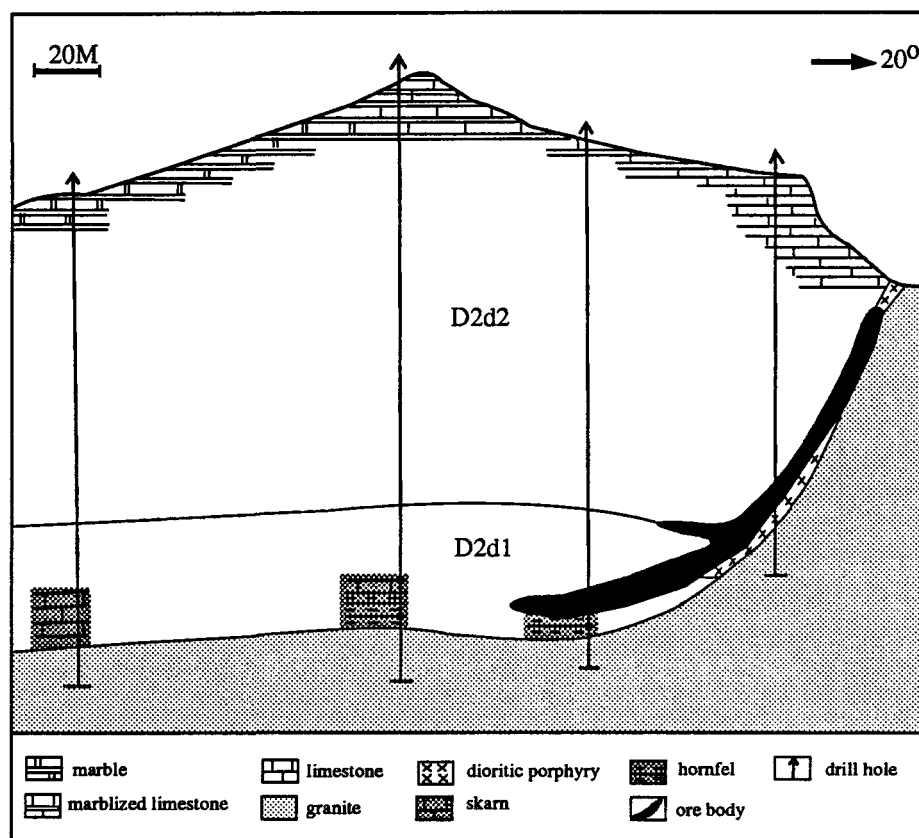


Fig. 13 No.O geological cross-section of the Liuhe'ao deposit (after Ping-Gui Mining Bureau, 1986).

fluorite, calcite, feldspar and mica. Most of the ores are massive, and some show banded structure. In some cases, pyrrhotite replaces fossil beds to form ores with lens-like structures.

At least two stages of skarn formation are identified: metamorphic skarn formation and ore skarn formation. Metamorphic skarns predate ore skarns, and ore skarns are superimposed on metamorphic skarns. Metamorphic skarns are mainly composed of garnet, diopside, and vesuvianite. Sn contents in metamorphic skarns and hornfels are generally low (0.02-0.06%, Lai and Zen, 1985). Tin cannot be exploited even though the content may sometimes be high (0.2-0.7%, Lai and Zen, 1985). Ore skarns are composed of sulfides and H₂O-bearing silicates as well as cassiterite (Plate 2-A) in addition to the simple skarn mineral assemblage.

Minor cassiterite-bearing greisen veins and quartz-fluorite veins are also observed superimposed on simple skarn or hornfels (Plate 2-B) or granite (Plate 2-C). This type of ore veins, although rich in Sn, are too small to be economic.

There are still other small sulfide ore bodies which are hosted by limestone or marble of the Donggangling Formation within about 100 m of the contact zone. These distal ore bodies are composed mainly of pyrrhotite, sphalerite, arsenopyrite and cassiterite, and are similar to those in Muqiaomian, Baimianshan and Shimen deposits, but on a much smaller scale.

3.2.3 Muqiaomian deposit

This deposit, situated in the west of Xinlu ore field (Fig. 10), is surrounded by granites on all the sides, and underlain by granites like a pot (Fig.14, 15). A bed of skarn with a varying thickness from one to six metres has developed between the marble of the Rongxian Formation (D_{3r}) and the unexposed granites (Fig. 15). The skarn contains small veins of sulfides such as pyrite and pyrrhotite, but the Sn content is generally low (average 0.223%, maximum 0.662%).

There are six ore bodies, all hosted by marbles. They occur in the shape of veins, trending NE and dipping to the SE from 45 to 75°. The length of individual ore bodies varies from tens of metres to 400 metres. The thickness is usually from 0.32-0.9 metres, but in some cases up to 6.8 metres. The shape of the main ore bodies is relatively regular in

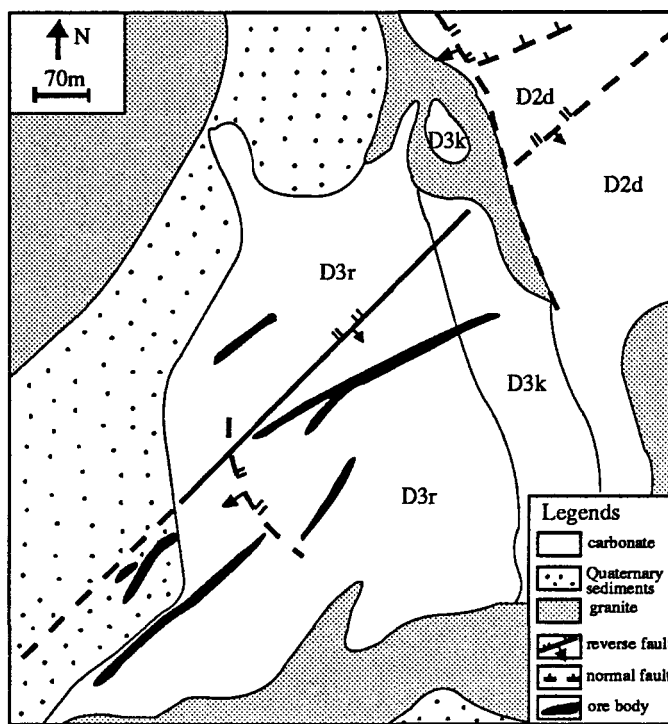


Fig. 14 Geological map of Muqiaomian deposit (after Ping-Gui Mining Bureau, 1986).

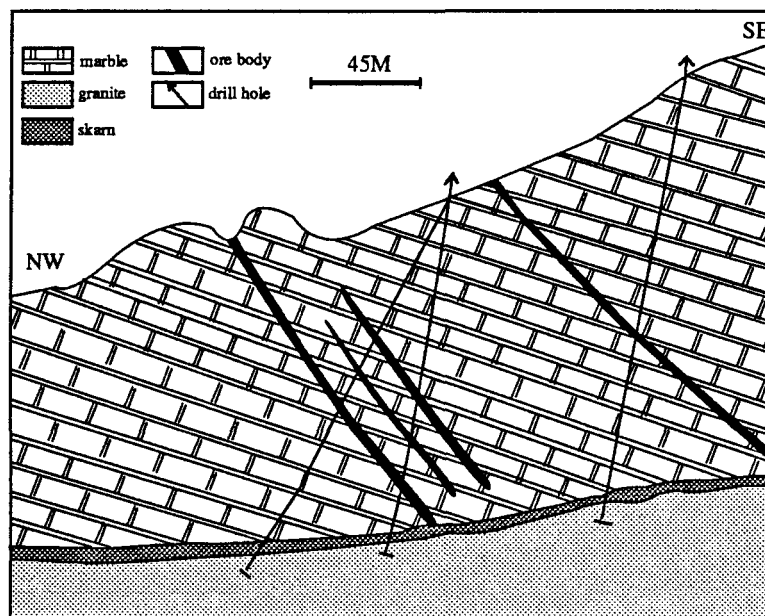


Fig. 15 No.5 geological cross-section of Muqiaomian deposit (after Ping-Gui Mining Bureau, 1986).

comparison with the other deposits in the Xinlu ore field, but there are numerous small, irregular veinlets of cassiterite-bearing sulfide developed in the marble (Plate 2-D). The vertical distance from the ore bodies to the unexposed intrusion surface varies from 20 to more than 100 metres. The intrusion surface beneath the ore bodies is mainly between 50 and 150 metres above sea level.

The upper parts of the ore bodies, exposed in elevated topography, are oxidized. They are composed of limonite, cassiterite, hematite, goethite, hydrozincite, smithsonite, malachite and gypsum. The primary ores in the lower parts of the ore bodies are mainly composed of pyrrhotite, Fe-rich sphalerite, arsenopyrite, pyrite, chalcopyrite, marcasite and cassiterite. Non-metallic minerals in the ores include quartz, calcite, diopside and a little fluorite. Most of the ores are massive.

3.2.4 Baimianshan deposit

The Baimianshan deposit is situated in the central-east part of the Xinlu ore field (Fig. 10). It is composed of two parts: the upper part is a buried placer ore body, which is spread along a fault valley and is the most productive part of the mine; the lower part is composed of three main primary cassiterite-sulfide ore bodies- No.I, No.II and No.25 (Fig. 16). The upper part of the deposit probably results from the combination of the weathering of the primary ore bodies in situ and reconcentration of cassiterite from adjoining areas (No.204 Geol. Team of Guangxi, 1979).

This deposit is relatively far from the exposed granites. No drill hole has so far encountered granites directly beneath the deposit, but some near the deposit (within 200 m horizontal distance from the deposit) have reached the unexposed granite. Therefore, there is little doubt that granites occur beneath the deposit. The intrusion surface beneath the deposit is estimated to be 350 to 250 metres below sea level, and the distance from the deepest ore bodies to the unexposed granites is estimated about 400-500 metres.

All the primary ore bodies are hosted by sedimentary rocks of Devonian age: the Donggangling Formation(D2a) and the Yujiang Formation(D2y), and partly by dioritic porphyry. Two of the three main ore bodies are stratabound (No.I and No. II). They are parallel to each other, conformable with the strata, and limited to a certain level of the strata (near the transition bed between D2a and D2y), but small branches of the ore bodies cut the strata (Plate 2-E). The transition bed is mainly composed of impure limestone, and is

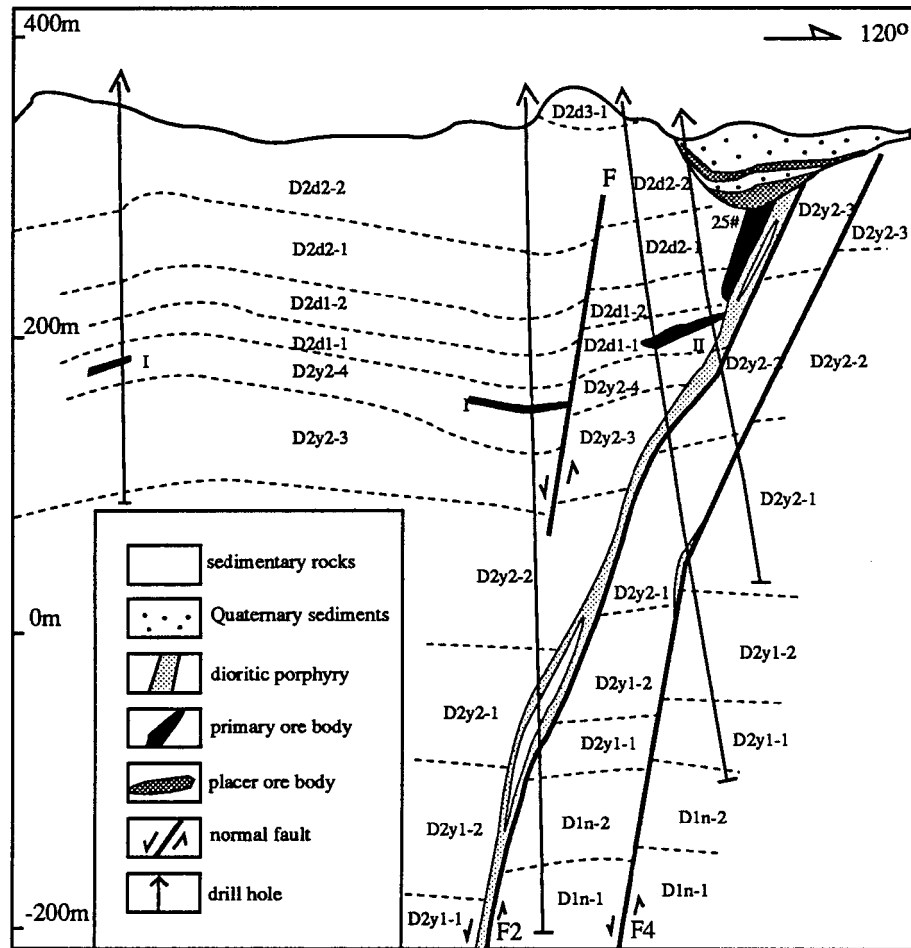


Fig. 16 A geological cross-section of the Baimianshan deposit (after Ping-Gui Mining Bureau, 1986).

characterized by the development of numerous calcareous lenses. The thickness of No. I is 6.16--0.33 m, with an average of 2.41m, and that of No. II is 15.69--0.42, with an average of 3.6 m. The No. 25 ore body is developed along a fault (F2), which is intruded by a dyke of dioritic porphyry, and is connected to No. II ore body. The ore body is very close to the dyke, and some ore veins cut through it. The thickness of the ore body varies from 0.85m to 17.38 m, with an average of 9.66 m.

The ores are mainly composed of pyrrhotite, Fe-rich sphalerite and pyrite. Minor components include arsenopyrite, cassiterite, jamesonite, galena, chalcopyrite, marcasite, scheelite, quartz, calcite, diopside, sericite, tremolite, actinolite, chlorite, wollastonite, fluorite and epidote. Some ores are composed predominantly of cassiterite (>90%) and minor sulfide, calcite and quartz (Plate 2-F). Most of the ores are massive, but some have lens-like bedding structures (Plate 3-A) which are parallel to the bedding of the strata. The Sn content is irregular, averaging 0.3%, with a maximum of 14.21%. It is higher in the upper part of the ore bodies and decreases downwards.

Deng (1984, 1985) proposed three categories of mineralization: (1) high-median temperature pyrrhotite--Fe-rich sphalerite--cassiterite association; (2) median temperature pyrite--Fe-rich sphalerite--cassiterite association; (3) median-low temperature galena--jamesonite association. The first category is the major mineralization of the Baimianshan deposit. The ores of this category are mainly composed of pyrrhotite(>50%), and are massive. The second category is rather limited, restricted only to the north part of the deposit. Pyrite and sphalerite are the main components, and pyrrhotite is absent. However, the first two categories have not been observed together. The third category (galena--jamesonite association) occurs in the form of small veins or masses within the first type of ore bodies.

Carbonate is extensively but heterogeneously bleached (Plate 3-B, -C) near the ore bodies and away from them. Alterations such as silicification, tremolitization, sericitization and epidotization occur near the ore bodies, but they are not extensive.

3.2.5 Shimen deposit

This deposit is situated in the south part of Xinlu ore field. It is relatively far from exposed granites and no drill hole has encountered the unexposed granites, but dykes of various compositions varying from diorite to quartz porphyry are well developed. The

deepest drill hole has reached a depth of 433 metres below sea level, which is probably still far above the unexposed granite. The intrusion surface of the unexposed granites is probably deeper than 800 metres below sea level, and the distance from the deepest ore bodies to the proposed intrusion surface is estimated to be over 600 metres.

There are 30 major ore bodies and numerous small ore veins (Plate 3-D) in Shimen deposit, trending in various directions (NE, NW, NS and EW), mainly in NE 40°-80°. The dip angles are steep, mainly 75°-85°. The lengths vary from several tens to several hundreds of meters, and the thickness is usually 0.3-1 metres, with a maximum of 8.6 m. Ore bodies of economic significance are generally above the 150 metres above sea level, but mineralization reaches a depth of the -230 metres. Most of the ore bodies have very complicated shapes with many branches (Fig. 17). All the ore bodies are hosted by marble of Rongxian Formation (D_{3r}) and controlled by fractures.

The main metallic minerals include pyrrhotite, Fe-rich sphalerite, pyrite, arsenopyrite, chalcopyrite, cassiterite, galena and jamesonite. Non-metallic minerals are quartz, calcite, fluorite, garnet and diopside. The contents of Sn and Zn vary greatly. The upper part of the ore bodies are relatively rich in Sn, while the lower part is relatively rich in Zn. Most of the ores are massive.

3.2.6 Dongjia'ao deposit

Dongjia'ao deposit is situated in the Shuiyanba ore field which is near the Xinlu ore field. Tin mineralization is mainly developed in a dolomite breccia pipe within the carbonates of the Guilin Formation (D_{3k}). The breccia fragments are mainly marble or dolomite, and some dioritic porphyry, limonite and hematite masses. They are rather irregular in shape (Plate 3-E). Their sizes vary greatly, ranging from 0.5 mm to 5 m in diameter. The matrix is mainly calcareous, dolomitic, ferruginous and argillaceous. The breccia pipe extends downward about 200 metres from the surface and then pinches out. Although no drill has so far encountered granite beneath the deposit, there is little doubt that unexposed granites occur as inferred from the attitude of the contact face of the Guposhan batholith which is less than 100 metres away from the pipe.

The main metallic minerals of the ore bodies are cassiterite, hematite and limonite. Hematite and limonite may be supergene. Only very minor sphalerite and pyrite occur in the ores. Cassiterite is predominantly distributed in the cements, and less commonly in the

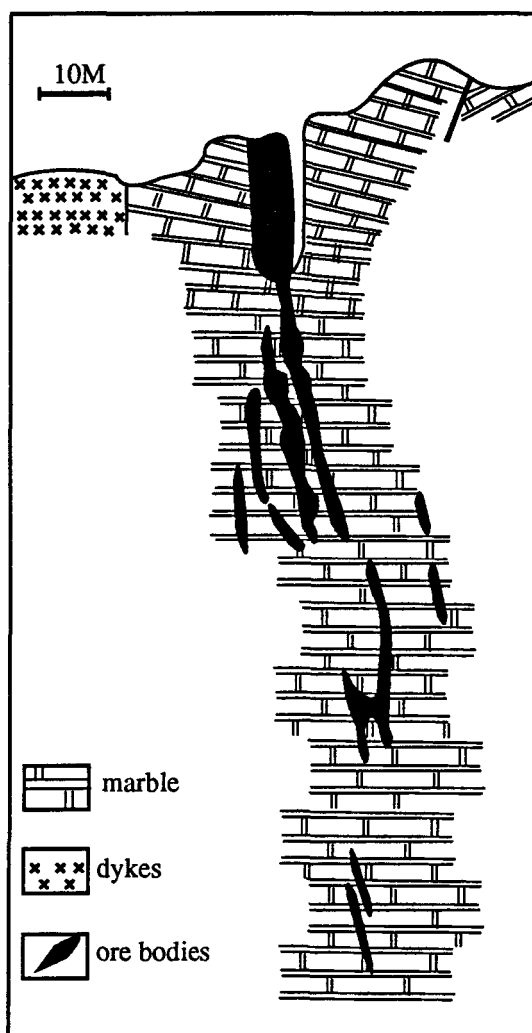


Fig. 17 A geological cross-section of the Shimen deposit (after Ping-Gui Mining Bureau, 1986).

fissures of the breccia. The cassiterite is yellowish in colour, much lighter than the dark brownish cassiterite in the sulfide ores in Xinlu ore field. Sn grade is generally very high. Besides the mineralization within the breccia pipe, some cassiterite veins have also developed in fractures in the dolomite near the breccia pipe. Cassiterite occurs in small veinlets or as individual crystals, which coexist with minor calcite and quartz (Plate 3-E).

3.3 Temporal and Spatial Relationship of Ore Deposits with Host Rocks

The geological features of individual deposits in the Xinlu ore field have been described above; their temporal and spatial relationships with the host rocks (granites, dykes and sedimentary rocks) will be summarized in this section.

3.3.1 Temporal relationship

As has been discussed in 3.1, the granites and dykes in the Xinlu ore field are of Mesozoic ages. The K-Ar ages of the granites range from 107 to 167 Ma, and those of dykes from 96 to 155 Ma. The sedimentary rocks are of Devonian ages (about 350-400Ma).

No precise age data of mineralization are available for any of the deposits in Xinlu. Five Pb-Pb model ages are reported by Deng (1984) and Qin (1985) for Baimianshan deposit: 118, 61, 280, 82, 319, 8 and 80 Ma (single-stage model) or 202, 137, 287, 263, 495, 85 and 158 Ma (two-stage model) (cited from Liu and Yuan, 1989). Two Pb-Pb model ages are reported by the same authors for Shimen deposit: 8 and 80 Ma (single-stage model) or 85 and 158 Ma (two-stage model). The Pb-Pb model ages are not sufficiently precise to constrain the age of mineralization.

Geological observations and geochemical reasoning (see Chapter 4) suggest that the mineralization in the Xinlu ore field is most likely related to the third phase intrusions of the Guposhan batholith.

3.3.2 Spatial relationship

The tin-polymetallic deposits in the Xinlu ore field can be divided into two types according to their spatial relationship with the granite intrusions: a proximal type which is situated at or near the contact zone between the intrusion and the country rocks and a distal

type which is hosted by the sedimentary rocks relatively far from the intrusions. Among the five deposits in the Xinlu ore field, two (Dachong and Liuhe'ao) are of proximal type, two (Baimianshan and Shimen) as well as the Dongjia'ao deposit are of distal type, and the Muqiaomian deposit is of transitional type.

There seems to be a corollary between the development of proximal and distal deposits: when proximal ore bodies are developed, only small distal ore bodies occur above the proximal ones (Liuhe'ao); on the other hand, when distal ore bodies are developed, no proximal ore bodies of economic significance are found beneath the distal ones (Baimianshan). A correlation between the site of mineralization and the depth of granite intrusion is observed: the proximal deposits are distributed in the northern part of the ore field, there the granites were emplaced at higher levels, while the distal deposits are mainly distributed in the southern part of the ore field, where the granites were emplaced deeper. Figure 18 clearly shows that the distance between the granite intrusions and the ore bodies increase from north to south with the increase of depth of magma emplacement. The Muqiaomian deposit is not projected on Fig. 18, but the fact that the depth of intrusion surface at Muqiaomian (50 to 150 m above sea level) is between that at Liuhe'ao (150 to 250 m above sea level) and that at Baimianshan (350 to 250 m below sea level) is consistent with its transitional characteristics between proximal and distal types.

The direct host rocks of the proximal ore bodies are skarns and hornfels, while those of the distal ones are mainly sedimentary rocks. Most distal ore bodies are controlled by fractures or fissures and have the shape of steep veins. Only a few distal ore bodies (No. I and II ore bodies in the Baimianshan deposit) are stratabound and in conformity with the strata. Statistical studies show that there is a preference of tin-polymetallic mineralization in Devonian strata (esp. D_{2y} and D_{2d}) in the Ping-Gui mineralization district and the Xinlu ore field (Qiu, 1989). However, the Devonian strata have a thickness of 1900 to 3900 metres, and the carbonates hosting the ore bodies in Shimen are about 600 m above those hosting the ore bodies in Baimianshan in the sedimentary sequence. Therefore, the localization of the distal deposits does not appear to be controlled by specific lithological units.

A close spatial correlation exists between the tin deposits and the dykes. On a regional scale, the four tin-polymetallic ore fields around the W-SW-S contact zone of the Guposhan batholith correspond well to the localities of the four groups of dykes (Fig. 8). In the Xinlu ore field, intimate spatial relationship between dykes and ore bodies can be seen in Liuhe'ao, Baimianshan, Shimen and Dongjia'ao. In Baimianshan deposit, the biggest ore

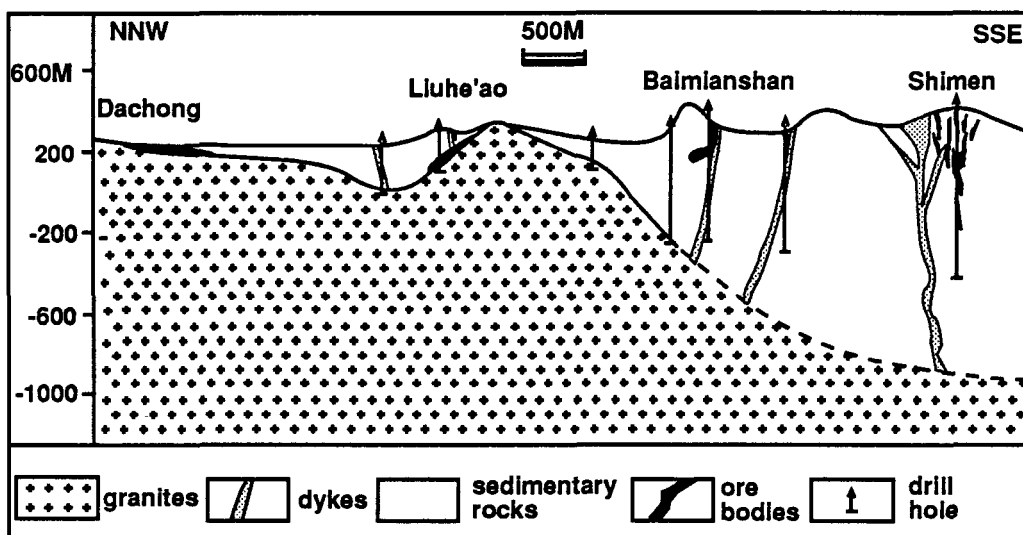


Fig. 18 A NNW-SSE synthetic geological cross-section of the Xinlu ore field, showing the correlation between the location of deposits and the depth of intrusions. The numbers on the vertical scale are referenced to sea level. The sizes of ore bodies and dykes are expanded because of the small scale of the diagram. Not all drill holes are shown for clarity.

body (No. 25) is developed along a N-S trending fault (F2), which is partly occupied by a dioritic porphyry dyke. It has been observed that ore bodies are better developed in parts of F2 which is occupied by the dyke than in those which is not occupied by the dyke.

CHAPTER IV

GEOCHEMICAL CHARACTERISTICS OF THE HOST ROCKS AND THEIR ORE-FORMING POTENTIAL

4.1 Introduction

This chapter examines the geochemical characteristics of the host rocks in order to discuss their genesis and evaluate their ore-forming potential. This is important for the localization of the proximal and distal deposits, because the source of the ore-forming components is one of the major factors determining the localization of ore deposits.

4.2 The Sedimentary Rocks

Sedimentary rocks are the principal host rocks of the tin ore bodies in the Xinlu ore field. Although only Devonian (and a little Carboniferous) sedimentary rocks occur in the Xinlu ore field, samples of older units from adjoining areas have also been studied, because these older units must have existed beneath the younger ones in the Xinlu ore field, and were later intruded by the magma of the Guposhan batholith. Petrographical characteristics of selected samples of sedimentary rocks are described in appendix A, and the geochemical characteristics are discussed as follows.

4.2.1 Major elements

Analyses of major elements in sedimentary rocks from Ping-Gui district (including some samples from Xinlu) and adjoining west Guangdong region are listed in table 2. Carbonate rocks are composed mainly of Ca, Mg and CO₂, and are generally poor in Si, Al, Fe, Na and K. Sandstone is characterized by high Si content, while mudstone is rich in Al, Fe, Mg, Ca and K. One outstanding feature of all the sedimentary rocks is the generally low Na/K ratios (Fig. 19) and high CO₂ contents (Xia and Liang, 1984) in comparison with the granites.

Table 2. Contents of major elements in sedimentary rocks from Ping-Gui and adjoining regions(wt%).

unit	sample number	rock type	SiO ₂	Al ₂ O ₃	Fe ₂ O ₃ (total)	MgO	CaO	Na ₂ O	K ₂ O	P ₂ O ₅	data source
C	No.12	limestone			0.34			0.03			1
P-D	158 samples	sandstone	78.20	9.70	2.65	0.76	0.42	0.11	2.31	0.02	2
	41 samples	mudstone	55.66	18.10	4.22	1.39	3.91	1.21	3.79	0.33	
	112 samples	carbonate	8.78	1.94	0.71	4.34	43.88	0.11	0.45	0.02	
D3k	CX053	limestone			0.09			0.01			1
D2d2-2	CX050	limestone			0.60			0.06			
D2y2-4	CX046	limestone			3.43			0.14	2.04		
D2y2-3	CX044	quartz sandstone			1.55			0.04			
D2y2-3	CX045	silty shale			2.83			0.24	4.17		
D1n	D1n-1	silty mudstone			5.05			0.11	7.41		
D1l	D1l-1	argillaceous siltstone			2.09			0.07	2.08		
Csh	No.11	siltstone			4.70			1.97			
	No.57	silty phyllite			14.73			0.11	5.93		
S-	164 samples	sandstone	71.89	13.42	3.53	1.06	0.24	0.45	2.94	0.04	2
Pt	69 samples	mudstone	60.65	18.84	3.78	1.25	0.18	1.00	4.57	0.03	

Data sources: (1) this study, analysed by INAA at UQAC, locality--see appendix-A; (2) Qian (1985), from western Guangdong region.

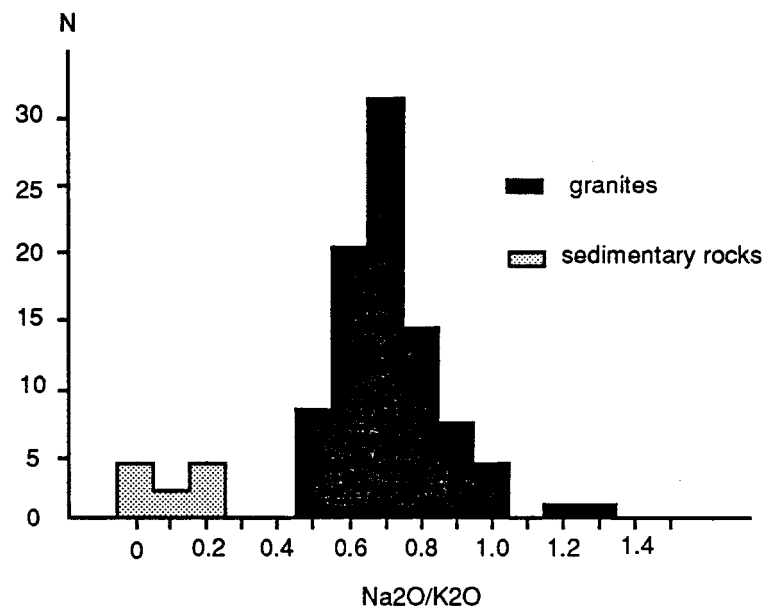


Fig. 19 Comparison of Na₂O/K₂O ratios of sedimentary rocks from the Ping-Gui district with granites from the Guposhan batholith.

4.2.2 Trace elements

Trace element analyses for the sedimentary rocks in the Xinlu ore field and adjoining regions are listed in table 3.

Sn, W, F, Cl, As, Rb, Cs and Ta concentrations in sedimentary rocks are generally lower than the average contents in the granites of the Guposhan batholith; Sr and Cr concentrations are generally higher in sedimentary rocks than in average granites of the Guposhan batholith (Fig. 20), and the content of Zn is similar in both. The concentrations of Co, Ba, Sb and Sc are higher in clastic rocks, but lower in carbonate rocks, than in average granites of the Guposhan batholith. Sn and W show a little concentration in certain sedimentary beds in comparison with the background of the Nanling region and the abundance in the crust, which is also indicated by the studies of Liang and Lu (1987) and Qiu (1989), but the concentration is not high enough to form syngenetic mineralization.

4.2.3 REE contents

A set of samples of sedimentary rocks from Cambrian to Carboniferous are analysed for the rare earth elements. The results are listed in table 4. Since all the rare earth elements were not analysed, three important parameters (i.e. ΣREE , δEu , and $\Sigma\text{LREE}/\Sigma\text{HREE}$) can not be calculated directly. In order to make the parameters of incomplete REE analyses comparable with those of complete REE analyses, the following parameters, $\Sigma\text{REE}'$, $\delta\text{Eu}'$, and $\Sigma\text{LREE}'/\Sigma\text{HREE}'$, were constructed (Appendix B). These parameters are comparable to ΣREE , δEu , and $\Sigma\text{LREE}/\Sigma\text{HREE}$ respectively (see Appendix B).

The sedimentary rocks as a whole have a very wide range of ΣREE as reflected by $\Sigma\text{REE}'$ (Table 4) and chondrite normalized REE patterns (Fig. 21). $\Sigma\text{REE}'$ ranges from 8.81 to 286.9 ppm. Light rare earth elements are generally enriched relative to heavy rare earth elements (Fig. 21), with $\text{LREE}'/\text{HREE}'$ ranging from 3.71 to 8.82. Eu depletion is generally small (Fig. 21), with δEu ranging from 0.61 to 0.9. These features show a contrast to those of the granites, which have higher and more steady content of REE and much more obvious Eu depletion.

Table 3. Contents of some trace elements in sedimentary rocks from Xinlu and adjoining regions (ppm).

unit	sample no.	rock type	locality	Sn	W	Zn	F	Cl	As	Cr	Co	Rb	Sr	Ba	Cs	Ta	Sb	Sc	data
C	no.12	limestone	Liantang	2.00	1.39	31.10	280.00	5.00	2.80	11.50	0.95	7.70	439.00		1.46		0.40	0.89	1
D3k	cx053			8.00			65.00	5.00	0.56		1.43		158.00				0.17	0.21	
D2d	cx050				6.50		31.10	195.00	38.00	13.50	9.00	1.70	17.70	322.00	31.00	2.24		0.25	
D2y	cx046	limestone	Xinlu	5.70	2.97	41.20	708.00	38.00	2.94	41.30	9.70	89.80	283.00	151.00	5.15		0.47	7.49	
	cx044	sandstone		1.70		44.70	170.00	53.00	2.90	22.30	8.02	26.30	15.00	121.00	3.06	7.13	2.34	5.04	
	cx045	silty shale		3.00	77.90	89.70	540.00	58.00	10.80	68.50	4.55	165.00	53.00	407.00	14.80	1.98	16.90	14.00	
D1n	D1n-1	silty mudstone	Shanhu	2.80	19.60	71.10	8000.00	31.00	9.00	99.40	7.87	530.00	179.00	428.00	52.00	1.08	72.70	17.50	
D1l	D1l-1	pelitic siltstone		1.50	13.70	27.30	340.00	36.00	7.37	41.30	4.08	78.50	52.00	272.00	9.08	0.83	3.78	6.92	
Csh	no.11	siltstone	Danin	8.40		58.00	660.00	6.00	4.75	73.00	11.20	137.00	60.00	806.00	5.10	1.71	0.75	12.00	
	no.57	silty phyllite		1.00	10.30	125.00	265.00	81.00		90.80	37.50	262.00	60.00	856.00	24.00	0.38	1.32	55.10	
C	abundance in Nanling region			2.80	1.29	41.52	416.30		4.64	35.62	4.67		178.40	112.70			0.55	4.78	2
D				3.93	2.11	40.40	592.30		10.27	38.44	4.85		115.70	327.20			1.21	6.37	
O				3.57	1.83	94.93	599.20		9.43	61.44	8.44		29.19	411.20			1.21	9.77	
C				2.92	1.88	86.95	626.00		14.61	78.72	11.08		30.04	640.60			1.71	12.04	
Z				2.86	2.45	96.28	634.80		3.34	82.21	11.84		33.20	638.20			0.53	12.86	
average content in the Guposhan batholith				28.32	36.20	59.10	1894.00	160.00	11.10	9.43	6.42	498.00	46.70	223.00	29.50	14.10	0.65	3.97	3
abundance in the crust				2.00	1.5	70.00	625.00	130.00	1.8	100.00	25.00	90.00	375.00	425.00	3.00	2.00	0.2	22.00	4

Data sources: (1) this study, analysed by INAA at UQAC (except for Sn, Sr, F, Cl which are analysed at HIAMP, see Appendix C); (2) Yu et al. (1987); (3) data from table 7 (phase E not included); (4) Mason (1966).

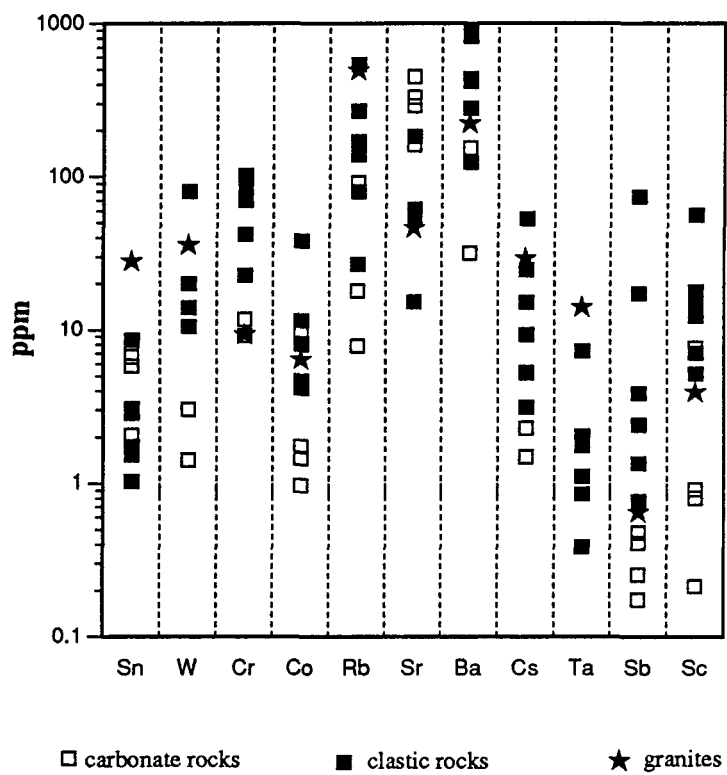


Fig. 20 Comparison of trace element contents in sedimentary rocks and the average from granites of the Guposhan batholith.

Table 4. REE contents in sedimentary rocks (ppm)* and some parameters.

unit	sample no.	rock type	La	Ce	Sm	Eu	Tb	Yb	Lu	TREE'	dEu'	L'/H'
Csh	No.57	silty phyllite	13.99	26.02	2.95	0.77	0.57	2.28	0.37	75.21	0.78	4.22
	No.11	siltstone	49.01	91.47	7.98	1.69	1.24	3.89	0.68	231.10	0.68	6.91
D1l	D1L-1	pelitic siltstone	27.66	54.81	3.84	0.69	0.49	1.99	0.34	126.61	0.61	8.82
D1n	D1n-1	silty mudstone	38.22	69.01	5.00	1.16	0.76	2.96	0.50	168.56	0.75	7.67
D2y	CX045	silty shale	65.64	116.85	8.94	2.09	1.33	3.86	0.60	286.90	0.76	8.37
	CX044	sandstone	29.85	55.58	5.58	1.14	0.90	2.09	0.49	145.52	0.65	6.54
	CX046		17.76	31.98	2.43	0.69	0.39	1.09	0.18	78.70	0.90	7.93
D2d	CX050	limestone	3.89	5.67	0.55	0.11	0.07	0.24	0.05	15.71	0.70	8.26
D3k	CX053		1.78	2.76	0.37	0.09	0.08	0.20	0.04	8.81	0.72	4.36
C	No.12		1.90	2.55	0.45	0.10	0.09	0.26	0.06	9.49	0.66	3.71
Average			24.97	45.67	3.81	0.85	0.59	1.89	0.33	114.66	0.72	6.68

* analysed by INAA at UQAC.

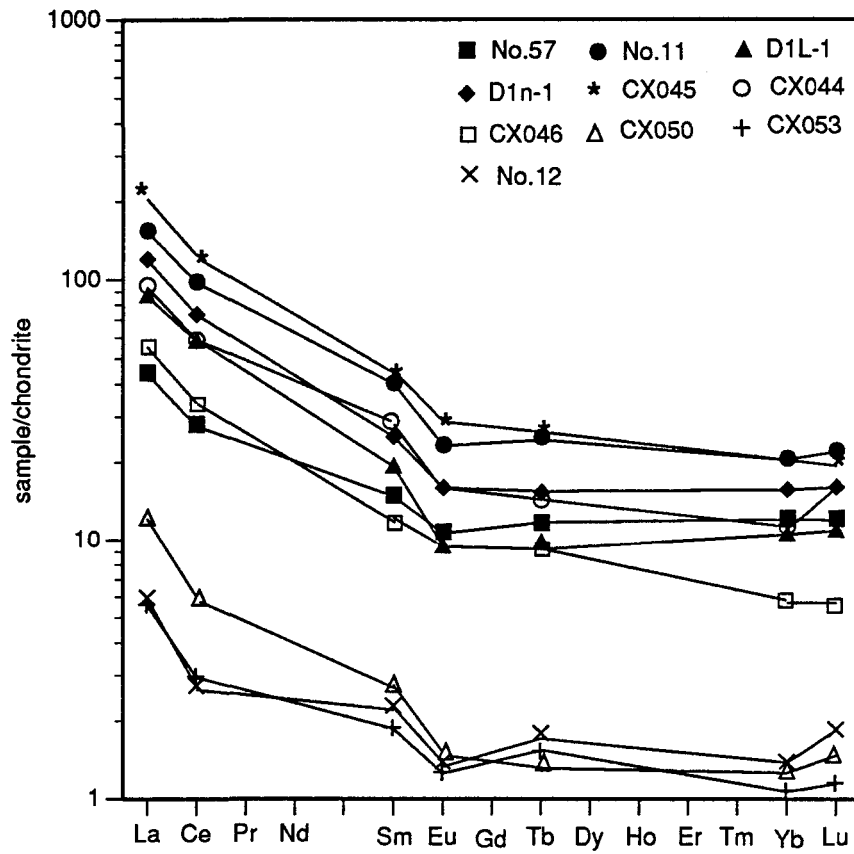


Fig. 21 REE patterns of sedimentary rocks from Xinlu and adjoining regions (data from Table 4).

4.2.4 The ore-forming potential

The observation that most of the distal ore bodies are hosted directly by sedimentary rocks instead of granites and that a few ore bodies are stratabound and are in conformity with the sedimentary beds has encouraged some authors (e.g. Zheng, 1987; Li, 1985; Li, 1986; Qiu, 1989) to suggest that certain sedimentary beds have provided most of the ore-forming components in the ore-forming fluids. The potential of the sedimentary rocks to provide ore-forming components to the hydrothermal fluids is mainly determined by the contents of the ore-forming elements in the rocks and the volume of the rocks which were affected by the hydrothermal fluids. The contents of the ore-forming elements in the sedimentary rocks are generally low in comparison with the granites, although they can be fairly high in certain beds (e.g. in some beds of the Donggangling Formation) and certain segments, even higher than in the granites (Qiu, 1989). The Xinlu ore field is one of the areas in the Nanling region, where Sn, Pb and Zn were originally enriched in certain beds of the Devonian strata relative to the regional background (Liang and Lu, 1987; Qiu, 1989). However, these elements are not rich enough to form syngenetic deposits. Therefore, the ore-forming potential of the sedimentary rocks is dependent on the extraction of the ore-forming elements by hydrothermal fluids. Since the ore-forming hydrothermal activities were mainly limited to faults, fractures and walls of dykes, which are mainly vertical or subvertical as reflected by the attitude of the ore bodies (steep veins), and are characterized by fairly rapid fluid flow, while the sedimentary beds are generally flatter, the volume of the rocks having high contents of ore-forming elements and being affected by the hydrothermal fluids is limited, so the sedimentary rocks may have contributed little to the ore-forming fluids. Only where the position of the sedimentary beds with higher than background contents of the ore-forming elements were in the flow paths of the ore-forming fluids, could the sedimentary rocks provide a significant part of the ore-forming materials, giving rise to concordant stratabound ore bodies, as in the case of the stratiform No.II and I ore bodies in the Baimianshan deposit.

4.3 The Granites

The geological environment of the Xinlu ore field, as characterized by the development of granites on three sides and beneath the ore field (Fig. 11, 12), suggests that the granites have played a critical role in Sn mineralization. The role of granites includes two

aspects: providing ore-forming materials and the dynamics that drive the ore-forming fluid flow. As to providing ore-forming materials, the evaluation of their ore-forming potentials is very important, which requires an understanding of the geochemical features and origins of the granites. Although only the marginal part of phase I (Im), and phase II and III of the Guposhan batholith occur in the Xinlu ore field, the transitional part (It), central part (Ic) of phase I and the dark enclaves (E) in phase I have been studied along with Im, II and III, because they compose parts of a series of genetically related granite intrusions. Petrographical characteristics of selected samples of granites are described in appendix A, and the geochemical characteristics are discussed as follows.

4.3.1 Major Elements

A number of analyses of major elements of the granites of Guposhan batholith are listed in table 5, and the CIPW calculation results are listed in table 6.

The CIPW normative values of ab are allocated to or and an to form Af and Pl by using the method proposed by Rittmann (1973). These data are plotted on the Qz-Af-Pl diagram of the IUGS classification of igneous rocks (Streckeisen, 1976) (Fig. 22). It is shown that most samples of phase III, II, Im and It plot on the areas of alkali-feldspar granite and normal granite; only three samples of phase II and one sample of phase It plot on the area of adamellite. On the other hand, the samples of Ic mainly plot on the area of adamellite, partly on that of normal granite and one on the area of quartz monzonite. The samples of the "dark enclaves" (E) plot over a wide range of area: quartz syenite, quartz monzonite, quartz monzodiorite, adamellite, monzonite and monzodiorite. Only one sample of E contains the norm of ne, and is not plotted on the Qz-Af-Pl diagram.

92% of phase III, 85% of II, 40% of Im, 70% of It, 50% of Ic, and 47% of Ie samples contain normative corundum, showing a decreasing degree of aluminous saturation from phase III through II to I (Fig. 23a). The values of differentiation index (DI) generally increase from phase I through II to III (Fig. 23b), but the difference between It, Im and II is very small --the DI value of average phase III, II, Im, It, Ic and E is 93.10, 89.89, 91.24, 89.92, 82.97, 68.89, respectively (see Fig. 24).

The variation of average major component contents and related parameters between different phases is shown in Fig.24. The following trends are observed: (1) SiO₂ increases from E through Ic, It, Im and II to III, but a decrease from Im to II is observed, (2) K₂O

Table 5 Major element contents in granites of the Guposhan batholith (wt%).

phase	sample No.	SiO ₂	TiO ₂	Al ₂ O ₃	Fe ₂ O ₃	FeO	MnO	MgO	CaO	Na ₂ O	K ₂ O	P ₂ O ₅	H ₂ O	CO ₂	L.O.I	Sum	data source	
III	Yguai3	76.91	0.21	13.86	0.14	1.74	0.02	0.12	1.42	2.52	5.36	0.42				102.72		
	Yjl	74.96	0.11	12.06	0.39	2.19	0.04	0.12	0.84	3.19	4.31	0.03	0.54		0.97	99.75		
	****	76.06	0.09	12.05	0.72	1.16	0.03	0.07	0.55	3.25	4.44	0.03	0.46		0.48	99.39		
	Pjhua5	74.93	0.10	11.64	0.46	1.42	0.02	0.09	0.62	2.80	4.62	0.02	0.59			97.31		
	Pjhua3	74.72	0.03	11.40	1.43	0.77	0.02	0.03	0.46	3.20	4.27	0.01	0.84			97.18	1	
	Pjhua4	75.90	0.06	10.25	0.79	1.22	0.02	0.05	0.56	2.80	4.20	0.01	0.84			96.70		
	Pjhua1	75.14	0.03	11.06	0.40	1.52	0.03	0.03	0.53	2.95	4.10	0.01	0.77			96.57		
	Bguai1	73.94	0.05	11.63	0.43	0.90	0.03	0.04	1.08	3.92	4.59	0.01					96.62	
	ZK209	73.98	0.08	13.00	0.39	2.09	0.09	0.03	0.38	3.49	3.60	0.05	0.84	0.53			98.55	
	****	74.47	0.22	12.64	0.92	1.87	0.04	0.29	0.99	2.80	4.44	0.06	0.56				99.30	2
	****	75.51	0.03	12.89	0.84	0.84	0.02	0.08	0.28	2.94	4.50	0.04	0.61				98.58	
	****	75.69	0.06	12.26	0.31	1.73	0.02	0.27	0.45	2.79	5.54	0.01	0.59				99.72	3
	****	76.28	0.11	12.00	0.65	1.22	0.04	0.08	0.43	2.96	4.37	0.03	0.30				98.47	4
	No.23	78.08	0.09	11.95	0.95	0.80	0.02	0.06	0.25	3.40	4.73	0.01					100.34	
	No.24	76.61	0.04	11.76	0.57	0.65	0.02	0.02	0.10	3.20	4.27	0.01					97.25	
	No.25	76.83	0.07	11.65	0.25	1.16	0.04	0.04	0.35	3.34	4.42	0.01					98.16	5
	No.26	80.20	0.07	11.17	0.37	0.92	0.01	0.05	0.15	2.53	4.42	0.01					99.90	
	No.1	75.25	0.09	12.59	0.29	1.74	0.03	0.23	0.67	3.20	5.40	0.02	0.86				100.37	
	No.2	75.60	0.03	12.59	0.36	1.16	0.02	0.11	0.78	3.85	4.88	0.02	0.60				100.00	6
	No.3	76.20	0.03	12.53	0.21	1.29	0.02	0.03	0.56	3.73	4.93	0.02	0.32				99.87	
	No.4	75.50	0.06	12.53	0.29	1.74	0.05	0.15	0.67	3.45	5.03	0.03	0.65				100.15	
f-1	74.45	0.04	13.07	0.17	1.72	0.03	0.08	0.64	3.82	4.94	0.02	0.36			0.46	99.80		
f-2	75.10	0.05	13.07	0.10	1.57	0.03	0.08	0.48	3.72	5.04	0.02	0.36			0.41	100.03	7	
f-3	75.18	0.05	13.07	0.08	1.66	0.03	0.08	0.48	3.62	4.94	0.02	0.32			0.50	100.03		
L84	75.00	0.02	13.22	0.10	1.23	0.03	0.74	0.58	3.13	5.19	0.03	0.60	0.18			100.05		
Average of III		75.70	0.07	12.24	0.46	1.37	0.03	0.12	0.57	3.22	4.66	0.04	0.58	0.36	0.56	99.07		
II	Bgua2	73.63	0.28	11.37	0.78	2.83	0.05	0.40	1.43	3.03	4.38	0.11				98.29		
	Yan2	73.15	0.33	12.30	0.57	2.77	0.05	0.42	1.36	2.94	4.13	0.09	0.05		0.70	98.86		
	Pjhua14	75.84	0.23	11.12	0.54	1.09	0.03	0.03	0.62	3.47	3.76	0.00				96.73		
	8207	71.63	0.50	13.39	1.35	2.44	0.05	0.53	3.25	2.00	4.30	0.11				99.55		
	8230	74.12	0.34	12.54	0.89	2.20	0.04	0.33	2.19	2.55	4.20	0.09				99.49		
	0233-1	74.50	0.27	13.40	0.50	1.98	0.04	0.23	2.07	2.38	4.30	0.04				99.71		
	Pjhua10	75.28	0.10	11.74	0.57	1.38	0.02	0.11	0.93	2.58	4.57	0.02	0.72		0.70	98.72		
	Pjhua12	74.01	0.23	12.89	0.43	2.38	0.04	0.22	0.99	2.56	4.30	0.04	0.56		0.16	98.81		
	Pjhua45	78.82	0.09	11.43	0.71	0.77	0.14	0.05	0.48	2.35	4.00	0.02	0.30			99.16		
	Ljm011	75.08	0.57	13.15	0.24	2.66	0.47	0.92	0.14	2.19	4.34	0.59				100.35		
	****	75.04	0.14	11.53	0.43	1.35	0.02	0.12	1.02	2.65	4.40	0.03	0.40			97.13	2	
	****	75.18	0.11	11.77	0.80	0.92	0.01	0.06	1.46	3.80	4.57	0.06	0.42			99.16		
	****	74.72	0.06	13.23	0.52	0.88	0.06	0.23	1.01	3.19	5.00	0.03	0.51			99.44	3	
	****	75.10	0.05	12.97	0.55	0.99	0.00	0.16	0.59	2.86	5.27	0.05	0.37	0.15		99.11	4	
	****	75.54	0.07	12.54	0.52	1.25	0.00	0.21	0.59	2.35	5.19	0.10	0.28	0.11		98.75		
	No.12	78.08	0.09	11.85	0.74	0.87	0.01	0.04	0.25	3.27	4.73	0.01				99.94		
	No.13	75.66	0.10	11.85	0.61	0.93	0.01	0.10	0.35	2.83	4.88	0.02				97.34		
	No.14	76.61	0.06	12.24	0.24	1.10	0.03	0.04	0.25	3.17	4.58	0.02				98.34	5	
No.16	76.36	0.64	14.64	0.93	1.08	0.04	0.29	0.10	2.63	4.30	0.05				101.06			
No.17	75.72	0.37	13.46	0.43	1.39	0.11	0.32	0.22	2.88	4.02	0.06				98.98			
Average of II		75.20	0.23	12.47	0.62	1.56	0.06	0.24	0.97	2.78	4.46	0.08	0.40	0.13	0.52	98.95		
Im	L65-2	74.96	0.14	11.14	0.33	1.50	0.07	1.02	0.48	2.95	5.72	0.04				98.35		
	8228	74.45	0.20	12.20	2.74	0.97	0.02	0.06	0.75	2.74	4.08	0.01				98.22		
	Slxj	75.11	0.14	13.02	0.20	2.06	0.03	0.27	1.25	3.05	5.25	0.06				100.44		
	Fan28	75.81	0.05	11.04	1.49	0.95	0.05	0.34	0.57	3.37	5.15	0.03				98.85		
	S3gu3	76.00	0.08	11.76	0.09	2.37	0.05	0.15	1.18	4.00	4.40	0.04	0.25			100.37		
	S5gu5	73.06	0.18	12.78	0.23	2.56	0.05	0.39	1.51	4.20	5.12	0.06	0.24			100.38		
	Ljm008	74.38	0.05	11.71	0.48	1.90	0.13	0.62	0.66	4.65	4.85	0.17				99.60		
	Fan17	75.46	0.10	11.60	0.70	2.06	0.08	0.52	0.69	3.40	5.25	0.00				99.86		
	Pjm-11	73.69	0.20	12.36	0.58	3.18	0.09	0.52	0.81	2.61	4.44	0.06				98.54		
	Pjhua51	76.78	0.13	12.09	1.43	1.67	0.21	0.10	0.73	2.80	4.15	0.01				100.10		
	Fan26	75.68	0.05	11.38	0.67	2.34	0.72	0.34	0.65	2.65	5.40	0.00				99.88		
	63-1a	76.26	0.11	12.04	0.16	1.47	0.03	0.12	1.00	3.46	4.68	0.15	0.28			99.76	8	
	****	74.70	0.32	11.92	1.45	1.82	0.01	0.45	0.93	2.72	4.72	0.04	0.04			99.12	2	
	No.6	76.34	0.30	11.75	0.77	2.09	0.04	0.72	0.85	3.00	4.27	0.06				100.19	5	
	No.7	77.27	0.06	12.55	0.46	0.71	0.03	0.06	0.30	3.67	6.02	0.01				101.14		
Average of Im		75.33	0.14	11.96	0.79	1.84	0.11	0.38	0.82	3.28	4.90	0.05	0.20			99.65		

Table 5 (continued)

phase	No.	SiO ₂	TiO ₂	Al ₂ O ₃	Fe ₂ O ₃	FeO	MnO	MgO	CaO	Na ₂ O	K ₂ O	P ₂ O ₅	H ₂ O	CO ₂	L.O.I	Sum	data source
It	Fan18	73.59	0.17	14.63	1.03	0.72	0.02	0.10	1.22	2.75	4.35	0.04				98.62	1
	8231	73.89	0.08	13.39	2.65	1.41	0.03	0.11	1.66	2.77	4.08	0.03				100.10	
	S9xn9	75.76	0.12	14.08	1.24	1.81	0.02	0.06	1.20	3.60	5.00	0.07				102.96	
	Pnm3	73.70	0.33	12.35	0.86	2.51	0.05	0.42	1.38	2.75	4.19	0.10	0.56		0.59	99.79	
	Pnhua49	73.93	0.25	12.86	1.14	1.96	0.03	0.22	0.85	2.80	4.30	0.04	0.08			98.46	
	Pnhua50	74.09	0.22	12.74	1.14	2.57	0.03	0.19	0.90	3.02	3.80	0.03	0.12			98.85	
	S6gu5	73.91	0.08	12.78	0.59	1.59	0.04	0.31	0.97	4.10	5.44	0.04	0.48			100.33	
	Ljm003	72.54	0.12	12.85	0.39	2.23	0.12	0.66	1.32	4.50	4.80	0.33				99.86	
	Fan19	74.13	0.10	12.96	0.84	1.49	0.08	0.69	0.65	3.65	5.00	0.05				99.64	
	65-1a	74.14	0.13	12.31	0.82	1.85	0.03	0.24	1.35	3.26	4.73	0.07	0.40	0.16		99.49	
Average of It		73.97	0.16	13.10	1.07	1.81	0.05	0.30	1.15	3.32	4.57	0.08	0.33	0.16	0.59	99.81	
Ic	L15-3	67.54	0.68	14.85	0.32	3.40	0.12	1.62	1.78	3.74	4.55	0.32				98.92	1
	Gu7	68.41	0.52	12.78	0.64	3.55	0.07	1.23	1.72	4.30	4.30	0.26				97.78	
	S6li6	69.45	0.46	14.13	0.67	3.46	0.04	1.02	2.09	4.10	4.10	0.22	0.72			100.46	
	Ljm001	66.36	0.08	14.56	1.65	3.33	0.18	1.93	1.78	4.40	4.65	0.32				99.24	
	Pghua46	69.26	0.50	14.03	1.57	2.57	0.52	0.70	1.50	3.25	3.85	0.21				97.96	
	L44-1	69.48	0.40	13.78	1.03	2.35	0.11	2.05	1.19	3.28	5.00	0.13				98.80	
	L47-1	70.54	0.47	13.12	0.64	2.90	0.11	1.37	1.66	3.49	4.64	0.14				99.08	
	****	70.01	0.10	13.32	0.85	2.30	0.06	0.65	2.26	3.68	3.94	0.25				97.42	
	L1-6	70.90	0.33	13.38	0.39	2.35	0.10	1.02	1.66	3.28	4.64	0.10				98.15	
	L41-1	71.25	0.28	13.55	0.45	2.00	0.09	1.28	1.07	3.28	5.00	0.06				98.31	
	S1li1	71.94	0.92	13.45	1.64	3.55	0.05	0.51	2.25	4.65	3.70	0.17				102.83	
	S5li5	70.69	0.32	14.61	0.70	2.44	0.02	0.52	2.04	3.69	3.05	0.13				98.21	
	56-1a	68.74	0.53	14.26	0.71	2.96	0.07	0.57	2.22	3.94	4.90	0.40	0.46			99.76	
	66-1a	71.23	0.43	13.14	1.21	2.29	0.06	0.65	2.26	3.68	3.94	0.25	0.37	0.02		99.53	
	61-1a	70.12	0.42	13.98	0.96	2.35	0.05	0.68	1.85	3.48	4.58	0.16	0.48	0.18		99.29	
	58-1a	70.60	0.40	13.82	0.85	2.30	0.06	0.53	1.83	3.88	4.74	0.28	0.56			99.85	
****	69.44	0.38	14.61	1.63	2.23	0.05	0.55	2.53	2.98	4.08	0.15	0.68		0.49	99.80		
****	69.52	0.41	14.36	1.30	2.59	0.07	0.55	2.54	3.18	4.20	0.17	0.68		0.56	100.13		
Average of Ic		69.75	0.42	13.87	0.96	2.72	0.10	0.97	1.90	3.68	4.33	0.21	0.56	0.10	0.53	99.20	
E	29	65.38	0.51	15.81	0.36	2.99	0.09	0.66	1.70	3.20	6.47	0.15	1.33		1.44	100.09	1
	30	54.70	1.86	16.06	0.98	9.91	0.26	3.20	3.90	4.15	3.19	0.57				98.78	
	Gu3	51.95	0.26	12.60	5.36	11.21	0.11	0.70	5.80	2.75	4.50	0.13	1.65		5.25	102.27	
	L43-2	57.73	1.56	15.22	2.41	6.25	0.17	4.44	2.16	4.16	1.78	0.27				96.15	
	L43-4	61.00	1.20	15.45	1.57	5.30	0.18	2.39	2.85	3.95	4.22	0.28				98.39	
	Gu2	62.30	2.07	15.92	1.63	3.00	0.54	2.80	2.43	3.00	4.77	0.52	0.54		0.75	100.27	
	Gu1	66.07	0.49	15.25	1.22	2.52	0.28	1.05	1.22	3.50	6.44	0.29				98.33	
	56-3	56.60	1.40	17.09	1.72	6.08	0.16	1.94	5.24	5.46	2.38	0.88	0.92			99.87	
	56-2	57.96	1.32	15.70	1.54	6.09	0.16	2.23	3.41	4.10	4.16	0.54	1.94	0.50		99.65	
	59-1	57.19	1.28	16.11	1.69	5.75	0.22	2.03	4.24	4.25	6.10	0.69	0.77			100.32	
	66-1	57.28	1.30	16.48	2.04	5.97	0.19	2.34	4.03	4.36	4.22	0.59	0.62	0.42		99.84	
	61-2	62.96	1.24	14.64	1.45	5.56	0.12	2.77	2.54	3.78	3.32	0.47	0.84	0.04		99.73	
	56-1	63.82	0.88	15.40	1.40	4.12	0.09	1.47	3.04	4.18	4.24	0.37	0.54	0.04		99.59	
	58-3	65.30	0.66	15.06	1.46	3.11	0.10	1.15	2.19	3.68	5.20	0.31	1.24	0.36		99.82	
Average of E		60.02	1.15	15.49	1.77	5.56	0.19	2.08	3.20	3.89	4.36	0.43	1.04	0.27	2.48	99.51	

Data sources: (1) cited from Pu (1986); (2) Deng (1984); (3) Qin (1985); (4) Xiong (1986); (5) Gong et al. (1985); (6) Dong (1989); (7) You (1990); (8) Zhang et al. (1985). **** sample number unavailable.

sample No.	qtz	ab	or	an	ne	ac	ns	di	wo	hy	ol	mt	il	hm	ap	cm	ag	DI
Ygua13	37.42	20.76	30.84	4.19	0	0	0	0	0	0	0	0	0	0	0.95	2.27	0.72	89.02
Y!!	37.03	27.48	25.93	4.04	0	0	0	0	0	0	0	0	0	0.07	0.70	0.82	93.50	
****	38.91	27.93	26.65	2.57	0	0	0	0	0	0	0	0	0	0.07	0.98	0.84	93.50	
Pguas5	39.91	24.50	28.23	3.05	0	0	0	0	0	0	0	0	0	0.05	0.99	0.83	92.63	
Pguas3	40.13	28.11	26.19	2.30	0	0	0	0	0	0	0	0	0	0.02	0.73	0.87	94.43	
Pguas4	43.39	24.72	2.83	2.83	0	0	0	0	0	0	0	0	0	0.02	0.11	0.89	94.00	
Pguas1	41.77	26.06	25.29	2.68	0	0	0	0	0	0	0	0	0	0.02	0.87	0.84	93.12	
Bguas11	32.77	34.33	28.07	0.60	0	0	0	2.70	0.76	0.00	0.65	0.10	0	0.02	0.00	0.98	95.18	
ZK209	38.66	30.39	21.89	1.60	0	0	0	0	0	0	0.58	0.16	0	0.12	2.87	0.74	90.94	
****	38.20	24.00	26.57	4.58	0	0	0	0	0	0	0	0	0	0.14	1.59	0.74	88.77	
****	41.03	25.39	27.14	1.15	0	0	0	0	0	0	0	0	0	0.09	2.83	0.75	93.57	
****	35.93	23.82	33.03	2.19	0	0	0	0	0	0	0	0	0	0.02	0.89	0.86	92.77	
****	41.41	25.51	26.31	1.97	0	0	0	0	0	0	0.96	0.21	0	0.07	1.72	0.80	93.23	
No23	39.21	28.67	27.86	1.17	0	0	0	0	0	0	1.37	0.17	0	0.02	0.80	0.90	95.74	
No24	42.29	27.84	25.95	0.44	0	0	0	0	0	0	0.76	0.08	0	0.02	1.76	0.84	96.08	
No25	39.58	28.79	26.61	1.70	0	0	0	0	0	0	0.37	0.14	0	0.02	0.77	0.88	94.98	
No26	47.66	21.43	26.15	0.68	0	0	0	0	0	0	0.54	0.13	0	0.02	1.98	0.80	95.24	
No1	33.11	27.21	32.07	3.21	0	0	0	0	0	0	0.42	0.17	0	0.05	0.31	0.88	92.39	
No2	32.35	32.77	29.01	2.67	0	0	0	0.95	0	1.61	0.53	0.06	0	0.05	0.00	0.92	94.14	
No3	33.60	31.70	29.27	2.66	0	0	0	0	0	2.27	0.31	0.06	0	0.05	0.09	0.92	94.58	
No4	33.43	29.34	29.88	3.14	0	0	0	0	0	3.34	0	0.42	0.11	0	0.07	0.26	89.92	
F1	30.83	32.66	29.49	3.08	0	0	0	0	0	3.24	0	0.25	0.08	0	0.05	0.33	92.99	
F2	32.06	31.71	30.01	2.27	0	0	0	0	0	3.00	0	0.15	0.10	0	0.05	0.67	89.97	
F3	33.04	30.88	29.43	2.27	0	0	0	0	0	3.18	0	0.12	0.10	0	0.05	0.95	86.34	
L84	33.92	26.68	30.90	2.70	0	0	0	0	0	4.07	0	0.15	0.04	0	0.07	1.48	81.49	
Bguas2	34.99	26.09	26.33	4.56	0	0	0	1.66	0	4.41	0	1.15	0.54	0	0.26	0.00	86.86	
Yana2	35.74	25.36	24.88	6.28	0	0	0	0	0	5.31	0	0.84	0.64	0	0.21	0.75	85.97	
Pguas4	40.66	30.35	22.97	3.18	0	0	0	0	0	1.35	0	0.81	0.45	0	0.00	0.22	88.93	
8207	35.17	17.00	25.53	14.93	0	0	0	0.46	0	3.74	0	1.97	0.95	0	0.26	0.00	77.70	
8230	37.19	21.69	24.95	10.33	0	0	0	0	0	3.66	0	1.30	0.65	0	0.21	0.03	83.82	
0233-1	38.35	20.20	25.49	10.04	0	0	0	0	0	3.43	0	0.73	0.51	0	0.09	1.17	84.03	
Pguas10	40.91	22.44	27.76	4.61	0	0	0	0	0	2.27	0	0.85	0.20	0	0.05	0.78	91.10	
Pguas5	39.39	22.08	25.91	4.74	0	0	0	0	0	4.34	0	0.64	0.45	0	0.09	2.37	87.38	
Pguas11	42.06	18.58	25.71	0.70	0	0	0	0	0	6.93	0	0.35	1.09	0	0.00	4.61	86.34	
****	40.97	23.18	26.88	5.03	0	0	0	0	0	2.30	0	0.64	0.27	0	0.07	0.65	91.03	
****	34.71	32.56	27.35	1.58	0	0	0	1.97	1.29	0.00	1.17	0.21	0	0.14	0.00	0.95	83.63	
****	34.43	27.28	29.87	4.87	0	0	0	0	0	1.79	0	0.76	0.12	0	0.07	0.81	91.58	
****	36.87	24.55	31.59	2.64	0	0	0	0	0	1.70	0	0.81	0.10	0	0.12	1.63	80.91	
****	40.58	20.22	31.18	2.31	0	0	0	0	0	2.31	0	0.77	0.14	0	0.24	2.26	91.98	
No12	40.02	27.69	27.97	1.18	0	0	0	0	0	0.96	0	1.07	0.17	0	0.02	0.92	89.68	
No13	40.27	24.60	29.63	1.65	0	0	0	0	0	1.34	0	0.91	0.20	0	0.05	1.36	84.50	
No14	39.96	27.28	27.52	1.13	0	0	0	0	0	1.91	0	0.35	0.12	0	0.05	1.69	83.76	
No16	43.53	22.02	25.15	0.17	0	0	0	0	0	0.94	0	1.33	1.20	0	0.11	5.54	90.70	
No17	42.42	24.62	24.00	0.71	0	0	0	0	0	2.61	0	0.63	0.70	0	0.14	4.16	89.04	
average II	39.29	23.87	26.72	4.34	0	0	0	0	0	2.73	0	0.91	0.45	0	0.18	1.51	89.69	
L65-2	33.34	25.38	34.37	0.26	0	0	0	1.56	0	4.23	0	0.49	0.27	0	0.09	0.99	93.09	
8228	41.98	23.61	24.55	3.72	0	0	0	0	0	0.15	0	2.66	0.39	0.96	0.02	1.97	80.13	
Shixi	32.65	25.70	30.89	5.78	0	0	0	0	0	4.10	0	0.29	0.26	0	0.14	0.19	89.24	
Fana8	35.64	28.44	30.79	0.00	0	0.36	0	2.18	0	0.42	0	2.01	0.10	0	0.07	0.00	1.01	
Fana28	32.25	33.81	25.97	1.14	0	0	0	3.92	0	2.55	0	0.13	0.15	0	0.09	0.00	92.03	
S3gua3	24.73	35.49	30.22	0.90	0	0	0	5.36	0	2.49	0	0.33	0.34	0	0.14	0.00	90.44	
Lim008	28.80	33.36	28.78	0.00	0	1.39	1.06	1.85	0	4.27	0	0.00	0.10	0	0.40	0.00	1.10	
Fana7	32.48	28.81	31.07	0.88	0	0	0	2.17	0	3.38	0	1.02	0.19	0	0.00	0.00	92.36	
Pfm-11	37.35	22.41	26.63	3.68	0	0	0	0	0	6.59	0	0.85	0.39	0	0.14	1.96	86.39	
Pguas51	41.94	23.67	24.50	3.55	0	0	0	0	0	2.07	0	2.07	0.25	0	0.02	1.69	90.11	
Fana26	35.47	22.45	31.95	3.21	0	0	0	0.02	0	5.85	0	0.97	0.10	0	0.00	0.00	89.87	
63-1a	35.50	29.43	27.80	3.52	0	0	0	0.42	0	2.53	0	0.23	0.21	0	0.35	0.00	89.73	
****	37.87	23.23	28.15	4.39	0	0	0	0	0	2.78	0	2.12	0.61	0	0.09	0.75	80.25	
No6	38.48	25.34	25.19	3.82	0	0	0	0	0	4.57	0	1.11	0.57	0	0.14	0.79	89.01	
No7	31.73	30.69	35.18	0.00	0	0.02	0	1.23	0	0.38	0	0.65	0.11	0	0.02	0.00	1.00	
average Im	34.26	27.91	29.07	3.42	0	0	0	0	0	3.50	0	1.14	0.27	0	0.11	0.00	0.90	

Table 6 CIPW norms of granites of the Cuposhan batholith*

Table 6 (continued)

phase	sample No.	qtz	ab	or	an	ne	ac	ns	di	wo	hy	ol	mt	il	hm	ap	cm	ag	DI
It	Fan18	38.73	23.60	26.07	5.87	0	0	0	0	0	0.48	0	1.51	0.33	0	0.09	3.32	0.63	88.39
	8231	38.34	23.42	24.09	8.03	0	0	0	0	0	0.60	0	3.84	0.15	0	0.07	1.47	0.67	85.84
	S9xm9	31.32	29.59	28.70	5.34	0	0	0	0	0	2.22	0	1.75	0.22	0	0.16	0.71	0.81	89.61
	Pnm3	37.30	23.59	25.10	6.28	0	0	0	0	0	4.56	0	1.26	0.64	0	0.23	1.04	0.73	86.00
	Pnhua49	38.73	24.08	25.83	4.02	0	0	0	0	0	2.90	0	1.68	0.48	0	0.09	2.18	0.72	88.64
	Pnhua50	38.77	25.88	22.75	4.32	0	0	0	0	0	3.99	0	1.67	0.42	0	0.07	2.12	0.71	87.39
	S6gu5	26.67	34.75	32.20	0.40	0	0	0	3.57	0	1.32	0	0.86	0.15	0	0.09	0.00	0.99	93.61
	Ljrm03	24.22	38.13	28.41	0.69	0	0	0	3.16	0	3.84	0	0.57	0.23	0	0.77	0.00	0.98	90.76
	Fan19	30.67	31.00	29.66	2.91	0	0	0	0	0	3.76	0	1.22	0.19	0	0.12	0.48	0.88	91.32
	65-1a	33.48	27.88	28.26	5.04	0	0	0	1.10	0	2.63	0	1.20	0.25	0	0.16	0.00	0.85	89.62
average It		33.60	28.21	27.12	5.20	0	0	0	0	3.03	0	1.56	0.31	0	0.19	0.80	0.79	89.92	
Ic	L15-3	20.96	31.99	27.18	6.81	0	0	0	0	0	9.22	0	0.47	1.31	0	0.75	1.32	0.75	80.13
	Gu7	21.08	37.21	25.99	2.93	0	0	0	3.42	0	6.79	0	0.95	1.01	0	0.62	0.00	0.92	84.28
	S6h6	22.45	34.78	24.29	8.06	0	0	0	0.76	0	7.29	0	0.97	0.88	0	0.51	0.00	0.79	81.53
	Ljrm001	15.15	37.52	27.69	6.29	0	0	0	0.41	0	9.63	0	2.41	0.15	0	0.75	0.00	0.84	80.35
	Pghua46	30.96	28.07	23.23	6.20	0	0	0	0	0	5.42	0	2.32	0.97	0	0.50	2.34	0.68	83.26
	L44-1	24.96	28.09	29.91	5.12	0	0	0	0	0	8.21	0	1.51	0.77	0	0.30	1.13	0.78	82.95
	L47-1	25.78	29.81	27.68	6.49	0	0	0	0.75	0	7.33	0	0.94	0.90	0	0.33	0.00	0.82	83.26
	****	27.86	31.96	23.90	8.41	0	0	0	1.21	0	4.61	0	1.27	0.19	0	0.59	0.00	0.77	83.72
	L1-6	28.13	28.28	27.94	7.72	0	0	0	0	0	6.29	0	0.58	0.64	0	0.24	0.19	0.78	84.35
	L41-1	28.11	28.23	30.06	5.00	0	0	0	0	0	6.30	0	0.66	0.54	0	0.14	0.96	0.80	86.40
	S1li1	24.35	38.26	21.26	4.76	0	0	0	4.29	0	2.67	0	2.31	1.70	0	0.38	0.00	0.87	83.88
	S5li5	31.79	31.79	18.35	9.44	0	0	0	0	0	4.79	0	1.03	0.62	0	0.31	1.87	0.64	81.94
	56-1a	21.23	33.57	29.16	6.80	0	0	0	1.42	0	4.83	0	1.04	1.01	0	0.93	0.00	0.83	83.96
	66-1a	29.11	31.41	23.49	7.76	0	0	0	1.60	0	3.46	0	1.77	0.82	0	0.58	0.00	0.79	84.00
	61-1a	27.69	29.76	27.35	6.11	0	0	0	0	0	4.66	0	1.41	0.81	0	1.12	1.09	0.76	84.80
	58-1a	25.00	33.07	28.21	6.34	0	0	0	0.82	0	3.91	0	1.24	0.77	0	0.65	0.00	0.83	86.28
	****	30.08	25.57	24.45	11.73	0	0	0	0	0	3.63	0	2.40	0.73	0	0.35	1.07	0.64	80.09
	****	28.05	27.21	25.10	11.62	0	0	0	0	0	4.56	0	1.91	0.79	0	0.40	0.38	0.68	80.36
	average Ic		25.44	31.50	25.85	8.17	0	0	0	0	6.17	0	1.40	0.81	0	0.48	0.17	0.77	82.97
E	29	16.18	27.82	39.29	7.66	0	0	0	0	0	6.33	0	0.54	1.00	0	0.36	0.83	0.78	83.29
	30	0.09	35.55	19.08	15.82	0	0	0	0	0	23.05	0	1.44	3.58	0	1.34	0.05	0.64	54.73
	Gu3	2.63	24.40	27.88	9.17	0	0	0	17.65	0	9.28	0	8.15	0.52	0	0.32	0.00	0.75	54.92
	L43-2	13.46	36.61	10.94	9.31	0	0	0	0	0	19.02	0	3.63	3.08	0	0.65	3.30	0.58	61.01
	L43-4	10.14	33.97	25.35	12.16	0	0	0	0.29	0	12.81	0	2.31	2.32	0	0.66	0.00	0.72	69.46
	Gu2	18.07	25.65	28.48	8.75	0	0	0	0	0	8.81	0	2.39	3.97	0	1.22	2.68	0.63	72.19
	Gu1	16.46	30.12	38.70	4.23	0	0	0	0	0	6.05	0	1.80	0.95	0	0.68	1.01	0.83	85.28
	56-3	1.71	46.69	14.21	15.25	0	0	0	4.38	0	10.49	0	2.52	2.69	0	2.06	0.00	0.68	62.61
	56-2	5.86	35.69	25.29	12.50	0	0	0	1.07	0	13.44	0	2.30	2.58	0	1.29	0.00	0.72	66.84
	59-1	0.00	35.72	36.21	6.89	0.22	0	0	8.14	0	0.00	6.31	2.46	2.44	0	1.61	0.00	0.84	72.15
	66-1	2.62	37.34	25.24	13.09	0	0	0	2.71	0	12.12	0	2.99	2.50	0	1.38	0.00	0.71	65.21
	61-2	16.94	32.36	19.85	9.64	0	0	0	0	0	14.25	0	2.13	2.38	0	1.10	1.35	0.67	69.15
	56-1	13.84	35.72	25.31	10.84	0	0	0	1.63	0	8.06	0	2.05	1.69	0	0.87	0.00	0.74	74.87
	58-3	17.13	31.70	31.29	9.00	0	0	0	0	0	6.58	0	2.16	1.28	0	0.73	0.14	0.78	80.12
	average E		9.09	33.57	26.23	12.15	0	0	0	0.94	0	12.17	0	2.62	2.22	0	1.02	0.00	0.72

*Note: calculated by the FORTRAN 77 program of Rock (1989), CO₂ ignored.

qtz-quartz; ab-albite; or-potash feldspar; an-anorthite; ne-nepheline; ac-aegirine; ns-Na₂SiO₃; di-diopside; wo-wallastonite; hy-hypersthene; ol-olivine; mt-magnetite; il-ilmenite; hm-hematite; ap-apatite; cm-corundum; DI (differentiation index)=qtz+or+ab+ne+lc; ag (agpaicity index)= molecular (Na+K)/Al

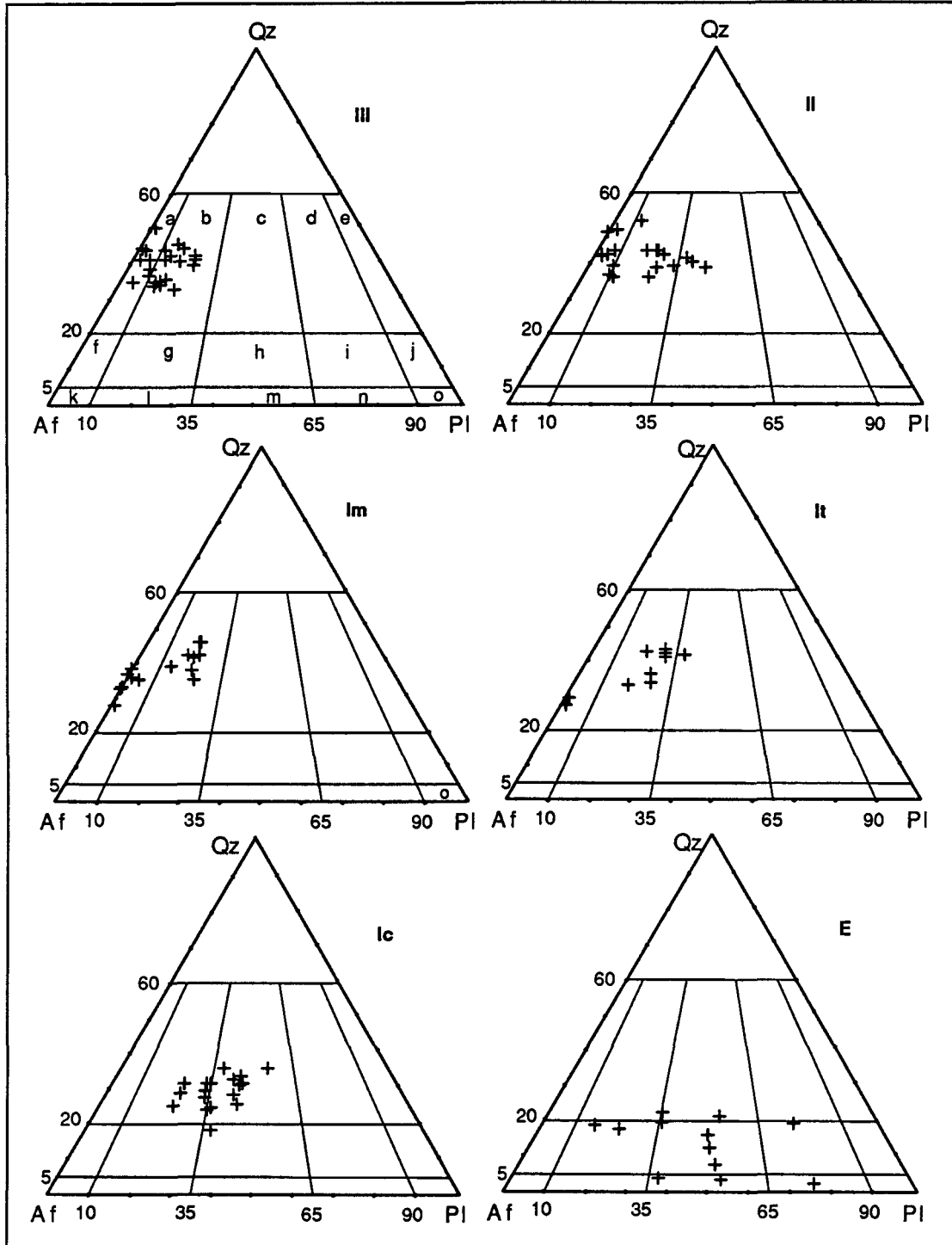


Fig. 22 Plots of Qz, Af and Pl data of the Guposhan batholith on the IUGS classification (Streckeisen, 1976). Qz-quartz; Af-alkaline feldspar; Pl - plagioclase. Af and Pl are calculated from the CIPW Ab, Or and An data according to the method proposed by Rittmann (1973); Qz is CIPW normative value.
 a-alkali-feldspar granite; b-granite; c-adamellite; d-granodiorite; e-tonalite; f-alkali-feldspar quartz syenite; g-quartz syenite; h-quartz monzonite; i-quartz monzodiorite/quartz monzogabbro; j-quartz diorite/quartz gabbro; k-alkali-feldspar syenite; l-syenite; m-monzonite; n-monzodiorite/monzogabbro; o-diorite/gabbro.

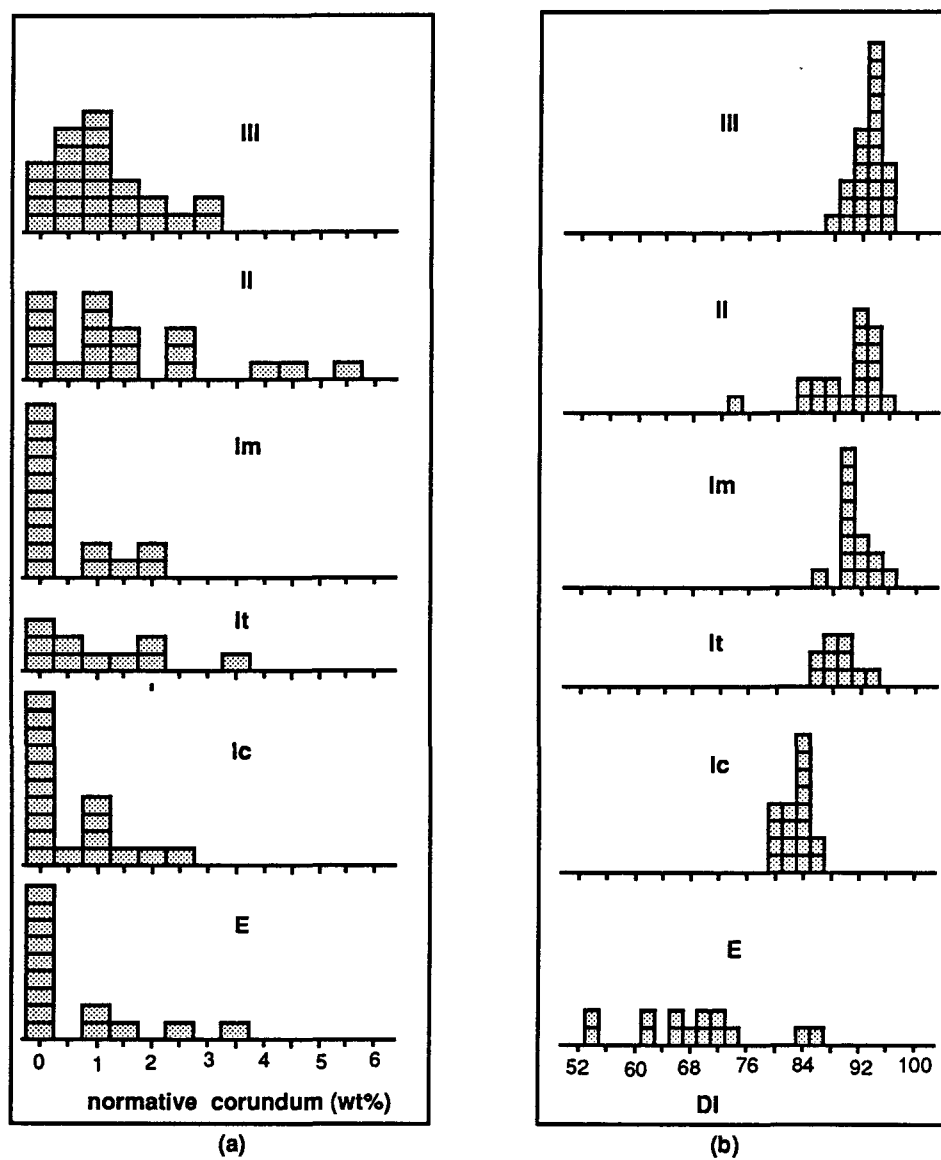


Fig. 23 Histograms of (a)-normative corundum (cm in table 6) and (b)-Differentiation index (DI in table 6) of granites of the Guposhan batholith.

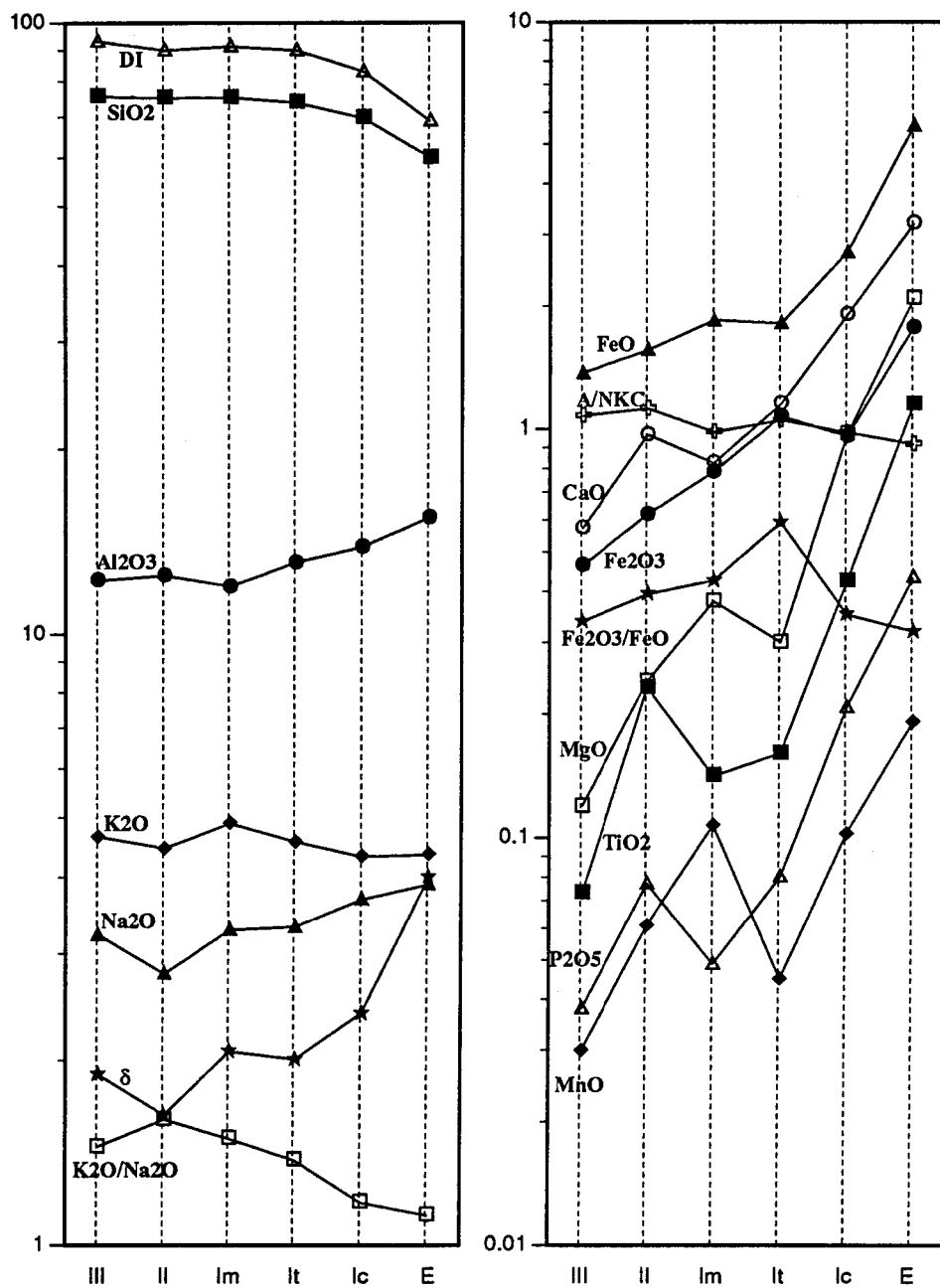


Fig. 24 Variation of major element contents and related parameters in different phases of the Guposhan batholith.

increases from E through Ic, It to Im, and from II to III, but a decrease from Im to II is obvious; (3) Na₂O decreases from E through Ic, It and Im to II, but increases from II to III; (4) FeO+Fe₂O₃, MnO, MgO, Al₂O₃, CaO, TiO₂ and P₂O₅ generally decrease from E through I, II to III, but an increase from It to Im is observed for MnO and MgO, and a general increase of Al₂O₃, CaO, TiO₂ and P₂O₅ is observed from Im to II; (5) K₂O/Na₂O increases from I to II, but decreases from II to III; (6) Fe₂O₃/FeO increases from E through Ic to It, and decreases from It through Im and II to III; (7) A/NKC (molecular Al₂O₃/(Na₂O +K₂O+CaO)) generally decreases from III through II and I to E (>1.0 for III, II and It, <1.0 for Im, Ic and E); (8) δ (Rittmann index= (Na₂O+K₂O)²/(SiO₂-43)) generally decreases from E through I and II to III, but an increase from II to III is observed.

The major element content in the granites shows an increasing felsicity (reflected by SiO₂), differentiation (reflected by DI) and aluminium saturation (reflected by normative corundum and A/NKC) degree and a decreasing mafic (reflected by MgO, MnO, FeO+Fe₂O₃ and TiO₂) and alkalinity (reflected by δ) degree from E through Ic, It, Im and II to III. The difference between Im and II & III in differentiation degree is less obvious than their difference in the degree of aluminium saturation and alkalinity. III and II are more aluminium-saturated and less alkaline than Im.

4.3.2 Trace Elements

A number of analyses of trace elements in the granites of the Guposhan batholith are listed in table 7.

The variation of contents of trace elements and some parameters in different phases of the Guposhan batholith are shown in table 8 and Fig.25. Some common features can be observed. The concentrations of Sn, Zn and Pb broadly increase from phase E through I and II to III, although a sample of Im contain 115 ppm Sn which makes the average Sn content in Im higher than in II and III and the contents of Zn and Pb are only very slightly lower in I than II. A decrease in Sn content from phase II to III is also noticed. The variation of W and Cu and F contents is very irregular. The Cl content decreases from E through I to II, but increases from II to III. The Sc content increases from III through I to E. The contents of Cr, Ni and Co do not increase from phase III through II and I to E. On the contrary, a reverse trend appears to exist. Parameters reflecting the differentiation degree of magma (Rb/Sr, Ba/Sr, Ta/Nb, Li/Mg, Rb/K and Ta/Ti) generally increase from phase E

Table 7 Contents of trace elements in granites of the Guposhan batholith (ppm)

phase	No.	Sn	W	Zn	Pb	Cu	F	Cl	B	As	Cr	Ni	Co	Rb	Sr	Ba	Cs	Li	Be	Nb	Ta	Sb	Sc	data	
III	No.17	18.0	28.0	34.0	25.0	14.0	1600							542	12	48	41.0	135.0		42.0	8.0				
	No.18	7.0	28.0	30.0	45.0	11.0	1400							549	60	96	26.0	39.0		24.0	8.0				
	No.19	7.0	12.0	32.0	30.0	10.0	1400							553	16	56	28.0	50.0		28.0	7.0				
	No.20	6.0	20.0	41.0	28.0	6.0	1300							455	57	165	20.0	19.0		21.0	0.0				
	No.21	8.0	24.0	50.0	28.0	11.0	1400							505	48	280	19.0	78.0		28.0	8.0				
	No.22	20.0	16.0	41.0	28.0	6.0	1200							727	18	74	38.0	113.0		63.0	16.0				
	No.23	6.0	63.0	98.0	43.0	19.0	1400							809	5	13	34.0	43.0		45.0	26.0				
	No.24	10.0	12.0	29.0	25.0	5.0	1200							514	8	34	19.0	72.0		63.0	11.0				
	No.25	18.0	135.0	128.0	320.0	21.0	2100							745	30	100	18.0	68.0	13.0	35.0	6.0				
	No.26	14.0	63.0	350.0	665.0	15.0	3300							544	95	385	31.0	143.0	2.0	38.0	16.0				
	No.27	7.0	11.0	10.0	28.0	10.0	500							567	7	38	15.0	22.0	11.0	57.0	12.0				
	No.28	14.0	3.0	39.0	20.0	11.0	1150							462	25	142	31.0	33.0	4.0	36.0	16.0				
	No.29	32.0	6.0	85.0	51.0	10.0	2500							480	22	74	21.0	12.0	22.0	56.0	16.0				
	No.30	53.0	59.0	86.0	64.0	20.0	2925							465	21	100	28.0	27.0	8.0	41.0	15.0				
	No.31	6.0	42.0	35.0	26.0	84.0	2700							480	40	120	57.0	60.0	8.0	48.0	26.0				
	No.32	12.0	26.0	80.0	95.0	13.0	2200				11.0	65.0	9.5	640	12	62	22.0	77.0	10.0	50.0	67.0				
	No.33	7.0	13.0	38.0	58.0	13.0	1200							540	2	14	13.0	33.0	20.0	46.0	8.0				
	No.34	21.0	27.0	30.0	45.0	12.0	2600							960	2	10	44.0	121.0	10.0	52.0	14.0				
	No.35	139.0	60.0	41.0	30.0	7.0	5900							936	2	4	15.0	217.0	50.0	83.0	41.0				
	****	7.0	27.0	61.0	31.0	73.0	2200				11.0	7.5	11.5					65.0		48.0	3.0			2	
	****	137.0	60.0	41.0	30.0	7.0	1300				8.2	22.5	8.5					27.0		83.0	41.0				
	****	20.0	100.0				7000		50	5.0				490	12	1164	29.0								
	****	82.0	1.0		105.0	14.0	810	130					7.1	400	20										
	no.38			11.2								10.3		490			24.2					9.1	0.8	4.3	7
	no.305-2	4.5	21.4	28.1			408	120			14.7	11.3		2.7	446	90	175	16.3				9.9	1.0	4.0	
	No.1	13.8	51.6				600							489	20	78		28.0	21.0	45.0	17.0				
	No.2	35.0	48.6				500							434	15	85		13.0	4.3	35.0	14.0				
	No.3	31.2	66.6				600							476	15	80		23.0	3.2	48.0	14.0				
	No.4	54.0	166.5				800							514	14	84		71.0	4.3	36.0	19.0				
	L84	7.6	4.1	17.0		4.0	780	130	12.0			1.0	2.0	8.0	380	340	82	100.0	32.0					3.0	
	II	No.7	4.0	26.0	31.0	23.0	35.0	1000						430	28	84	14.0	23.0		28.0	10.0				
		No.8	3.0	16.0	48.0	20.0	7.0	480						398	78	320	19.0	77.0		21.0	13.0				
		No.9	3.0	16.0	28.0	20.0	5.0	1300						446	60	258	26.0	31.0		31.0	8.0				
		No.10	81.0	11.0	129.0	110.0	22.0	3625						500	30	80	47.0	22.0	4.0	62.0	21.0				
		No.11	27.0	14.0	81.0	54.0	67.0	4250						459	8	45	28.0	27.0	11.0	33.0	17.0				
No.12		23.0	15.0	56.0	45.0	73.0	3000						620	10	70	42.0	20.0	7.0	26.0	29.0					
No.13		38.0	4.0	60.0	31.0	53.0	3500						420	30	110	42.0	16.0	7.0	62.0	8.0					
No.14		8.0	16.0	59.0	22.0	172.0	3488						336	101	480	39.0	41.0	9.0	41.0	8.0					
No.15		12.0	14.0	55.0	30.0	2.0	2200				11.0	55.0	12.5	432	155	568	23.0	77.0	4.0	49.0	5.0				
****		106.0	8.0	40.0	70.0	4.0	2390						4.0	410	32			55.0						4	
****	20.0	140.0				500	60	8.0					300	58	1674	11.0									
Im	No.5	7.0	5.0	51.0	33.0	7.0	1300				12.2	10.5	11.0	484	74	393	15.0	63.0	10.0	48.0	3.0				
	****	7.9		42.0	34.0	43.0	1700				5.3	2.2	1.6						27.0	6.0					
	****	3.2	17.7	60.0	45.0	74.0	970	110					5.8	330	200		73.0								
	no.19	115.0	21.1				1760	308		16.1	14.0		2.3	447	20		14.7				7.8	0.4	3.5	7	
It	****	12.0	198.0	64.0	30.0	5.0	1300				11.0	11.0	10.0	341	57		64.0		64.0	7.0					
	no.17	5.2	15.0	31.5			2380	265		10.6	9.2		3.2	371	95	317	10.7				3.6	0.3	4.4	7	
Ic	****	12.0		56.0	38.0	29.0					9.8	2.8	5.4						18.3					2	
	cx058	9.3	17.4	84.8	36.4	29.5	1320	250		9.9	6.7		6.1	272	181	275	40.7				6.3	1.1	4.3	7	
	cx055-2	9.0	10.7	34.9			1480	172		4.0	9.5		5.1	319	94	281	15.7				4.3	0.3	4.2		
E	****	6.4		73.0	20.0	29.0					7.2	3.0	14.0						10.2					2	
	****	1.0		122.0	32.0	22.0					7.2	2.7	10.0						14.3						
	cx060-2			139.0	43.0	37.0					13.3	10.5	35.2		276	210								6	
	no.43	11.3	17.9	97.5			2880	412		6.3	16.9		11.1	451	113	188	44.3				8.1	0.3	10.7	7	
cx055-1	22.0	71.8	128.3			4800	488		6.5	10.0		13.6	250	482	566	15.3				5.0	0.7	7.3			

Data sources:

(1)No.204 Geol. Team of Guangxi (1986); (2)Deng (1984); (3) Qin(1985); (4) Xiong (1986); (5) Dong (1989); (6) this study (Cr, Ni, Co, V, Sr and Ba are analysed at HIMG, the others are analysed at HIAMP); (7) this study (Sn, F, Cl, Sr are analysed at HIAMP, the others are analysed by INAA at UQAC); (8) You (1990).

Table 8 Average content (ppm) of trace elements and some parameters in different phases of the Guposhan batholith

Elements/ratios	III	II	Im	It	Ic	E
Sn	27.5	29.5	33.3	8.6	10.1	10.2
W	40.2	25.5	14.6	107.0	14.1	44.9
Zn	61.9	58.7	51.0	47.8	58.6	22.4
Pb	82.7	42.5	37.3	30.0	37.2	31.7
Cu	17.2	44.0	41.3	5.0	29.3	29.3
F	1827	2339	1433	1840	1400	3840
Cl	108	60	209	265	211	450
B	8.5	8.0				
As	14.7		16.1	10.6	7.0	6.4
Cr	8.8	11.0	10.5	10.1	8.7	10.9
Ni	20.8	55.0	6.4	11.0	2.8	5.4
Co	7.0	8.3	5.2	6.6	5.5	16.8
Rb	557	432	420	356	296	351
Sr	37.3	56.3	24.7	76	138	290
Ba	137	369	393	317	278	321
Cs	30.0	29.1	34.2	10.7	28.2	29.8
Li	62.3	38.9	63.0	64.0		
Be	12.7	7.0	10.0			
Nb	46.0	39.2	37.5	64.0		
Ta	16.6	13.2	5.6	5.3	5.3	6.6
Sb	0.9		0.4	0.3	0.7	0.5
Sc	3.8		3.5	4.4	4.3	9.0
Rb/Sr	14.930	7.670	17.004	4.684	2.145	1.210
Cs/Rb	0.054	0.067	0.081	0.030	0.095	0.085
Ba/Sr	3.670	6.550	8.300	4.171	2.014	1.107
Ta/Nb	0.361	0.337	0.149	0.083		
Rb/K	0.0144	0.0117	0.0103	0.0094	0.0082	0.0097
Li/Mg	0.087	0.027	0.028	0.035		
Ta/Tl	0.0380	0.0095	0.0066	0.0055	0.0021	0.0010

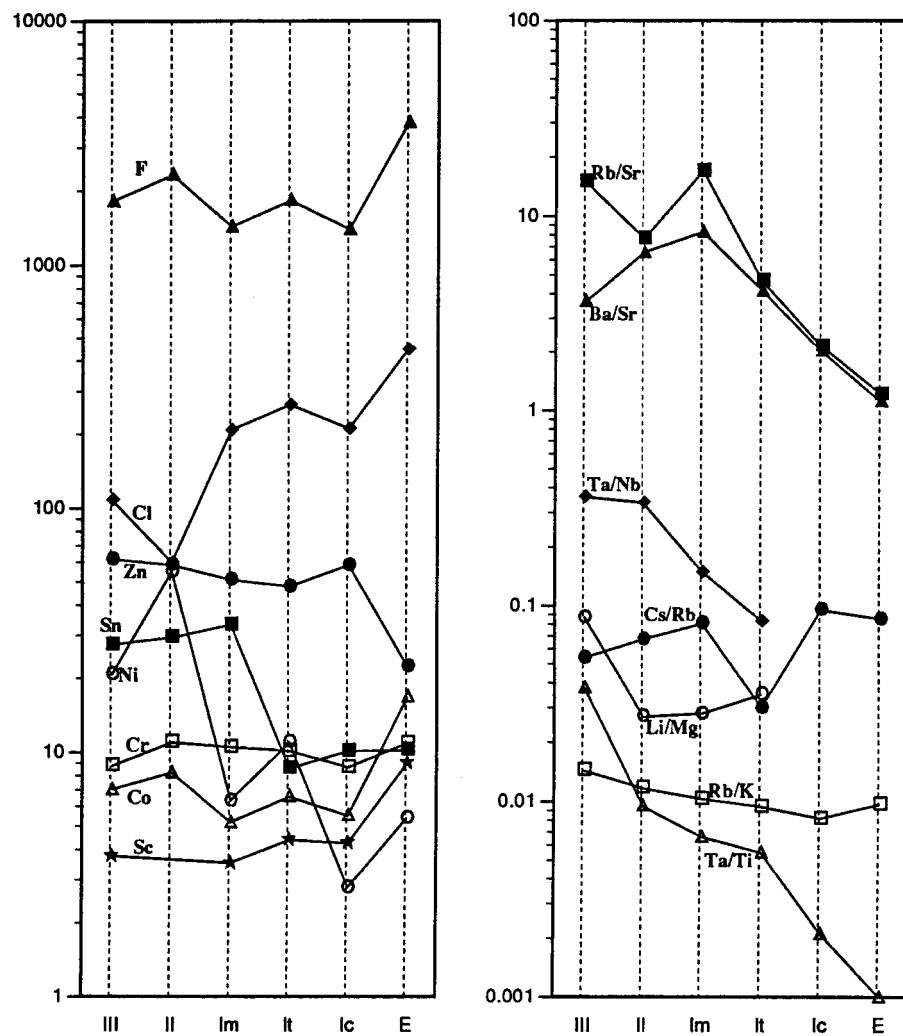


Fig. 25 Variation of trace element concentrations and magma differentiation-related parameters between different phases of the Guposhan batholith (data from Table 8).

through I and II to III, but reverse trends are also observed between Im and II (Rb/Sr, Ba/Sr, Cs/Rb and Li/Mg), and Cs/Rb seems to decrease from phase I through II to III. The only ratio that continuously increases from phase E through Ic, It, Im and II to III is Ta/Ti.

4.3.3 REE patterns

REE analyses and some parameters of REE patterns of different phases of the Guposhan batholith are listed in table 9.

The ranges of Σ REE in all the phases are fairly limited in comparison with those of the sedimentary rocks. Σ REE ranges from 129.24 to 175.47 ppm for phase III, from 193.89 to 236.99 for phase II, from 205.13 to 333.78 for phase I and from 217.52 to 221.81 for E. Σ LREE/ Σ HREE ranges from 2.47 to 5.30 for phase III, from 2.69 to 7.10 for phase II, from 4.68 to 10.86 for phase I and 4.30 to 7.65 for phase E. δ Eu ranges from 0.09 to 0.18 for phase III, from 0.07 to 0.23 for phase II, from 0.18 to 0.56 for phase I and 0.44 to 0.59 for phase E. The variation of REE patterns between different phases is shown in table 9 and Fig. 26, and the following variation tendency is observed: (1) δ Eu decreases gradually from E through Ic, It, Im, II to III; (2) Σ LREE/ Σ HREE decreases from Ic through It, Im, II to III, that of E is identical to Im and It; (3) Σ REE is higher in phase I as a whole than in II and III; in phase I, Σ REE decreases from Im through It to Ic.

4.3.4 Isotopic characteristics

Whole-rock Rb-Sr isotopic compositions have been determined for phase I and II granites and the dark enclaves (E) of the Guposhan batholith by several authors (Yuan, 1982--cited from Pu, 1986; Zhang et al., 1985 and Xiong, 1986). The whole-rock isochrons are shown in Fig. 27 and the calculated results of $(^{87}\text{Sr}/^{87}\text{Sr})_i$ and ages are listed in table 10. The values of $(^{87}\text{Sr}/^{87}\text{Sr})_i$ decrease from phase E (0.7056) through phase I (0.7088) to phase II (0.7211). The whole-rock isochron age for phase I (148.24 Ma) and II (148.16 Ma) are almost the same, indicating very short time interval between the emplacement of phase I and phase II intrusion. Only one whole-rock sample of phase III granite is analysed for Rb-Sr isotopic compositions (You, 1990), with $^{87}\text{Rb}/^{86}\text{Sr}=42.573$ and $^{87}\text{Sr}/^{86}\text{Sr}=0.80542$. By using the K-Ar age of the same sample (120Ma), the value of $(^{87}\text{Sr}/^{86}\text{Sr})_i$ is calculated to be 0.7328 ($\lambda^{87}\text{Rb}=1.42 \times 10^{-11}/\text{year}$). Although this value is

Table 9 REE contents and some parameters for granites of different phases of the Guposhan batholith

phase	sampleNo.	La	Ce	Pr	Nd	Sm	Eu	Gd	Tb	Dy	Ho	Er	Tm	Yb	Lu	TREE	dEu	L/H	Data
III	L112-2	25.85	58.60	8.09	26.90	6.70	0.33	5.61	1.13	6.73	1.30	3.87	0.63	4.05	0.56	150.35	0.18	5.30	1
	162-2	28.98	45.36	9.21	35.98	10.18	0.38	10.33	2.09	12.95	2.58	7.66	1.16	7.57	1.04	175.47	0.13	2.87	2
	r5-4	16.63	43.15	5.90	21.53	7.20	0.22	7.71	1.75	11.69	2.43	7.74	1.30	0.74	1.25	129.24	0.10	2.73	3
	No.38	21.14	58.25			10.50	0.25		2.84					9.80	1.67				4
	f-1	23.00	43.00	5.80	27.00	7.50	0.22	10.00	1.70	12.00	2.60	8.00	1.14	6.80	0.90	149.66	0.09	2.47	5
	f-2	27.00	54.00	6.70	30.00	8.50	0.26	10.10	1.90	12.00	2.60	6.90	1.00	6.00	0.85	167.81	0.10	3.06	
	f-3	27.00	54.00	6.80	31.00	8.80	0.26	10.30	1.80	12.30	2.50	7.00	1.00	6.10	0.88	169.74	0.09	3.05	
		No.305-2	22.04	57.34			9.90	0.54		2.37					8.86	1.57			
Average III		23.96	51.71	7.08	28.74	8.66	0.31	9.01	1.95	11.28	2.34	6.86	1.04	6.24	1.09	157.05	0.11	3.25	
II	L116	46.03	97.36	12.40	41.56	9.82	0.56	8.10	1.55	8.68	1.56	4.21	0.66	3.98	0.52	236.99	0.21	7.10	1
	O36	29.07	65.31	8.85	31.75	9.72	0.39	10.44	2.24	14.70	2.91	8.89	1.39	9.66	1.35	196.67	0.13	2.81	2
	r5-3	32.22	81.50	9.61	32.07	8.05	0.50	7.14	1.41	8.30	1.66	4.90	0.81	5.05	0.67	193.89	0.23	5.48	3
	Average II		35.77	81.39	10.29	35.13	9.20	0.48	8.56	1.73	10.56	2.04	6.00	0.95	6.23	0.85	209.18	0.19	5.13
Im	L65-2	71.33	141.63	17.67	57.89	11.74	0.85	9.39	1.71	9.14	1.74	4.92	0.77	4.37	0.63	333.78	0.28	9.22	1
	183-3	53.26	97.67	13.97	49.89	12.24	0.90	11.87	2.33	13.48	2.63	7.69	1.26	8.26	1.15	276.60	0.26	4.68	2
	No.19	28.12	62.13			12.84	0.23		3.36					11.82	2.00				4
Average Im		50.90	100.48	15.82	53.89	12.27	0.66	10.63	2.47	11.31	2.19	6.31	1.02	8.15	1.26	305.19	0.27	6.95	
It	L64-2	60.36	122.07	15.59	51.17	11.42	0.56	9.59	1.83	10.41	2.01	5.96	0.93	5.73	0.75	298.38	0.18	7.02	1
	No.17	81.51	155.85			12.19	0.89		2.06					4.58	0.71				4
Average It		70.94	138.96	15.59	51.17	11.81	0.73	9.59	1.95	10.41	2.01	5.96	0.93	5.16	0.73	298.38	0.18	7.02	
Ic	L41-2	42.39	84.85	10.62	35.64	7.69	1.13	6.16	1.13	6.19	1.20	3.45	0.56	3.62	0.50	205.13	0.56	7.99	1
	L47-2	69.43	127.39	15.63	48.24	9.81	1.16	7.07	1.29	6.65	1.31	3.78	0.63	3.74	0.54	296.67	0.48	10.86	
	L15-3	57.69	117.33	14.28	44.52	9.16	1.33	7.17	1.24	6.67	1.26	3.55	0.56	3.54	0.48	268.78	0.56	9.98	
	116	58.75	134.33	15.57	51.31	11.84	1.31	10.56	1.99	11.00	2.15	6.42	1.06	7.06	1.05	314.40	0.40	6.61	2
	CX055-2	74.92	139.19			10.28	0.79		1.53					4.87	0.84				4
	CX058	78.78	144.36			9.77	1.07		1.46					4.76	0.82				
Average Ic		63.66	124.58	14.03	44.93	9.76	1.13	7.74	1.44	7.63	1.48	4.30	0.70	4.60	0.71	271.25	0.50	8.87	
E	L43-2	40.22	86.87	12.24	45.59	9.76	1.50	7.82	1.31	6.96	1.33	3.68	0.58	3.48	0.47	221.81	0.59	7.65	1
	L43-4	28.63	74.61	11.54	47.87	12.31	1.48	10.75	1.94	11.38	2.17	6.40	0.99	6.58	0.87	217.52	0.44	4.30	4
	No.43	94.36	156.03			9.32	2.27		1.30					3.98	0.65				
	CX055-1	60.45	136.11			15.68	0.96		2.82					9.43	1.58				
Average E		55.91	113.41	11.89	46.73	11.77	1.55	9.29	1.84	9.17	1.75	5.04	0.79	5.87	0.89	219.65	0.51	5.98	

Data sources:

(1) Pu (1986); (2) Qin (1985); (3) Xiong (1986); (4) this study, analysed by INAA at UQAC; (5) You (1990).

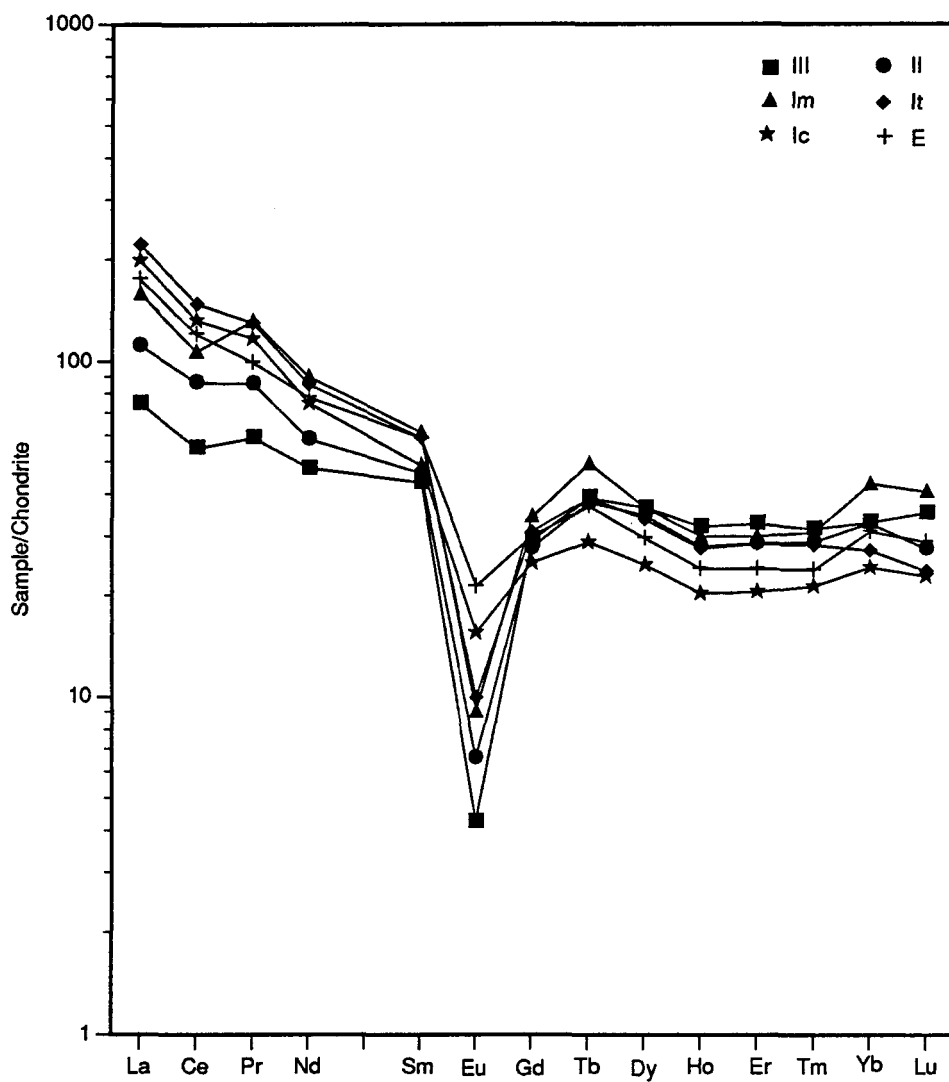


Fig. 26 Comparison of average REE pattern of each phase of the Guposhan batholith.

Table 10 Sr isotopic compositions of granites of the Guposhan batholith.

Phases	Sample number	$^{87}\text{Rb}/^{86}\text{Sr}$	$^{87}\text{Sr}/^{86}\text{Sr}$	$(^{87}\text{Sr}/^{86}\text{Sr})_i$	Age (Ma)	Data sources	
II	82007	4.3046	0.72230	0.7211	148.16	Yuan, 1982*	
	82009	9.9963	0.73250				
	82027	263.6101	1.23760				
	82030	7.4798	0.72700				
	8233-1	12.4018	0.73520				
	G1-1	216.7453	1.16964			Xiong, 1986	
	G1-2	144.3564	0.98265				
	G1-4	82.5591	0.88962				
	G1-5	286.3376	1.34352				
	G1-6	414.2647	1.63497				
	G1-7	588.6332	1.93460				
	G1-9	125.1393	0.98472				
G1-10	116.7538	1.06635					
Im	82020	17.1656	0.74890	0.7088	148.24	Yuan, 1982*	
	82028	71.0898	0.85760				
	63-1a	23.7075	0.75667			Zhang et al, 1985	
It	82031	23.1551	0.75980			Yuan, 1982*	
	54-1a	12.2353	0.73300				Zhang et al, 1985
	65-1a	19.2012	0.75098				
Ic	82017	4.5373	0.71640			Yuan, 1982*	
	82019	4.5332	0.71730				
	58-1a	3.7021	0.71812				
	66-1a	4.1793	0.71573				
	61-1a	5.0523	0.71888				
	62-1a	12.5078	0.73640				
E	56-3	3.1118	0.71266	0.7056	164.39	Zhang et al, 1985	
	56-1	3.7733	0.71489				
	62-1	6.4067	0.72039				
	58-2	7.5373	0.72315				
	59-1	8.3607	0.72527				
	57-1	10.4483	0.73012				

* cited from Pu (1986).

 λ $^{87}\text{Rb}=1.42 \times 10^{-11}/\text{year}$ (Neumann and Huster, 1974).

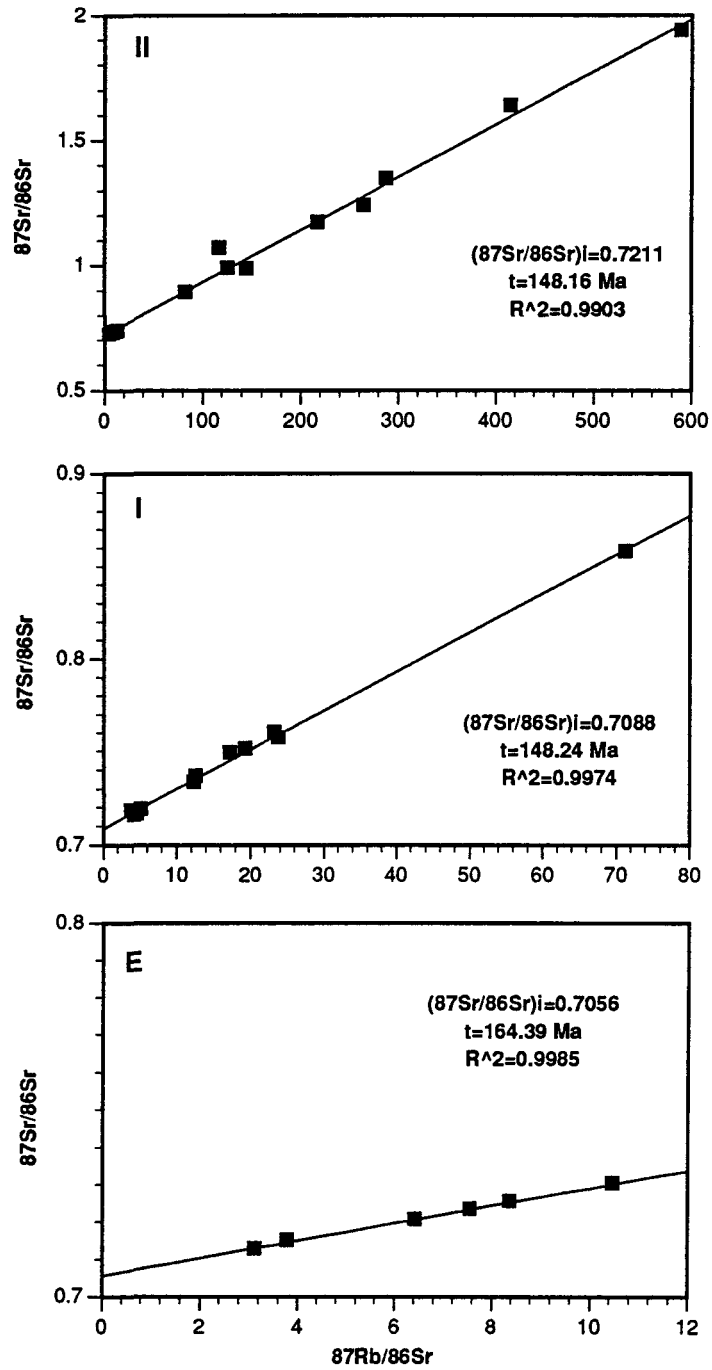


Fig. 27 Rb-Sr isotope whole-rock isochrons for different phases of the Guposhan batholith (data from table 10).

not well constrained, it is reasonable to suppose that phase III granite has similar initial Sr isotopic composition as phase II.

A few O and H isotope data have been reported for the granites of the Guposhan batholith. According to Xiong (1986), δD in biotite and $\delta^{18}O\text{‰}$ in quartz in phase III granite from Shuiyanba ore field are -88.35‰ and 12.2‰ respectively. According to Liu and Yuan (1989), $\delta^{18}O\text{‰}$ in quartz in phase III granite from Liuhe'ao and in phase II granite from Dawantang are 11.5‰ and 13.38 respectively. No O and H isotope data are reported for phase I granites. The O isotope characteristics of phase II and III are consistent with those of S-type granites: $\delta^{18}O$ of I-type granites $=6-8\text{‰}$ and that of S-type granites $=8-12\text{‰}$ (Ohmoto, 1986).

4.3.5 Genesis

The genetic problem of the Guposhan batholith includes (1) the origin of the initial magma for each phase--are they derived from a common initial magma? and (2) the cause of compositional variation within each phase--various degrees of fractional crystallization, magma mixing, partial melting, restite unmixing, or sedimentary contamination? These questions are related to the evaluation of the ore-forming potential of various phases.

Available geochemical data indicate that phase II and III are not derived from the same initial magma as phase I and E. This is reflected, first of all, by their obvious difference in the value ($^{87}\text{Sr}/^{86}\text{Sr}$)_i (table 10, 11). Moreover, a number of geochemical parameters indicate a trend between the most felsic part of phase I (Im) and phase II which is contradictory to a differentiation model: phase II has lower values of SiO₂, K₂O, DI (Fig. 24), Rb/Sr, Ba/Sr, Cs/Rb and Li/Mg (Fig. 25) and higher values of CaO, TiO₂, P₂O₅ (Fig. 24), Ni, Cr and Co (Fig. 25) than Im. Since phase II is more felsic than phase I as a whole, if the magma of phase II were derived from the same initial magma of phase I, an opposite trend should be observed. ΣREE slightly increases from Ic through It to Im, but sharply decreases from Im to II (table 9), so a contrasting gap is evident between Im and II, which can not be explained by fractional differentiation or partial melting of a common source. From Sr isotope data, there are at least three different sources for the granites of the Guposhan batholith, each responsible for phase E, I and II (+III). Since all the phases are emplaced close to each other spatially, their difference in source rocks lies most probably in the difference in depth. According to Sr isotope data and other geochemical criteria (table

Table 11 Comparison of some geochemical parameters of various phases of the Guposhan batholith with S- and I-type granites.

	phase III	phase II	phase I	phase E	S-type *	I-type*
mole Al ₂ O ₃ / (Na ₂ O+K ₂ O+CaO)	0.87-1.26 mean: 1.08	0.85-1.54 mean: 1.14	0.83-1.28 mean: 1.00	0.63-1.20 mean: 0.93	normally >1.05	normally <1.1
C.I.P.W. norma- tive corundum	0-2.87% mean: 1.04%	0-5.54% mean: 1.58%	0-3.32% mean: 0.67%	0-3.30% mean: 0.67%	normally >1%	normally <1%
K ₂ O/Na ₂ O	1.03-2.1 mean: 1.47	1.08-2.21 mean: 1.64	0.80-2.04 mean: 1.36	0.43-2.02 mean: 1.18	relatively high	relatively low
Fe ₂ O ₃ /FeO	0.05-1.86 mean: 0.42	0.09-0.92 mean: 0.47	0.04-2.82 mean: 0.51	0.10-0.54 mean: 0.33	significantly lower	relatively high
major element variation	narrow spectrum of composition; irregular inter- element variation.	narrow spectrum of composition; irregular inter- element variation.	relatively broad spectrum of com- position; rela- tively regular inter-element variation.	relatively broad spectrum of com- position; rela- tively regular inter-element variation.	relatively restrict- ed in composition to high SiO ₂ types; inter- element variation more irregular.	broad spectrum of composition from felsic to mafic; regular inter- element variation.
hornblende	absent	absent	existent in the central part, but absent in the transitional and marginal part.	common	absent	common in more mafic varieties, and generally present in felsic varieties.
Pb (ppm)	20-665 mean: 82.7	20-110 mean: 42.5	30-45 mean: 36.1	20-43 mean: 31.7		
Cr (ppm)	1-11.3 mean: 8.8	11	5.3-14 mean: 9.7	7.2-16.9 mean: 10.9	relatively high	relatively low
Ni (ppm)	2--65 mean: 20.8	55	2.2-6.1 mean: 6.6	2.7-10.5 mean: 5.4		
(⁸⁷ Sr/ ⁸⁶ Sr) _i and Rb-Sr isochrons	0.7328	0.7211; isochron slightly more irregular.	0.7088; isochron relative- ly regular.	0.7056; isochron very regular.	>0.708 isochrons show some scatter.	0.704-0.706; isochrons regular.

* after Chappell and White (1974), White and Chappell (1977, 1983) and Chappell (1984).

11), a preliminary conclusion is that phase II and III are S-type granites which originated from sedimentary rocks in the crust, phase I is I-S transitional type which originated from a mixture of sedimentary rocks and igneous rocks, while phase E is closer to I-type which originated between the lower crust and the upper mantle. The relationship between the different phases is probably a common "hot spot" which causes different source rocks (at different depth) to melt rather than a common source rock or initial magma which produces different phases through magmatic processes, although the mixing of different magmas at upper levels cannot be excluded due to their spatial consistence.

Concerning the genetic relationship between phases II and III, there are, theoretically, six possibilities: (1) phase III is the result of fractional crystallization of the same magma which forms phase II; (2) phase III is the result of lower degree partial melting from the same source which produces the magma of phase II; (3) phase III and phase II are derived from different sources, even though they are both S-type; (4) phase II and III are from the same magma (melt+restite), but phase III contains more melt than phase II due to restite unmixing; (5) phase III and II are from the same magma, but phase II is incorporated by a more mafic magma (magma mixing); (6) phase III and II are from the same magma, but phase II is contaminated by sedimentary rocks. Although none of these six possibilities can be completely excluded based on the available geochemical data, the fractional crystallization and partial melting models seem to be more reasonable and are examined as follows. It is difficult to distinguish the fractional crystallization and partial melting models simply by the variation trend of average compositions between phases III and II (table 8, Fig. 24, 25 and 26). Therefore, more quantitative approach is needed. First of all, the major element variation has been studied. On Harker diagrams (Fig. 28), no clear trends are observed, as is common for S-type granites (Chappell and White, 1974). This may result from either heterogeneous source (Chappell, 1984) or that the major element variation does not represent the liquid line of descent because the "magma" was not entirely liquid but was the product of crystal accumulation (Carmichael et al., 1974). The fact that phase I, which is porphyritic and is coarser-grained, has more regular trends on Harker diagrams (Fig. 29), implies that the heterogeneous source hypothesis cannot be excluded. Therefore, by major elements alone, all the three possibilities (fractional crystallization, partial melting, difference in source rocks) cannot be excluded.

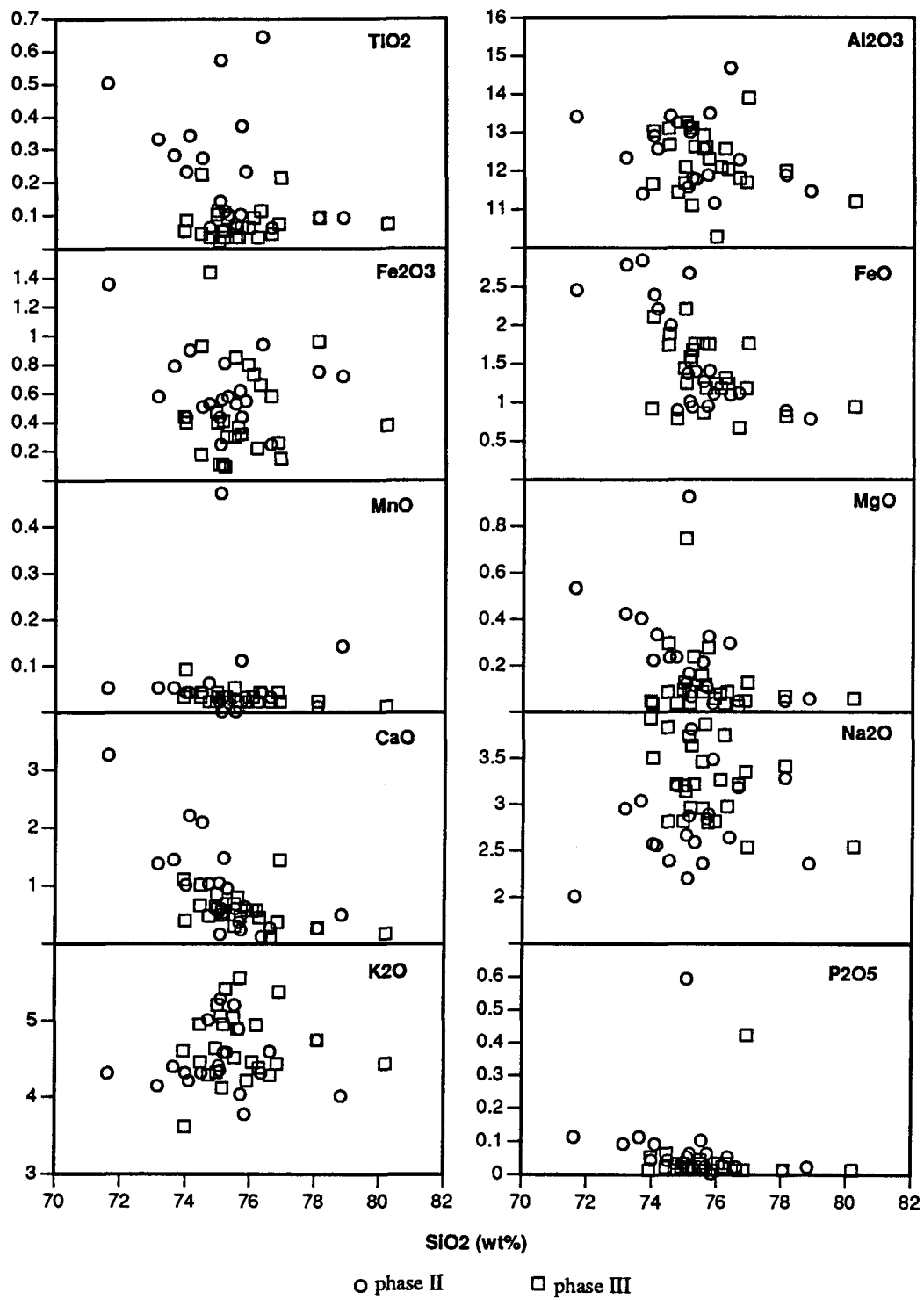


Fig. 28 Harker diagrams of phase III and II of the Guposhan batholith.

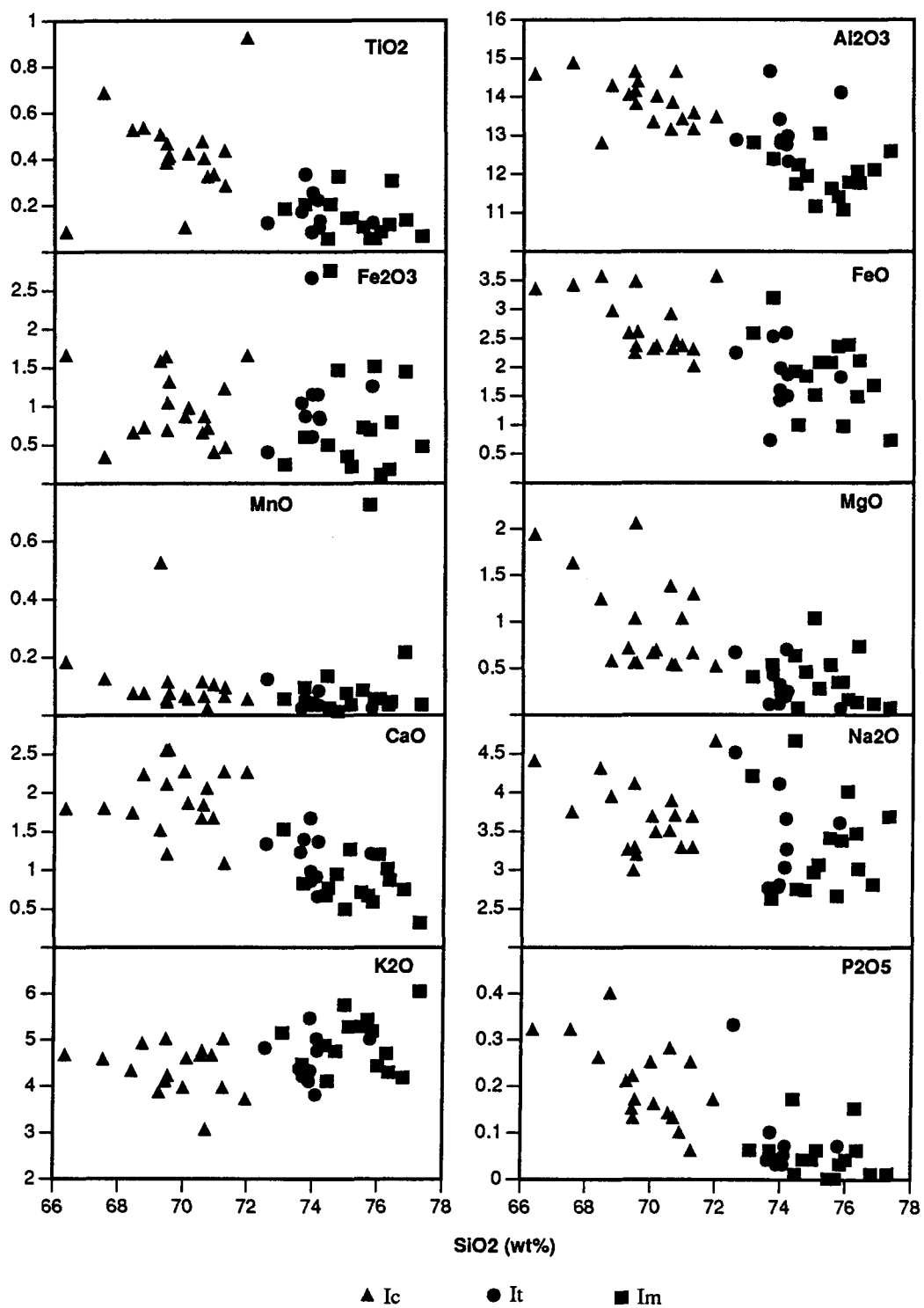


Fig. 29 Harker diagrams of phase I granite of the Guposhan batholith.

Next, let us examine the trace element variation. A two-element variation diagram method, which was proposed by Hanson (1978) to distinguish fractional crystallization and partial melting, is adopted here. The two trace elements must have contrasting values of D (bulk distribution coefficient between the solid phases and the melt). The principle of this method is that the content of the element with very low D value (close to zero) changes very little during fractional crystallization but changes greatly during partial melting, while the behavior of the element with high D value is opposite, so the two-element variation diagram is apparently different for different processes. According to Hanson (1978), Rb and Sr have systematically different K_d (distribution coefficient between mineral and melt) values for most rock-forming minerals in granitic rocks: garnet (0.0085 (Rb)-0.015 (Sr)); hypersthene (0.0027-0.0085); clinopyroxene (0.032-0.516); hornblende (0.014-0.22, 0.0077-0.094); biotite (3.26-0.12); K-feldspar (0.659-3.87); anorthoclase (0.45-5.57); plagioclase (0.041-4.4, 0.016-1.45, 0.048-2.84). For all these minerals excepting biotite, Sr has much higher K_d than Rb. For phase III and II granites, the minerals involved in the fractional crystallization/partial melting are mainly K-feldspar, plagioclase and biotite. The effect of K-feldspar and plagioclase appears to be more important than that of biotite for the differentiation of phase III and phase II granites. This is reflected by the decreasing LREE/HREE and δEu from phase II to III, which cannot be caused by the crystallization of biotite which is HREE enriched and has $\delta Eu < 1$ (Hanson, 1978). The proportion of K-feldspar, plagioclase and biotite involved in partial melting or fractional crystallization is difficult to determine, but by comparing the contents of these minerals in phase II and III (K-feldspar: 36.5% in II vs. 33.5% in III; plagioclase: 23% in II vs. 17.5% in III; biotite: 4.4% in II vs 3.1% in III), a rough estimate can be made: 2 (Kf) : 5.5 (Pl) : 1.3 (Bi). Taking this proportion and the K_d values (for plagioclase, the average of the three values is used) provided by Hanson (1978), the bulk distribution coefficient (D) of Rb and Sr is calculated to be 0.65 and 2.71 respectively. For partial melting model, $C_1/C_0 = 1/(D(1-F)+F)$, while for fractional crystallization model, $C_1/C_0 = F^{(D-1)}$, where C_1 is the content of the element in the melt, C_0 is the content of the element in the original parent, F is the weight fraction of melt relative to original parent, and D is the bulk distribution coefficient. Supposedly the lowest Rb content (300 ppm) and the highest Sr content (155 ppm) in phase II represent the result of 99% partial melting or 1% fractional crystallization, then two contrasting curves for the two different processes can be plotted (Fig. 30). By comparing the actual data points of phase II and III granites with these two curves, it is obvious that the fractional crystallization

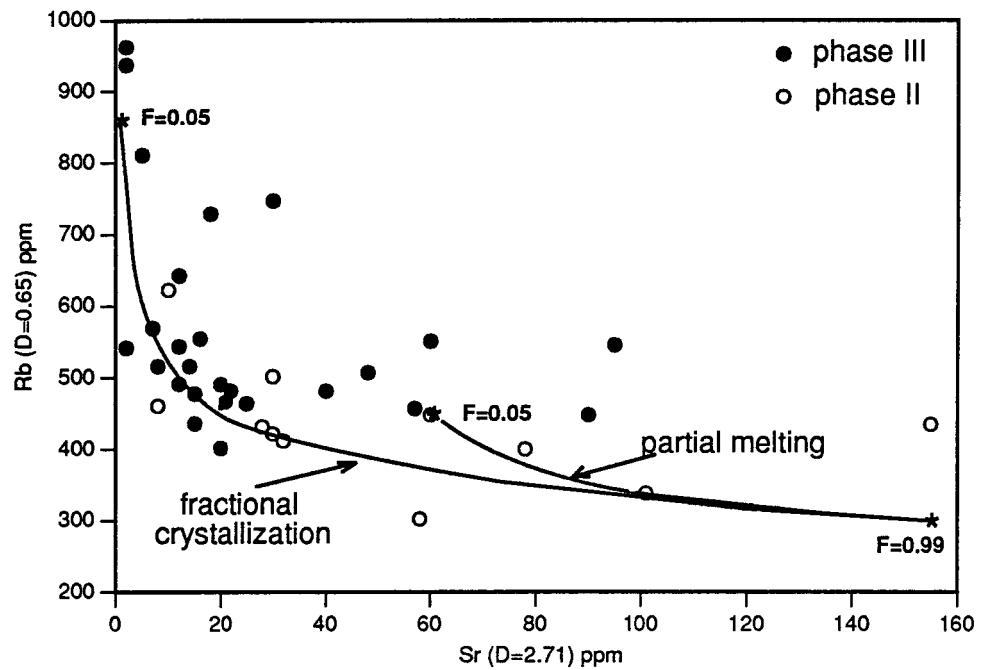


Fig. 30 A Rb-Sr variation diagram of phase II and III granites of the Guposhan batholith, in comparison with the curves of partial melting and fractional crystallization models (both with Rb=300 ppm and Sr=155 ppm at F=0.99, where F is the weight fraction of melt relative to original parent).

model fits the actual data much better than the partial melting model, the latter being unable to produce Rb content > 460 ppm and Sr content < 58 ppm. In fact, the average Rb content in the source rocks is most probably < 300 ppm, so the maximum Rb concentration by minimum partial melting is most unlikely to be < 460 ppm. Therefore, the fractional crystallization model is more reasonable than the partial melting model to explain the evolution of phase II and III granites. The variation trend of most major and trace elements (Fig. 24, 25) between phase II and III is consistent with the fractional crystallization model. The decrease of LREE/HREE and δEu from phase II to III can also be explained by the fractional crystallization model, since the minerals involved in the process have bulk distribution coefficients (D) which decrease from HREE to LREE and are >1 for Eu according to the data of Hanson (1978). The decrease of ΣREE from phase II to III is contradictory to the data of Hanson (1978). A similar variation trend has been observed in the South Mountain batholith of Nova Scotia (Muecke and Clarke, 1981), where ΣREE , Eu/Eu^* and La/Sm show a systematic decrease from early phases to late phases (granodiorite-monzogranite-leucocratic monzogranite). This is explained by the fractional crystallization of a mixture of biotite (K_d is >1 instead of <1 as in Hanson's paper), plagioclase and zircon and by the partitioning of REE into late hydrothermal fluids as fluoride complexes (Muecke and Clarke, 1981). Similar processes may have played a role in the Guposhan batholith.

In summary, the chemical variation between phase II and III and within individual phases is mainly caused by the fractional crystallization of a mixture of plagioclase, biotite and K-feldspar. The partitioning of REE into late hydrothermal fluids may have played a significant role in the decrease of ΣREE from phase II to III. The heterogeneity in source rocks is likely the cause of the scatter and irregularity of the data.

Concerning the chemical variation between central (Ic), transitional (It) and marginal (Ic) part of phase I intrusion, two additional processes, sedimentary contamination and restite unmixing, besides the fractional crystallization and partial melting models, have to be considered, since a large number of dark enclaves (phase E) are developed in Ic, some of which show the features of sedimentary rocks (Yuan, 1981) and some are argued to be restites of the source rocks (Zhang et al., 1985). None of these processes or models can be excluded simply by examining the average chemical variation trend between different parts (Fig. 24, 25, 26 and 29). More quantitative methods are needed as is for phase II and III.

The two-element variation diagram method is used again. The minerals involved in the fractional crystallization/ partial melting are probably mainly plagioclase, biotite, hornblende and apatite. The effect of plagioclase appears to be more important than that of biotite, hornblende and apatite, as is reflected by the increase of Σ REE and decrease of LREE/HREE and δ Eu from phase Ic to Im, since hornblende and apatite have K_d values greatly >1 and are Eu-depleted, and biotite and hornblende are HREE-enriched (Hanson, 1978). The proportion of these minerals is broadly estimated by comparing their contents in Ic vs. in It & Im (plagioclase: 42.5% vs. 27.15% ; biotite: 10.3% vs. 3.45%; hornblende: 0.6% vs. 0%; apatite: 0.48% vs. 0.15%; data from Pu (1986), except for apatite, the data of which is from the C.I.P.W. norm (ap) in table 6): 15.35 (Pl) : 6.85 (Bi) : 0.6 (Hbl) : 0.33 (Ap). Taking this proportion and the K_d values of Rb and Sr (for plagioclase, the average of the three values are used) provided by Hanson (1978) and the K_d values for apatite deduced from the data of Zhao et al. (1987) ($K_d=0.00023$ and 0.013 for Rb and Sr respectively), the bulk distribution coefficient (D) of Rb and Sr is calculated to be 0.989 and 1.96 respectively. The D value of Rb is so close to 1 that the Rb-Sr pair is not suitable. Alternatively, Lu is used to make Sr-Lu pair. The K_d values of Lu is 0.049, 0.44, 8.38 and 23.9 for plagioclase, biotite, hornblende and apatite respectively. The D value is calculated to be 0.56. Four pairs of Sr-Lu data are available (see table 7 and 9): 20.0 (Sr)-2.0 (Lu); 95-0.71; 181-0.82; 94-0.84. Another element, Eu, can also be used to make Eu-Lu pair. The K_d values of Eu is 2.15, 0.24, 5.14 and 30.4 for plagioclase, biotite, hornblende and apatite respectively. The D value is calculated to be 2.07. The data of Eu-Lu pairs are listed in table 9. Supposedly the lowest Lu content (0.48 ppm) and the highest Sr (181 ppm) and Eu (1.33) content represent the original concentration in the parent, then two contrasting curves for the two different processes (fractional crystallization and partial melting) can be plotted for the Sr-Lu pair (Fig. 31 a) and Eu-Lu pair (Fig. 31b) respectively. According to the restite unmixing model, the dark enclaves in Ic represent restites. Theoretically the restite unmixing process results in a straight line linking the restite and the minimum melt (supposedly represented by the sample with highest Lu content) (White and Chappell, 1977; Wall et al., 1987). The sedimentary contamination model predicts that the distribution of the data points is along a straight line linking the least contaminated melt (supposedly represented by the sample with highest Lu content) and the sedimentary end member (assumed to be represented by a half of clastic rocks and a half of carbonate rocks, a ratio pertinent to the construction of the host rocks of the batholith). Both restite unmixing line

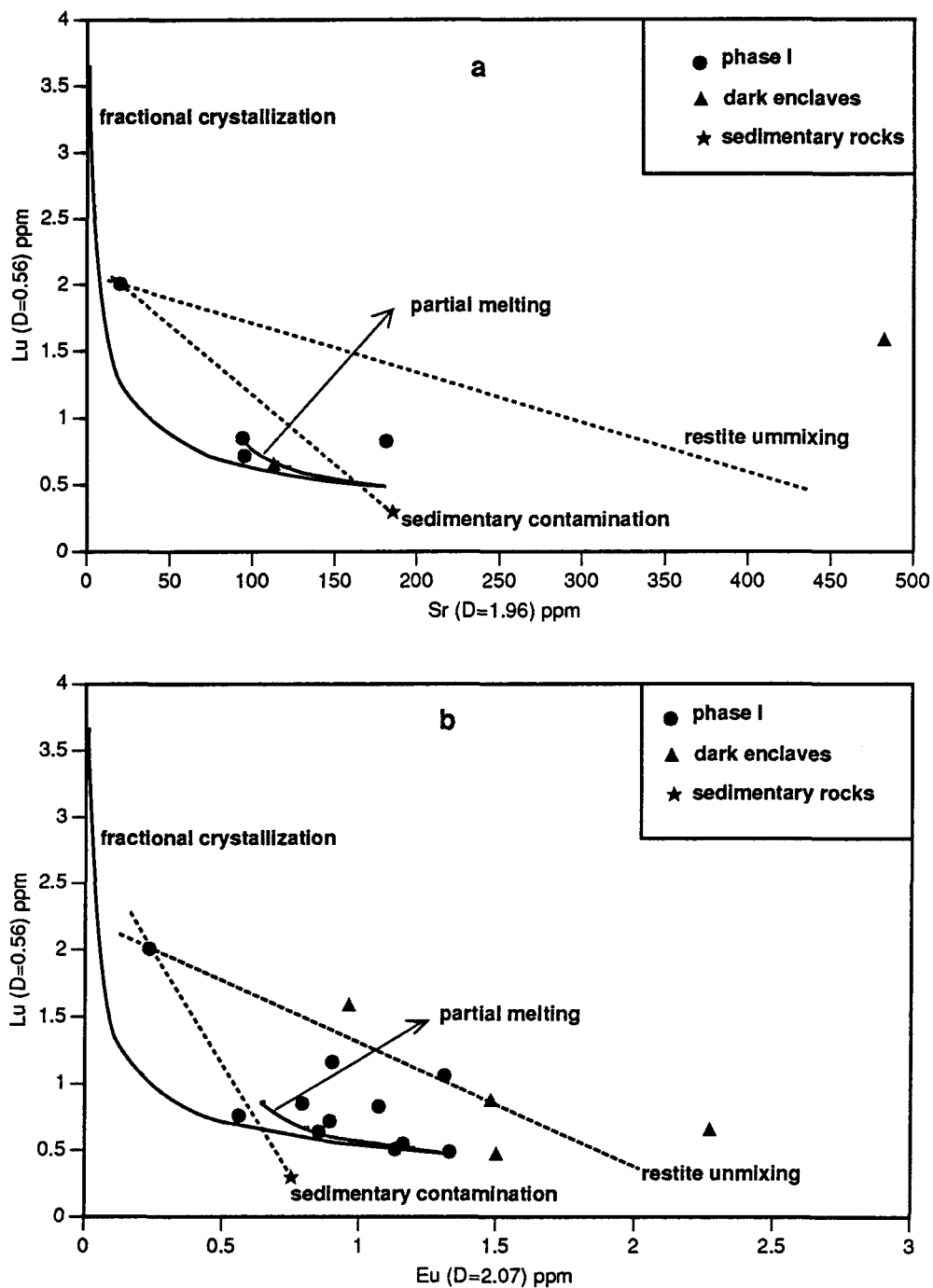


Fig. 31 Sr-Lu (a) and Eu-Lu (b) variation diagrams of phase I granites of the Guposhan batholith, in comparison with the curves of partial melting and fractional crystallization models (both Sr=181ppm, Eu=1.33ppm and Lu=0.48 ppm in the original parent) and lines of restite unmixing model (restite represented by dark enclaves) and sedimentary contamination (sedimentary end member represented by a half of clastic rocks and a half of carbonate rocks, with Sr=185 ppm, Eu=0.752 ppm, Lu=0.288 ppm).

and sedimentary contamination line are shown as a dashed line on Fig. 31. By comparing the actual data points with the model lines, it is obvious that none of the models fit well with the data. However, if the Sr and Eu contents in parents are slightly higher than those used in the fractional crystallization/partial melting models, the fractional crystallization model will fit much better with the actual data, whereas the partial melting model cannot result in similar effect. The restite unmixing and sedimentary contamination models are not desirable because of the scatter of end members and/or the deviation of the actual data points from the theoretical lines. Therefore, fractional crystallization is probably the most important process which produces the chemical variation within the phase I of the Guposhan batholith, although other processes may also have played a role to a lesser extent.

In conclusion, the various phases of the Guposhan batholith have different origins. Phase II and phase III are probably derived from a common S-type source (although the source rocks may be fairly heterogeneous), and fractional crystallization is most likely to be the process responsible for the differentiation between phase II and III and within each phase. The partitioning of REE (and probably other ore-forming elements such as F, Sn) into late hydrothermal fluids may be responsible for the depletion of these elements in phase III relative to phase II, which cannot be simply explained by fractional crystallization model. Phase I is derived from a S-I transitional source (closer to I type), and fractional crystallization is most likely responsible for the chemical variation between different parts (Ic, It and Im). No depletion of REE like that in phase III is observed in Im and It relative to Ic, indicating that there was not a strong partitioning of these elements into hydrothermal fluids. The dark enclaves in Ic have very complicated origins, including sedimentary xenoliths and restites of source rocks, but the fact that they have fairly homogeneous initial Sr isotope composition (Fig. 27) and that most dark enclaves have magmatic texture and structure indicates they are mainly the results of an unrelated magmatic intrusion (close to I type) which was captured as xenoliths by later intrusion (phase I).

4.3.6 The ore-forming potential

The ore-forming potential of granites is determined by three factors: (1) the contents of the ore-forming elements in the melt; (2) whether the ore-forming elements are partitioned (enriched) into the hydrothermal fluids or dispersed in the rock-forming

minerals; (3) whether or not the ore-forming elements originally dispersed in rock-forming minerals are remobilized by later hydrothermal fluids.

A number of criteria distinguishing tin-generating granites and "barren" or normal granites have been proposed by many authors (Tischendorf et al., 1972; Tischendorf, 1977; Beus and Sitnin, 1968; Boissavy-Vinau and Roger, 1980 and Lawrence, 1975), and is summarized by Tischendorf (1977). These include major elements, trace elements and element ratios (table 12). Some diagrams for distinguishing tin-generating granites and "barren" or normal granites have also been proposed (e.g. Biste, 1982; Neiva, 1984). The average data of each phase of the Guposhan batholith are compared to these criteria (table 12 and Fig. 32). As shown in table 12, every phase has some parameters which are within the range of the "tin-generating granite", but the percentage of this positive comparison decreases from phase III (90%) and II (90%), through Im (75%) and It (68%) to Ic (29%). On the other hand, the percentage of the data that are within the range of "barren" granites increases from phase III (15%) through II (30%), Im (35%) and It (37%) to Ic (82%). Only one criterion (TiO_2/Ta) can distinguish the latest phase (phase III) from all the other phases. In Rb-Cs-Ba diagram (Fig. 32a), almost all the samples of every phase plot in area A and B, which are areas of granites associated with Sn-W deposits (Neiva, 1984), but differences still exist between different phases: phase III plots mainly in area A, phase II plots mainly in A and B (only one sample in C), while Im, It and Ic plot mainly in B. This indicates an increase in ore-forming potentials from phase I to phase III. In Rb-Sr-Ba diagram (Fig. 32b), most samples of phase III and II plot in the area of granites associated with Sn, W and Mo deposits proposed by Biste (1982), while those of Im, It and Ic plot mainly outside (although near) the boundary. In general, there is no absolute division between tin-generating granites and barren granites, but phase III seems to have better ore-forming potential than the other phases.

The argument that phase III has the best tin ore-forming potential is also supported by the common observation that tin mineralization is generally related to the latest phase of granite intrusions (e.g. Hesp and Varlamoff, 1977). Another important factor is the partitioning of the ore-forming elements between the melt and the hydrothermal fluids. The obvious decrease of REE in phase III relative to phase II implies a preferential partitioning of REE into the hydrothermal fluid phase, which is thought to be related to late-magmatic stages rather than postmagmatic processes (Muecke and Clarke, 1981). Bandurkin (1961), Mineyev et al. (1966) and Balashov and Krigman (1975) have suggested that carbonate and

Table 12 Some geochemical parameters for distinguishing tin-generating granites and barren or normal granites, in comparison with the average data of each phase of the Guposhan batholith

Parameters	phase III	phase II	phase Im	phase It	phase Ic	proposed distinguishing criteria		references	
						Sn-generating granites	barren granites		
major elements	SiO ₂	75.70	75.20	75.33	73.97	69.75	73.38+/-1.39	70.84+/-1.41	1
	TiO ₂	0.07	0.23	0.14	0.16	0.42	0.16+/-0.10	0.34+/-0.08	
	Al ₂ O ₃	12.24	12.47	11.96	13.10	13.87	13.97+/-1.07	14.33+/-0.23	
	Fe ₂ O ₃	0.46	0.62	0.79	1.07	0.96	0.80+/-0.47	1.31+/-0.29	
	FeO	1.37	1.56	1.84	1.81	2.72	1.10+/-0.47	1.78+/-0.38	
	MgO	0.12	0.24	0.38	0.30	0.97	0.47+/-0.56	0.81+/-0.23	
	CaO	0.57	0.97	0.82	1.15	1.9	0.75+/-0.41	1.89+/-0.40	
	Na ₂ O	3.22	2.78	3.29	3.32	3.68	3.20+/-0.61	3.44+/-0.32	
K ₂ O	4.66	4.46	4.90	4.57	4.33	4.69+/-0.68	4.34+/-0.52		
trace elements	Sn	27.50	29.50	33.30	8.60	10.1	30+/-15	1--8	
	F	1827	2339	1433	1840	1400	3700+/-1500	250--1500	
	Li	62.30	38.90	63.00	64.00		220+/-100	31--150	
	Rb	557	432	420	356	296	550+/-200	130--300	
	Be	12.70	7.00	10.00			13+/-6	2.6--8	
element ratio	K/Rb	69.44	85.47	97.09	106.38	121.95	20--100	100--300	2
	TiO ₂ /Ta	43.98	175.76	251.79	301.89	800.00	0.94--71.6	57--4896	3
	Mg/Li	11.49	37.04	35.71	28.57		75+/-30	270+/-80	4
	Rb/Sr	14.93	7.67	17.00	4.68	2.15	>4	<4	5
others	DI	93.20	89.90	91.20	89.10	83.00	90.06	83.64	6
	cm	1.04	1.58	0.49	1.13	0.58	2.30	0.54	

References: (1) Tischendorf (1977), with 962 samples for tin-generating granites and 2327 samples for normal granites for the statistics of major elements; (2) Tischendorf et al. (1972); (3) Boissavy-Vinau and Roger (1980); (4) Beus and Sitnin (1968); (5) Lawrence (1975); (6) calculated from the data of Tischendorf (1977).

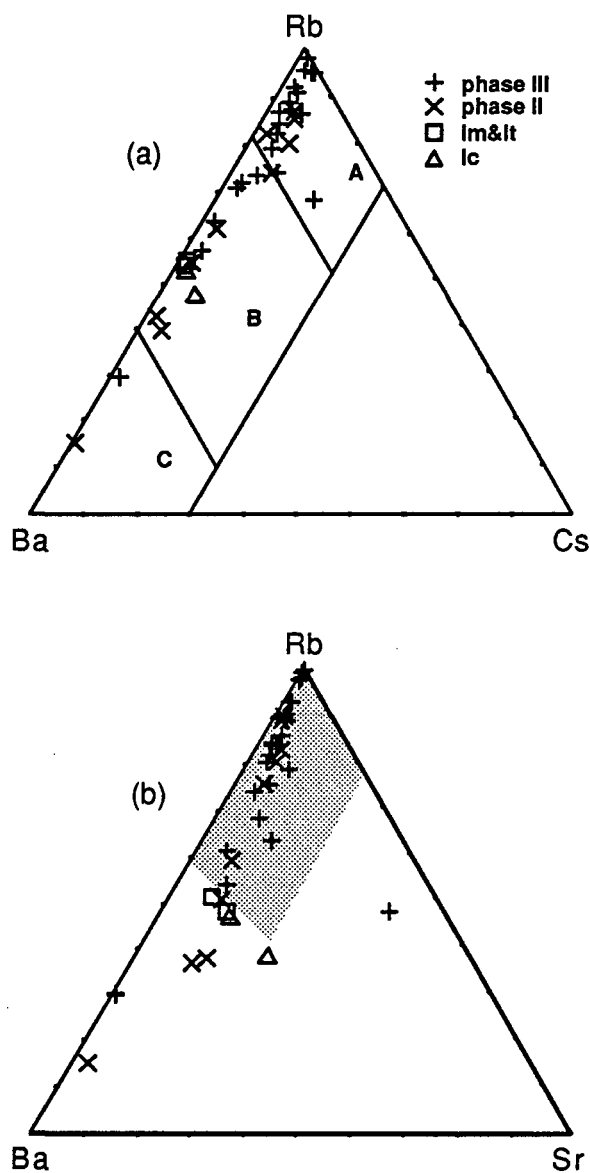


Fig. 32 Different phases of the Guposhan batholith plotted on (a) Rb-Cs-Ba diagram (Neiva, 1984), and (b) Rb-Sr-Ba diagram (Biste, 1982). In (a), Area A--muscovite granite, greisenized granite, aplites and pegmatite related to Sn-W mineralization; Area B--muscovite and biotite granite and hybrid granodiorite associated with Sn-W mineralization and Area C--granites without related Sn-W mineralization. In (b), the shaded area is granites associated with Sn, W and Mo deposits. Data are from Table 7.

fluoride anionic complexes are the most effective means of stabilizing and mobilizing REE in aqueous solutions at the magmatic stage. The strong partitioning of REE into CO₂-rich fluids at elevated T and P has been experimentally verified by Wendlandt and Harrison (1979), and the experimental data by Flynn and Burnham (1978) suggest that fluoride is effective as a complexing agent of REE under magmatic conditions. The role of F is implied by the high F content in phase III granites (the lower F content in phase III relative to II may also be caused by its partitioning into the hydrothermal fluid phase), and the role of CO₂ is indicated by the existence of CO₂ inclusions associated with melt inclusions in phase III granites (see Chapter 5). The decrease of average Sn content in III relative to phase II implies that Sn may have a behavior similar to REE in partitioning between melt and hydrothermal fluids. The low oxygen fugacity property of the phase III granites is favourable for tin to occur in Sn²⁺ instead of Sn⁴⁺, which is in turn favourable for tin to be partitioned into hydrothermal fluids instead of being dispersed in the rock-forming minerals. The peraluminous property of phase III granites is favourable for the partitioning of ore-forming elements into hydrothermal fluids. The experimental data by Urabe (1985) reveal that the partition ratio of Zn (Zn_{fluid}/Zn_{melt}) for aluminous melt (CIPW normative corundum is 2.42 %) is more than two orders of magnitude larger than that for the alkaline melt (CIPW normative corundum is 0 %), and a similar contrast was observed for the partition ratio of Pb. From his experiments he concluded that only aluminous granite is capable of producing hydrothermal fluids which contain a significant amount of ore metals while alkaline melt tends to retain these metals instead of releasing them into the hydrothermal fluids. Sn may also have similar behavior as Zn and Pb, as is reflected by the fact that most tin deposits are related to peraluminous granites (Strong, 1988).

In addition to the partitioning of ore-forming elements between melt and hydrothermal fluids, their partitioning between the hydrothermal fluids and the granite rocks during postmagmatic hydrothermal alteration may have also contributed to the enrichment of the ore-forming elements in the fluids. In the phase III granites at Liuhe'ao, alteration is extensive, characterized by the replacement of biotite by muscovite (Dong, 1989). Dong (1989) studied the Sn contents of a set of altered and unaltered granites from Liuhe'ao and showed that the average Sn content is 33.5 ppm in unaltered granite (4 samples) but 16.64 ppm in altered granite (7 samples). This means that a large amount of Sn was released from the granite in the process of alteration. It is possible that the majority of ore-forming fluid did not escape from the intrusion at the moment the magma was emplaced, but stayed

within the intrusion and reacted with the granites until the pressure of the fluid exceeded the tensile strength of the enclosing rock and emanated into the contact zone and fractures in the country rocks. This is supported by the observation that the principal mineralization event at the contact zone postdates unmineralized skarn formation which probably took place immediately following the intrusion of magma, a phenomenon common for W-Sn skarn deposits (Kwak, 1987). The high percentage of fit of phase II (90%) and Im (75%) into tin-generating granites indicates that they may also have good ore-forming potential. However, as the partitioning of ore-forming elements between melt and hydrothermal fluids is concerned, these two phases are not as favourable as phase III. Although the highly peraluminous property of phase II is favourable for the partitioning of ore-forming elements into hydrothermal fluids, the fact that it precedes phase III is a default, since Sn, like other granophile elements, tends to remain in the residual phase of melt during fractional crystallization. Experimental data by Burnham (1967, 1979), Burnham and Nekvasil (1986), Chorlton and Martin (1978), Dingwell (1985; 1988), Holland (1972), Kovalenko (1978), Manning (1981), Manning and Pichavant (1988), Pichavant and Wyart (1981), Stewart (1978), and Wyllie and Tuttle (1961), as summarized by Strong (1988), show that H₂O and HF can lower the melting temperature, which is favourable for magma differentiation, while HCl and CO₂ tend to raise the melting temperatures of granitic melts, which may cause the melt to be solidified before fully differentiated. The role of H₂O and HF is probably more important than HCl and CO₂ during the differentiation of phase II and III granite magmas, so that magmatic fraction overwhelm melt-fluid segregation, leading to the enrichment of ore-forming elements in the latest magmatic phase. Although Im represents the last product of the intrusion of phase I, its more alkaline property (63% samples have CIPW normative corundum = 0) prevent the partitioning of ore-forming elements into the hydrothermal fluids, thus retaining Sn in the rock. Therefore, for phase II and Im, a postmagmatic hydrothermal alteration is necessary in order to release the ore-forming elements from the granite rocks into the hydrothermal fluids. Since phase II and Im are less capable of producing postmagmatic fluids (for phase II, the fluids tend to remain in the residual magmas during fractional crystallization, and for Im, the melt may be undersaturated in water due to its deeper origin (Strong, 1988)), additional fluids may be required from phase III intrusion.

In summary, phase III granites have the best tin ore-forming potential. This is supported by the comparison with the distinguishing criteria between Sn-generating granites

and barren granites, by the partitioning of ore-forming elements into hydrothermal fluids in the late-magmatic stage as reflected by the decrease of REE and Sn in phase III relative to phase II, and by the release of Sn into hydrothermal fluids during postmagmatic alteration as reflected by the depletion of Sn in altered granites relative to unaltered granites. Phase II and Im do not favor the partitioning of ore-forming elements into hydrothermal fluids during late-magmatic stage, but the high concentration of ore-forming elements in the rocks make them a potential source in postmagmatic alteration, if there are sufficient hydrothermal fluids (provided by themselves or by later intrusions). Phase It and Ic have the least ore-forming potential.

4.4 The Dykes

The dykes in the southwest contact zone of the Guposhan batholith including the Xinlu ore field show a spatial correlation with the tin deposits (Fig. 8; Chi, 1989a). This correlation may be explained by mechanical aspect that the dyke-controlling structures provide favourable channels for the migration of the ore-forming fluids and/or chemical aspect that the dykes themselves provide some ore-forming elements or are linked to the major sources of the ore-forming fluids. The latter aspect is closely related to the geochemical characteristics and ore-forming potential of the dykes and their genetic relationship with the granites. Petrographical characteristics of selected samples of dykes are described in appendix A, and the geochemical characteristics are discussed as follows.

4.4.1 Major Elements

The major element analyses of 12 representative samples of dykes from the Xinlu ore field are presented in table 13. The CIPW norms are calculated for each sample (table 13).

The normative values of ab are allocated to or and an to form Af and Pl by using the method proposed by Rittmann (1973). These data are plotted on the Qz-Af-Pl diagram of the IUGS classification of igneous rocks (Streckeisen, 1976) (Fig. 33). It is shown that the samples cover a range from granite through adamellite, granodiorite, quartz monzonite to quartz monzodiorite. Most samples have DI values < 70. Six samples contain fairly high normative corundum (>1), five samples do not contain normative corundum.

Table 13 Major element contents and CIPW norms for dykes from the Xinlu ore field

Sample No.	V12-1-4	V14-1-1	V11-3	V22-2	Bk193-1-1	V44-1	L127	L132	No.5	No.6	No.7	No.8
Rock type	fine-grained granite	quartz porphyry	biotite quartz dioritic porphyry	fine-grained biotite granodiorite	dioritic porphyry	quartz dioritic porphyry	dioritic porphyry	dioritic porphyry	dioritic porphyry	dioritic porphyry	dioritic porphyry	dioritic porphyry
SiO ₂	75,77	74,29	68,39	60,79	59,86	59,68	59,02	57,06	58,92	52,54	59,40	58,10
TiO ₂	0,06	0,08	0,40	1,40	1,40	0,65	1,29	1,51	1,44	1,20	1,48	1,50
Al ₂ O ₃	12,36	13,30	15,04	13,68	14,17	15,34	16,00	16,12	16,07	17,06	16,07	15,87
Fe ₂ O ₃	0,25	0,57	0,75	3,12	1,36	0,78	0,21	0,59	0,93	1,22	0,86	1,00
FeO	0,50	0,74	2,53	4,38	6,46	3,61	6,64	7,60	7,40	6,11	6,43	7,59
MnO	0,04	0,01	0,09	0,14	0,08	0,13	0,11	0,14	0,14	0,13	0,10	0,18
MgO	0,38	0,20	0,58	2,88	3,24	1,52	2,35	1,75	1,95	1,90	2,00	2,50
CaO	1,10	1,42	2,13	4,55	4,46	3,97	4,73	3,36	5,47	13,83	5,28	4,67
Na ₂ O	3,23	1,82	2,21	2,50	0,93	2,55	2,66	0,93	2,54	1,10	2,80	2,50
K ₂ O	5,05	5,69	5,43	4,68	5,14	4,12	3,42	3,89	3,88	1,58	3,65	2,73
P ₂ O ₅	0,01	0,00	0,09	0,35	0,38	0,29	0,56	0,61	0,47	0,45	0,46	0,77
H ₂ O	0,38	0,60	0,78	1,45	2,10	2,66	1,28	2,68				
CO ₂	0,08	0,12	0,69	0,52	0,70	4,85	0,53	2,55				
L.O.I.									2,12	2,76	2,25	3,44
Sum	99,21	98,84	99,11	100,44	100,28	100,15	98,80	98,79	101,33	99,88	100,78	100,85
data source	this study						You (1990)		Dong (1989)			
qz	35,20	39,25	30,36	16,33	19,83	18,11	15,64	25,18	11,88	11,58	12,89	16,99
ab	27,65	15,68	19,02	21,37	8,02	23,29	23,08	8,41	21,66	9,58	24,05	21,72
or	30,20	34,23	32,63	27,94	30,94	26,28	20,73	24,57	23,11	9,61	21,89	16,56
an	4,36	6,40	5,71	12,41	15,50	19,21	16,87	13,56	21,15	38,04	20,81	18,62
di	0,48	0,00	0,00	3,85	0,00	0,00	0,00	0,00	2,64	24,96	2,30	0,00
hy	1,42	1,30	5,06	8,83	16,96	9,65	16,35	16,67	14,35	0,99	12,87	17,66
mt	0,37	0,84	1,11	4,57	2,01	1,22	0,31	0,91	1,36	1,82	1,27	1,49
il	0,12	0,15	0,77	2,69	2,71	1,33	2,51	3,07	2,76	2,35	2,85	2,92
ap	0,02	0,00	0,21	0,82	0,90	0,69	1,33	1,47	1,10	1,07	1,08	1,83
cc	0,18	0,28	1,60	1,19	1,62	0,00	1,24	0,00	0,00	0,00	0,00	0,00
cm	0,00	1,88	3,53	0,00	1,53	0,17	1,94	6,13	0,00	0,00	0,00	2,21
ag	0,87	0,69	0,63	0,67	0,50	0,56	0,50	0,36	0,52	0,21	0,53	0,45
DI	93,05	89,16	82,01	65,64	58,78	67,68	59,44	58,16	56,65	30,77	58,83	55,27

*CIPW norms are calculated by the FORTRAN 77 program of Rock (1989).

qtz-quartz; ab-albite; or-potash feldspar; an-anorthite; di-diopside; hy-hypersthene; mt-magnetite; il-ilmenite; ap-apatite; cm-corundum; cc-calcite; DI (differentiation index)=qtz+or+ab+ne+lc; ag (agpaicity index)=molecular (Na+K)/Al

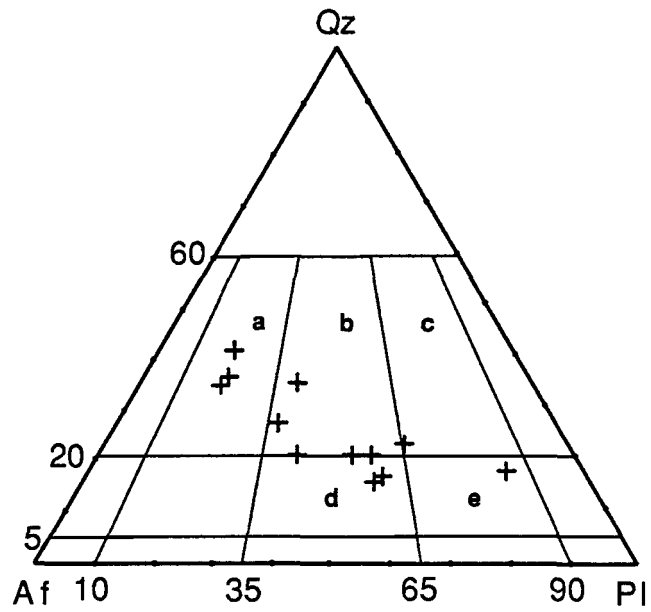


Fig. 33 Plots of Qz, Pl and Af data of dykes from the Xinlu ore field on the IUGS (1972) classification. Af and Pl are calculated from the CIPW Ab, Or and An data according to the method proposed by Rittmann (1973), Qz is CIPW normative values. a-granite; b-adamellite; c-granodiorite; d-quartz monzonite; e-quartz monzodiorite.

The Harker diagrams of major elements are shown in Fig. 34. The contents of major elements vary greatly, e.g. the contents of SiO₂ cover a range from 52.54% to 75.77%, which is obviously different from the granites which have relatively homogeneous compositions in a wide area. Broadly there is a negative correlation between SiO₂ and TiO₂, Al₂O₃, Fe₂O₃, FeO, MnO, MgO, CaO, P₂O₅ (Fig. 34) and CO₂ (Fig. 35a), and a positive correlation between SiO₂ and K₂O & Na₂O (Fig. 34), but a very wide range of variation of TiO₂, Al₂O₃, Fe₂O₃, MnO, MgO, Na₂O, K₂O, P₂O₅ and CO₂ exists in the range of SiO₂ from 57.06 to 60.79, almost independent of SiO₂, shown by nearly vertical distribution of data points on Fig. 34 and 35a. K₂O/Na₂O-SiO₂ variation is very irregular (Fig. 35b).

4.4.2 Trace Elements

The trace element analyses of 15 samples of dykes from the Xinlu ore field are presented in table 14. The contents of Rb, Ba, F, Cl, Be, W, Sn, Nb, Ta, Cu, Pb, Zn, Sb, Bi in the intermediate dykes from the Xinlu ore field are remarkably higher than average intermediate rock of the world (Vinogradov, 1962--cited from Sun and Peng, 1985). In comparison with the contents of the trace elements in the granites, the intermediate dykes are generally richer in Sr, Ba, Cr, Co, Cu, Zn, Ti, Cl but poorer in Rb, Li, Be, W, while the Sn, Cs and F contents of dykes are comparable to those of the granites.

The correlation between trace elements and SiO₂ is generally poor (Fig. 36). The contents of Sn, W, Pb, F, Co, Sr, Ba, Cs, Li and Sc are, to different extents, in reverse correlation to the contents of SiO₂. The contents of Zn, Cu, As, Cl, B, Cr, Rb, Ta, Nb and Sb show no obvious correlation with SiO₂. Rb/Sr and Ta/Ti increase with SiO₂, and Cs/Rb decreases with SiO₂, while Ba/Sr, Ta/Nb and Rb/K show no correlation with SiO₂ (Fig. 37). A very wide range of variation of Sn, Zn, F, Cr, Co, Rb, Sr, Ba, Cs, Li, B, Nb, Ta and Sb exists in the range of SiO₂ from 57.06 to 60.79, almost independent of SiO₂.

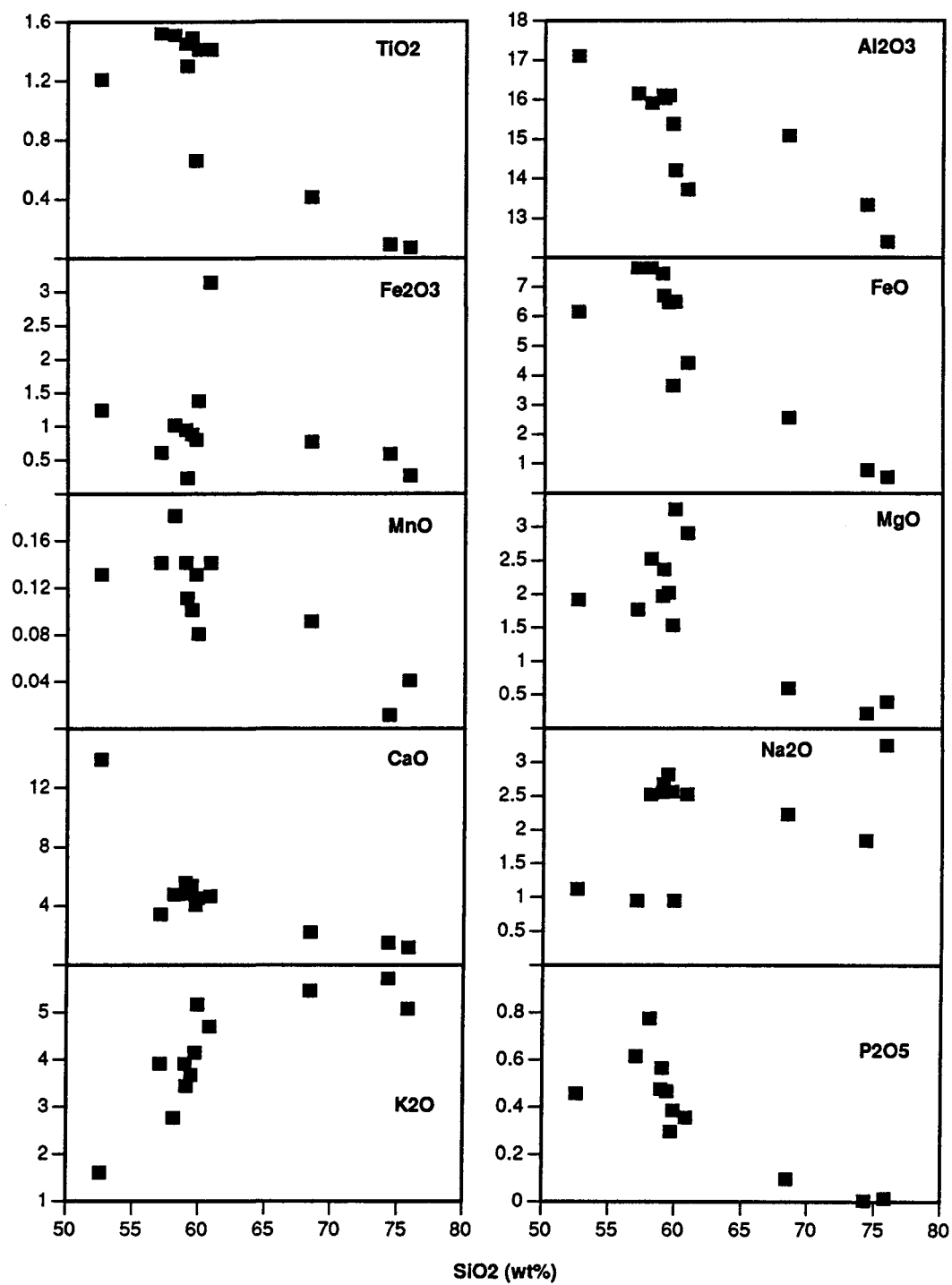


Fig. 34 Harker diagrams of major elements for dykes from the Xinlu ore field.

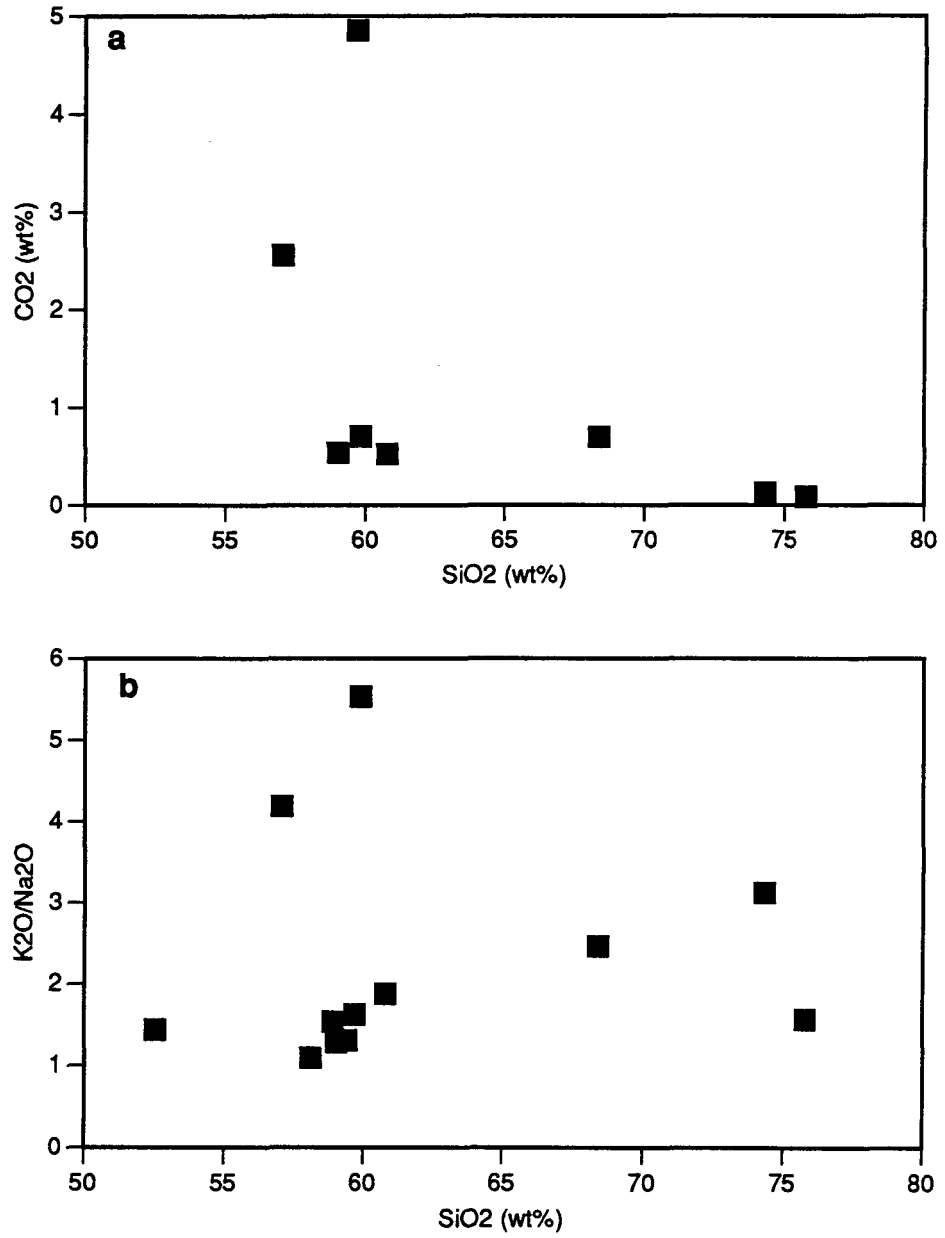


Fig. 35 SiO₂-CO₂ (a) and SiO₂-K₂O/Na₂O (b) variation diagrams for dykes from the Xinlu ore field.

Table 14 Contents of trace elements in dykes from the Xinlu ore field (ppm)

Sample No.	Sn	W	Zn	Pb	Cu	F	Cl	B	As	Cr	Co	Rb	Sr	Ba	Cs	Li	Be	Nb	Ta	Sb	Sc	data
V12-1-4			23.3	18.2	49.1				57.5	18.5	1.9	394	91	76	8.6				7.1	0.9	3.7	1
V14-1-1	18.0	1.9	270.0	27.0	168.0	750	200	12.4		10.3	3.8	430	122	255	9.5	8.0	2.5	47.4	16.0			
V11-3	15.0	7.0	76.0	25.8	46.8	1420	600	14.6	10.3	19.0	3.0	240	369	1093	19.4	15.0	3.0	42.1	3.0	8.6	7.3	
V22-1			97.6	56.3	63.6				31.3	25.8	17.0	143	725	998	4.0				1.2	3.8	16.8	
V22-2	15.5	0.6	109.0	54.9	105.0	1000	600	9.8		114.0	28.0	114	447	1012	4.5	25.5	2.3	28.3	16.0			
V44-1			96.3	42.3	38.6				6.1	15.5	5.5	129	404	938	7.8				2.6	0.9	7.6	
Bk193-1-1	230.0	18.4	872.0	72.9	86.0	2240	407	9.0	750.9	68.8	17.7	445	309	365	109.9	22.5	5.5	32.8	2.2	6.9	17.4	
No.305-1	18.0		98.0			5880	192		14.2	9.7	11.7	283	586	733	36.1				2.3	1.3	16.3	
CX086	152.0	84.5	147.0	52.0	72.6	26400	400	9.5		45.8	22.3	212	506	849	12.0	61.3	3.8	45.0	15.3			
L127	51.0	23.0	285.0		47.0	5420	580	7.6		1.5	10.0	450	410	1030	47.0	105.0					13.0	
L132	39.0	26.0	137.0		54.0	3050	280	60.0		1.0	12.0	750	195	485	71.0	128.0					14.0	
No.5	42.0	52.3										194	565	1175		48.8	2.5	38.0	15.0			
No.6	365.0	123.3										165	214	100		61.6	5.2	58.0	15.4			
No.7	128.4	42.8										309	615	985		59.2	3.2	43.0	17.0			
No.8	76.2	119.7										180	520	840		75.5	4.2	41.0	14.0			

Data sources: (1) this study, Sn, F, Cl, B, Rb, Sr, Ba, Li, Be and Nb are analysed at HIAMP, W, Zn, As, Cr, Co, Cs, Ta, Sb and Sc (except for V14-1-1, V22-2 and CX086, which are analysed at HIAMP) are analysed by INAA at UQAC; (2) You (1990); (3) Dong (1989).

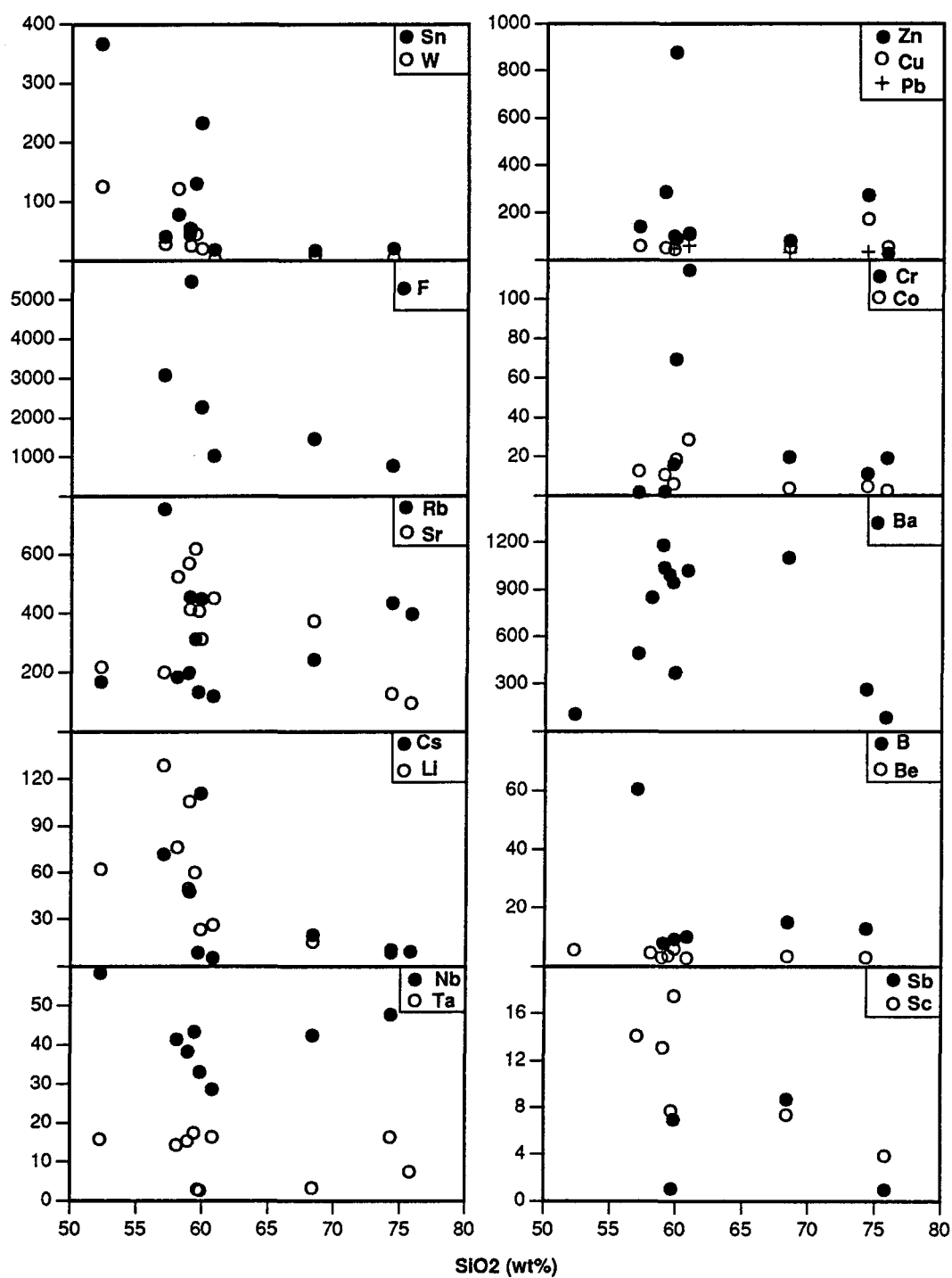


Fig. 36 SiO₂-trace element variation diagrams for dykes from the Xinlu ore field.

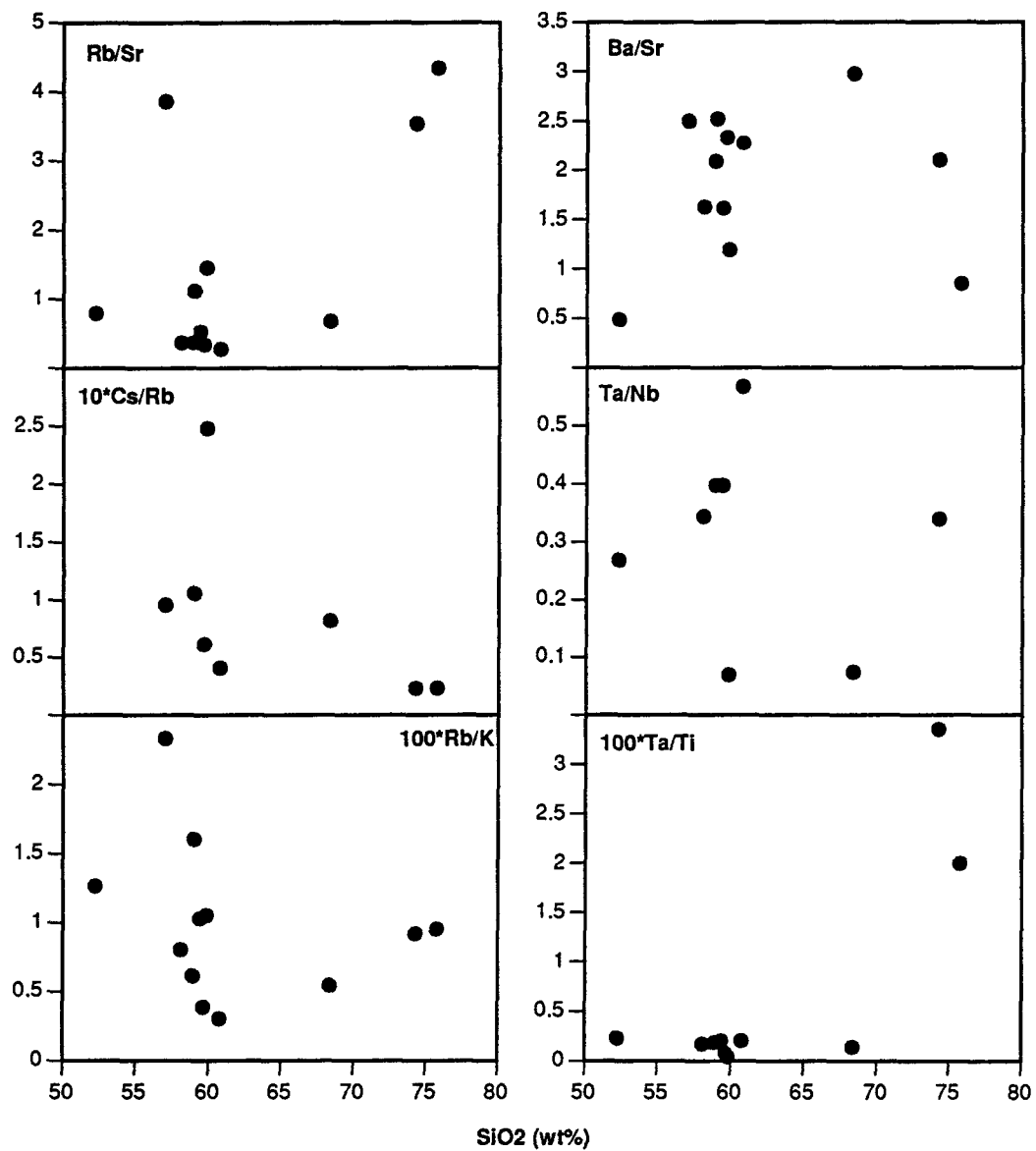


Fig. 37 SiO₂-element ratio variation diagrams for dykes from the Xinlu ore field.

4.4.3 REE patterns

Rare earth elements have been analysed for 8 samples of dykes from Xinlu. The results are listed in table 15. $\Sigma\text{REE}'$, $\delta\text{Eu}'$ and $\text{LREE}'/\text{HREE}'$ are calculated in the same way as in 4.1.3 (see appendix B) and the results are listed in table 15.

The REE patterns of representative dykes are shown in Fig. 38. The felsic dyke is characterized by strong Eu depletion ($\delta\text{Eu}'=0.073$) and no LREE enrichment (Fig. 38), while the intermediate dykes are remarkably less Eu-depleted ($\delta\text{Eu}'=0.79-0.97$) and much more LREE-enriched ($\text{LREE}'/\text{HREE}'= 9.05-12.86$). The ΣREE of the felsic dyke is similar to that of the phase III granite of the Guposhan batholith, while the ΣREE of the intermediate dykes are similar to those of phase II and III of the Guposhan batholith. There is no obvious trend between SiO_2 and ΣREE & δEu , but a negative correlation between LREE/HREE and SiO_2 is noticeable (Fig. 39).

4.4.4 Sr Isotopes

Sr isotope analyses of six samples of dioritic porphyry in the adjoining Shuiyanba ore field yield a $(^{87}\text{Sr}/^{86}\text{Sr})_i$ value of 0.71567 (table 16 and Fig. 40, Yichang Inst. of Geol., 1985). Three K-Ar ages and Sr isotopes in corresponding samples of dykes are analysed from the Xinlu ore field. $(^{87}\text{Sr}/^{86}\text{Sr})_i$ values are calculated on the basis that the K-Ar ages are treated as equal to their Rb-Sr isochron ages (table 16 and Fig. 40). It is believed that the difference between K-Ar ages and Rb-Sr whole-rock isochron ages is small, because the dykes are small in size and must have cooled fairly rapidly. The calculated results of the $(^{87}\text{Sr}/^{86}\text{Sr})_i$ are: 0.7047 for V22-1 (monzonite), 0.71179 for V11-3 (quartz dioritic porphyry) and 0.71449 for V14-1-1 (quartz porphyry). It is obvious that the initial Sr isotope ratios vary greatly for different dykes.

4.4.5 Genesis

Most of the dykes in Xinlu are intermediate rocks, which are obviously different from the granites. However, the origin of the dykes may be related to the granites of the Guposhan batholith, as reflected by the radial distribution of the dykes around the batholith (Fig. 8). The irregularities of the variation of major elements, trace elements and rare earth

Table 15. REE contents (ppm) and parameters for dykes from the Xinlu ore field

Sample no.	rock type	La	Ce	Sm	Eu	Tb	Yb	Lu	TREE'	LREE'/HREE'	dEu'
V12-1-4	fine-grained granite	21.21	52.08	8.68	0.24	2.42	8.83	1.47	176.84	2.10	0.07
V11-3	Bi Q dioritic porphyry	70.63	123.35	9.04	2.16	1.19	3.43	0.67	298.26	9.71	0.81
V22-1	fine-grained monzonite	57.46	96.71	6.48	1.90	0.92	2.25	0.42	232.24	10.48	0.97
V22-2	fine-grained Bi granodior	45.33	88.27	7.29	1.72	0.93	2.42	0.35	211.17	9.05	0.81
V44-1	Q dioritic porphyry	69.60	129.35	7.33	1.67	0.89	2.46	0.41	286.28	12.86	0.79
CX086	Bi Q dioritic porphyry	54.83	110.18	9.38	2.39	1.16	2.79	0.41	262.00	9.20	0.88
Bk193-1-1	dioritic porphyry	53.73	103.46	7.59	1.85	1.02	2.55	0.44	241.75	9.66	0.82
No.305-1	Bi Q dioritic porphyry	62.08	123.89	9.63	2.45	1.30	3.23	0.55	290.72	9.08	0.86

* analysed by INAA at UQAC except V22-2 and CX086 which are analysed at Hubei Institute of Geology, China.

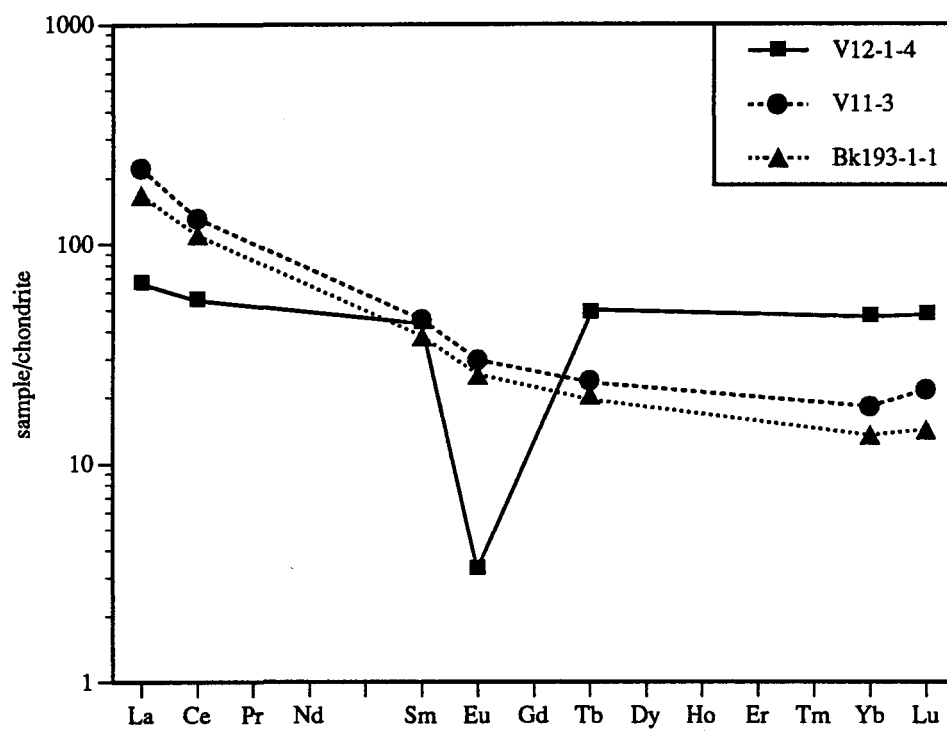


Fig. 38 REE patterns of representative dykes from the Xinlu ore field.

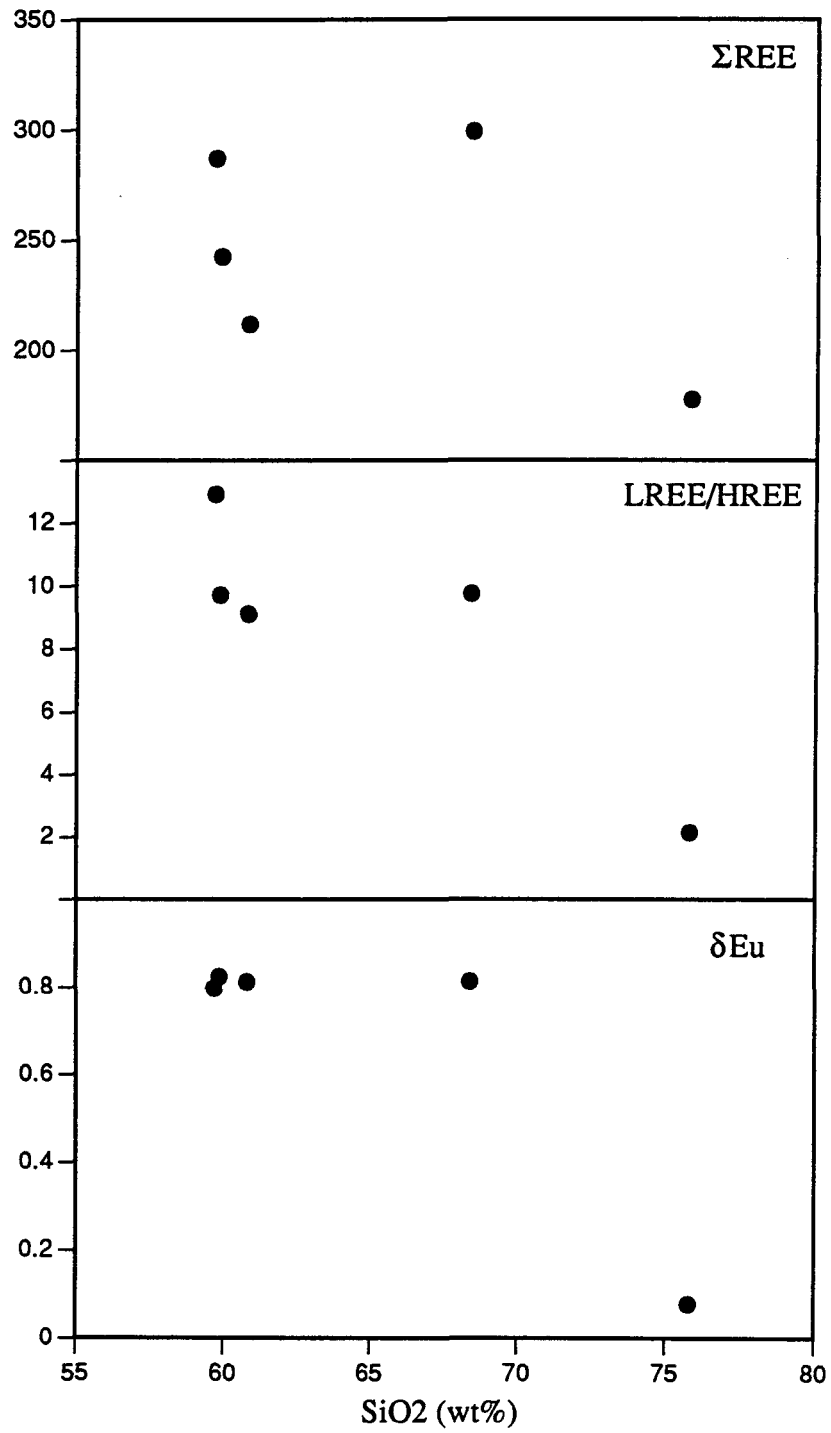


Fig. 39 SiO₂-REE parameter variation diagrams for dykes from the Xinlu ore field.

Table 16 Sr isotope compositions of dykes from Xinlu and Shuiyanba

Sample no.	Locality	$^{87}\text{Rb}/^{86}\text{Sr}$	$^{87}\text{Sr}/^{86}\text{Sr}$	$(^{87}\text{Sr}/^{86}\text{Sr})_i$	age (Ma)	data
M1-2	Shuiyanba	105.5980	0.95317	0.71567	149.31 (Rb-Sr)	1
M1-3		5.0680	0.72204			
M1-4		234.8182	1.25866			
M1-7		59.9748	0.86952			
M1-8		19.7098	0.75241			
M1-10		177.9381	1.01825			
V11-3	Xinlu	1.8947	0.71552	0.71179	138.63 (K-Ar)	2
V22-1		0.6002	0.70606	0.70474	155.06 (K-Ar)	
V14-1-1		9.0473	0.72684	0.71449	91.60 (K-Ar)	

Data sources: (1) Yichang Inst. of Geol. (1985); (2) this study, $(^{87}\text{Sr}/^{86}\text{Sr})_i$ is calculated by using the K-Ar ages as substitution of Rb-Sr ages.

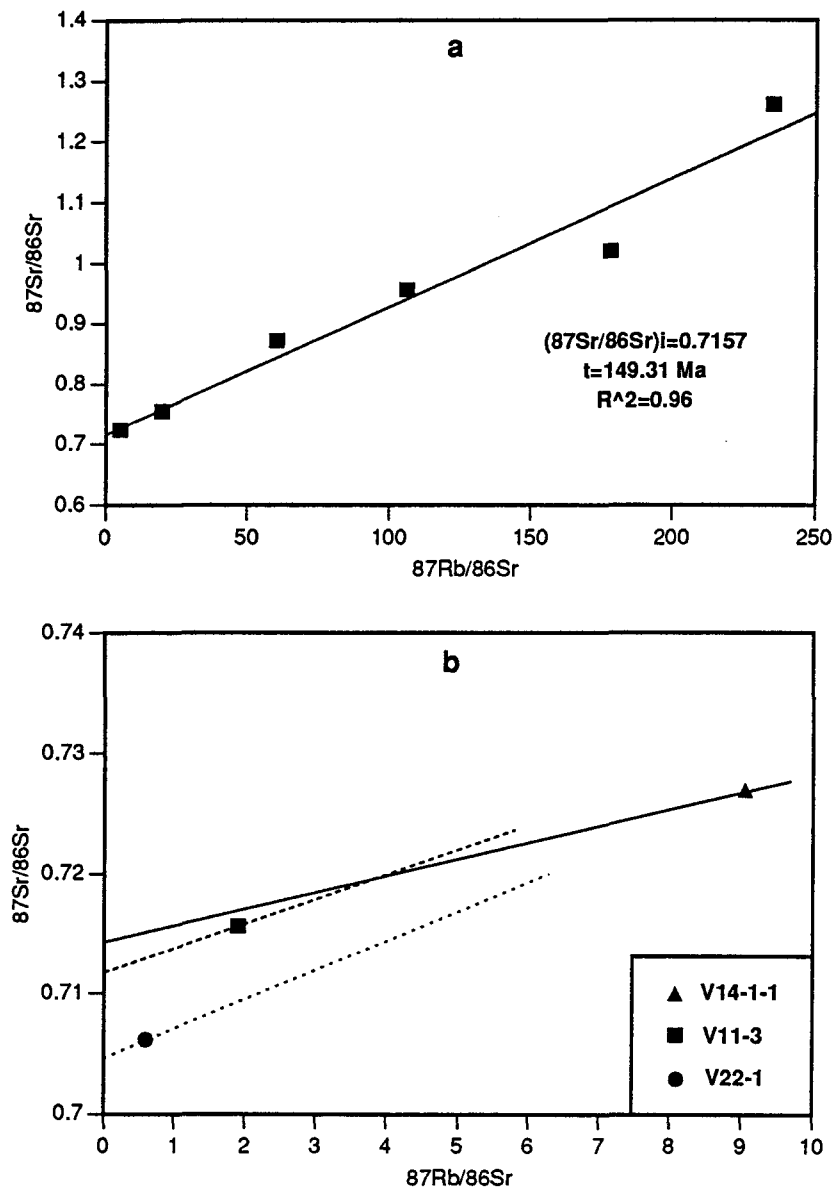


Fig. 40 Rb-Sr isotope whole-rock isochron for intermediate dykes from Shuiyanba (a) and single-sample Rb-Sr isotope points and inferred $(^{87}\text{Sr}/^{86}\text{Sr})_i$ values for dykes from Xinlu (b) with Rb-Sr whole-rock ages approximated by K-Ar ages.

elements, and the variety in $(^{87}\text{Sr}/^{86}\text{Sr})_i$ and K-Ar ages indicate that the dykes are not derived from a common initial magma through magmatic processes. According to available K-Ar age and Sr isotope data, there are probably three magma sources for different dykes: (1) the magma of most dark enclaves (phase E) in phase I granites of the Guposhan batholith, represented by sample V22-1 (monzonite), which has a K-Ar age of 155 Ma and a $(^{87}\text{Sr}/^{86}\text{Sr})_i$ of 0.7047; (2) the magma of phase I granites of the Guposhan batholith, represented by sample V11-3 (biotite quartz dioritic porphyry), which has a K-Ar age of 139 Ma and a $(^{87}\text{Sr}/^{86}\text{Sr})_i$ of 0.7118; (3) the magma of phase III granites of the Guposhan batholith, represented by sample V14-1-1, which has a K-Ar age of 92 Ma and a $(^{87}\text{Sr}/^{86}\text{Sr})_i$ of 0.7145. It must be pointed out, however, that contamination of sediments, as discussed below, may have modified the $(^{87}\text{Sr}/^{86}\text{Sr})_i$ values of the dykes.

An obvious difference in major element content is observed between the intermediate dykes and corresponding granites of the Guposhan batholith. This difference, characterized by the decrease of SiO_2 content in intermediate dykes relative to the granites, is most likely to be caused by the incorporation of sedimentary rocks, which have generally much lower SiO_2 contents (Chi, 1989a). This is evidenced by the petrological features of the dykes. Mineral components, textures and structures in dykes vary greatly for different dykes or even for different parts of individual dykes. This is characteristic of contaminated rocks. It is probably due to the difference of contamination degree and the heterogeneous nature of the contaminated magmas. Textitic structures are developed in the intermediate dykes, which is a reflection of the heterogeneity of the magmas. Most of the intermediate dykes contain calcite and carbonate and argillaceous fragments (plate 4A, B, C), whereas acidic dykes contain very little (if any) of these components. If it is proposed that dykes of different compositions result from magmatic differentiation, it is unreasonable that calcite and carbonate fragments are preferentially developed in intermediate dykes. Oscillatory zoning is developed in plagioclase (plate 4D), which may be (although not necessarily) a reflection of unsteady supply of Ca in the magma due to contamination of sedimentary rocks. Abundant titanite and needle-like apatite occur in intermediate dykes (plate 4E, F), which may be (although not necessarily) the reflection of extra supply of Ca from the sedimentary rocks. The wide range of variation of major and trace elements in the dykes and their irregularities in relation to the variation of SiO_2 content are most likely to be explained by the model of sedimentary contamination, since the sedimentary rocks are highly heterogeneous. The generally low content of Na_2O in the intermediate dykes is consistent with the fact that all the

sedimentary rocks are fairly poor in Na₂O (table 2 and Fig. 19). The reverse correlation between CO₂ and SiO₂ also supports the contamination model, since CO₂ is characteristic of all the sedimentary rocks.

Since different dykes may have different magma sources, and because of the compositional heterogeneity of the sedimentary rocks, it is difficult to use the geochemical data of all the dyke samples to model the contamination process quantitatively, but a qualitative comparison between individual sample and corresponding (inferred) granite is possible. For example, V₁₁₋₃ is inferred to be derived from the magma of phase I granite of the Guposhan batholith based on its K-Ar age and Sr isotope data. Its lower Σ REE and higher δ Eu values than Im are broadly consistent with the fact that the sedimentary rocks as a whole have lower Σ REE and higher δ Eu than Im, although the much higher LREE/HREE and δ Eu values in the dyke require additional enrichment of LREE and Eu besides the incorporation of sedimentary rocks, which may be related to volatile activities due to decarbonation and dehydration of sedimentary rocks during magma contamination. The higher (87Sr/86Sr)_i value (0.7118) in the dyke than phase I granite (0.7088) can be explained by the generally higher (87Sr/86Sr)_i values in sedimentary rocks.

In conclusion, different dykes in the Xinlu ore field are derived from the magmas of different phases of the Guposhan batholith. Sedimentary incorporation is the major process causing the dykes to be less felsic than their corresponding granites. The compositional complexities of the sedimentary rocks and the involvement of volatile components due to decarbonation and dehydration of sedimentary rocks may be responsible for the irregularities of major, trace and rare earth element content in the dykes.

4.4.6 The ore-forming potential

The same criteria for distinguishing tin-generating granites and barren granites are applied to the evaluation of the ore-forming potential of the dykes in the Xinlu ore field (table 17). The percentage of the criteria which are within the range of Sn-generating granites are: 80% for V₁₂₋₁₋₄, 60% for V₁₄₋₁₋₁, 25% for V₁₁₋₃, 15% for V₂₂₋₂, 35% for Bk₁₉₃₋₁₋₁, 13% for V₄₄₋₁, 33% for L₁₂₇, 44% for L₁₃₂, 11% for No.5, 16% for No.6, No.7 and No.8. In Rb-Cs-Ba (Fig. 41a), 7 of the 11 samples plot on area C, which are considered to be without related tin mineralization (Neiva, 1984). In Rb-Sr-Ba diagram (Fig. 41b), most of the samples are outside the area suitable for tin mineralization (Biste, 1982). Therefore,

Table 17 Some geochemical parameters for distinguishing tin-generating granites and barren or normal granites, in comparison with dykes from the Xinlu ore field

Samples of dykes	Major element									Trace elements					Element ratio				Others	
	SiO ₂	TiO ₂	Al ₂ O ₃	Fe ₂ O ₃	FeO	MgO	CaO	Na ₂ O	K ₂ O	Sn	F	Li	Rb	Be	K/Rb	TiO ₂ /Ta	Mg/Li	Rb/Sr	DI	cm
V12-1-4	75.77	0.06	12.36	0.25	0.50	0.38	1.10	3.23	5.05				393.8		106.44	84.27		4.32	93.05	0.00
V14-1-1	74.29	0.08	13.30	0.57	0.74	0.20	1.42	1.82	5.69	18.0	750	8.0	430.0	2.5	109.83	50.00	150.75	3.52	89.16	1.88
V11-3	68.39	0.40	15.04	0.75	2.53	0.58	2.13	2.21	5.43	15.0	1420	15.0	239.9	3.0	187.87	1337.79	233.16	0.65	82.01	3.53
V22-2	60.79	1.40	13.68	3.12	4.38	2.88	4.55	2.50	4.68	15.5	1000	25.5	114.0	2.3	340.74	875.00	681.04	0.26	65.64	0.00
Bk193-1-1	59.86	1.40	14.17	1.36	6.46	3.24	4.46	0.93	5.14	230.0	2240	22.5	445.0	5.5	95.87	6334.84	868.32	1.44	58.78	1.53
V44-1	59.68	0.65	15.34	0.78	3.61	1.52	3.97	2.55	4.12				128.9		265.29	2519.38		0.32	67.68	0.17
L127	59.02	1.29	16.00	0.21	6.64	2.35	4.73	2.66	3.42	51.0	5420	105.0	450.0		63.08		134.96	1.10	59.44	1.94
L132	57.06	1.51	16.12	0.59	7.60	1.75	3.36	0.93	3.89	39.0	3050	128.0	750.0		43.05		82.44	3.85	58.16	6.13
No.5	58.92	1.44	16.07	0.93	7.40	1.95	5.47	2.54	3.88	42.0		48.8	194.3	2.5	165.74	960.00	240.95	0.34	56.65	0.00
No.6	52.54	1.20	17.06	1.22	6.11	1.90	13.83	1.10	1.58	365.0		61.6	164.6	5.2	79.67	779.22	185.99	0.77	30.77	0.00
No.7	59.40	1.48	16.07	0.86	6.43	2.00	5.28	2.80	3.65	128.4		59.2	308.6	3.2	98.17	870.59	203.72	0.50	58.83	0.00
No.8	58.10	1.50	15.87	1.00	7.59	2.50	4.67	2.50	2.73	76.2		75.5	179.8	4.2	126.02	1071.43	199.67	0.35	55.27	2.21
Sn-generat. granites	73.38 +/-1.39	0.16 +/-0.10	13.97 +/-1.07	0.8 +/-0.47	1.1 +/-0.47	0.47 +/-0.56	0.75 +/-0.41	3.2 +/-0.61	4.69 +/-0.68	30 +/-15	3700 +/-1500	220 +/-100	550 +/-200	13 +/-6	20-- 100	0.94-- 71.6	75 +/-30	>4	90.06	2.3
Barren granites	70.84 +/-1.41	0.34 +/-0.08	14.33 +/-0.23	1.31 +/-0.29	1.78 +/-0.38	0.81 +/-0.23	1.89 +/-0.40	3.44 +/-0.32	4.34 +/-0.52	1-- 8	250-- 1500	31-- 150	130-- 300	2.6-- 8	100-- 300	57-- 4896	270 +/-80	<4	83.64	0.54
References	Tischendorf (1977), with 962 samples for tin-generating granites and 2327 samples for normal granites for the statistics of major elements.													Tischendorf, 1972	Boissavy-Vinau and Roger, 1980	Beus and Sitnin, 1968	Lawrence, 1975	calculated from the data of Tischendorf, 1977		

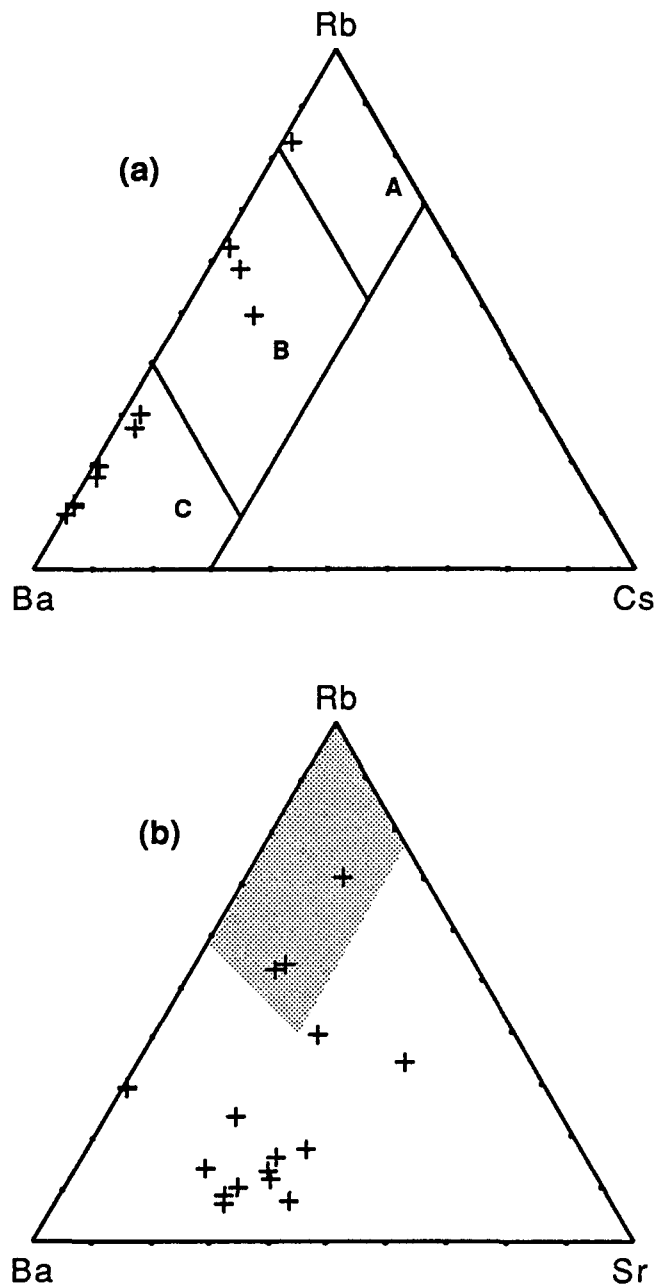


Fig. 41 Samples of dykes from the Xinlu ore field plotted on (a) Rb-Cs-Ba diagram (Neiva, 1984), and (b) Rb-Sr-Ba diagram (Biste, 1982). In (a), Area A--muscovite granite, greisenized granite, aplites and pegmatite related to Sn-W mineralization; Area B--muscovite and biotite granite and hybrid granodiorite associated with Sn-W mineralization and Area C--granites without related Sn-W mineralization. In (b), the shaded area is granites associated with Sn, W and Mo deposits. Data are from Table 14.

according to the distinguishing criteria, most of the dykes have very poor ore-forming potential.

However, the Sn contents in all the dyke samples are within the range of Sn-generating granites (Tischendorf, 1977). Since it is suggested that the dykes are derived from the magmas of the granites of the Guposhan batholith through sedimentary contamination, and the sedimentary rocks are generally poorer in Sn than the granites (phase III, II and Im), it may be deduced that Sn tends to retain in the contaminated melt in partitioning between the melt and coexisting fluids. This may be caused by the effect of large amounts of CO₂ released by decarbonation during magma-sedimentary rock interaction, because CO₂ tends to raise the melting temperatures of the magma (Strong, 1988), promoting quick solidification of the magma and hence hindering the partitioning of the granophile elements such as Sn into fluid phases.

The high content of Sn in the dykes provides a potential Sn source if it can be released during later hydrothermal alteration. However, Sn can be enriched in altered rocks instead of being released into hydrothermal fluids during alteration, e.g. 18 ppm in No.305-1 (unaltered sample) vs. 39 ppm in No.304 (altered sample of the same dyke). Besides, the size of the dykes is generally small (one to two metres wide and several hundred metres long), which lowers their potential of total Sn. Therefore, the contribution of Sn in the ore-forming fluids by the dykes may be limited.

CHAPTER V

GEOCHEMICAL CHARACTERISTICS OF THE ORES AND THE SOURCES OF THE ORE-FORMING FLUIDS

5.1 Introduction

The discussions in chapter 4 indicate that granite intrusions (esp. the latest phase) have the best ore-forming potential, and that sedimentary rocks and dykes may provide minor ore-forming elements. In this chapter, the geochemical characteristics of ore minerals and the ores themselves, including their isotope compositions, REE patterns and fluid inclusions, will be discussed. These characteristics provide direct evidence for the origin of the ore-forming fluids.

5.2 Geochemical Characteristics of the Ores

5.2.1 S isotopes

Sixty one samples of sulfides from the Xinlu ore field and two samples of syngenetic pyrite from Haodong which is relatively far from the deposits have been analysed for sulfur isotopes. The data are listed in table 18.

The characteristics of S isotopes of different deposits are shown by histograms of $\delta^{34}\text{S}$ (Fig. 42). In general the S isotopes are rather restrained in comparison with biogenetic deposits, which have very wide range of $\delta^{34}\text{S}$ (e.g. pyrite from the Santa Catalina Basin has $\delta^{34}\text{S}$ from +11.2‰ to -42.0‰, Jensen, 1967), although those of the Baimianshan deposit are a bit divergent in comparison with typical magmatic hydrothermal deposits (e.g. 33 samples from four different mines in the O'okiep Copper Mines of Southwest Africa have $\delta^{34}\text{S}$ values of +0.8±1.0‰, Jensen, 1967). The S isotopes of all the ores are quite different from those of the syngenetic pyrite, which has $\delta^{34}\text{S}$ as low as -22.91‰ (table 18).

The range of $\delta^{34}\text{S}$ is from -5.0 to +1.7‰ for the proximal ores, and from -3.3 to +8.6 ‰ for the distal ores. The majority of the $\delta^{34}\text{S}$ values lies between -1 and +4‰ for

Table 18 Sulfur isotope compositions of ore minerals from the Xinlu ore field

Deposits	Occurrence	Sample No.	Locality	Mineral	d34S‰	Data source
Liuhe'ao	Proximal Deposit	Z002	Minglong	Pyrrhotite	1.70	1
		SI-23	Minglong	Arsenopyrite	-1.20	2
		SI-24	Minglong	Arsenopyrite	0.80	
Dachong		SI-26	Dachong	Pyrrhotite	0.10	1
		Z009	Jiaochong	Jamesonite	-5.00	
Hebao		SI-17	Hebao	Pyrite	0.40	2
	SI-20	Hebao	Arsenopyrite	0.60		
	SI-25	Qingshuitang	Molybdenite	-3.90		
Muqiaomian	Vein-type Distal Deposit	Z006	No.6 vein	Arsenopyrite	1.10	1
Shimen		Z032	No.6 vein	Pyrrhotite	4.20	
		Z001	Level 115	Fe-Sphalerite	-0.10	
		Z007	Level 65	Pyrite	-1.10	
		Z002	Level 65	Arsenopyrite	1.80	
		S255-6	Level 255	Pyrrhotite	0.20	
	SI115-8	Level 115	Pyrrhotite	-0.30		
Baimianshan	Vein-type Distal Deposit	SI-28	Shimen	Arsenopyrite	0.60	2
		****	Level 205	Pyrite	-0.62	3
		****	Level 205	Pyrite	1.18	
		B301	Level 257	Fe-Sphalerite	2.90	1
		Z031	Level 257	Fe-Sphalerite	7.00	
		Z031	Level 257	Arsenopyrite	8.60	
		B351-2	Level 257	Pyrrhotite	-3.00	
		Z029	Level 257	Jamesonite	5.70	
		F-6	Level 257	Pyrrhotite	1.28	4
		XQ116	Level 257	Pyrrhotite	3.23	5
		B469	Level 193	Pyrrhotite	3.40	1
		SI-01	Level 193	Pyrrhotite	-1.82	2
		SI-02	Level 193	Pyrrhotite	0.80	
		SI-04	Level 193	Pyrite	2.26	
		SI-05	Level 193	Fe-Sphalerite	-2.73	
	SI-06	Level 193	Fe-Sphalerite	2.00		
	SI-09	Level 193	Pyrrhotite	1.91		
	SI-10	Level 193	Pyrrhotite	-2.73		
	SI-11	Level 193	Pyrite	0.95		
	SI-12	Level 193	Fe-Sphalerite	1.16		
	SI-14	Level 193	Fe-Sphalerite	1.07		
	SI-15	Level 193	Pyrite	-0.50		
	SI-16	Level 193	Fe-Sphalerite	0.60		
	SI-18	Level 193	Jamesonite	5.90		
	SI-19	Level 193	Galena	3.10		
	SI-27	Level 193	Sphalerite	6.10		
	Stratiform Distal Deposit	F-1	Level 193	Pyrrhotite	2.76	4
		F-4	Level 193	Pyrrhotite	3.66	
		F-5	Level 193	Pyrrhotite	1.21	
		GN-29	Level 193	Sphalerite	-1.49	3
GN-30		Level 193	Pyrite	2.48	1	
Z026		****	Pyrite	-3.20		
SI-21		Shanbaling	Pyrrhotite	-3.30	2	
SI-22		Shanbaling	Fe-Sphalerite	-2.90	1	
B482		Level 193	Fe-Sphalerite	4.00		
Z028		Level 193	Fe-Sphalerite	-0.40		
Z019		Level 193	Pyrite	4.20		
Z035		Level 193	Arsenopyrite	3.10		
B482		Level 193	Pyrrhotite	4.20	5	
Z027		Level 193	Pyrrhotite	2.00		
XQ109		Level 193	Sphalerite	0.00		
XQ112	Level 193	Sphalerite	0.11			
XQ063	Level 193	Pyrrhotite	-1.25			
XQ058	Level 193	Pyrrhotite	1.51	5		
XQ104	Level 150	Arsenopyrite	-0.78			
XQ004	Level 150	Pyrrhotite	2.90			
Haodong	syngenetic pyrite	SI-07	Haodong	Pyrite	-20.44	2
		SI-08	Haodong	Pyrite	-22.91	

Data sources: (1) No.204 Geol. Team of Guangxi (1979); (2) Deng (1984); (3) Yichang Institute of Geology (1985); (4) Fu (1984); (5) Qiu (1989).

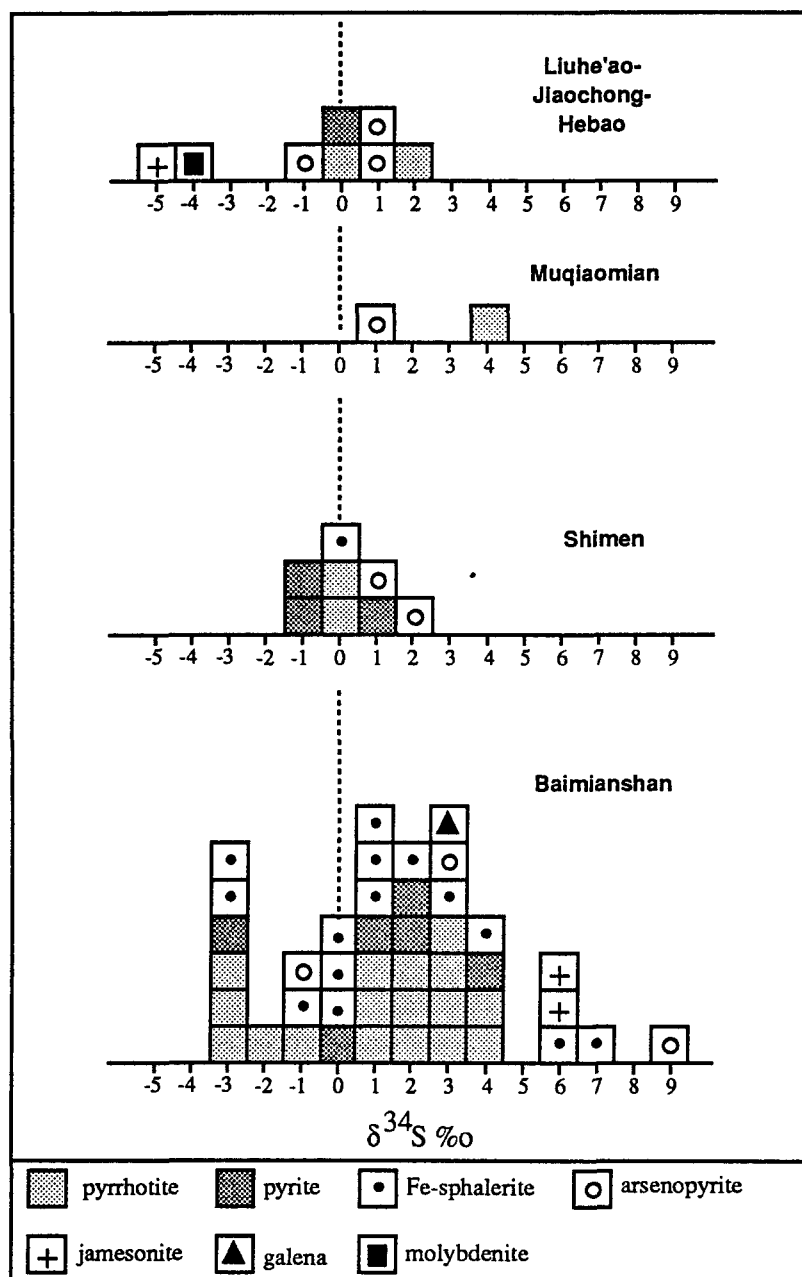


Fig. 42 Histograms of S isotope composition of ore minerals from different ore deposits in the Xinlu ore field.

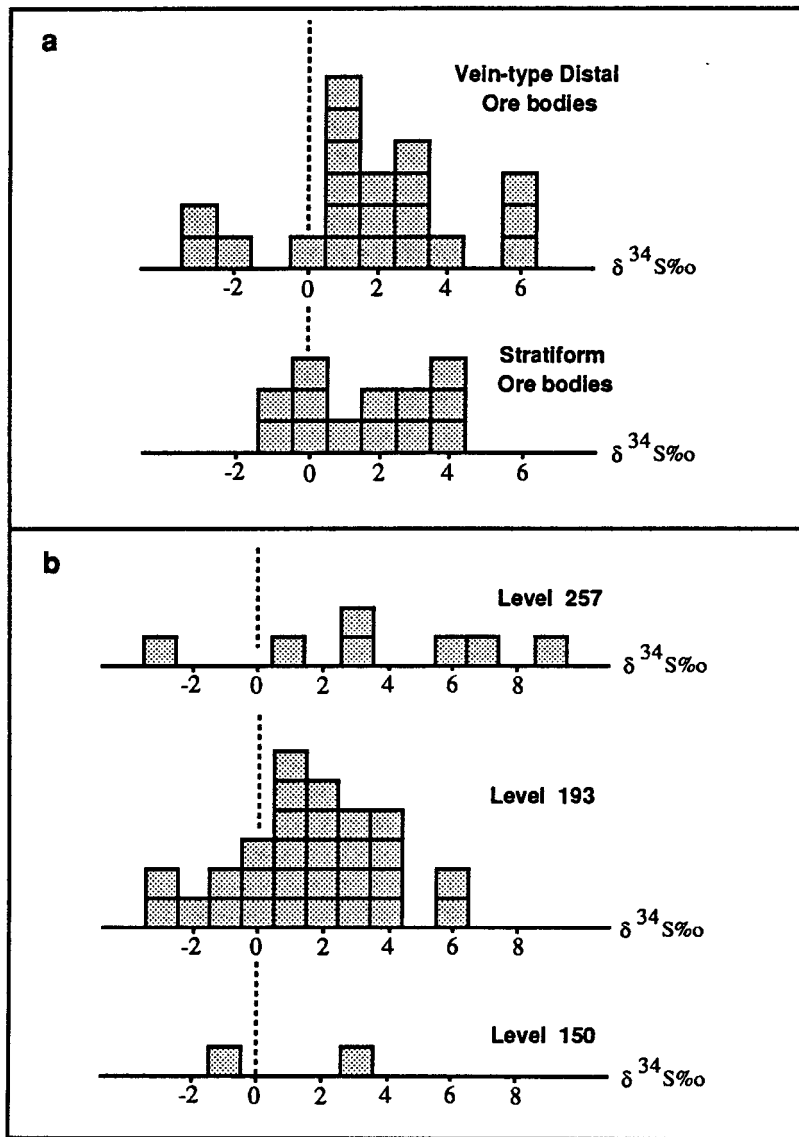


Fig. 43 Comparison of S isotope composition between different types of ore body (a) and between different levels of the Baimianshan deposit (b).

both proximal and distal ores, which are comparable with the sulfur isotope compositions of most igneous rocks which are mainly $0\pm 5\%$ (Ohmoto and Rye, 1979). Since pyrrhotite occurs as a stable and major sulfide mineral in both proximal and distal ores, and the pH values of the ore-forming fluids have been estimated to be 3.98 to 5.15 for the Baimianshan deposit (Deng, 1985), it can be assumed that the dominant sulfide species in the fluids is H_2S and that $\delta^{34}S_{\text{sulfide}}$ is similar to $\delta^{34}S_{\Sigma S}$ (Ohmoto, 1986) in both proximal and distal ore-forming fluids. Therefore, the $\delta^{34}S$ values of sulfides are diagnostic of the source of sulfur, and a principal magmatic source is most likely for both proximal and distal ores. The slightly heavier and wider characteristics of S isotopes of the ores from the Baimianshan deposit may imply a little incorporation of sulfur from the country rocks during the ascending of the ore-forming fluids and from the depositional sites. Although the two samples of syngenetic pyrite give $\delta^{34}S$ values far below zero, most parts of the host rocks may have higher $\delta^{34}S$ values than the magmatic sources. For example, Xu (1987 a) reported two samples of Devonian syngenetic pyrite from Dachang area of Guangxi with $\delta^{34}S$ of -3% and $+17.7\%$; Zen et al. (1987) reported $\delta^{34}S$ values of $+0.66\%$ to $+14.43\%$ for the Devonian syngenetic pyrite from Hongyan, Nanling region and -11.52% to $+9.8\%$ for the Devonian syngenetic pyrite from Beishan, Nanling region.

The comparison of S isotopes between vein-type ore bodies and stratiform ore bodies in the Baimianshan deposit (Fig. 43a) shows that they have similar S isotope compositions, although the former has slightly wider range of $\delta^{34}S$ than the latter. This implies that the sulfur of the stratiform ore bodies are mainly from the magmatic sources like that of the vein-type ore bodies. Similar comparison is also made between different levels of the Baimianshan deposit (Fig. 43b). Sulfides from higher levels have slightly wider range of $\delta^{34}S$ than those from lower levels, implying an increasing degree of incorporation of sedimentary sulfur during the ascending of the ore-forming fluids.

5.2.2 O isotopes

O isotopes have been analysed for 12 samples of quartz, garnet and cassiterite from granite, skarn and ores from the Xinlu ore field (Yichang Geol. Inst., 1985; Liu and Yuan, 1989; Zheng, 1987; Qiu, 1989). The data are listed in table 19. Most of the samples are pure cassiterite, which ensures that the results are related to the ore-forming fluids and are consistent with other geochemical characteristics (fluid inclusions and REE pattern).

Table 19 Oxygen isotope compositions of quartz, garnet and cassiterite in granites, skarns and ores from the Xinlu ore field as well as the calculated values of associated water

Sample No.	Locality	Occurrence	Mineral	δ 18O‰ (mineral)	δ 18O‰ (H ₂ O)	T (°C)	Data source
****	Liuhe'ao	phase III granite	quartz	11,5	10,1	630	Yichang Institute of
****	Dawantang	phase II granite	quartz	11,6	10,2	630	Geology, 1985
No.2	Liuhe'ao	proximal skarn	quartz	13,4	8,1	350	Liu and Yuan,
No.3	Shimen	distal skarn	garnet	8,7	10,1	450	1989
C150	Baiminashan, Level 150	distal Sn sulfide deposit	cassiterite	6,4	8,3	340	Xie, 1989
C193	Baiminashan, Level 193		cassiterite	5,2	7,0	340	
C257	Baiminashan, Level 257		cassiterite	5,1	6,9	340	
No.5	Baiminashan		cassiterite	6,7	8,6	340	Liu and Yuan,
No.6	Shanbaling		cassiterite	7,6	9,5	340	1989
****	Baiminashan, Level 193		cassiterite	5,1	6,9	340	Yichang Institute of
****	Shimen		cassiterite	6,3	8,2	380	Geology, 1985
No.4	Shimen		cassiterite	6,0	7,9	380	Liu and Yuan, 1989

$\delta^{18}\text{O}$ (SMOW) of water in equilibrium with the mineral at the temperature of formation (estimated from fluid inclusion data) are calculated (table 19). The calculation formula of quartz-water O isotope fractionation is adopted from Matsuhisa et al.(1979):

$$\Delta\delta^{18}\text{O}\text{‰}(\text{quartz-water})=2.05(10^6\text{T}^{-2})-1.14 \quad (500-800\text{ }^\circ\text{C})$$

$$\Delta\delta^{18}\text{O}\text{‰}(\text{quartz-water})=3.34(10^6\text{T}^{-2})-3.31 \quad (250-500\text{ }^\circ\text{C})$$

The garnet-water fractionation formula is adopted from Bottinga and Javoy (1973):

$$\Delta\delta^{18}\text{O}\text{‰}(\text{garnet-water})=1.22(10^6\text{T}^{-2})-3.70$$

The oxygen isotope fractionation factor for cassiterite-water pair has not been determined either experimentally or theoretically (Sun and Eadington, 1987). However, the quartz-cassiterite fractionation factor provided by Borshchevskiy (1979), combined with the quartz-water formula of Matsuhisa et al. (1979), gives the following relation:

$$\Delta\delta^{18}\text{O}\text{‰}(\text{cassiterite-water})=2.05(10^6\text{T}^{-2})-1.14 \quad (300-450\text{ }^\circ\text{C})$$

With this formula, the O isotopes of water in equilibrium with cassiterite may be calculated (table 19). $\delta^{18}\text{O}$ values are +10.1-- +10.2‰ for magmatic water, +8.1‰ for the water coexisting with the inner skarn in Liuhe'ao, +10.1‰ for the water coexisting with the outer skarn in Shimen, +6.9 -- +9.5‰ for the water in the distal ore-forming fluids. The oxygen isotope data demonstrate that the O isotope composition of the water in the distal ore-forming fluids is slightly lighter than those in granite and is roughly identical to that in proximal skarn. A decrease in $\delta^{18}\text{O}(\text{H}_2\text{O})$ is noticed from lower levels to higher levels in Baimianshan deposit, i.e. +8.3‰ (Level 150) through +7.0‰ (Level 193) to +6.9‰ (Level 257).

No hydrogen isotopes have been analysed for samples from the Xinlu ore field. However, three pairs of $\delta\text{D}-\delta^{18}\text{O}$ analyses are obtained by Liu and Yuan (1989) from the adjoining Shuiyanba ore field. Two samples are from the W-Sn quartz veins hosted by carbonate rocks and one is from granite. All the samples plot to the right of the meteoritic line in a $\delta\text{D}-\delta^{18}\text{O}$ diagram, and are within the scope of or very close to the "magmatic water" ($\delta\text{D} = -75$ to -30‰ and $\delta^{18}\text{O} = +7$ to $+13\text{‰}$, Ohmoto, 1986). The samples from Xinlu ore field, if coupled with H isotope data, would probably have similar situation.

The $\delta^{18}\text{O}$ of the magmatic water from Xinlu ore field (from +10.1 to +10.2‰) is well within the scope of the average magmatic water of Ohmoto (1986). The explanation for the depletion of $\delta^{18}\text{O}$ in the distal ore-forming fluids relative to the magmatic water can possibly be associated to incorporation of meteoric water, although the deviation of $\delta^{18}\text{O}$ of distal ore-forming fluids from the magmatic water is small in comparison to examples

with strong incorporation of meteoritic water (e.g. $\delta^{18}\text{O}$ (H_2O) from -5.0 to -3.7‰ for the mineralization solutions vs. +9.0‰ for magmatic water in the Mole granite, New South Wales of Australia (Sun and Eadington, 1987)). In the Baimianshan deposit, the $\delta^{18}\text{O}$ of ore-forming fluid decreases from +8.3‰ at lower level (level 150) to +6.9‰ at higher level (level 257), indicating a rate of $\delta^{18}\text{O}$ decrease of 1.3‰/100 m. If the $\delta^{18}\text{O}$ value of the ore-forming fluid is 10.05‰ at the departure of the intrusion (level -350 m), the rate of $\delta^{18}\text{O}$ decrease from level -350 to level 150 is 0.35‰/100 m. This possibly indicates a greater interaction of meteoric water closer to the paleosurface.

Two samples of modern meteoric water at Shanhu (about 30 km from Xinlu) were analysed for oxygen isotopes (Liu and Chang, 1987), both having $\delta^{18}\text{O}$ value of -4.75‰. This is in accordance with the data of global distribution of mean $\delta^{18}\text{O}$ of Sheppard (1986) (Xinlu plots in his $\delta^{18}\text{O} = -4$ to -6 ‰ zone). At the time of ore formation (100 to 150 Ma), the latitude of Xinlu was 13.5 to 20° higher than present day according to the arctic-pole wandering diagram of Irving (1979), and the present-day coast area in SE China was already part of the continent (so that the distance from Xinlu to the coastal line was about the same as present day). Therefore, $\delta^{18}\text{O}$ of meteoric water at that time would be in Sheppard's (1986) -6 to -8‰ zone. If the $\delta^{18}\text{O}$ value of meteoric water is taken as -7‰, the proportion of meteoric water in the distal ore-forming fluids is about 14.6% (average) for Baimianshan and 11.7% (average) for Shimen. These proportions may be minimum values because the magnitude of $\delta^{18}\text{O}$ shift of the meteoric water caused by water-rock interaction is not known.

5.2.3 Pb isotopes

Seven samples of ore minerals from the Baimianshan and Shimen deposits have been analysed for Pb isotopes. The data are listed in table 20.

In $^{207}\text{Pb}/^{204}\text{Pb}$ -- $^{206}\text{Pb}/^{204}\text{Pb}$ and $^{208}\text{Pb}/^{204}\text{Pb}$ -- $^{206}\text{Pb}/^{204}\text{Pb}$ diagrams (Fig. 44), most of the samples plot close to the single-stage growth curve (Doe and Stacey, 1974). The model ages of the ores are calculated based on the single-stage model. The equation used in the calculation is as follows:

$$\frac{((^{207}\text{Pb}/^{204}\text{Pb})_t - (^{207}\text{Pb}/^{204}\text{Pb})_T) / ((^{206}\text{Pb}/^{204}\text{Pb})_t - (^{206}\text{Pb}/^{204}\text{Pb})_T)}{(1/137.8) * ((e^{\lambda_2 T} - e^{\lambda_2 t}) / (e^{\lambda_1 T} - e^{\lambda_1 t}))} =$$

Table 20 Pb isotope composition of ore minerals from the Baimianshan and Shimen deposits in the Xinlu ore field

Sample No.	Locality	Mineral	206Pb/204Pb	207Pb/204Pb	208Pb/204Pb	single-stage model age (Ma)*	Data source
Pb-1	Baimianshan Level 193	Jamesonite	18.679	15.717	38.905	118.3	Deng, 1984
Pb-2	Baimianshan Level 193	Galena	18.741	15.707	38.945	61.1	
Pb-3	Baimianshan Level 193	Fe-sphalerite	18.293	15.623	38.479	280.2	
240-1	Baimianshan	Fe-sphalerite	18.96	15.85	38.27	82.4	Qin, 1985
331-1	Baimianshan	Fe-sphalerite	18.62	15.85	38.22	318.6	
514-1	Shimen	Fe-sphalerite	18.82	15.71	38.44	7.6	
529-2	Shimen	Fe-sphalerite	18.72	15.71	38.82	80.0	

* The equation and parameters used in the calculation of the model ages are taken from Doe and Stacey (1974), see the text.

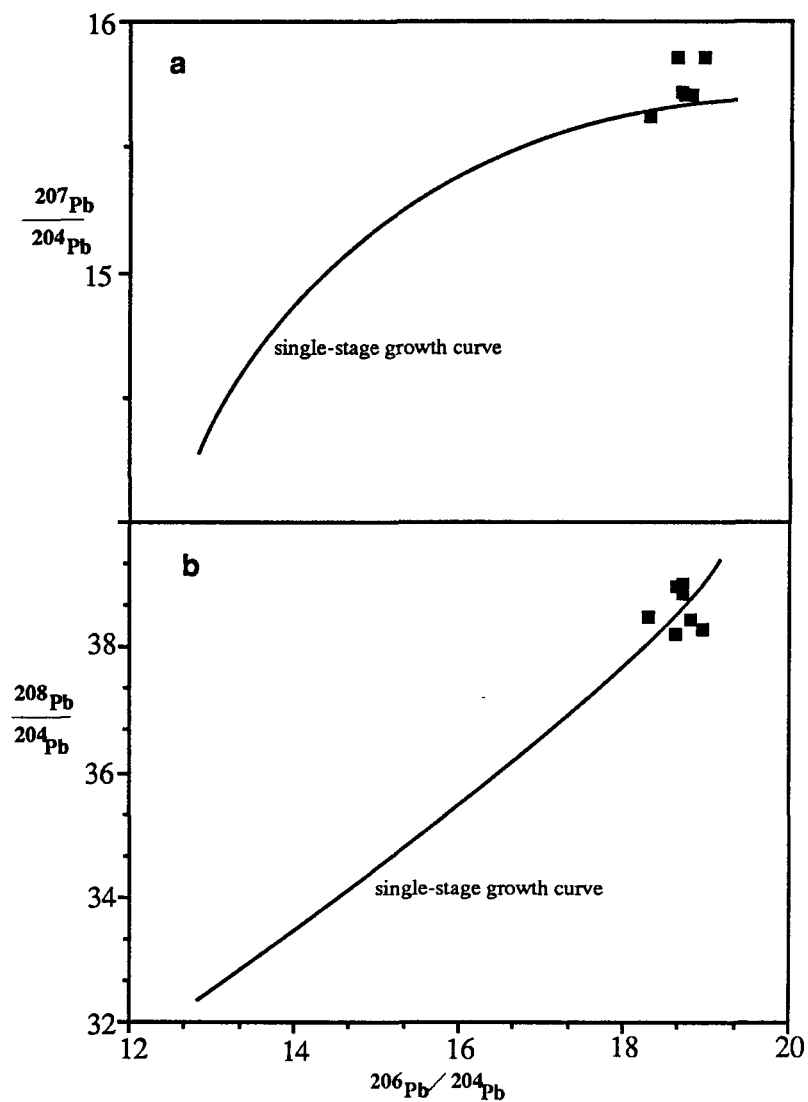


Fig. 44 Pb isotope data of ore minerals from the Xinlu ore field plotted on $^{207}\text{Pb}/^{204}\text{Pb}$ - $^{206}\text{Pb}/^{204}\text{Pb}$ diagram (a) and $^{208}\text{Pb}/^{204}\text{Pb}$ - $^{206}\text{Pb}/^{204}\text{Pb}$ diagram (b), in comparison with the single-stage growth curves. The parameters of the curve in (a) are: $T_0=4.43$ b.y., $(^{206}\text{Pb}/^{204}\text{Pb})_0=9.307$, $(^{207}\text{Pb}/^{204}\text{Pb})_0=10.294$; $(^{238}\text{U}/^{204}\text{Pb})_0=9.58$; the parameters of the curve in (b) are: $T_0=4.57$ b.y., $(^{208}\text{Pb}/^{204}\text{Pb})_0=29.476$, $(^{206}\text{Pb}/^{204}\text{Pb})_0=9.307$, $(^{232}\text{Th}/^{204}\text{Pb})_0=36.50$, $(^{238}\text{U}/^{204}\text{Pb})_0=9.1743$ (from Doe and Stacey, 1974).

where T =age of the earth=4.43 b.y., t =age of the ore-formation, $(^{207}\text{Pb}/^{204}\text{Pb})_T$ =isotope ratio of primeval lead in the earth T years ago=10.294, $(^{206}\text{Pb}/^{204}\text{Pb})_T$ =9.307, λ_1 =decay constant for ^{235}U = $9.85 \times 10^{-10} \text{y}^{-1}$, λ_2 =decay constant for ^{238}U = $1.55 \times 10^{-10} \text{y}^{-1}$ (Doe and Stacey, 1974).

The model ages calculated are 128, 61, 280, 82 and 318 Ma for the samples from the Baimianshan deposit, and 8 and 80 Ma for the Shimen deposit. Most of the ages are slightly younger (i.e. 61, 82 and 80 Ma) than or similar (i.e. 128 Ma) to the ages of the granites, and two ages (280 and 318 Ma) are apparently older than the granites but younger than the host sedimentary rocks (350--400 Ma). These model ages can not be used as precise ages of mineralization, but are broadly consistent with major magmatic sources. In general, the Pb isotope characteristics in Xinlu are similar to those of intrusion-related ore deposits in "rejuvenated cratons" such as the Rocky Mountain and Colorado Plateau Regions (Doe and Zartman, 1979). Minor Pb may be derived from the host sedimentary rocks (Devonian). The data points of Pb isotopes do not plot along a straight line on the $^{207}\text{Pb}/^{204}\text{Pb}$ -- $^{206}\text{Pb}/^{204}\text{Pb}$ and $^{208}\text{Pb}/^{204}\text{Pb}$ -- $^{206}\text{Pb}/^{204}\text{Pb}$ diagrams (Fig. 44), implying several end members of Pb or various proportions of Pb mixing.

5.2.4 REE patterns

Three samples of ores and seven samples of cassiterite from the Xinlu ore field have been analysed for rare earth elements (Dong, 1989; Qiu, 1989 and this study). The results are listed in table 21.

The REE patterns of the ores and cassiterite are illustrated in Fig. 45. Some remarkable features are noticed. The sulfide ores from the Baimianshan deposit have variable ΣREE , from 1.303 (S-3) to 233.79 (S-2), and are LREE-enriched, with very slight Eu depletion (δEu =0.90-0.93). The skarn plus cassiterite quartz veinlets (No.21) from the Liuhe'ao deposit has similar ΣREE and LREE/HREE as S-2, but is much more Eu-depleted (Fig. 45a). All the cassiterite samples have small ΣREE values (1.05-8.63). The samples of cassiterite from the Liuhe'ao deposit are characterized by small LREE/HREE (1.86-1.99) and obvious Eu depletion (δEu =0.33-0.38) (Fig. 45b). The cassiterite sample from the Shimen deposit is also Eu-depleted (δEu =0.36), but is LREE-enriched (LREE/HREE=5.77) (Fig. 45c). The samples of cassiterite from the Baimianshan deposit are characterized by high LREE/HREE (4.16-10.58) and δEu (0.66-1.21) values (Fig. 45d).

Table 21 REE contents (ppm) and some parameters in cassiterite and ores from the Xinlu ore field

Sample number	Locality	Object	La	Ce	Pr	Nd	Sm	Eu	Gd	Tb	Dy	Ho	Er	Tm	Yb	Lu	TREE	LREE/HREE	dEu	data source
No.21	Liuheao	skarn + cas. qtz. veins	44.97	83.41			6.46	0.88		0.84					2.18	0.38	198.96	9.50	0.46	1
No.1	Liuheao	cassiterite	0.38	0.95	0.30	0.35	0.18	0.03	0.46	0.05	0.20	0.04	0.10	0.04	0.20	0.09	3.37	1.86	0.38	2
No.4	Liuheao	cassiterite	0.97	2.51	0.34	1.30	0.56	0.06	0.73	0.15	0.67	0.14	0.04	0.09	0.85	0.22	8.63	1.99	0.33	
No.3	Shimen	cassiterite	0.78	1.73	0.24	0.90	0.23	0.03	0.24	0.05	0.16	0.03	0.06	0.02	0.08	0.04	4.58	5.77	0.36	3
No.2	Baimianshan	cassiterite	0.17	0.75	0.30	0.09	0.06	0.01	0.05	0.01	0.03	0.02	0.02	0.02	0.06	0.05	1.63	5.25	0.72	
S-2	Baimianshan	cas.-bearing sulfide	61.00	100.00	11.00	40.00	6.70	1.50	4.50	0.77	4.20	0.67	1.60	0.28	1.40	0.17	233.79	16.20	0.93	
S-3	Baimianshan	cas.-bearing sulfide	0.28	0.45	0.09	0.25	0.06	0.02	0.06	0.01	0.04	0.01	0.02	0.00	0.02	0.00	1.30	7.09	0.90	
S-4	Baimianshan	cassiterite	0.50	1.00	0.10	0.38	0.13	0.02	0.08	0.02	0.05	0.02	0.03	0.02	0.04	0.03	2.40	7.71	0.66	
S-5	Baimianshan	cassiterite	1.40	2.30	0.23	0.75	0.20	0.03	0.10	0.03	0.09	0.02	0.05	0.04	0.10	0.05	5.37	10.58	0.70	
S-6	Baimianshan	cassiterite	0.14	0.45	0.10	0.10	0.05	0.02	0.04	0.02	0.03	0.01	0.02	0.01	0.04	0.03	1.05	4.16	1.21	

Data sources: (1) this study, analysed by INAA at UQAC; (2) Dong (1989); (3) Qiu (1989)

The calculation of TREE, LREE/HREE and dEu for No.21 is explained in Appendix B

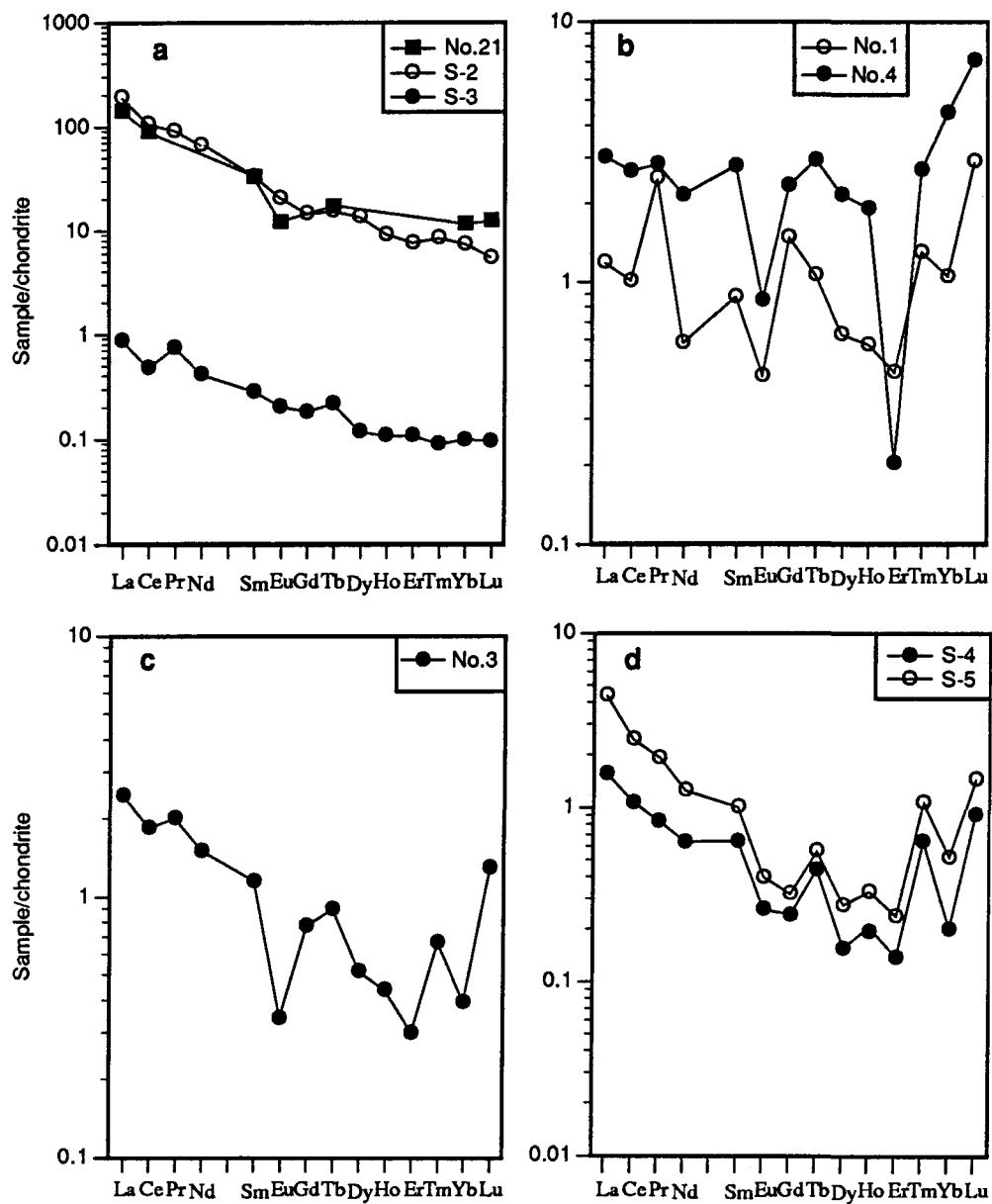


Fig. 45 REE patterns of ores (a), cassiterite from Liuhe'ao (b), cassiterite from Shimen (c) and cassiterite from Baimianshan (d).

A significant difference between the cassiterite from proximal deposit (Liuhe'ao) and distal deposit (Baimianshan and Shimen) is that the latter is much more LREE-enriched (LREE/HREE=4.16-10.58) than the former (LREE/HREE=1.86-1.99). Σ REE values are slightly higher in proximal cassiterite (3.37-8.63) than in distal one (1.05-5.37). Eu depletion is less strong in some distal cassiterite (Baimianshan) than in proximal cassiterite (Liuhe'ao), but is obvious for the other distal deposit (Shimen). These features probably indicate that some REE in the distal ore-forming fluids are derived from the country rocks, which are characterized by LREE enrichment and less Eu depletion, but can also be the results of differential stability of complexes between different rare earth elements during the ascent of ore-forming fluids. Taylor and Fryer (1982) pointed out that under low pH conditions the lightest REE are the most soluble along with Eu^{2+} , and that in simple chloride solutions the intermediate to heaviest REE are progressively less soluble, while in hydrothermal fluids containing active F^- and $\text{CO}_3^{=}$, the heaviest REE form complexes preferentially along with the lightest REE. Since the ore-forming fluids in the Xinlu ore field mainly belong to the $\text{H}_2\text{O}-\text{CO}_2-\text{NaCl}$ system (as indicated by fluid inclusion study, it can be expected that the distal ore-forming fluids were relatively rich in LREE over HREE, and the heaviest REE as well as Eu^{2+} were also relatively enriched, because these elements are more soluble and can be transported through a longer distance. This is in accordance with the REE patterns of the cassiterite from distal deposits, which are characterized by higher LREE/HREE (table 21), the enrichment of the lightest and heaviest REE (Fig. 45 c, d) and less depletion of Eu (table 21 and Fig. 45 c, d).

5.3 Fluid Inclusions

5.3.1 Selection of fluid inclusion samples

Fluid inclusion studies were carried out on proximal (Liuhe'ao) and distal deposits (Baimianshan, Shimen and Dongjia'ao) as well as on granites near the proximal ores (Liuhe'ao). This work includes fluid inclusion petrography and microthermometric measurement by using the U.S.G.S. gas-flow heating/freezing system. Primary fluid inclusions in cassiterite instead of quartz have been chosen, since it has been reported that the primary fluid inclusions in cassiterite and associated quartz which seems to have been formed at the same time have quite different compositions (Schwartz and Askury, 1989) and

that coexisting wolframite, cassiterite and quartz have systematically different Th and salinities (Campbell and Panter, 1990); for granites, quartz is chosen as the host mineral of fluid inclusions for study. Only large (mainly $>10\mu$) fluid inclusions in cassiterite were chosen for the study and many of them have negative crystal shape. Some are distributed along growth zones in cassiterite. None of the apparent secondary inclusions were used. It is believed that most of the inclusions studied in cassiterite are primary, thus ensuring that the majority of the fluid inclusions studied in the ores represent the ore-forming fluids. For fluid inclusions in quartz of granites, both primary inclusions in secondary quartz associated with hydrothermally altered granite and secondary inclusions in primary quartz were studied. These inclusions, although exhibiting complex interrelationship, represent the fluids that existed in the intrusion after the solidification of the magma. Melt inclusions and associated fluid inclusions, which represent the initial fluid derived from the magma, have also been examined.

5.3.2 Types and microthermometric features of fluid inclusions

The fluid inclusions in proximal and distal ores and granites can be divided into five types according to the composition and phase assemblage at room temperature and homogenization temperature. The major characteristics of each type are described as follows. The results of some microthermometric runs are listed in table 22, and the histograms of homogenization temperatures and density are shown in Fig. 46 and 47.

Type-I: Fluid inclusions containing a halite crystal, an aqueous phase and a bubble (plate 5A), without detectable CO_2 . The whole inclusion homogenizes to the liquid phase. Homogenization temperatures range from 220°C to 571°C (Fig. 46). The melting temperature of halite (halite melted before vapour bubble disappearance) ranges from 70 to 411°C . The salinity has been calculated (Potter et al., 1977) from the melting temperatures of halite and ranges from 27.24 to 47.08 wt% NaCl equiv.. The bulk densities of the inclusions are between 0.87 and 1.09 g/cm^3 (Fig. 47). The eutectic temperature of the aqueous phase ranges from -52.7 to -59.8°C , indicating the existence of Ca and other bivalent cations. This type of inclusion is mainly found in cassiterite from proximal ores and in quartz from granites near the contact zone.

Type-II: Fluid inclusions containing an aqueous phase and a relatively large bubble (50-80%, plate 5B, C), with detectable CO_2 (1.3--14.2 mole%, calculated by the $\text{H}_2\text{O}-\text{CO}_2$

Table 22 Microthermometric measurements of some fluid inclusions in cassiterite and granites from the Xinlu ore field and Dongjia'ao deposit

Occurrence	Sample number	run	type	vapor ratio at 25oC	solid ratio at 25oC	Tm CO2	Th CO2	Tm1st	Tm NaCl	Tm NaCl.2H2O	Tm H2O	Th	NaCl eqv. (wt%)	bulk density (g/cm3)	CO2 (mole%)	
proximal ores (cassiterite)	No.24	a	I	0.30	0.10			-57.3	127		-27.9	429.5 (L)	28.84	0.87		
		b	I	0.30	0.05			-59.8	313		-30.1	358.6 (L)	38.86	1.04		
		c	II	0.80		-60.6	20.6 (V)						350.0 (V)		0.36	24.66
		d	IV	0.50				-56.6		-32.3	-20.2	431.2 (L)	22.80	0.80		
	No.25	a	IV	0.25					-59.8		-29.0	-19.2	427.0 (L)	22.10	0.80	
		b	I	0.25	0.05			-57.0	285			-30.4	425.7 (L)	36.88	0.95	
		c	I	0.30	0.25			-58.8	314			-29.2	398.2 (L)	38.93	1.00	
		d	I	0.30	0.20			-57.7	291			-28.1	369.4 (L)	37.29	1.01	
		e	I	0.20	0.20			-54.3	275			-35.5	426.9 (L)	36.21	0.94	
		f	I	0.20	0.20			-55.6	331			-24.0	415.2 (L)	40.21	1.00	
		g	I	0.15	0.05			-56.4	70			-34.9	347.3 (L)	27.24	0.94	
		h	I	0.20	0.05			-52.7	182			-30.8	362.9 (L)	31.04	0.96	
		i	I	0.40	0.10			-56.4	232			-42.1	353.3 (L)	33.59	0.99	
		j	I	0.30	0.05			-54.6	383			-29.4	411.0 (L)	47.08	1.09	
		k	I	0.40	0.05			-57.0	136			-27.0	392.1 (L)	29.16	0.91	
		l	I	0.35	0.10			-56.3	163			-34.4	440.0 (L)	30.21	0.87	
		m	I	0.25	0.05			-52.5	329				479.0 (L)	40.06	0.99	
		n	II	0.80		-64.3	8.8 (V)						400.7 (V)		0.30	17.50
	No.302	a	III	0.40	0.03	-56.2	-22.0 (L)	-66.4	189			-24.6	398.0 (L)	31.37	1.36	21.60
	granite near contact zone (quartz)	CX071	a	II	0.70		-57.5	29.9 (L)					447.0 (C)		0.72	36.50
CX072		a	II	0.60		-62.2	28.9 (L)	-54.3			-13.0	364.7 (V)	17.00	0.78	28.10	
CX004		a	I	0.35	0.05			-54.8	234			-20.8	330.0 (L)	33.71	1.02	
		b	I	0.30	0.05				221				448.0 (L)	32.99	0.99	
		c	II	0.80		-62.1	24.8 (V)						335.2 (V)		0.39	28.30
		d	II	0.50		-60.4	29.6 (V)	-55.7				-18.5	371.2 (C)	19.77	0.66	11.90
		e	II	0.90		-59.2	28.2 (V)						350.0 (V)		0.37	52.50
		f	II	0.80		-61.9	18.7 (L)						380.0 (V)		0.83	56.40
		g	III	0.30	0.05	-59.2	-6.7 (L)	-54.5	260			-21.6	425.0 (L)	35.26	1.29	10.40
		h	III	0.35	0.03	-60.2	-4.9 (L)	-60.2	244			-23.6	394.9 (L)	34.29	1.33	11.90
i		III	0.35	0.05	-61.8	9.5 (V)		201				330.0 (L)	31.93	1.05	1.96	
distal deposit (cassiterite)		XQ132	a	II	0.60		-73.2	16.0 (L)	-58.0			-26.7	349.3 (C)		0.89	33.30
			b	II	0.65		-70.7	16.0 (V)					335.1 (C)		0.46	11.30
			c	II	0.60		-72.2	-46.0 (V)						336.7 (C)		0.41
	d		II	0.60		-67.7	-6.0 (V)						360.4 (C)		0.45	4.70
	e		II	0.70		-67.9	-36.0 (V)						340.0 (C)		0.32	2.80
	f		II	0.50		-73.8	11.0 (V)						334.0 (C)		0.57	5.40
	g		V	0.40		-73.2	-5.0 (V)						262.0 (L)		0.63	2.20
	h		V	0.40		-65.2	2.0 (V)	-51.8		-23.3	-12.9	312.8 (L)	16.90	0.64	2.80	
	i	II	0.80		-64.6	-7.0 (V)					-14.8	341.0 (C)	18.60	0.26	11.40	
	No.28	a	V	0.40		-56.3	-19.0 (V)	-61.8		-29.7	-15.1	412.9 (L)	18.85	0.62	1.40	
		b	II	0.80		-58.8	1.0 (V)	-61.5		-28.1	-11.5	366.2 (C)	15.55	0.28	14.20	
		c	V	0.40		-56.9	-15.0 (V)	-63.1		-28.1	-7.2	405.4 (L)	10.77	0.62	1.60	
		d	II	0.50		-60.0	-18.0 (V)	-64.1		-25.6	-14.3	366.9 (C)	18.18	0.53	2.20	
		e	II	0.50		-58.0	-15.0 (V)	-58.8		-25.5	-12.0	393.2 (V)	16.03	0.53	2.40	
f		II	0.50		-60.0	1.0 (V)	-53.0		-25.9	-8.8	366.0 (C)	12.65	0.55	4.00		
CX035	a	II	0.50		-57.6	7.0 (V)						330.3 (C)		0.56	4.80	
	b	II	0.60		-58.3	7.0 (V)						329.5 (C)		0.47	7.00	
	c	II	0.50		-57.5	7.0 (V)						330.0 (C)		0.56	4.80	

Notes: Vapour ratio and solid ratio are estimated at 25oC; TmCO2--the melting temperature of CO2; ThCO2--the homogenization temperature of liquid and vapour CO2 (V-homogenized to vapour; L- homogenized to liquid); Tm1st--first melting temperature in the aqueous phase; TmNaCl--the melting temperature of NaCl; TmNaCl.2H2O--the melting temperature of hydrohalite; TmH2O--the melting temperature of ice; Th--the homogenization temperature of the bulb with the fluid inclusion (L-homogenized to liquid; V-homogenized to vapour; C-critical); NaCl eqv.--total salinity equivalent to NaCl (calculated according to the formula provided by Potter et al., 1977 and Roedder,1984 a). Bulk density and CO2 (mole%) are calculated by FLINCOR (Brown, 1989).

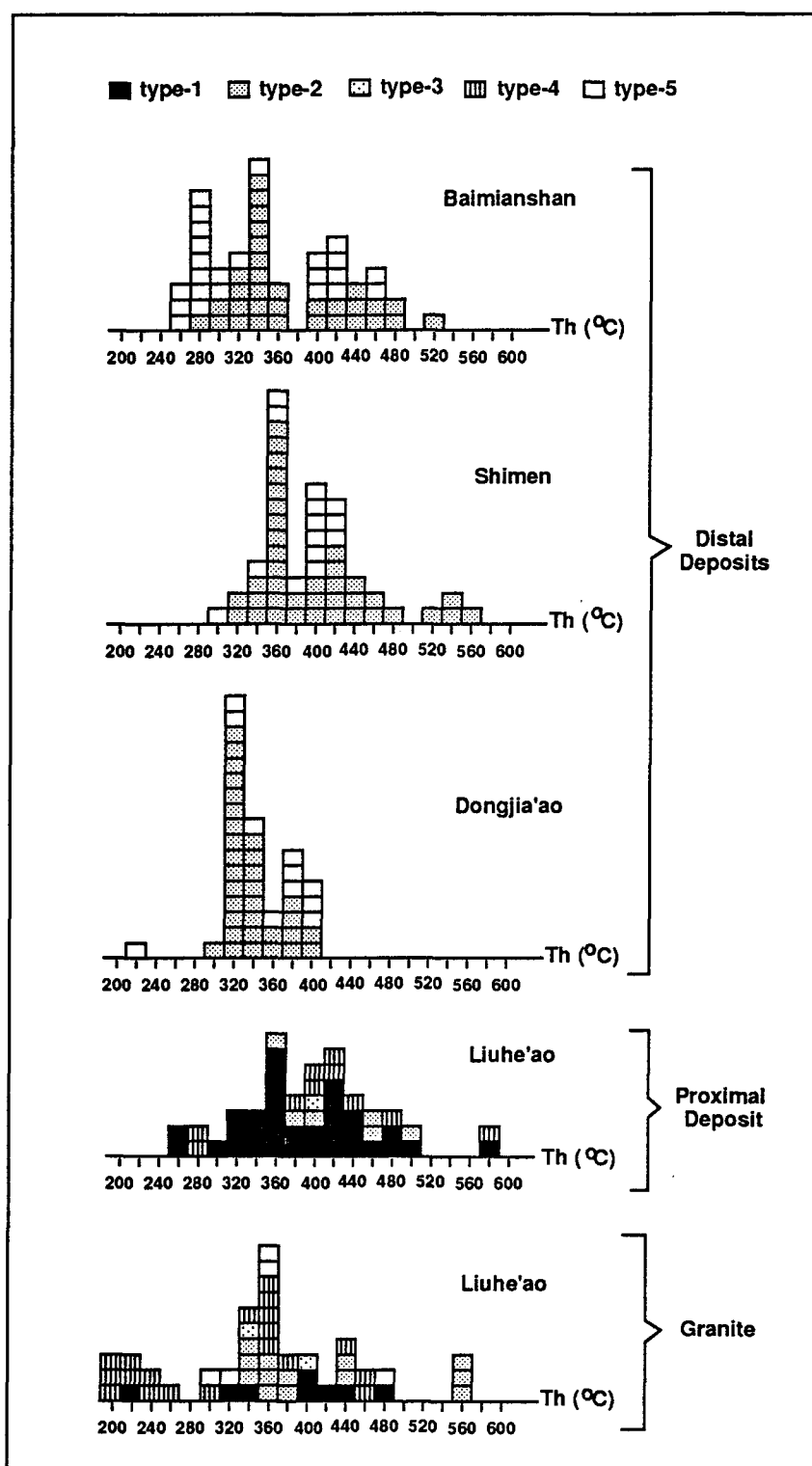


Fig. 46 Histograms of homogenization temperatures of fluid inclusions in cassiterite from proximal and distal deposits and in quartz from granite associated with the proximal deposit in the Xinlu ore field. The types of fluid inclusions shown on the figure are the same as explained in the text.

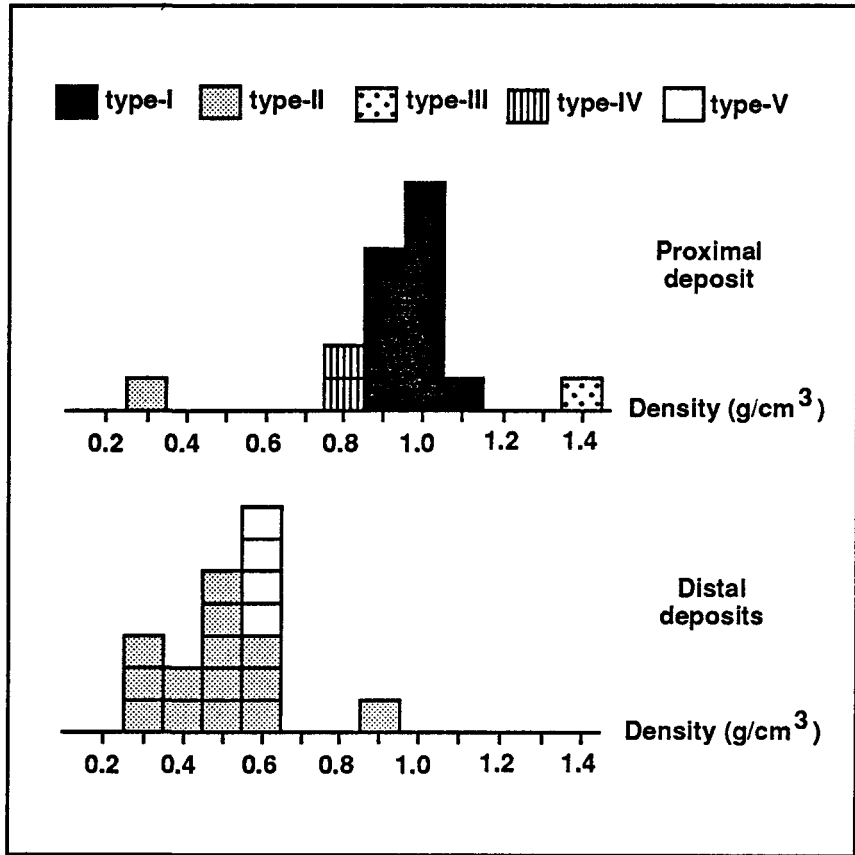


Fig. 47 Histograms of density of fluid inclusions in cassiterite from proximal and distal deposits. The types shown on the figure are the same as explained in the text.

system in the FLINCOR program of Brown, 1989); the whole inclusion homogenizes to the vapour phase or by fading of the meniscus between liquid and vapour (critical). Homogenization temperatures range from 275 to 564 °C (Fig. 46). In some inclusions, the presence of other solutes in addition to NaCl are indicated by eutectic temperatures (between -51.8 and -64.1 °C). Melting temperatures of liquid CO₂ range from -57.5 to -64.3 °C (generally higher than -60 °C) for inclusions from Liuhe'ao and Shimen, but range from -64.6 to -73.8 °C for those from Baimianshan. This indicates the presence of other gases besides CO₂, but not identifiable by the microthermometric method. The melting temperature of ice was determined for a few inclusions (-8.8 to -18.5 °C), which yielded salinity values between 12.65 and 19.77 wt% NaCl equiv.. These values are higher than true salinity due to the effect of CO₂ (and other gases) hydrates which takes up H₂O from the liquid (Collins, 1979). Clathrate melting temperatures were measured for some type II and V inclusions. However, these inclusions have very low CO₂ density so that the clathrate is not coexistent with liquid CO₂+gas CO₂+solution at the temperature of melting, which makes it difficult to use the clathrate melting temperatures to calculate salinity. Moreover, some inclusions have clathrate melting temperatures >10 °C, indicating that the vapour in the bubble is not pure CO₂. An indirect method has been used to estimate the "true salinity" of some inclusions from distal deposits showing critical behaviour by using the concentration of CO₂ (mole%) and recalculating from the H₂O combined to form the clathrate (H₂O.5.75CO₂). One inclusion from Baimianshan shows a "true salinity" of 12.6 wt% NaCl equiv., and three inclusions from Shimen indicates "true salinities" of 10.6, 10.9 and 16.5 wt% NaCl equiv.. These values represent the salinities of the homogeneous distal ore-forming fluids. The densities of type-II inclusions are generally lower than those of type-I inclusions, ranging from 0.26 to 0.89 g/cm³ (Fig. 47). This type of inclusions is mainly observed in distal ores, but also occurs in proximal cassiterite and in quartz in granites.

Type-III: Fluid inclusions containing a halite crystal, an aqueous phase and a bubble (plate 5D), with detectable CO₂ (1.4--2.8 mole%); the whole inclusion homogenizes to the liquid phase. Homogenization temperature ranges from 330 to 399 °C (Fig. 46). The first melting temperature in the aqueous phase was observed between -54.5 and -66.4 °C. The melting temperature of liquid CO₂ is between -56.2 and -61.8 °C. Bulk densities are between 1.05 and 1.36 g/cm³ (Fig. 47). This type of inclusion is observed only rarely in the granite and proximal ores.

Type-IV: Fluid inclusions containing an aqueous phase and a bubble (plate 5E), without halite or detectable CO₂. The whole inclusion homogenizes to the liquid phase. Homogenization temperatures range from 197 to 584 °C (Fig. 46). The first melting temperature in the aqueous phase was observed between -56.6 and -59.8 °C. Salinities range from 22.1 to 22.8 wt% NaCl equiv. Densities are about 0.8 g/cm³ (Fig. 47). This type of inclusions is similar to type-I except that it does not contain halite at room temperature. It is mainly found in proximal ores and granite.

Type-V: Fluid inclusions containing an aqueous phase and a bubble (plate 5F), with measurable liquid CO₂ (1.4--2.8 mole%, calculated by the H₂O-CO₂ system in the FLINCOR program of Brown, 1989); the whole inclusion homogenizes to the liquid phase. Homogenization temperatures range from 260 to 475 °C (Fig. 46). The first melting temperature in the aqueous phase was observed between -51.8 and -63.1 °C. The melting temperature of liquid CO₂ is between -56.3 and -56.9 °C for inclusions from Shimen and between -65.2 and -73.2 °C for inclusions from Baimianshan. Ice melting temperatures range from -7.2 to -15.1 °C, which yielded apparent salinity values between 10.8 and 18.9 wt% NaCl equiv. Bulk densities range from 0.62 to 0.64 g/cm³ (Fig. 47). This type of inclusion is similar to type-II except that its bubble is smaller and homogenizes to the liquid phase. For a pair of type-II and type-V inclusions closely associated in a cassiterite from Shimen, the apparent salinities are 16.0 and 18.9 wt% NaCl equiv. respectively. The composition of type-II and type-V inclusions is very similar. Type-V inclusions are mainly found in distal ores and granites.

A few melt inclusions were observed in quartz in the granite associated with the proximal ores. They contain silicate minerals and a dark bubble (plate 6A and B). A group of fluid inclusions usually surround the melt inclusion. These fluid inclusions belong to types-I, II and IV. Homogenization temperatures range from 220 to 324 °C. Some of these fluid inclusions are distributed in arrays which radiate from the melt inclusion, probably indicating that they were derived from the melt inclusion in the process of crystallization of the melt inclusion. Thus the initial fluid derived from the granite is probably composed of H₂O, CO₂ and NaCl (including bivalent cations such as Ca²⁺).

5.3.3 Association of fluid inclusions and phase separation

The association of these five types of fluid inclusions varies from one ore type to another. In the proximal ores, type-I, -II, -III and -IV fluid inclusions are present, and have the same range of homogenization temperatures, but type-I and type-IV fluid inclusions are more abundant than the other types. A pair of Type-I and type-II inclusions were observed to coexist in the same cassiterite crystal in very close proximity (plate 6D and E) and with similar homogenization temperature (400.7°C for the type-I inclusion and 392.1°C for the type-II inclusion). It is likely that a phase separation event took place at the contact zone and divided the initial $\text{H}_2\text{O}-\text{CO}_2-\text{NaCl}-(\text{CaCl}_2)$ one phase fluid into two phases: a liquid phase rich in H_2O and NaCl (represented by type-I and type-IV) and a vapor phase rich in H_2O and CO_2 (represented by type-II). In the distal ores, type-II and type-V fluid inclusions generally coexist in the same cassiterite crystal, and have the same range of homogenization temperatures. Some type-II and type-V inclusions were observed in the same growth zone of a cassiterite crystal (plate 6C). It is possible that these two types of inclusions were derived from the same fluid containing two phases: a liquid phase and a vapour phase, and that there had been a phase separation event. The fact that these two types of fluid inclusions have quite similar composition and that many of the type-II fluid inclusions have critical homogenization behaviour implies that the phase separation condition (T-P) is very close to the critical point of the fluid system. In the granite associated with proximal ores, all the five types of fluid inclusions exist (plate 6F), and have about the same range of homogenization temperatures except that those of type-IV are slightly lower. Although the association of different types of inclusions in the granite is complicated because both primary and secondary quartz exists and the generations of the inclusions are not easily distinguished, it is possible to conclude from the fluid inclusion data that phase separation occurred at the margin of the intrusion at some stage of solidification of the magma.

Phase separation is likely a major mechanism of ore deposition for the proximal deposits, and may have also played a role in the deposition of the distal deposits. Phase separation has been proven to be a major process responsible for the deposition of a variety of hydrothermal deposits (e.g. Kelly and Turneure, 1970; Kamilli and Ohmoto, 1977; Barton et al., 1977, and Cunningham, 1978), and cassiterite is one of the minerals which are most likely to deposit from boiling hydrothermal solutions (Drummond and Ohmoto, 1985). This is related to the fact that phase separation results in exsolution of CO_2 and other

gases and increase in pH values in the liquid phase, and the increase in pH values has been shown by many authors (e.g. Jackson and Helgeson, 1985; Wilson and Eugster, 1990) to be an effective cause of cassiterite deposition.

Because cassiterite precipitation is sensitive to phase separation, it is reasonable to assume that ore deposition took place at the same site as or not far from the onset of phase separation. The vertical distance of two-phase flow without significant precipitation of cassiterite is considered to be small. Similar reasoning or observation has been made elsewhere. In the Boss Mountain molybdenite deposit, British Columbia, for example, it was observed that the development of MoS₂ in veins and breccia pipes coincides spatially with the onset of CO₂ effervescence at the 4440' elevation (Macdonald, 1983).

5.3.4 Systematics of composition, temperature and pressure of proximal versus distal fluids

The chemical system of the fluid inclusions can be circumscribed by H₂O-CO₂-NaCl-CaCl₂. For type-I and -IV fluid inclusions, CO₂ is not detected, and the composition can be shown on a H₂O-NaCl-CaCl₂ diagram (Fig. 48) using the method described by Williams-Jones and Samson (1990). For type-II, -III and -V inclusions, the aqueous phase (and halite in type-III) is treated as a H₂O-NaCl-CaCl₂ system and can also be shown on Fig. 48, although the data points should be closer to H₂O than where they are because of the effect of CO₂ hydrate. Chemical analyses of fluid inclusions from the Baimianshan deposit by Shong (1984) and Deng (1984) also indicate that the ore-forming fluid is rich in Ca²⁺, and F⁻ is present besides Cl⁻. One remarkable feature in the H₂O-NaCl-CaCl₂ diagram is that the inclusions from the granites contain less CaCl₂ than those from the proximal and distal deposits, probably indicating that some Ca in the ore-forming fluids is derived from the country rocks, because the country rocks (mainly carbonates) are richer in Ca than the granites.

The salinities of the distal ore-forming fluids before phase separation, estimated from inclusions showing critical behaviour, are from 10.6 to 16.5 wt% NaCl equiv.. These salinity values are believed to be lower than those of the proximal ore-forming fluids before phase separation, which lie at a point between the salinities of the vapour phase and the liquid phase. If the salinity of the proximal fluid before phase separation is assumed to be 22.1 wt% NaCl equiv. (this is the minimum salinity of the liquid phase after phase

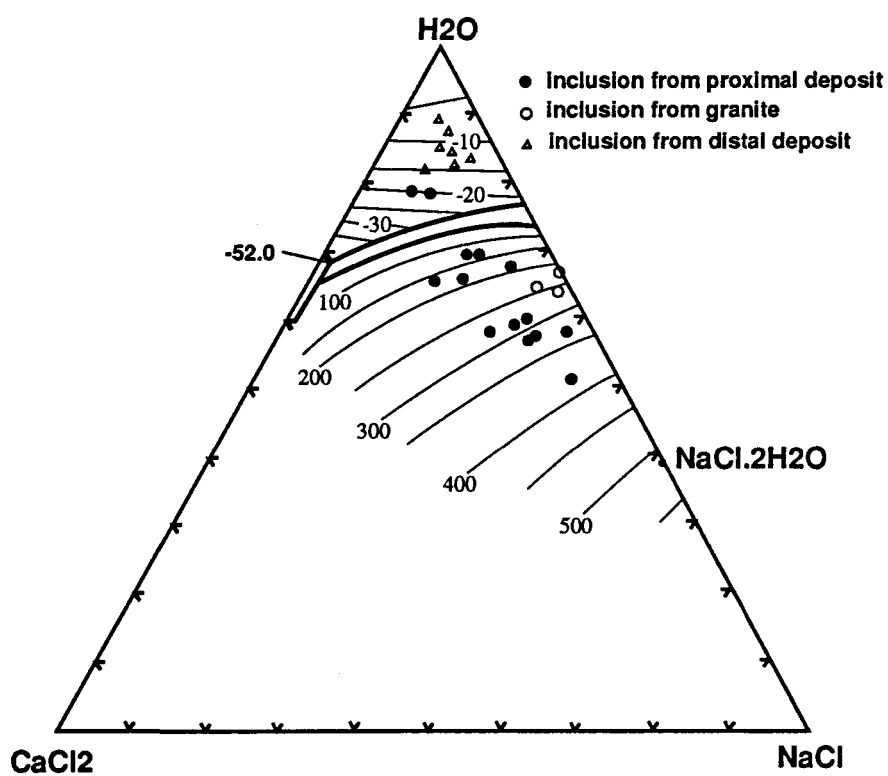


Fig. 48 Composition of fluid inclusions from proximal deposits, granites and distal deposits plotted on a H₂O-NaCl-CaCl₂ diagram. The isotherms are compiled from Sheets et al. (1990), Oakes et al. (1990) and Vanco et al. (1988).

separation, and is the maximum value for the fluid before phase separation), and that of the meteoric water is assumed to be zero, a maximum proportion of meteoric water in the distal ore-forming fluids is estimated to be about 43%. As a minimum proportion of meteoric water in the distal ore-forming fluids has been estimated to be about 14.6% (average) for Baimianshan and 11.7% (average) for Shimen from O isotopic data, the proportion of meteoric water may be between 11.7% and 43%.

The ranges of homogenization temperatures of fluid inclusions are compared between different deposits in Xinlu (Fig. 46). The values are mainly between 280 and 460 °C for the Baimianshan deposit, 320 and 460 °C for the Shimen deposit, 320 and 500 °C for the Liuhe'ao deposit. The temperature of the distal ore-forming fluids is apparently only slightly lower than that of the proximal ones (Fig. 46), possibly indicating very small temperature gradients in the hydrothermal systems.

Isochores (Fig. 49) were calculated by using the computer program FLINCOR of Brown (1989). Type-I and type-IV inclusions were treated using the H₂O-NaCl system. Type-III inclusions were not calculated due to their rarity. For type-II and type-V inclusions, the H₂O-CO₂ system was used because of the uncertainty of the other gases and the true salinities. The errors caused by the presence of other gases in the CO₂ vapour might be relatively small, because densities of the vapour are generally small (as indicated by inclusions with relatively pure CO₂), and the slope of isochores is relatively small (especially in the 300 to 400 °C interval, Fig. 49). The errors caused by computing 12.3 wt% NaCl equiv. in the aqueous phase depend on the choice of equations of state: for the equations of Brown and Lamb (1989), the errors may be as large as a few Kb, but for the equations of Bowers and Helgeson (1983), the errors are generally smaller than 200 bars. As the equations of Brown and Lamb (1989) yield the highest values of pressure among all the equations of state proposed by various authors listed in the FLINCOR program, and not considering the presence of salt and other gases that tend to decrease the pressures, the use of the equations of state of Brown and Lamb (1989) for both H₂O-CO₂ and H₂O-NaCl systems has been preferred in this study.

The fluid pressure corresponding to the homogenization temperature is shown by open squares on figure 49. This pressure is considered to represent the fluid pressure during the mineralizing episode. The calculated pressures range from 469 to 630 bars for the Baimianshan deposit, from 446 to 792 bars for the Shimen deposit, from 148 to 404 bars for the Liuhe'ao deposit, and from 124 to 2303 bars for the granites at Liuhe'ao (Fig. 49).

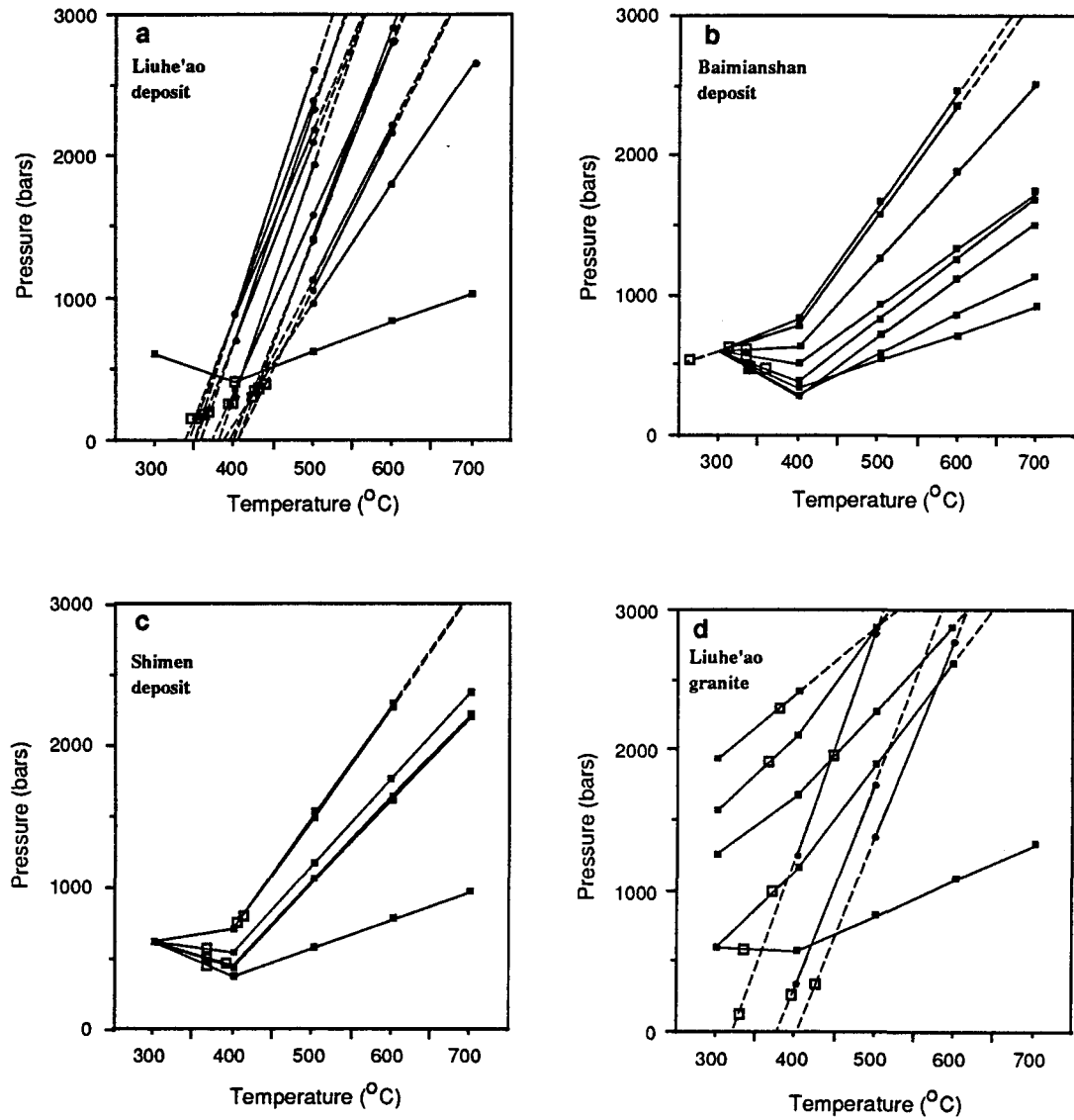


Fig. 49 Isochores of fluid inclusions from : (a) the proximal deposit at Liuhe'ao; (b) the distal deposit at Baimianshan; (c) the distal deposit at Shimen; (d) the granite associated with the proximal deposit at Liuhe'ao. Solid lines represent the isochores within the calculated values by the program FLINCOR, and dash lines represent the isochores inferred from the calculated values. Black points are H₂O-NaCl system, black squares are H₂O-CO₂ system, and open squares indicate temperature and pressure at homogenization temperature.

These pressure values are a broad estimate of the fluid pressures, considering the uncertainties of fluid composition and the differences between equations of state by different authors. According to the stratigraphic data of the region (No.204 Geol. Team of Guangxi, 1986), the maximum thickness of the strata above the deposits is between 2600 and 3900 metres. Considering the effect of tectonic shortening and thickening caused by the Mesozoic Indo-Sinian movements which predated the mineralization, a thickness of 3900 metres is adopted for the cover above the level of distal deposits and proximal deposits at the time of ore formation. At this depth, the hydrostatic pressure is 382 bars (for a water density of 1 g/cm³), and the lithostatic pressure is 1032 bars (for a rock density of 2.7 g/cm³). Therefore, the pressure of the ore-forming fluids is between hydrostatic and lithostatic, but is closer to the former, at the site of ore deposition. The pressure of the fluids in the intrusion varies from <hydrostatic to >lithostatic, probably because of the fluctuation of pressure systems in the intrusion. The pressure which is larger than lithostatic pressure is probably due to the overpressure caused by the exsolution of hydrous liquids from the magma (Burnham, 1979). Therefore, a fluid pressure contrast may have existed between the fluids within the intrusions and those in the conduits and the contact zone outside the intrusion.

5.4 The Generation Processes of the Ore-forming Fluids

From the studies of the ore-forming potential of host rocks and the geochemical characteristics of the ores, it is clear that the majority of the ore-forming fluids is derived from the granite intrusions, and some ore-forming components may be extracted from the country rocks.

Granite intrusions as a major source of ore-forming fluids of both proximal and distal deposits are supported by (1) the predominantly restrained and close-to-zero characteristics of $\delta^{34}\text{S}$ values of the ore minerals from most of the deposits S, which is comparable with typical magmatic hydrothermal deposits; (2) the $\delta^{18}\text{O}$ values of ore-forming fluids which are only slightly lower than magmatic water; (3) the Pb isotopes which yield model ages identical or only slightly younger than late-stage granite intrusions; (4) the REE patterns of cassiterite which is characterized by obvious Eu depletion (Liuhe'ao and Shimen), a feature typical of the late-stage granites, and (5) the high ore-forming potential of the granites, esp. the late-stage granites, relative to the sedimentary rocks and dykes.

Once the source of the ore-forming fluids is determined, a further question is how the ore-forming elements are extracted from the source. This includes magma-fluid segregation in the late magmatic stage and hydrothermal fluid-granite rock interaction in the post-magmatic stage for the generation of the majority of the ore-forming material, and fluid-rock interaction for the extraction of some ore-forming components from the sedimentary rocks and dykes. REE patterns may be used to trace these processes to some extent. Since the cassiterite from the proximal deposit (Liuhe'ao) has similar REE pattern (except for Σ REE) to that of the latest granite intrusion, characterized by small δ Eu and LREE/HREE values, it is supposed that the original ore-forming fluid derived from melt-fluid segregation inherits the REE pattern from the melt. This pattern will be modified if there is incorporation of fluids from later water-rock interaction, which is characterized by Eu and HREE depletion in the altered rocks and relative Eu and HREE enrichment in the fluids thus generated. Three pairs of altered-unaltered samples of granites, sedimentary rocks and dykes are analysed for REE and some ore elements. The results are listed in table 23, and the REE patterns are illustrated in Fig. 50. It is shown that the altered granite (No.306), dyke (No.314) and limestone (No.315-1) have smaller δ Eu' values than correspondent unaltered granite (No.305-2), dyke (BK193-1-1) and limestone (No.315-1). LREE'/HREE' decreases from unaltered granite (No.305-2) to altered granite (No.306). A decrease of ore-forming elements such as Sn, Zn and Cl is also observed from unaltered sample to altered sample. Therefore, the slight increase of δ Eu and decrease of LREE/HREE values in proximal cassiterite relative to phase III granite in Liuhe'ao probably indicate that fluid-rock interaction in the post-magmatic stage may have contributed some ore-forming elements to the ore-forming fluids, which is originally generated by melt-fluid segregation. The increase of δ Eu and LREE/HREE values in distal cassiterite may also reflect the incorporation of ore-forming components released by sedimentary rock-fluid or dyke-fluid interaction, but the extent of this incorporation is likely to be low.

Table 23 Comparison of REE and some ore element content in altered and unaltered rock pairs (ppm) from the Xinlu ore field.

Pairs	Sample No.	Rock type	La	Ce	Sm	Eu	Tb	Yb	Lu	TREE'	LREE/ HREE'	dEu'	Sn	Zn	F	Cl
1	No.305-2	unaltered granite	22.04	57.34	9.90	0.54	2.37	8.86	1.57	188.20	2.29	0.15	4.5	28.1	408	120
	No.306	altered granite	20.38	58.02	10.09	0.26	2.57	10.76	1.81	193.30	2.01	0.07	2.2	16.8	2360	61
2	BK193-1-1	unaltered dyke	53.73	103.50	7.59	1.85	1.02	2.55	0.44	241.90	9.60	0.82	230.0	872.0	2240	407
	No.314	altered dyke	79.98	142.70	7.88	1.50	0.81	2.93	0.56	317.00	14.07	0.70	220.0	433.3	1200	36
3	No.315-2	unleached limestone	1.43	2.00	0.20	0.16		0.06	0.01	5.80	8.35	2.60	3.8	16.3	33	39
	No.315-1	leached limestone	1.03	1.30	0.15	0.12		0.05	0.01	4.11	7.44	2.53	1.8	5.8	28	5

* REE and Zn are analysed by INAA at UQAC, Sn, F and Cl are analysed at HIAMP.

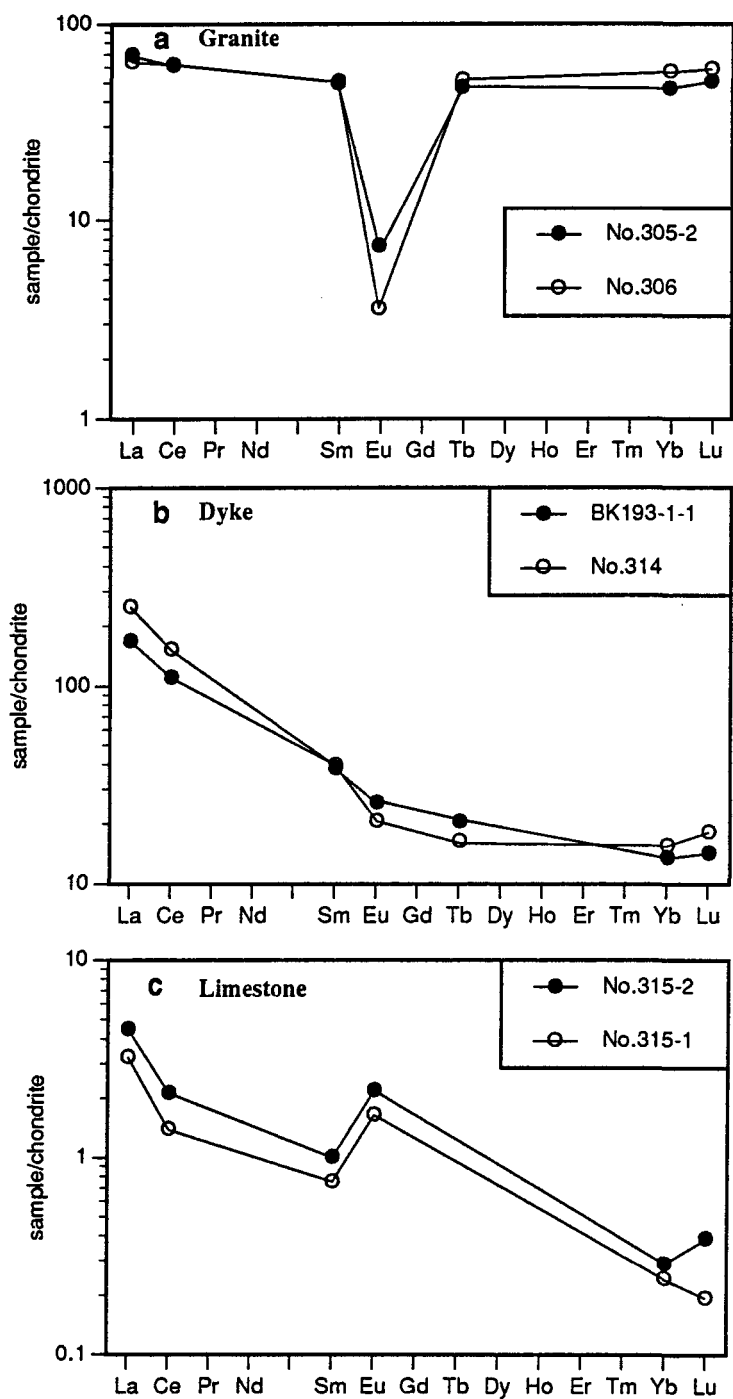


Fig. 50 Comparison of REE patterns between altered and unaltered granites (a), dykes (b) and limestone (c) from the Xinlu ore field (data from table 23).

CHAPTER VI

DYNAMICS OF THE MIGRATION OF THE ORE-FORMING FLUIDS

6.1 Introduction

It has been shown in the previous chapters that the ore-forming fluids of both proximal and distal deposits in the Xinlu ore field are principally derived from the magmatic intrusions. Therefore, the separation of proximal and distal deposits does not appear to be controlled by a difference in the source of ore-forming fluids. Although a zoning pattern of REE--Nb, Ta--W--Sn, W, Cu, Bi--Sn, Cu, Pb, Zn--Sn, Au--Pb, Zn from within the intrusion to the country rocks has been proposed by Shan (1987) for the polymetallic ore fields around the Guposhan batholith, the ore mineral assemblages of proximal and distal ores in the Xinlu ore field are hardly distinguishable. Both proximal and distal ores are mainly composed of pyrrhotite, sphalerite, pyrite, arsenopyrite, chalcopyrite, galena, cassiterite, marcasite and scheelite. Therefore, the separation of proximal and distal deposits does not seem to be the effect of metal zonation either. The localization of proximal and distal deposits must have been controlled by other factors, among which the fluid dynamics of the ore-forming fluids and the depositional condition play a most critical role. In this chapter, the dynamic aspects of the ore-forming fluids are discussed.

6.2 The System of Conduits

One of the necessary conditions for the separation of distal deposits from proximal ones is the existence of conduits linking the sources of the ore-forming fluids to the favourable distal sites of deposition. In homogeneous media, the fluid flow pattern is controlled by the shape of intrusion. Since the major lithology in the Xinlu ore field is carbonate, whose permeability is generally low, ore-forming fluid flows are in fact mainly constrained in the segments where the permeability is much higher than the adjoining blocks. The conduits in the Xinlu ore field can be divided into two systems: the vertical or subvertical system and the horizontal or subhorizontal system, the former being represented by faults,

fractures, dyke walls and parts of contact of granite, the latter being represented by bedding planes and interlayer fractures of the sedimentary rocks (see Fig. 11).

The ore-forming fluids expelled from the granite intrusion were mainly conducted along the vertical system, because the fluid flow tendency in the horizontal system is toward the intrusion instead of away from the intrusion due to the density decrease of the fluid near the intrusion (Norton and Cathles, 1979). On the other hand, the incorporation of ore-forming components from the sedimentary rocks is more likely to come from the horizontal system, in which the fluids have more contact with the sedimentary rocks.

The vertical conduit system is mainly controlled by fractures and faults in the country rocks. Not all the fractures and faults in the country rocks are suitable as conduits of ore-forming fluids. There are two important aspects concerning the validity of conduits for mineralization: one is that the conduits must be connected to the major source of the ore-forming fluids, and the other is that they must be active (having high permeability) during ore-forming fluid activity. The structures which may meet these two demands can be either magmatic intrusion-generated fractures or intrusion-reactivated pre-existent fractures and faults, as is also the case in the vein and dyke systems of the S.W. England (Moore, 1975). Pre-existent structures may be more important than intrusion-generated ones, because before the intrusion of the Guposhan batholith the Xinlu ore field had experienced strong tectonic movement (Indo-Sinian), which developed the structural framework in the sedimentary rocks. The reactivation of these pre-existent structures is easier than the generation of new fractures under the stress field of magmatic intrusion.

Both newly-generated and reactivated pre-existent structures associated with granitic intrusion can be filled by dykes. The fact that most of the dykes are genetically related to the granites enhances the possibility that the dyke-controlling structures are connected to the major source of the ore-forming fluids and retain high permeability during mineralization, and are thus most likely to be used as conduits. This is supported by the observation that the distribution of most distal deposits in the Xinlu ore field and adjoining ore fields surrounding the Guposhan batholith are closely related to the dykes. The orientation of the dykes in a radial pattern around the Guposhan batholith (Fig. 51) indicates that the intrusion of the dykes are controlled by the granite intrusions. The deviation of dyke orientation from this pattern in the Xinlu ore field may result from the influence of pre-existent structures and the local bay-like shape of the intrusion (Fig. 52). The W-E orientation of dykes in the central part of the Xinlu ore field is consistent with the compression imposed by the granite

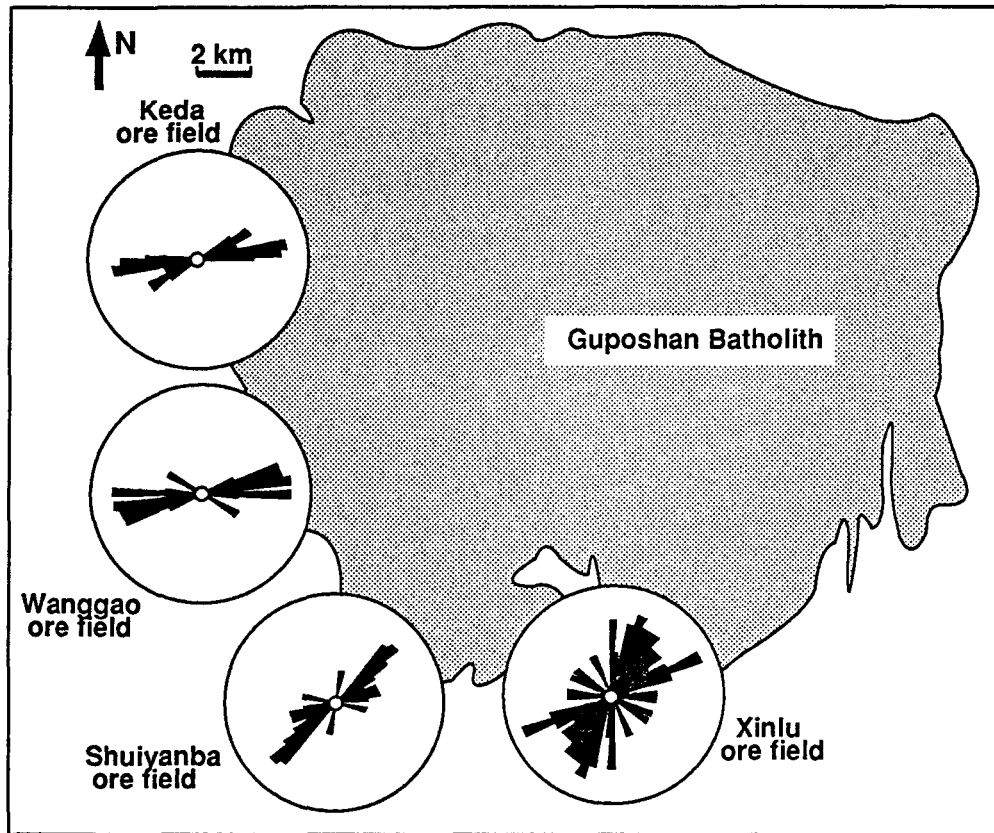


Fig. 51 Rose diagrams showing the radial orientation of the dykes in the four dyke intrusion centres which correspond to the four tin-polymetallic ore fields surrounding the Guposhan batholith (the dykes in the central and northern part of the Xinlu ore field are not included).

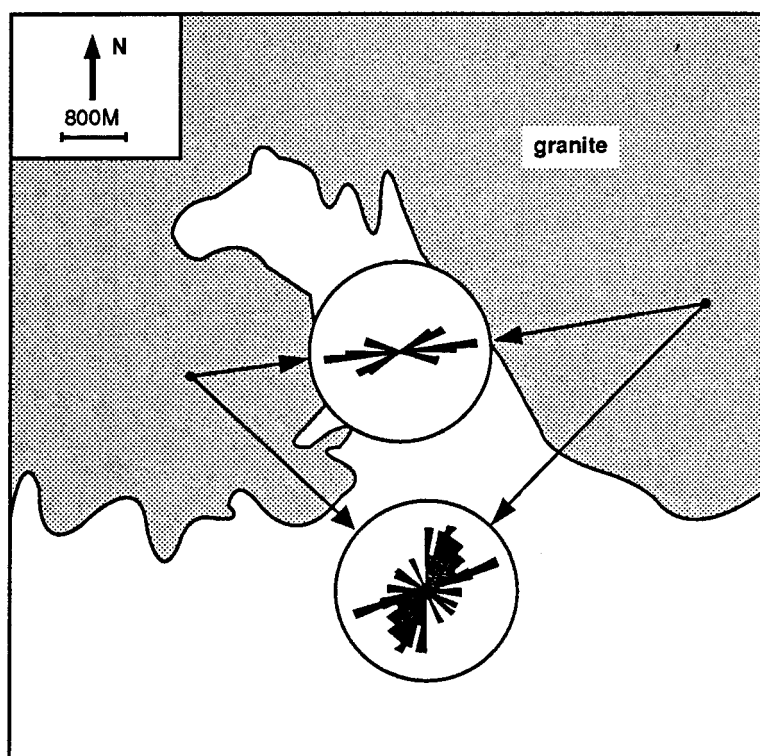


fig. 52 Rose diagrams showing the orientation of dykes in the central and southern parts of the Xinlu ore field in relation to the local geometry of the granite intrusions.

intrusion from the western and eastern sides (Fig. 52). Therefore, the dyke-controlling structures are generally consistent with the principal compressive stress generated by granite intrusions, which greatly promotes the extension of the structures.

Pre-existent structures that are not along the principal compressive stress may exhibit variable structural effect during the reactivation caused by intrusion, depending on their geometric position with respect to the intrusion. Since the Xinlu ore field has a NW-trending bay-like shape and the depth of intrusion is smaller in the northern part than in the southern part, the spatial relationship between NNW-NS-trending pre-existent faults, which are the major fault system in the Xinlu ore field, and the intrusion, is variable along the strike of the faults, and a rotational movement can be expected. This is best illustrated by the No.2 fault in the Baimianshan deposit. This is a nearly N-S trending fault (Fig. 53a) with the expression of a normal fault (Fig. 16). Structural analysis shows that it was formed as a reverse fault during Indo-Sinian movement, more than 50 Ma before the intrusion of the Guposhan batholith (Xie, 1989). The expression of normal fault is most likely to be caused by the intrusion of the Guposhan batholith. The displacement is different along the strike, increasing from south to north toward the intrusion (Fig. 53b). This is possibly the reflection of rotation movement caused by intrusion (Fig. 53c), because the northern part of the footwall is closer to the intrusion than the southern part. F2 is partly filled by a dyke and hosts the biggest primary body (No.25) in the Xinlu ore field.

In summary, the fractures and faults which have steep attitude and which are related (generated or reactivated) to granite intrusions may be used as conduits of ore-forming fluids. Structures filled by dykes represent a relatively extensional and permeable space which is more likely to be connected to the major source of ore-forming fluids.

6.3 Fluid Flow Dynamics

Conduits are necessary for the flow of the ore-forming fluids; however, having well-developed conduits does not necessarily mean the separation of proximal and distal deposits. For example, in the Liuhe'ao deposit, structures and associated intermediate dykes are developed and extended from the ore-forming granite to distal sites in the country rocks, but proximal ore bodies are much better developed than the distal ones. This implies that the ore-forming components in the fluids do not tend to migrate upwards even when there are

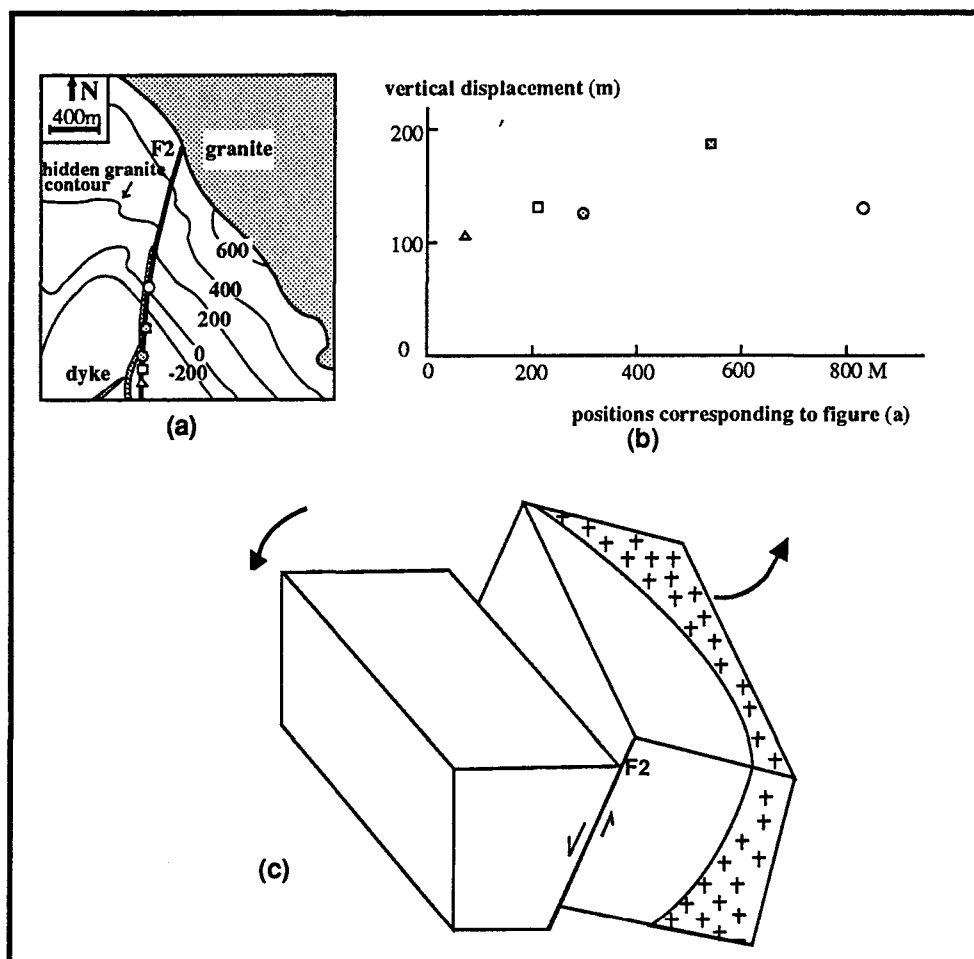


Fig. 53 a-the position of fault F2 with respect to the granite intrusion in the Baimianshan deposit; b-variation of displacement of F2 along the strike (data from Xie, 1989); c-block diagram showing the rotation of F2 caused by magmatic intrusion.

good conduits. This is related to the mechanism of ore deposition at the contact zone and the dynamics of the ore-forming fluids.

In general, the contact zone has extraordinary ability to trap ore-forming materials (causing them to precipitate) to form proximal deposits mainly because: (1) all the ore-forming fluids derived from the intrusion have to pass the contact, which enhances the possibility of trapping the ore-forming elements at the contact; (2) skarns which are usually developed at the contact zone represent a highly unusual deposition environment or chemical trap to components introduced by passing ore fluids (Kwak, 1987); (3) the contact zone represents a pressure transition zone between the lithostatic and the hydrostatic systems (Cunningham, 1978), which promotes the possibility of phase separation of the ore-forming fluids, which has been proved to be a major process responsible for the deposition of a variety of hydrothermal deposits and cited in a number of literature (e.g. Cunningham, 1978; Kelly and Turneure, 1970; Kamilli and Ohmoto, 1977; Barton et al., 1977; Drummond and Ohmoto, 1985; Kwak, 1987; Eadington, 1988; Weisbrod, 1981; Pichavant et al., 1982 and Ramboz et al., 1982). Kelly and Turneure (1970) suggested that the high salinity of the early ore-forming fluids of the Bolivian tin deposits may be related to the concentrating effect of phase separation. When phase separation takes place, ore metals are deposited from the liquid phase mainly as a result of: (1) sudden cooling of the liquid phase because of the larger molar enthalpy of vapor H₂O than liquid H₂O; (2) increasing pH values as a result of degassing; (3) decreasing proton concentration associated with CO₂ exsolution (Drummond and Ohmoto, 1985).

Therefore, if the contact zone has very strong capacity of trapping ore-forming components and the ore-forming fluids do not have a migration capacity strong enough to break through the contact zone, proximal deposits will form even if conduits are well developed. However, the contact zone does not always possess the three favourable depositional conditions discussed above, and if the ore-forming fluids have a migration capacity strong enough to overcome the trapping capacity of the contact zone, distal deposits will be dominant. Thus, the separation of proximal and distal deposits is principally controlled by the contrast between the capacity of the contact zone to catch ore-forming components and the capacity of the ore-forming fluids to break through the trap of the contact zone.

As has been described in chapter 3, there appears to be a correlation between the site of mineralization and the depth of granite intrusion in the Xinlu ore field: the proximal

deposits are distributed in the northern part of the ore field, there the granites were emplaced at relatively shallow depth, while the distal deposits are mainly distributed in the southern part of the ore field, where the granites were emplaced more deeply. It can be shown that both the possibility of phase separation at the contact zone and the migration capacity of the ore-forming fluids are related to the depth of emplacement of the intrusion.

First, the migrational capacity of the ore-forming fluids is related to the depth of emplacement of the intrusion. The fluid inclusion study indicates that the temperatures of the ore-forming fluids of the distal deposits are only slightly lower than those in the proximal deposit (Liuhe'ao), despite their difference of several hundred to more than 1000 metres in distance from the intrusion. This implies that the ore-forming fluids must have ascended very rapidly so that the cooling effect of the country rocks is greatly reduced. A similar phenomenon has been observed by Bodnar and Beane (1980) for a deeply buried copper-type mineralization system at Red Mountain of Arizona, where a vertical thermal gradient of less than 25°C/km is indicated by fluid inclusion studies. The preliminary data of fluid pressure inferred from the fluid inclusion study indicate that the fluid pressure of the ore-forming fluids at the site of ore deposition is between hydrostatic and lithostatic, but is closer to the former, and the pressure of the fluids in the intrusion varies from <hydrostatic to >lithostatic. It is possible that a pressure contrast existed between the conduit system (hydrostatic), which consists of faults, fractures and dyke-controlling structures, and the interior of the intrusion (lithostatic) at the contact zone (Cunningham, 1978). This pressure contrast is proportional to the depth of emplacement of the intrusion, as illustrated in Fig. 54. As the fluid flow rate is proportional to the pressure contrast, it can be seen that the fluid flow rate increases with increasing depth of emplacement of the intrusion.

Three consequences of high fluid flow rate, which are related to transport and deposition of ore components, can be expected. First of all, a temperature drop of the ore-forming fluid will be minimized, and the ore-forming components can be transported through a longer distance before they are precipitated. Secondly, the level of effective incorporation of meteoric water (fluid mixing) will be raised, because at the departure of the ore-forming fluid the fluid flow rate is so high that the overpressure caused by fluid resistance to upward flow (Cathles, 1981) will resist the incorporation of meteoric water; effective incorporation of meteoric water will not occur until the ore-forming fluid flows to higher level and the flow rate slows down. This is supported by the observation that $\delta^{18}\text{O}$ of ore-forming fluid decreases from 8.3 ‰ at level 150 to 6.9‰ at level 257 in the

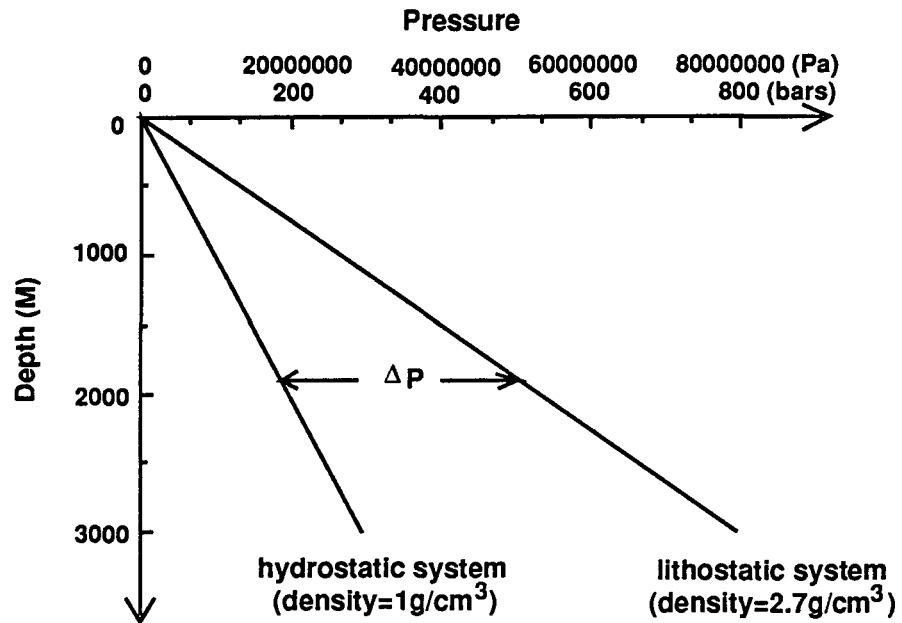


Fig. 54 Depth-pressure diagram showing that the contrast of hydrostatic and lithostatic pressures increases with depth.

Baimianshan deposit (a decrease rate of $\delta^{18}\text{O}$ of 1.3 ‰/100m) but decreases from 10.05‰ at level -350 to 8.3‰ at level 150 (a decrease rate of $\delta^{18}\text{O}$ of 0.35‰/100m), indicating that the incorporation of meteoric water is more intense at higher levels than at lower levels. Thirdly, effective wallrock reactions will not take place until the ore-forming fluid flows to shallow levels and the flow rate slows down, because high flow rate reduces the time of water-rock reactions.

Secondly, the possibility of phase separation at the contact zone, which is part of the ore-trapping potential of the contact zone, is also related to the depth of the intrusion emplacement. It has been discussed by many authors (e.g. Cunningham, 1978) that a sharp drop in pressure in an epizonal environment is more likely to cause extensive boiling than a comparable change in a deeper environment. Donaldson (1968) has studied the case of boiling of a geothermal system where temperature is assumed fixed at some depth and fluid flow is vertical upward, and calculated the maximum depth at which boiling can occur. It is found that the depth of the beginning of boiling is related to the rate of fluid flow (Donaldson, 1968)--the higher the fluid flow rate, the more shallow the depth of boiling will be. Since the fluid flow rate is higher for the distal ore-forming fluids due to the higher lithostatic-hydrostatic pressure contrast, it can be expected that the distal ore-forming fluids can ascend a longer distance before reaching the level of boiling.

Figure 55 shows schematically how the depth of emplacement of the intrusion controls the sites of phase separation with respect to the intrusion. This figure has no quantitative significance except that the topological shape of the phase boundaries resembles that of the H_2O -rich side of the H_2O - CO_2 - NaCl system (Gehrig et al., 1979), which is probably the case in the Xinlu ore field. A and C represent the points of departure of the ore-forming fluids near the contact zone of the intrusion. The depth of emplacement of the intrusion is small at A and large at C. The flow paths of the ore-forming fluids responsible for proximal and distal deposits are represented by AB and CD respectively.

In the case of proximal deposits, supposedly the ore-forming fluid was originally at point A. Under the lithostatic system, this point is in the one-phase domain. When the ore-forming fluid becomes part of the hydrostatic system, point A is in the two-phase area. Therefore, phase separation happens immediately at the contact zone before the fluid can ascend a long distance. The result of the phase separation is a NaCl -rich and CO_2 -poor liquid phase and a CO_2 - H_2O vapor phase. One direct effect of phase separation is ore deposition at the contact, which is related not only to increasing pH and decreasing proton

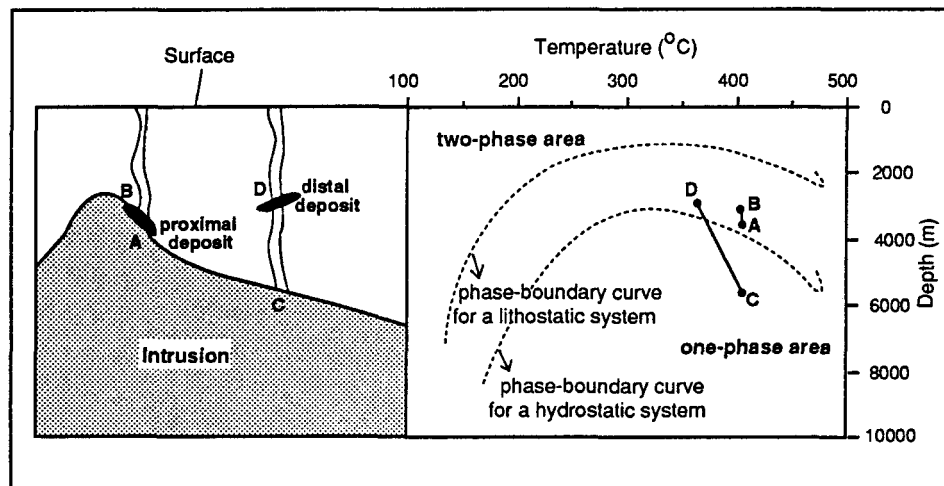


Fig. 55 A schematic model showing how the depth of emplacement of the intrusion controls the sites of phase separation with respect to the intrusion. A-B and C-D represent the flow paths of the ore-forming fluids. For more detailed explanation see the text.

concentration associated with CO₂ exsolution (Drummond and Ohmoto, 1985), but also to the fact that the liquid phase becomes heavier and has lesser ability to move up, since once the ore-forming fluids joined the hydrostatic system, density gradient plays an important role in driving the movement of the ore-forming fluids. The lower the density of the ore-forming fluids, the stronger moving ability they have. The joining of Ca into the ore-forming fluid in the skarn environment at the contact zone may have promoted phase separation, as CaCl₂ has stronger ability than NaCl to raise the domain of phase separation to a higher temperature and pressure (Zhang and Frantz, 1989).

In the case of distal deposits, the ore-forming fluid was supposedly originated at point C. Under the lithostatic system, this point is in the one-phase domain. When the ore-forming fluid becomes part of the hydrostatic system, point C is still in the one-phase area. Therefore, the ore-forming fluid can ascend a longer distance before reaching the two-phase area of the hydrostatic system. The greater the depth from which the fluid originated, the longer distance it has to travel to reach the two-phase status. Figure 55 assumes that the composition and density of the fluid do not change during the migration, but temperature drops slightly. If the composition and density of the ore-forming fluid is changed during the migration (from C to D), the phase boundaries will change correspondingly. This will change the position of the fluid in relation to the phase boundaries. The difference in the extent of phase separation between the proximal and distal deposits in the Xinlu ore field is probably caused by the composition change of the distal ore-forming fluids during the migration. For the proximal ore-forming fluid at Liuhe'ao, the position of the fluid is probably relatively far from the critical point in the immiscible loop in a P-T coordinate, so the composition of the coexistent liquid and vapour phases is well differentiated, underlining the extensive phase separation; for the distal deposits, the composition of the ore-forming fluids underwent changes (by incorporation of meteoric water) such that the position of the fluid was very close to the critical point, so the composition of the coexistent liquid and vapour phases was similar, thereby diminishing the extent of phase separation.

In summary, the dynamics of the ore-forming fluids is one of the most important factors controlling the localization of the proximal and distal deposits in the Xinlu ore field. The flow rate of the ore-forming fluids increases with the depth of emplacement of the intrusions, which reduces temperature drop rate and raises the level of effective meteoric incorporation and water-rock interaction. The influence of the depth of emplacement of intrusions on phase separation is such that the ore-forming fluid issuing from intrusions are

more likely to be subject to a phase separation at the contact zone (where there is a sudden pressure drop) when the magmatic intrusion is emplaced at higher levels than when the intrusion is emplaced more deeply. In the former case, a proximal deposit may form as a result of phase separation; in the latter case, the fluid can carry the ore-forming components to a high level to form a distal deposit where phase separation may or may not occur, depending on the extent of temperature and compositional change of the fluid during its ascent.

CHAPTER VII

MODELLING OF DEPOSITIONAL THERMAL CONDITIONS

7.1 Introduction

It has been shown in chapter 6 that ore-forming fluids with a strong migrational ability to break through the "contact trap" is necessary for distal deposits to form. However, this condition alone is not sufficient. The formation of a deposit requires favourable deposition conditions, which lead to the focussing of the ore-forming materials in limited area instead of the scattering of them over a wide area. Such conditions can be provided by certain sedimentary beds which represent a geochemical trap to passing ore-forming components, e.g. the transitional bed between the Yujiang Formation and the Donggangling Formation which is composed of impure limestones (Li, 1986), as in the case of the stratiform ore bodies in the Baimianshan deposit. However, the majority of the distal type ore veins in the Xinlu ore field are steep, which cut through a series of different lithological units, indicating that ore deposition is not simply controlled by lithology. Therefore, other depositional conditions should be considered.

Temperature drop of the ore-forming fluids is one of the most important causes of the precipitation of hydrothermal ores (Skinner, 1979). In the case of temperature drop as the major cause of ore deposition, the ore deposits occur where the temperature of the ore-forming fluids drops in a localized area (Skinner, 1979). This is most likely to take place in the high-temperature-gradient segments in the surrounding rocks, e.g. the Sn mineralization in SW England (Sams and Thomas-Betts, 1988). Demin and Zolotarev (1980) studied the relationship between the thermal field associated with granite intrusions and the distribution of mineral deposits in a polymetallic mineralization district in USSR. They found out that 80% of the rare-metal deposits in the district are located in the zone where the temperature gradient was sharp and the temperature remained about 400 °C for a relatively long time, and all the Pb-Zn deposits occur in the 320-240 °C temperature-stable zone which also had a sharp temperature gradient.

For intrusion-associated hydrothermal deposits, the temperature gradient in the country rocks is determined mainly by the intrusion. The thermal gradients associated with intrusions are closely related to the shapes of the intrusions (Norton and Cathles, 1979; Sams and Thomas-Betts, 1988). Thermal fields and fluid flow patterns associated with intrusions has been studied by many authors (e.g., Norton and Knight, 1977; Norton, 1978; Norton and Cathles, 1979; Cathles, 1981; Sams and Thomas-Betts, 1988). These authors' works are all based on the assumption that the intrusion has a convex shape. However, in the Xinlu ore field, the country rocks are surrounded by granites in three sides and beneath (see Fig. 11, 12), which gives a concave intrusion environment for the ore field as a whole. The thermal field in this kind of intrusion environment has not been described.

A set of models of heat conduction are established below, with emphasis on the thermal gradient patterns of concave intrusion environments, characteristic of the Xinlu ore field, and their contrast with convex models, as well as the significance of this contrast on the localization of proximal vs. distal deposits. Although only heat conduction models are studied, it is believed that the results may be applicable to situations which include heat convection, because it has been noticed that the isotherm distribution around an intrusion is barely discernible between models of heat conduction and convection (Norton and Knight, 1977); moreover, the major lithology in Xinlu ore field is carbonate, whose (limestone) permeability is between 10^{-12} cm² and 10^{-14} cm²ch (Turcotte and Schubert, 1982), in which heat conduction is more important than heat convection (when permeabilities (k)= 10^{-17} cm², heat transfer is almost purely conductive; when k= 10^{-14} cm², convective heat flux is about 10% of the total heat flux, and when k= 10^{-12} cm², convective heat flux becomes greater than conductive one (Norton and Knight, 1977; Cathles, 1981)).

7.2 Analytical Models

Two simplified models simulating concave and convex intrusions are illustrated in Fig. 56. These models shed light on the difference in thermal field pattern between concave and convex intrusions.

In Fig. 56a, the area inside the semi-circle is a homogeneous medium in contact with a magma at 750 °C outside the semi-circle. The heavy black lines are heat insulators and heat flow is directed toward the centre (within a radius of one metre) of the semi-circle,

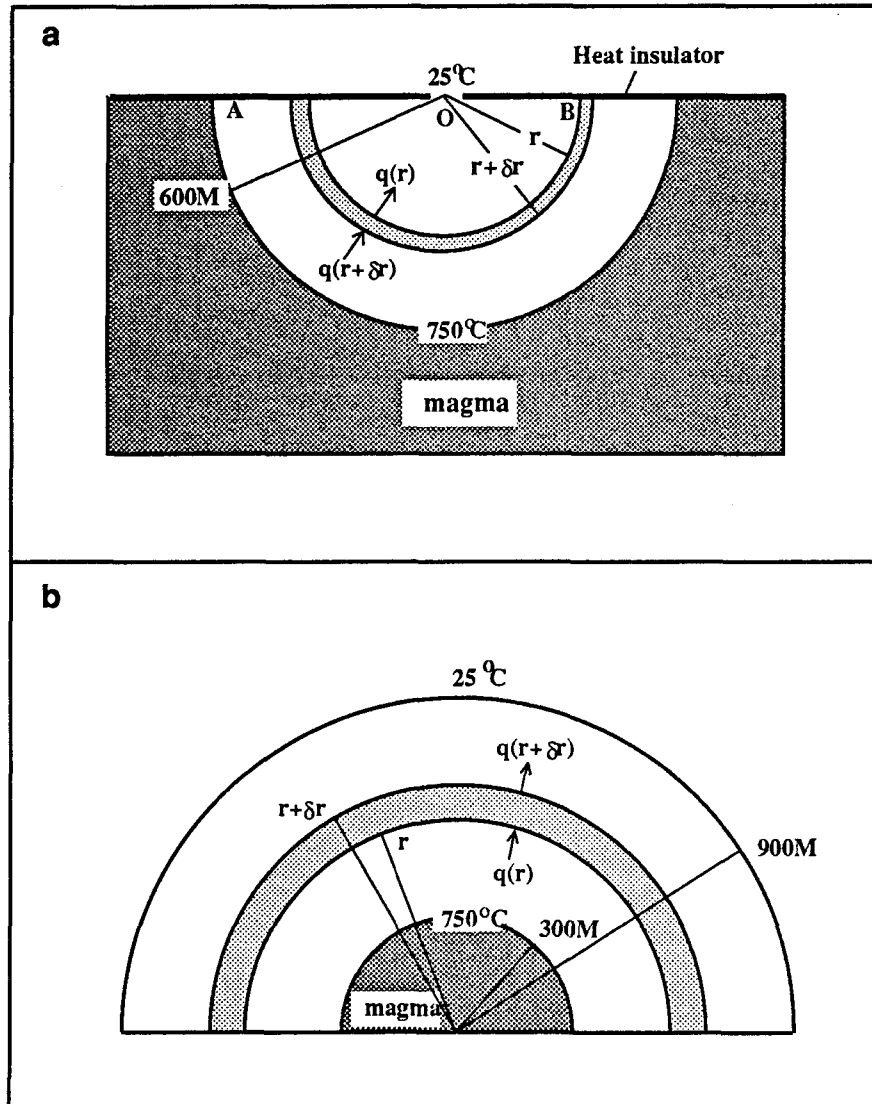


Fig. 56 Analytical models of heat conduction in concave (a) and convex (b) environments.

where the temperature is maintained at 25 °C. The heat conduction in this model is similar to the case of radial heat conduction in a spherical shell (Turcotte and Schubert, 1982).

According to energy conservation principle,

$$\pi.r.c.q_r = \pi.(r+\delta r).c.q_{r+\delta r} \dots\dots\dots(1)$$

where q_r and $q_{r+\delta r}$ are the heat flow at radius r and $r+\delta r$ respectively; c is the thickness (perpendicular to the paper) of the semi-circle. Equation (1) can be simplified as:

$$r.q_r = (r+\delta r).q_{r+\delta r} \dots\dots\dots(2)$$

Since δr is infinitesimal, $q_{r+\delta r}$ can be expanded in a Taylor's series as:

$$q_{r+\delta r} = q_r + \delta r.(dq_r/dr) + \delta r^2.(d^2q_r/dr^2)/2! + \dots + \delta r^n.(d^nq_r/dr^n)/n! \dots\dots\dots(3)$$

Neglecting powers of δr , then

$$q_{r+\delta r} = q_r + \delta r.dq_r/dr \dots\dots\dots(4)$$

replacing (4) into (2) produces

$$(r+\delta r).(dq_r/dr) = -q_r \dots\dots\dots(5)$$

According to Fourier's law,

$$q_r = -k.dT/dr \dots\dots\dots(6)$$

where T is temperature and k is the coefficient of heat conductivity. Setting $k = \text{constant}$ and replacing (6) into (5), we get:

$$-d^2T/dr^2 = (1/(r+\delta r)).dT/dr \dots\dots\dots(7)$$

Neglecting δr in the term $r+\delta r$ produces

$$-d^2T/dr^2 = (1/r).dT/dr \dots\dots\dots(8)$$

or:

$$-(1/(dT/dr)).d(dT/dr) = (1/r).dr \dots\dots\dots(9)$$

Solving equation (9):

$$T = (1/e^{C1}).\ln(r) + C2 \dots\dots\dots(10)$$

According to Fig. 56a, $T = 750^\circ\text{C}$ at $r = 600$ m, and $T = 25^\circ\text{C}$ at $r = 1$ m, so:

$$T = (10^3/8.823).\ln(r) + 25 \dots\dots\dots(11)$$

or:

$$r = e^{8.823 \cdot 10^{-3}(T-25)} \dots\dots\dots(12)$$

Setting the temperature interval to be 100°C , a set of temperature-radius data is obtained:

T(°C)	750	650	550	450	350	250	150	50
r (m)	600	248	103	43	18	7	3	1

The result is illustrated in Fig. 57a, and it is shown that the temperature gradient increases sharply away from the intrusive body.

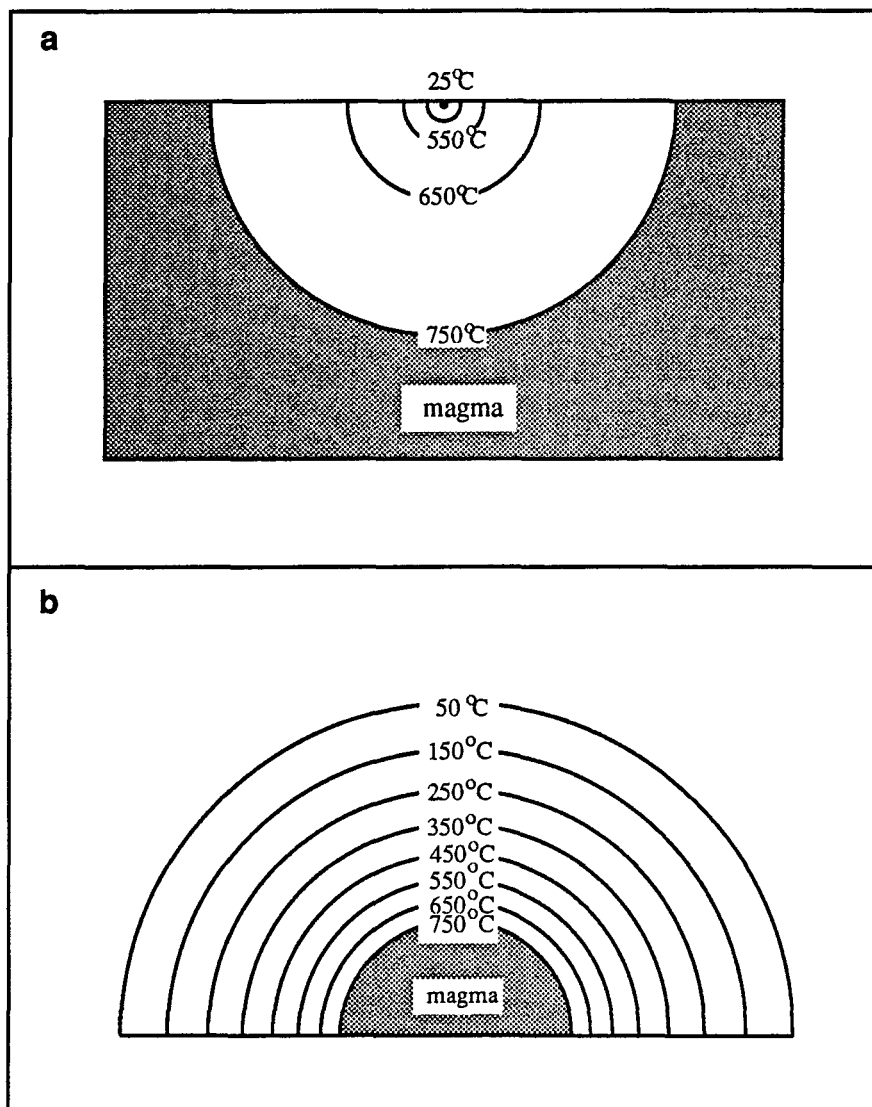


Fig. 57 Isotherms of the concave (a) and convex (b) models illustrated in Fig. 56.

In Fig. 56b, a semicircular magma body with a radius of 300 metres is supposed to intrude a semicircular medium with a radius of 900 metres. The temperature of the magma is 750 °C, and that on the upper surface of the medium is 25 °C.

Through a series of deduction similar to the above model, the following equation may be obtained:

$$d(dT/dr)/dr = -(1/r) \cdot (dT/dr) \dots \dots \dots (13)$$

Solving equation (13) produces

$$T = -e^{C1} \cdot \ln(r) + C2 \dots \dots \dots (14)$$

According to Fig. 56b, $T = 25$ °C at $r = 900$ m and $T = 750$ °C at $r = 300$ m, then:

$$T = 4508.79 - 659 \ln(r) \dots \dots \dots (15)$$

or:

$$r = e^{(4508.79 - T)/659} \dots \dots \dots (16)$$

Setting temperature interval to be 100 °C, the following temperature-radius data are obtained:

T(°C)	750	650	550	450	350	250	150	50
r (m)	300	349	406	473	550	641	746	867

The result is illustrated in Fig. 57b. It is shown that the temperature gradient increases toward the intrusive body.

7.3 Two-Dimension Steady-State Numerical Models

The above models are indicative of the difference of thermal field between concave and convex intrusion environments, but they are too idealized. The following two models (Fig. 58) are constructed to simulate real geological situations, although the thickness of the cover above the intrusion is reduced in order to emphasize the effect of concave shape on thermal field. The temperature of the magma is fixed at 750 °C, and that on the surface of the cover is fixed at 25 °C. The cover rocks are supposed to be homogeneous. These models describe the thermal field in heat balance state, regardless of the time required to reach this balance. Therefore the physical property of the medium is not considered.

The method of iterative relaxation finite difference (Yu, 1979) is used in this study. The cover area above the intrusion is divided into regular squares of the same size, with the width of the sides being Δx and Δy . Each node is supposed to stand for the centre of a

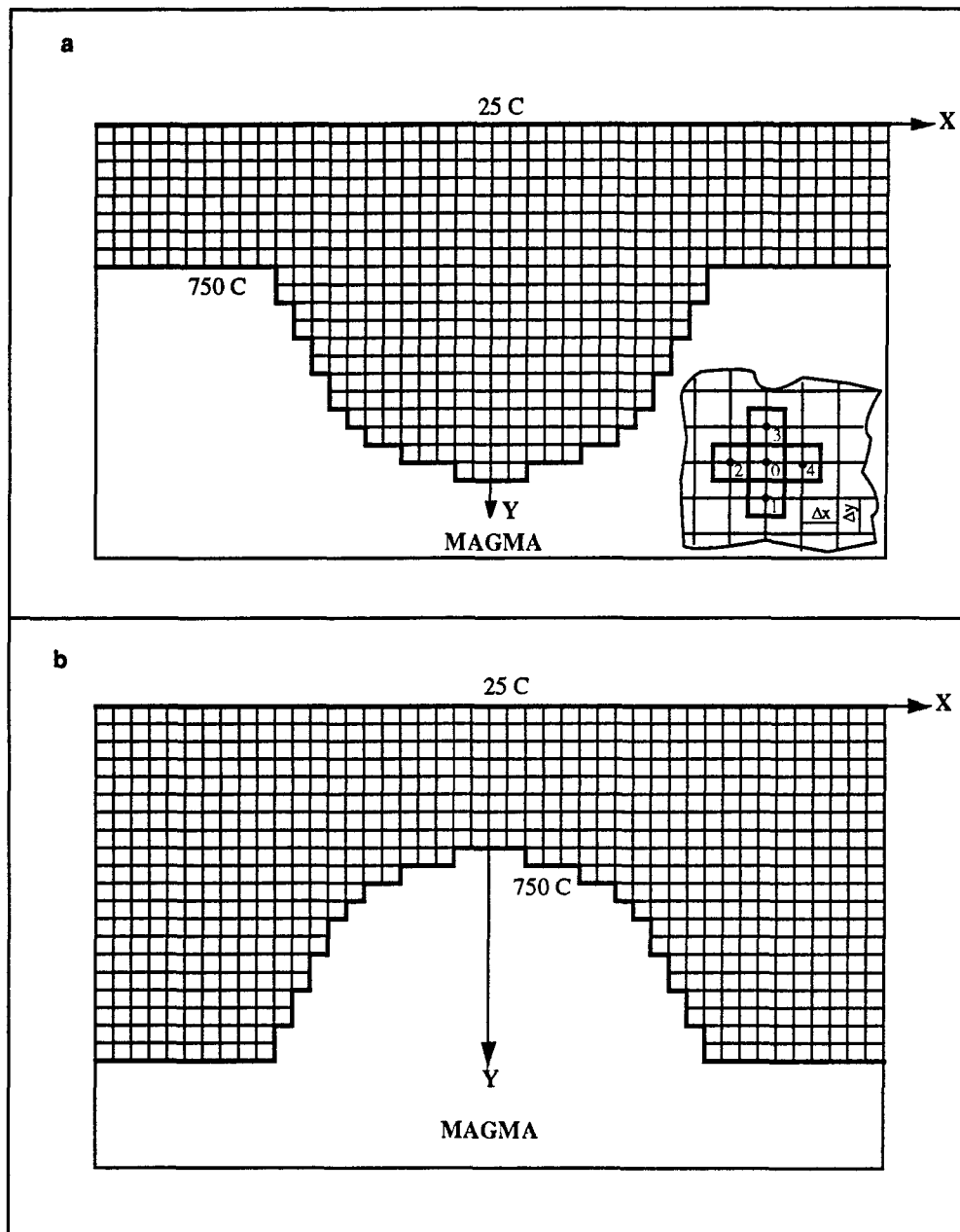


Fig. 58 Two-dimension steady state heat conduction models simulating concave (a) and convex (b) magma intrusion environments. Explanations see the text.

unit grid around the node, as is illustrated in the inset of Fig. 58a. In steady state, net heat flow from surrounding units into any of the units is zero. For example, for unit 0, we have:
 $Q_0=Q_{1-0}+Q_{2-0}+Q_{3-0}+Q_{4-0}=0$(17)

where Q_0 is the net heat flow through unit 0, Q_{1-0} is the heat flow from unit 1 to unit 0, Q_{2-0} is the heat flow from unit 2 to unit 0, and so on.

$$Q_{1-0}=k.\Delta x.C.(T_1-T_0)/\Delta y$$
.....(18)

$$Q_{2-0}=k.\Delta y.C.(T_2-T_0)/\Delta x$$
.....(19)

$$Q_{3-0}=k.\Delta x.C.(T_3-T_0)/\Delta y$$
.....(20)

$$Q_{4-0}=k.\Delta y.C.(T_4-T_0)/\Delta x$$
.....(21)

where k is the coefficient of heat conductivity, Δx and Δy are the width of the grids, C is the thickness (perpendicular to the paper) of the grids and is constant, T_1 is the temperature at node 1, T_2 is the temperature at nodus 2, and so on.

Since the grids are regular squares, $\Delta X=\Delta Y$. Replacing (18), (19), (20) and (21) into (17):
 $T_0=(T_1+T_2+T_3+T_4)/4$(22)

Similarly, an equation for every node (i, j) can be obtained:

$$T_{i,j}=(T_{i+1,j}+T_{i,j+1}+T_{i-1,j}+T_{i,j-1})/4$$
.....(23)

In order to solve this set of equation, a temperature value is set to each node according to the original temperature condition. Then, the new temperature (toward steady state) for each node (i, j) is calculated in the following steps. Set:

$$T'_{i,j}=T_{i+1,j}+T_{i,j+1}+T_{i-1,j}+T_{i,j-1}-4*T_{i,j}$$
.....(24)

For the most right column (column 22) of node in the model (Fig. 58), $T'_{22,j}$ is calculated by:

$$T'_{22,j}=T_{22,j-1}+T_{22,j+1}+T_{21,j}-3*T_{22,j}$$
.....(25)

Dividing $T'_{i,j}$ by 4 and adding it to $T_{i,j}$, a new value of $T_{i,j}$ for each node is determined. This process is repeated until $T'_{i,j}$ is small enough (0.001 in this study). The computer program is listed in Appendix E-1 (for concave model) and E-2 (for convex model).

The isotherms of these models are illustrated in Fig. 59. The difference between concave (a) and convex (b) intrusion environments is still obvious. In the concave intrusion model, the temperature gradient decreases toward the intrusion in the central part, but tends to be uniform in the right and left sides of the model (Fig. 59a). In the convex model, on the other hand, the temperature gradient slightly increases toward the intrusion in the central part of the model (Fig. 59b), which is more apparently shown in numerical results (Fig. 60).

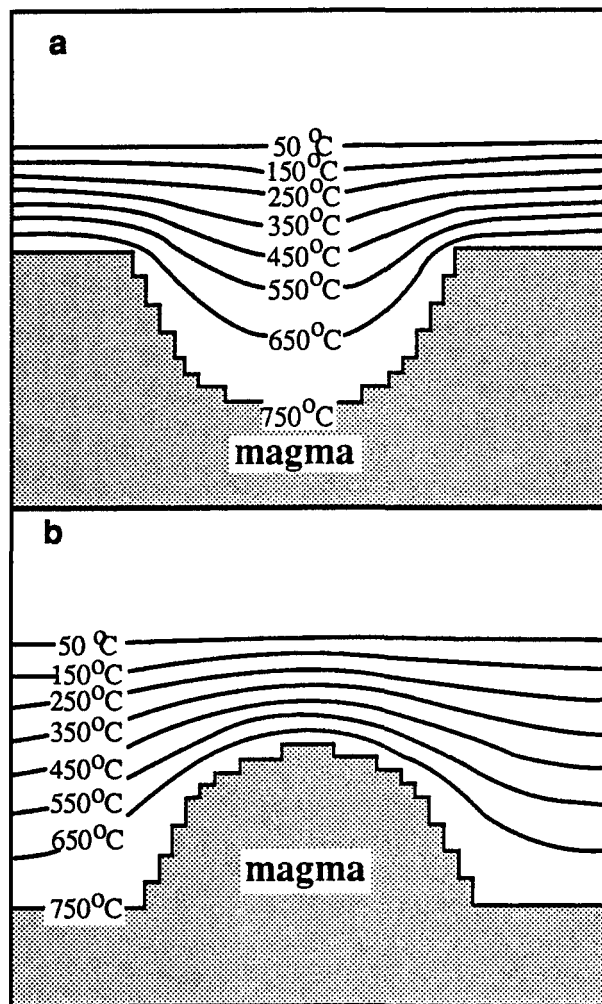


Fig. 59 Isotherms of concave (a) and convex (b) models of steady heat conduction illustrated in Fig. 58.

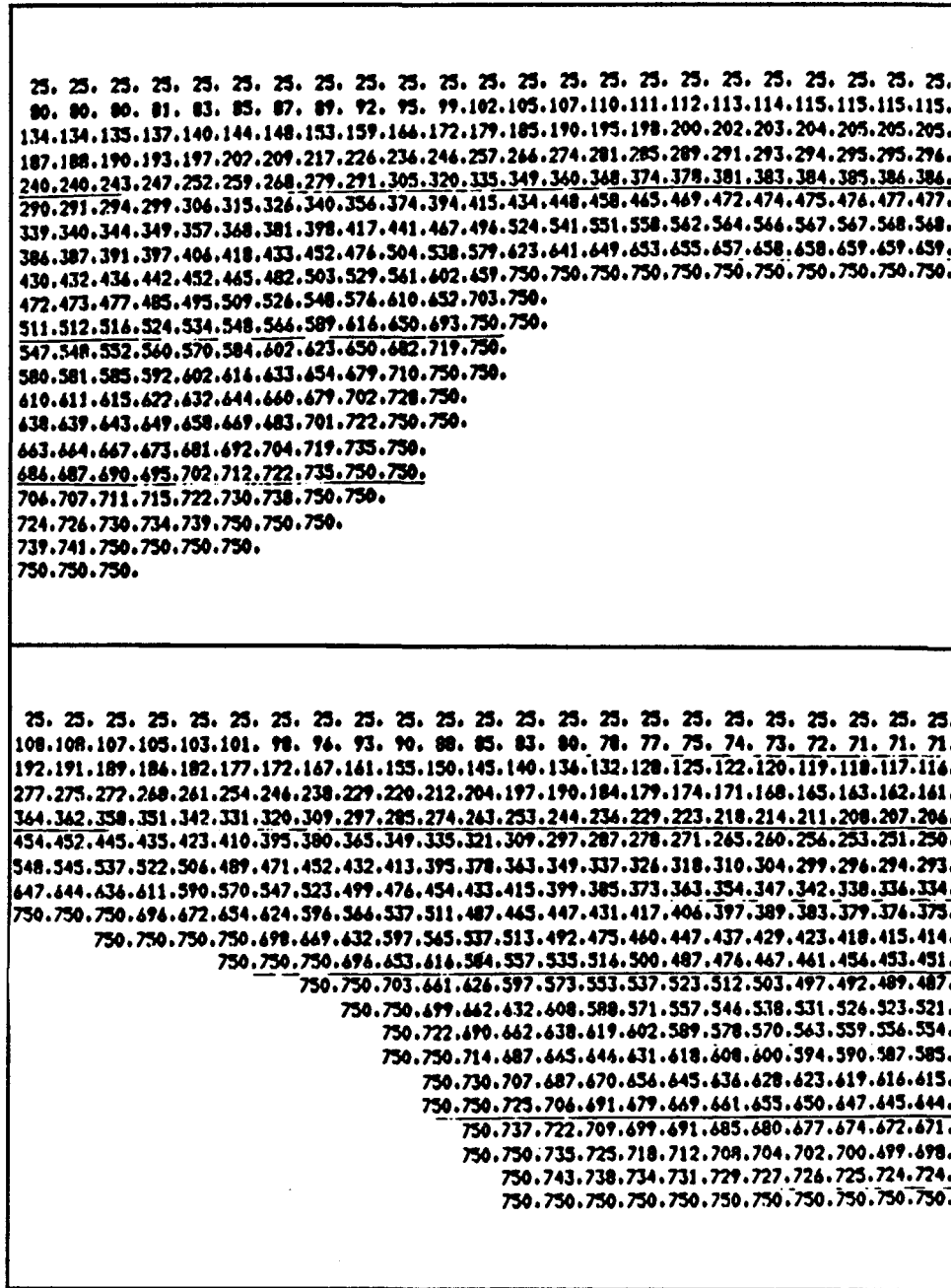


Fig. 60 Calculation results of the steady state heat conduction models in concave (upper) and convex (lower) environments (Fig. 58).

7.4 Two-Dimension Transient Numerical Model

This model describes the variation of the thermal field with time after the emplacement of the intrusion. Since the convex model is much better known, only a concave model is constructed here. The framework of the model (Fig. 61) is similar to Fig. 58a, but the following conditions are added: (1) The temperature of the magma is decreasing with time linearly, presumably being 750 °C (the temperature at which the geochronological clock of whole rock Rb-Sr isotopes begins to work) at the beginning of magma emplacement and being cooled to 300 °C (the temperature at which the geochronological clock of K-Ar isotopes in biotite begins to work) after a period of time of 3.9 Ma (this time interval is not well constrained because of the scatter of K-Ar ages, but it does not influence the significance of the unsteady-state model); (2) The temperature gradient in the cover medium at the moment magma intrudes is assumed to be 3 °C/100m (after Turcotte and Schubert, 1982); the surface temperature is fixed at 25 °C; (3) The vertical and horizontal length of each of the grids is 50 metres; (4) The property of the medium is supposed to be homogeneous and the same as limestone.

The governing equation of two-dimensional heat conduction is written as Fourier's equation, neglecting the influence of energy consumption or release (in the processes of thermal metamorphism), :

$$\partial^2 T / \partial x^2 + \partial^2 T / \partial y^2 = (1/\alpha) \partial T / \partial t \dots \dots \dots (26)$$

where T is temperature, α is heat diffusivity and t is time. This equation can be written in the explicit finite-difference representation (modified from Kreith and Bohn, 1986):

$$(T_{i+1,j}^t + T_{i-1,j}^t - 2T_{i,j}^t) / \Delta x^2 + (T_{i,j+1}^t + T_{i,j-1}^t - 2T_{i,j}^t) / \Delta y^2 = (1/\alpha) \cdot (T_{i,j}^{t+1} - T_{i,j}^t) / \Delta t \dots \dots \dots (27)$$

where $T_{i,j}^t$ is the temperature at nodus (i, j) at time t, Δx and Δy are the width of the grids, α is heat diffusivity; and Δt is the time interval between time t and time t+1.

Since $\Delta x = \Delta y$ in our model (Fig. 61), Eq.(27) can be written as:

$$T_{i,j+1}^t + T_{i,j-1}^t + T_{i+1,j}^t + T_{i-1,j}^t - 4T_{i,j}^t = M(T_{i,j}^{t+1} - T_{i,j}^t) \dots \dots \dots (28)$$

where

$$M = \Delta x^2 / \alpha \Delta t \dots \dots \dots (29)$$

In the model in Fig. 61, $\Delta x = \Delta y = 50$ metres, $\alpha = 0.00158 \text{ m}^2/\text{hr}$ (for limestone, after Kreith and Bohn, 1986), Δt is set to be 45 years, then $M = 4$. Solving Eq.(28), we get:

$$T_{i,j}^{t+1} = (T_{i+1,j}^t + T_{i-1,j}^t + T_{i,j+1}^t + T_{i,j-1}^t) / 4 \dots \dots \dots (30)$$

Since the change of the temperature (T) of intrusion with time (t) can be constrained by:

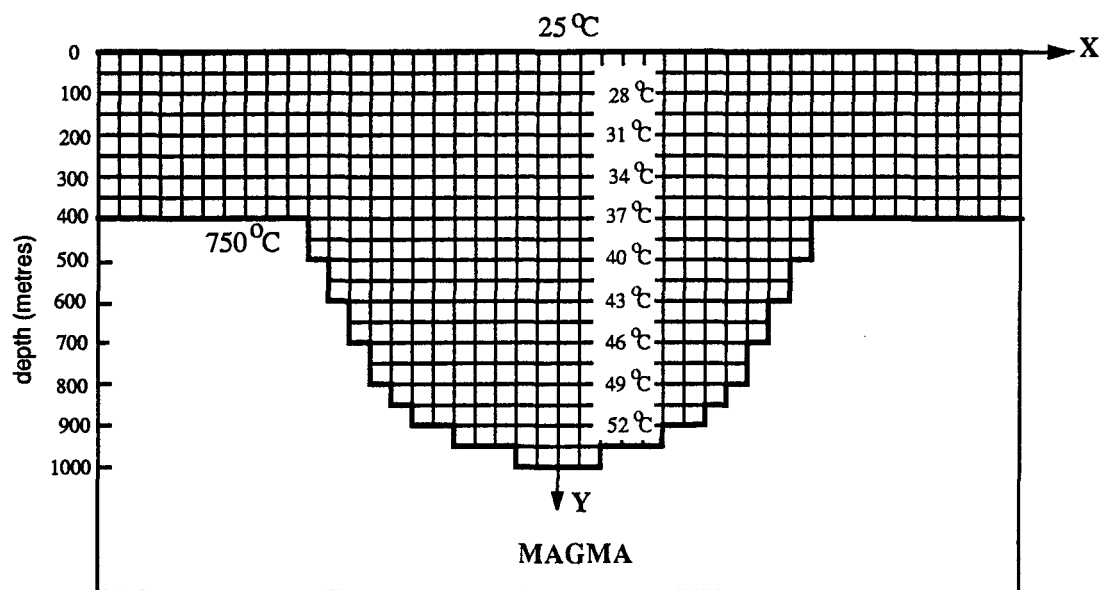


Fig. 61 Unsteady state heat conduction model simulating concave magma intrusion environment. Explanations see the text.

$$T=750-450*t/3.9*10^6 \dots\dots\dots(31)$$

according to the assumption that the temperature of intrusion is 750 °C at the beginning and reduces to 300 °C after a period of 3.9 Ma, and the initial temperature distribution in the medium is assumed to be normal geothermal gradient (3 °C/100m), the temperature at any point (i,j) at any time (t) after the intrusion can be calculated with Eq.(30). The computer program is listed in appendix E-3.

Some of the calculation results are illustrated in Fig. 62. It is clearly shown that (1) temperature gradient decreases sharply towards the intrusion in the central part of the model; this tendency remains throughout the cooling history of the intrusion; (2) the extent of the temperature decrease with time increases toward the intrusion; that is to say, the thermal field is less stable near the intrusion than away from the intrusion. In fact, when the temperature of the magma begins to decrease, the temperature is still increasing in the central part of the model.

7.5 Implication for the Localization of Proximal vs. Distal Deposits

All the above models clearly indicate that the thermal field associated with a concave intrusion environment, as in the case of the Xinlu ore field, differs significantly from that of the better known convex environment. The temperature gradient associated with magmatic intrusion is lowest at the contact zone and increases away from the intrusion in a concave environment, while that associated with convex environment is highest at the contact zone and decreases away from the intrusion.

The significance of this thermal field difference on the localization of proximal vs. distal deposits is based on the principle that mineralization tends to take place in the segments where temperature gradient is sharp and relatively stable through time, provided other conditions (e.g. conduits, chemical and mechanical barriers, ect.) are the same. The reason for this is, if the temperature gradient is large, the space suitable for ore deposition is small, so the ore-forming materials are enriched; on the other hand, if the temperature gradient is small, the space suitable for ore deposition is large, and ore-forming components tend to disperse. For the same reason, stable temperature field is more suitable for mineralization than an unstable one, because if the thermal field changes very quickly through time, the limited ore-forming matter is distributed widely instead of being enriched in certain segments. Therefore, proximal deposits are more likely to be related to convex

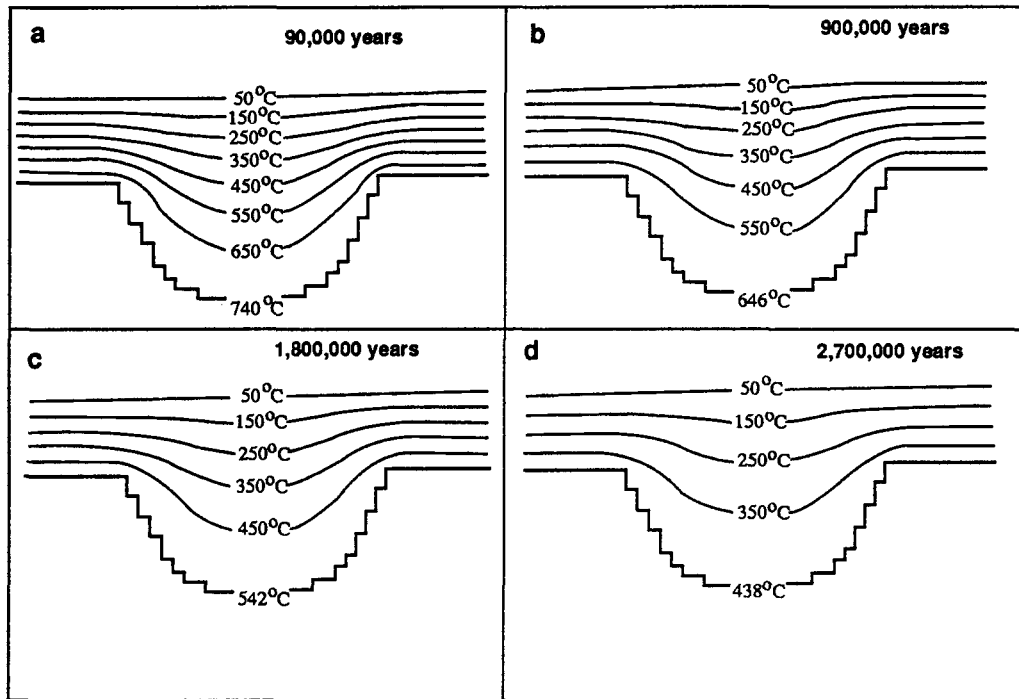


Fig. 62 Isotherms of the unsteady model illustrated in Fig. 61, showing the thermal patterns of 90,000 years (a), 900,000 years (b), 1,800,000 years (c) and 2,700,000 years (d) after magmatic intrusion.

intrusion environments, while distal deposits are more likely to form in a concave intrusion environment.

The general thermal field in the Xinlu ore field can be approached by the concave models, because the granites of phase I and II, which are exposed on the eastern and western sides of the ore field respectively, were emplaced at similar time. Although the thermal history of the intrusions themselves is not well constrained because of the scatter of K-Ar ages, it is believed that the special thermal pattern generated by the concave intrusion environment may have influenced the localization of mineralization in the Xinlu ore field which are mainly related to late-stage granite intrusions. The low temperature gradient in the contact zone hinders the enrichment of the ore-forming components to form proximal deposits, and promote the upflow of the ore-forming fluids with less cooling effect, while the relatively high temperature gradient in the distal sites in the central part of the ore field provides favourable depositional condition for distal deposits to form. This is consistent with the observation that distal deposits are better developed than proximal ones in the Xinlu ore field, and is also consistent with the model of intrusion depth and fluid dynamics discussed in chapter 6, because a concave intrusion environment is more likely to be associated with deeper intrusion than a convex environment does. The better development of proximal deposits in the northern part of the Xinlu ore field results from a combination of a more shallow depth and somewhat convex shape of the late-stage intrusion (at Liuhe'ao).

CHAPTER VIII

DISCUSSIONS ON THE APPLICATION OF THE INTRUSION DEPTH-FLUID FLOW AND THERMAL FIELD MODELS

8.1 Introduction

From the discussion of the data in the preceding chapters it is apparent that the models of fluid flow dynamics related to the depth of magmatic intrusion and the thermal field associated with the shape of intrusions are of practical significance for the further prospecting in the Xinlu ore field. However, the applicability of these models to other regions with similar geological environment remains to be examined. The importance of the extension of these models are beyond question because they focus on the localization of intrusion-associated hydrothermal deposits which is a problem of practical importance for prospecting geologists, and which can not be simply explained by available models such as the metal zoning models.

In this chapter, the models are discussed in a wider perspective both geologically and theoretically. Examples from other regions are cited, and, based on available experimental data, the fields of phase separation of other fluid systems are discussed. The difference of the pressure system within and outside a magmatic intrusion is reviewed, and the relationship between forced venting and convection of ore-forming fluids is discussed. All these discussions lead to a conclusion that the models established in the Xinlu ore field may be applied to other regions with similar geological settings, although caution is advisable because of the variability of specific geological conditions.

8.2 Geological Examples from Other Regions

8.2.1 Examples of relationship of ore localization and intrusion depth

The observation that the distance between hydrothermal deposits and associated granite intrusions is proportional to the depth of the emplacement of the intrusion in the Xinlu ore field can be observed in many other major rare metal and base metal ore fields

(Chi et al., 1991a). Geological sections showing this relationship can be found in the Dachang (Lu et al., 1979 and Zheng, 1987), and Xianghualing (Huang et al., 1985) tin-polymetallic ore fields and the Xihuashan-Dangping-Piaotang tungsten mineralization district (Tanelli, 1982) in southern China, the tin-polymetallic deposits in Cornwall (Charoy, 1979), the Pb-Zn-Ag-Sn deposits in Zeehan-Renison Bell area of west Tasmania (Laznicka, 1985), the Lake George W-Mo mineralization in southern New Brunswick (Seal et al., 1987), the Panasqueira W-Cu (Ag)-Sn deposits in Portugal (Polya, 1989), the Kara W-skarn deposit of Tasmania (Kwak, 1987), the Ban Ban Zn-Fe sulfide-bearing skarn in southeastern Queensland (Ashley and Plimer, 1989), the Deputatskoye tin-polymetallic deposit and the Kazakhstan tungsten deposit (Rundqvist, 1982), the Camsell River Ag-Ni, Co Arsenide mineralization in N.W.T. Canada (Badham, 1975) and the Logtung W-Mo deposit, Yukon Territory, Canada (Kirkham and Sinclair, 1988).

Some of these geological sections are shown in Fig. 63. Among them are the Dachang tin-polymetallic ore field, which is the biggest Sn-producing camp in China, the Xihuashan-Dangping-Piaotang tungsten mineralization district, which is the second largest W-producing camp in China and the Cornwall tin-polymetallic ore field, which is one of the most famous tin ore producers in the world. In all these examples, it can be seen that mineralization occurs at the contact zone where the intrusion is emplaced at shallow depth and occurs relatively far above the intrusion where the intrusion is emplaced at deeper levels. In the cases of Cornwall and Deputatskoye (Fig. 63c and d), metal zonation is shown to influence the distance of mineralization with respect to the intrusion, but it does not influence the intrusion depth-ore localization correlation. In the other cases, the separation of proximal and distal mineralizations does not seem to be simply the effect of metal zoning either. The majority of the ore-forming fluids have been proved to be derived from the magmatic intrusions in all the cases, so the separation of proximal and distal deposits does not seem to be controlled by a variation of the source.

In the Xihuashan-Dangping-Piaotang tungsten district, the Xihuashan wolframite-quartz-K feldspar vein deposit (to the left of Fig. 63a) and the Dangping wolframite-quartz-beryl vein deposit are localized on the top of the Yanshanian granite intrusion (Lu, 1983 and Tanelli, 1982), while the Piaotang W-Sn-Cu-Pb-Zn stockwork deposit is mainly located in the Cambrian low-grade metamorphosed sediments above the hidden granite intrusion (Tanelli, 1982 and Liu and Chang, 1987). $\delta^{34}\text{S}$ values of ore minerals vary from -3.4 to +6‰ for both proximal (Xihuashan and Dangping) and distal (Piaotang) deposits (Tanelli,

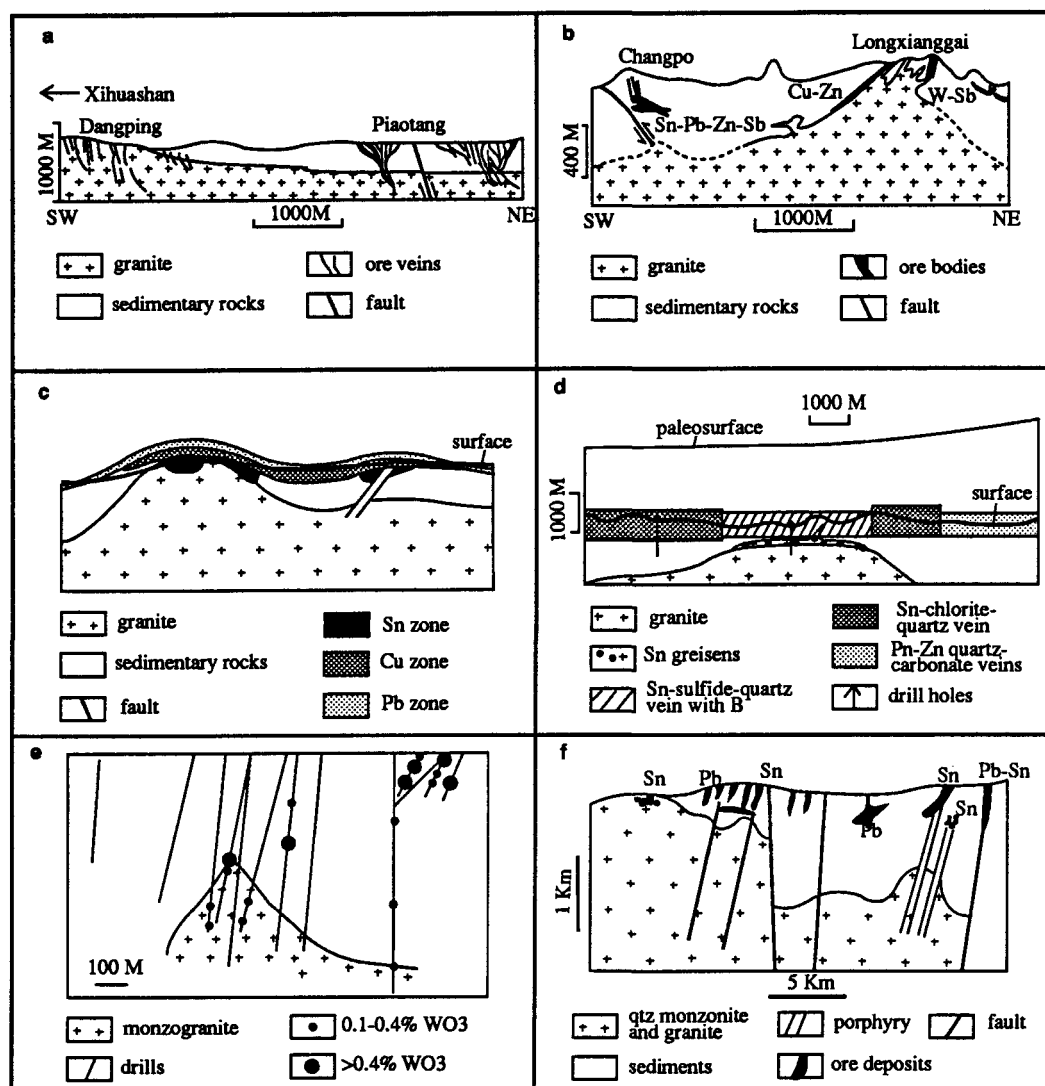


Fig. 63 Examples showing the relationship between the depth of emplacement of intrusions and the localization of associated mineralization. a-Schematic cross section of Xihuashan-Dangping-Piaotang tungsten mineralization district (after Tanelli, 1982); b-Cross section from Longxianggai to Changpo in the Dachang Sn-polymetallic ore field (simplified from Zheng, 1987 and Chen, et al., 1987); c-Schematic section from the Cornwall Sn-polymetallic ore field (after Charoy, 1979); d-Cross section of the Deputaskoye Sn-polymetallic deposit (after Rundqvist, 1982); e-Cross section depicting the distribution of W grades in the Lake George Sb-W-Mo deposit (after Seal et al., 1987); f-Schematic section of the Sn-Pb-Zn-Ag mineralization district in the Zeehan-Renison Bell area (after Laznicka, 1985). For explanations see text.

1982). $\delta^{18}\text{O}$ values of water in the ore-forming fluids are similar between Xihuashan (+5.39 to +8.16‰), Dangping (+6.1 to +6.43‰) and Piaotang (+4.69 to +5.40‰), and $\delta^{13}\text{C}$ values of carbonate associated with wolframite-quartz mineralization are comparable between Xihuashan (-4.51 to -7.53‰) and Piaotang (-3.03 to -9.03‰) according to Liu and Chang (1987). The isotopic ages of the ore veins are comparable to those of associated granite intrusion (Lu, 1983). These characteristics, along with the study of the geochemical characteristics of the granites, have led to the conclusion that the ore-forming fluids are predominantly derived from the Yanshanian granite intrusion (Tanelli, 1982; Lu, 1983 and Liu and Chang, 1987). The dominant mineralogy is quite similar between Xihuashan, Dangping and Piaotang (Tanelli, 1982), although the contents of Sn, Cu, Pb and Zn minerals at Piaotang are higher.

In the Dachang tin-polymetallic ore field, mineralizations of a variety of Sn, W, Cu, Pb, Zn and Sb association are developed around a centre at Longxianggai with an outcrop of Yanshanian granite. Proximal deposits occur near the outcrop of granite, while distal deposits occur in the areas away from the granite outcrop. The correlation between the depth of the intrusion and the vertical distance of mineralization relative to the intrusion is shown by the geological section from Longxianggai to Changpo (Fig. 63b). At Longxianggai, where granite is exposed, mineralization is developed near the contact zone; at Changpo, where the granite is more deeply emplaced, mineralization is from 290 metres to more than 900 metres above the top of the intrusion (Zheng, 1987 and Chen et al., 1987). $\delta^{34}\text{S}$ values of ore minerals vary from -5.4 to +4.2‰ in the "central zone" around Longxianggai, and from -4.3 to +6.6‰ at Changpo (Xu, 1987 b). $\delta^{18}\text{O}$ values of water in the ore-forming fluids are from +3.8 to +7.5‰ for the proximal deposits in the "central zone", and those from the Changpo are from +8.6 to +9.8‰ for the early mineralization stages and from +3 to +16.2‰ for the late mineralization stages (Xu, 1987 b). Comprehensive study of the geochemical characteristics of the ores, granites and sedimentary rocks have led to the conclusion that the majority of Sn, W and Cu and parts of Pb, Zn, As are derived from the Yanshanian granite, and considerable amounts of Pb, Zn, As and Sb are provided by the sedimentary rocks (Tu, 1987; Chen et al., 1987 and Xu, 1987b). The difference in metal assemblage between the proximal deposits in the "central zone" (Cu and Zn sulfides) and the distal deposit at Changpo (Sn-Pb-Zn-Sb sulfides) is not responsible for the spatial separation of proximal and distal deposits, because Sn would have been closer to the intrusion than Cu

and Zn if metal zonation were the major mechanism of the separation of proximal vs. distal mineralization (Strong, 1988).

The Cornwall tin-polymetallic ore field is often cited as a classic example of metal zoning, which is an important factor controlling the localization of ore deposits with respect to the intrusion. According to Willis-Richards and Jackson (1989), all significant wolframite production is from within the granite or within a 700 m distance of an observed or projected granite contact; 90-100% of Sn, Cu and As production occurs within 1500 m of a contact; 30% of the Zn production and >80% of the Pb and Ag production is from distance of >1500 m from a granite contact. However, the relationship that the distance of mineralization from the granite contact is proportional to the depth of the granite emplacement is still apparent for a certain "metal zone". This is well demonstrated by the schematic section of Dines (1956, cited from Charoy, 1979) (Fig. 63c): the Sn mineralization zone is situated at the contact where the intrusion is projecting, but occur in the country rocks above the intrusion where the intrusion is more deeply buried, and Cu and Pb mineralization zones show the same relationship. Similar relationship can be observed in the geological sections of the Cornwall ore field reported by other authors (e.g. Laznicka, 1985), although not as ideal as the diagrammatic section. Although O and H isotope data indicate that the hydrothermal fluids, from which minerals of economic interest were deposited, were overwhelmingly of meteoric origin, and S isotope data suggest that some sulfur was derived from the Devonian sedimentary rocks (Jackson et al., 1989), it is believed that fluids of magmatic derivation contributed to the fluid budget and chemical makeup of the hydrothermal systems, supported by geological and geochemical evidence, the mode of formation of some of the ore bodies, and the clear linkage between the evolution of boro-silicate melts and the emplacement of tourmaliniferous vein material (Jackson et al., 1989).

In the Deputatskoye tin-polymetallic deposit of Yakutia, three laterally extending mineralized zones are recognized (Rundqvist, 1982). It has been shown that both the upper and lower boundaries of each mineralized zone are nearly horizontal, while the depth of the granite intrusion increases away from the central zone, so the distance between the lower boundary of each mineralized zone and the granite contact is proportional to the depth of the emplacement of the intrusion. The ore-forming fluids were possibly derived from the intrusion, although no detailed reports of geological and geochemical evidence are available.

In the Lake George polymetallic (Sn-W-Mo-Au-base metal) hydrothermal deposits, it is observed that the W grade is highest at the contact zone between the monzogranitic intrusion and the country rocks where the intrusion is protruding, while the high-grade W mineralization is far above the contact where the intrusion is relatively deeply emplaced (Fig. 63e, Seal et al., 1987). The W-Mo mineralization exhibits an intimate association with the magmatic activity both spatially and temporally (Seal et al., 1988), and it is concluded that the ore-forming fluid of W and Mo is derived from the monzogranite intrusion by Seal et al. (1988), mainly based on geological, petrological, mineralogical and fluid inclusion studies.

In the case of the Zeehan-Renison Bell area of west Tasmania, a variety of Pb-Zn-Ag and Sn deposits are developed, in the form of stratabound replacement bodies or veins, in the Proterozoic to Devonian sediments and minor volcanics, which are intruded by Devonian granites. Sn mineralization in greisen occurs on the top of the granite intrusion where the intrusion is exposed, and the vertical distance from the site of mineralization to the granite contact increases in areas away from the granite outcrop (Fig. 63f). The ore-forming fluids responsible for the main stages of mineralization are derived from the granite, according to the data of H, O, S and C isotopes and fluid inclusions (Patterson et al., 1981).

Therefore, neither metal zoning alone nor non-magmatic sources of ore-forming fluids can explain the separation of proximal and distal deposits in the examples discussed above similar to the case of the Xinlu ore field. The mechanism must be related to processes which have something to do with the depth of the magmatic intrusion.

8.2.2 Examples of concave intrusion environments

The concave intrusion environment may seem rare in comparison with convex one. However, the region between two protruding intrusions has a concave shape provided the two convex intrusions are connected at depth. This situation is not rare. Therefore, the concave thermal patterns established for the Xinlu ore field may be applied to a wide range of situations, although the extent of the concaveness may be larger or smaller.

Among the many regions probably having a concave intrusion environment, the Camsell River area in N.W.T., Canada, is cited as an example, where the concave shape of the intrusion may have controlled the distribution of the Ag-Ni, Co Arsenide mineralizations. The area is underlain by pendants of calcalkaline volcanic and volcanoclastic sequences which lie between comagmatic plutonic "highs" (Fig. 64 a and b), including

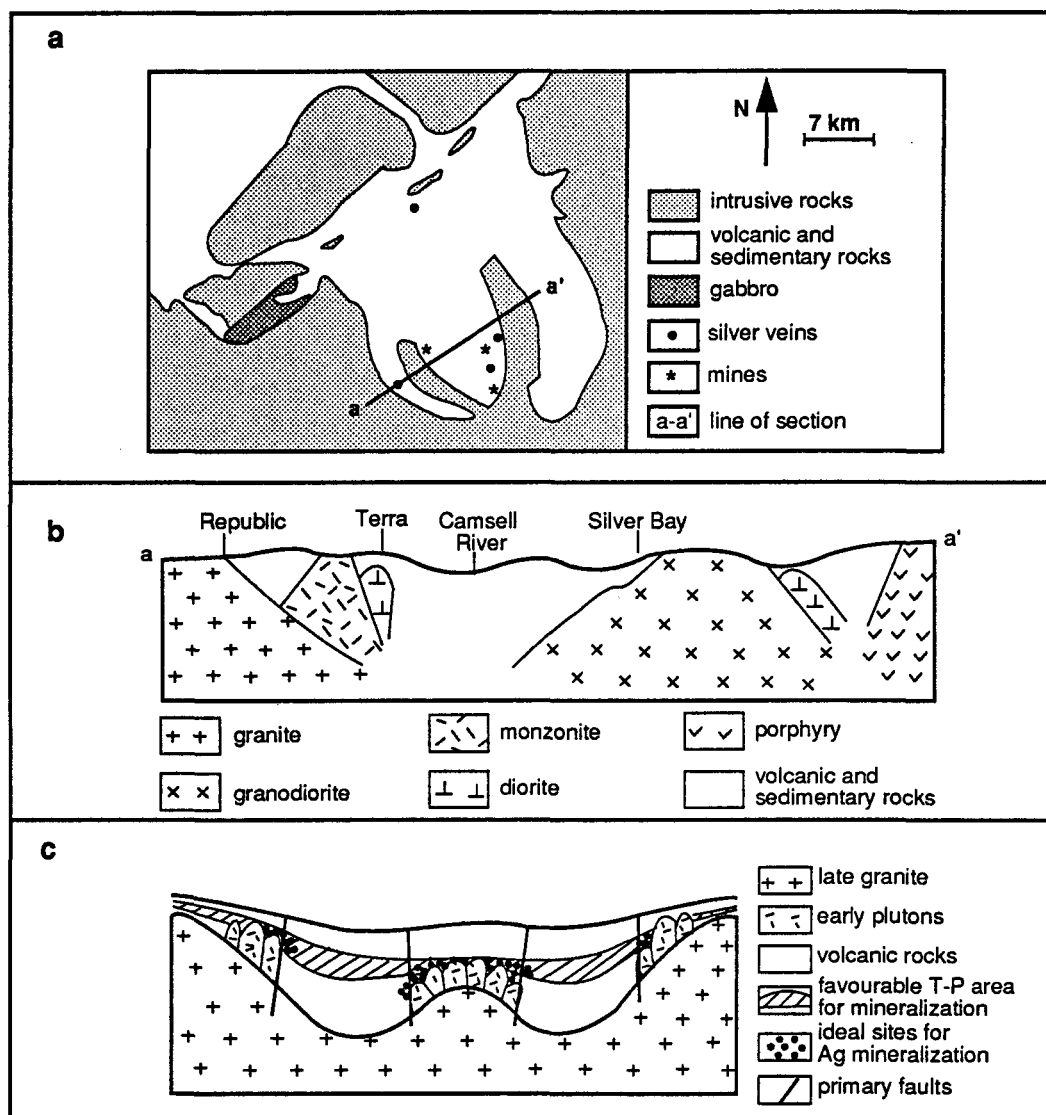


Fig. 64. (a) Geological map of the Camsell River Area, N.W.T. Canada; (b) Sketch section of a-a' line shown in a; (c) Sketch section illustrating the most suitable sites for the late magmatic hydrothermal mineralization in the Camsell River Area. Simplified after Badham (1975).

earlier intermediate stocks and later granites of batholithic dimensions. Large, complex strike slip faults were initiated during the latter phases of intrusion and were active intermittently for some 300 Ma afterwards. Ore veins are located in splays and tension-fractures from these faults which are developed in the volcanic and volcanoclastic rocks (Badham, 1975). Geological and chemical data continually point to a magmatic origin for the ore-fluids (Badham, 1975). The suitable T-P zone for hydrothermal mineralization proposed by Badham (1975), as is shown Fig. 64c, is consistent with the thermal patterns for concave intrusion model and the intrusion depth model.

8.3 Lithostatic vs. Hydrostatic Systems

The intrusion depth-ore localization relationship is intimately related to the presumption that the ore-forming fluids are under lithostatic pressure within the intrusion while those in the conduit (mainly fractures) system in the country rocks are under hydrostatic pressure so that a great pressure contrast exists between within the intrusion and outside the intrusion, which influences the migration capacity and phase status of the ore-forming fluids. The conditions under which this hypothesis is valid are discussed in this section.

First, let us examine whether the pressure system in the conduits in the country rocks can be approached by hydrostatic pressure, a so-called "osmotic" condition (Fyfe et al., 1978), and whether the difference between the fluid pressure and lithostatic pressure increases with depth to the depth of magmatic intrusion. It has been observed, in an oil well of Pakistan, that the pressure of interstitial water is nearly the same as hydrostatic pressure above the depth of 300 metres, but deviates from the hydrostatic toward the lithostatic after this depth and approaches the lithostatic pressure at depth exceeding 1.5 km (Hubbert and Rubey, 1959); the difference between lithostatic and hydrostatic pressures ($P_{\text{litho}} - P_{\text{hydro}}$) increases from the surface to the depth of about 900 metres, but decreases after this depth. In the conduit system, where the fluid is hosted by fractures, the depth at which the fluid pressure begins to deviate from the hydrostatic pressure and the depth at which $P_{\text{litho}} - P_{\text{hydro}}$ reaches its maximum value must be greater than what is indicated above, because theoretically, if the fracture is open to the surface, the fluid pressure in the fracture can be approached by hydrostatic pressure to a depth as great as the wall rocks remain rigid. Although this depth has not been practically determined, geophysical evidence suggests that

rocks fail by fracture and have interconnected pore spaces to at least 15 km in the crust (Norton and Knight, 1977); it is believed that the fluid pressure may be approximated by hydrostatic pressure in the conduits of ore-forming fluids for the conditions of most granite intrusion-associated hydrothermal mineralizations. This is because the hydrothermal mineralization-associated granites mainly occur in the upper part of the crust where the country rocks are more likely to be rigid, and the conduits (fractures) are mainly in an extensional status due to the influence of the stress generated by the intrusion. Fournier (1969 and 1972) noted that at shallow depths in highly faulted regions, sudden pressure drops from lithostatic to hydrostatic conditions are likely. In models of heat transfer and fluid convection generated by magmatic intrusions, a hydrostatic system is generally assumed (e.g., Norton and Knight, 1977; Norton and Cathles, 1979; Cathles, 1981). Even if the fluid pressure deviates from hydrostatic to lithostatic at a depth above the depth of intrusion (point A in Fig. 65), the relation that the contrast between the fluid pressure and the lithostatic pressure ($P_{\text{litho}} - P_{\text{fluid}}$) increases with depth may still be valid to the depth of intrusion (point B in Fig. 65) unless the intrusion is emplaced below the depth where $P_{\text{litho}} - P_{\text{fluid}}$ is maximum (point C in Fig. 65). There are no available data about the depth where $P_{\text{litho}} - P_{\text{fluid}}$ is maximum, but it appears that this depth is greater than that at which P_{fluid} begins to deviate from P_{litho} .

Secondly, let us examine whether the fluid pressure within the magmatic intrusion can be approximated by lithostatic pressure. At the moment the intrusion is emplaced, it is in a viscous state, and the lithostatic pressure exerted on the intrusion is transferred to the fluids in the magma. Therefore, at that time, the fluid pressure within the intrusion is equal to the lithostatic pressure imposed by the overlying rocks (Whitney, 1975), and can even be greater than the lithostatic pressure if the stress caused by the dynamics of intrusion is considered. After the first loss of heat of the intrusion to the country rocks, a crystallized shell forms at the margin of the intrusion, containing a less-crystallized interior where the fluid pressure is equal to the lithostatic pressure exerted on the outer shell (Cunningham, 1978 and Burnham, 1979). This fluid pressure may be retained until the intrusion is fractured and connected with the hydrostatic system in the country rocks. Cathles (1981) has discussed the forced venting of magmatic volatiles as a result of the high fluid pressure (lithostatic) within the intrusion in contrast with the low fluid pressure (hydrostatic) of the ground waters outside the intrusion. The fluid pressure within the intrusion can even exceed the lithostatic pressure during crystallization of anhydrous minerals (Burnham, 1979), but

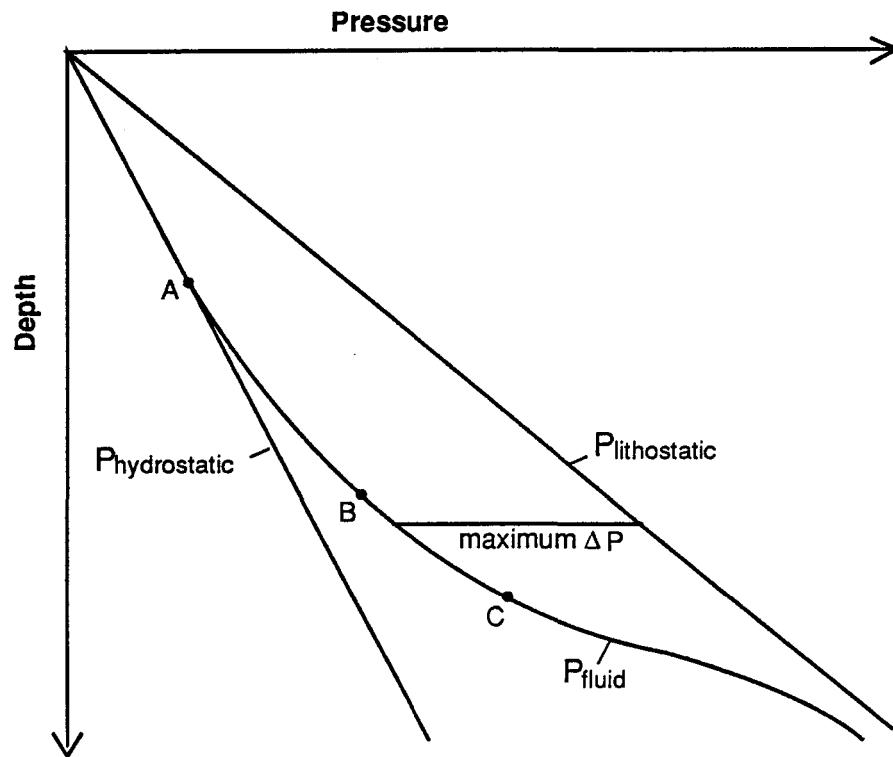


Fig. 65 Diagrammatic relationship between the fluid pressure in a fracture and the lithostatic and hydrostatic pressures in relation to depth, showing the deviation of fluid pressure from the hydrostatic pressure. Points A, B and C are explained in the text.

this overpressure ($P_{\text{fluid}} - P_{\text{litho.}}$) is constrained by the tensile strength of rock which rarely exceeds 400 bars (Macdonald, 1983). If joints are formed during the solidification of the outer shell of the intrusion, the tensile strength of rock may be significantly reduced.

Although there are some uncertainties about the state of fluid pressure in the conduit system and within the intrusion, it appears feasible that, in a regime of granitic intrusion-associated hydrothermal mineralizations, ore-forming fluids are under lithostatic pressure within the intrusion while those in the conduit (mainly fractures) system in the country rocks are near hydrostatic pressure and the difference between the fluid pressure inside the intrusion and that in the conduits outside the intrusion increases with depth.

8.4 Phase Separation Fields of the Most Common Fluid Systems

Phase separation is an effective mechanism causing precipitation of ore-forming components (e.g. Cunningham, 1978; Kelly and Turneure, 1970; Kamilli and Ohmoto, 1977; Barton et al., 1977; Drummond and Ohmoto, 1985; Kwak, 1987; Eadington, 1988; Weisbrod, 1981; Pichavant et al., 1982 and Ramboz et al., 1982, Skinner, 1979). In most of the examples cited in 8.2, evidence of phase separation has been observed at the sites of ore deposition. Although it cannot be said that phase separation is the only or major mechanism for ore deposition in these examples, it is quite likely that phase separation contributed to ore deposition. In the Xihuahan-Dangping-Piaotang W-mineralization district, liquid fluid inclusions ($\text{H}_2\text{O}-\text{NaCl}$) are more common than other types (gas-rich, liquid CO_2 -bearing and NaCl -bearing) in the ore veins (Lu, 1983). However, it is observed that most gas-rich and liquid CO_2 -bearing inclusions are developed at the top of the veins, and the content of CO_2 decreases from the top to the bottom in the same vein (Lu, 1983). It is likely that phase separation took place at the sites of ore deposition, producing a vapor phase which moves more quickly to the top of the veins and a liquid phase from which the majority of ore-forming components were deposited, although more fluid inclusion evidence is needed. In the Dachang tin-polymetallic ore field, the coexistence of daughter mineral-bearing aqueous inclusions and gas-rich inclusions with approximately the same homogenization temperatures is commonly observed in cassiterite, quartz and calcite of ores from proximal and distal deposits in most of the mineralization stages, obviously indicating boiling (Liu et al., 1987). In the Cornwall tin-polymetallic mineralization district, there is some evidence for minor effervescence of a $\text{CO}_2\text{-H}_2\text{O}$ vapor although oxygen isotope

studies suggest a significant non-magmatic component in the ore-forming fluid (Spooner, 1981). In the Lake George polymetallic (Sn-W-Mo-Au-base metal) hydrothermal deposits, fluid inclusions are studied in the W-Mo veinlets (Seal et al., 1987, 1988). Two distinctive assemblages of inclusions, defined by the variability of brine/CO₂ ratios, were recognized. Those occurring within or adjacent to the intrusion are typically three-phase (brine+liquid CO₂+vapor) and exhibit fairly constant brine/CO₂ ratios from inclusion to inclusion within a given sample, thus suggesting the presence of a one-phase fluid at the time of entrapment, while those away from the intrusion in the country rocks exhibit highly variable brine/CO₂ ratios, strongly suggesting fluid immiscibility at the time of entrapment (Seal et al., 1987, 1988). It is shown that the W grade is higher in the sites where fluid immiscibility occurs than in the sites where there is no fluid immiscibility (Seal et al., 1987). According to Patterson et al. (1981), no phase separation evidence has been found in the Renison Bell Pb-Zn-Ag-Sn mineralization area of west Tasmania.

Whether phase separation takes place at the contact zone or in distal sites, and the distance which the ore-forming fluids can migrate before phase separation takes place, are dependent on the composition, temperature and pressure of the fluids, the last being closely related to the depth of the emplacement of the intrusion and the state of pressure system (lithostatic or hydrostatic). For a given fluid system and pressure condition (e.g. hydrostatic), the level of phase separation, or the phase separation boundary (at and above which phase separation takes place), is determined by geometry and P-T condition of the intrusion. If the migration of the hydrothermal fluid is an isothermal process (no temperature drop during the ascent of the fluid), the phase separation boundary will be a horizontal plane (Fig. 66), which is closer to the contact zone where the intrusion is protruding but is further away from the contact when the intrusion is more deeply emplaced. This effect may be increased (for H₂O-salts system) or decreased (for low-temperature part of H₂O-CO₂-salts system, see Fig. 67) in the event where there is a decrease of temperature of the fluid during transport (Fig. 66). If the phase separation surface intersects the contact zone, proximal mineralization is likely to occur in the part of the contact zone which is above the phase separation boundary, and distal deposits are more likely to form in the parts horizontally away from the protruding part of the intrusion.

On the other hand, for a given geometry and P-T condition of an intrusion, the phase separation boundary is dependent on the composition of the fluid and the conditions of pressure (lithostatic or hydrostatic). It has been shown that the existence of NaCl and CO₂ in

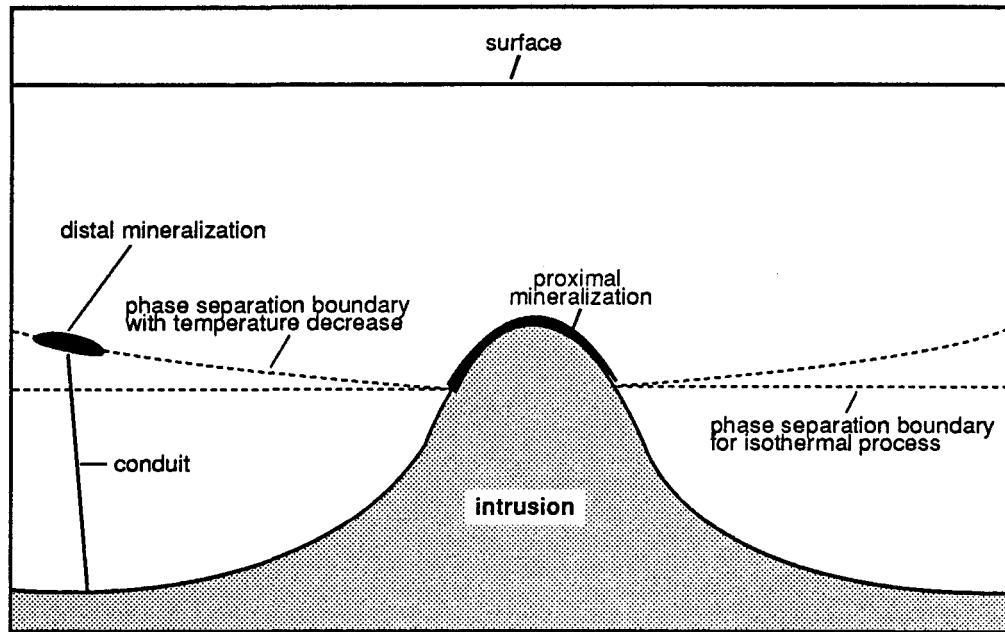


Fig. 66 Diagrammatic demonstration of the relationship between the phase separation boundary and the geometry of the magmatic intrusion for a given composition of fluid (here H₂O-salt system) and T-P condition.

the fluid can increase the depth at which phase separation begins to occur (Cunningham, 1978; Henley, 1985 and Bodnar et al., 1985). The experimental data of Zhang and Frantz (1989) indicate that the existence of CaCl_2 in the fluid can increase the immiscible domain to a higher temperature and pressure than NaCl does. The extent of the enlargement of phase separation field is related to the concentration of these solutes. A comprehensive and detailed study of the depth-temperature field of phase separation for various fluid systems is out of the scope of this thesis, and is limited by the availability of P-V-T-X experimental data, but a brief consideration of the most common compositional systems in natural ore-forming fluids is necessary. The temperature-depth fields of phase separation for both lithostatic and hydrostatic systems are diagrammatically represented in Fig. 67 for selected compositional systems.

The shape of the phase separation field for salt- H_2O binary systems (Fig. 67b, c, d) is similar to that of pure H_2O (Fig. 67a), with slow depth increase at low temperatures and rapid depth increase at high temperatures, but the T-Depth values of the critical point (the intersection between the phase boundary and the critical curve) are greatly increased by addition of salt into H_2O , thus the phase separation field is enlarged. It can be shown by the experimental data of Zhang and Frantz (1989) and Bodnar et al. (1985) that the enlargement of phase separation field is proportional to the concentration of the salt. In the low-temperature part of the binary systems (Fig. 67b, c, d), T-Depth correlation is similar for different salts, but in the high-temperature part, the depth of phase separation is much greater for the H_2O - CaCl_2 system than for the H_2O - NaCl and H_2O - KCl systems.

The fluid systems containing CO_2 have quite different topologic shape of phase separation field in comparison with the salt- H_2O systems. When the CO_2 content is low (<10 mole%, see Roedder, 1984a) there is a negative correlation between temperature and depth at low temperatures and positive correlation at high temperatures (Fig. 67e, f); when the CO_2 content is high (>58.9 mole%, see Roedder, 1984a), the phase boundary is almost independent of pressure (depth) and mainly defined by temperature. It can also be shown that the addition of salt greatly enlarge the field of phase separation (Fig. 67 f, g).

In all the selected fluid systems, it is clear that the phase separation field in hydrostatic system is very much larger than in lithostatic system. If the fluid is situated at a point which is in the one-phase domain under lithostatic pressure but in the two-phase domain under hydrostatic pressure, phase separation will take place immediately when the pressure system changes from lithostatic to hydrostatic. If the fluid is still in the one-phase

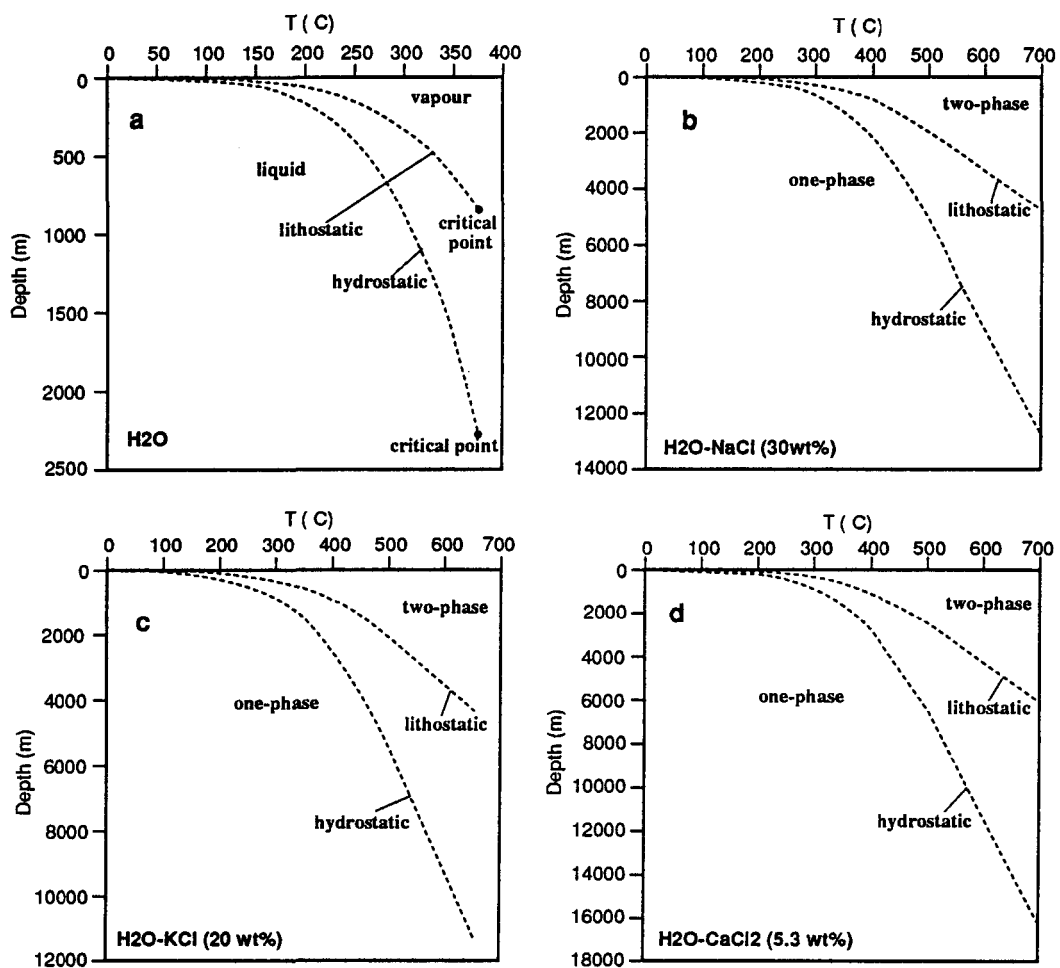


Fig. 67 (Continued on the following page)

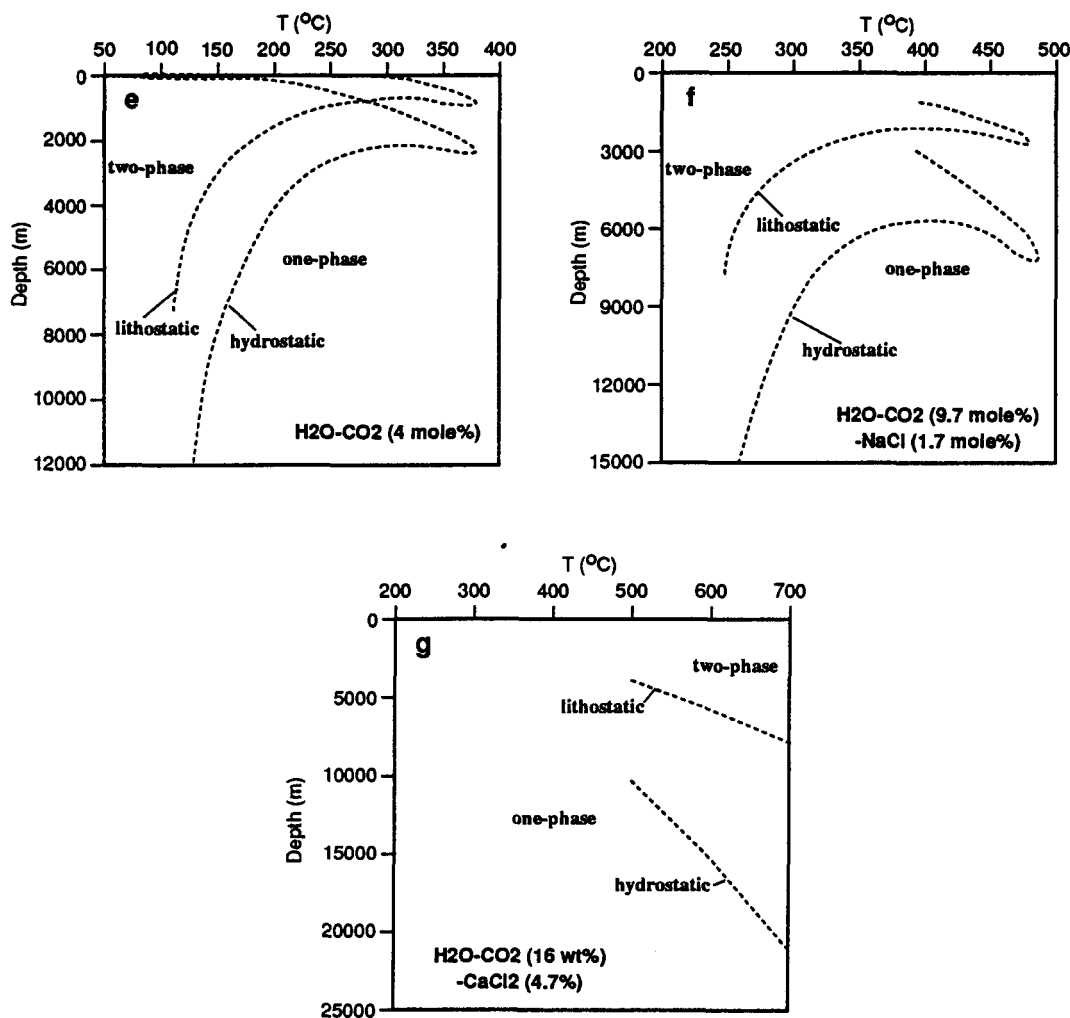


Fig. 67 Phase boundaries plotted on a temperature-depth diagram, showing the phase separation domains, for various fluid systems. (a) H₂O, P-T data from Raznjevic, 1975; (b) H₂O-NaCl (30 wt%), P-T data from Sourirajan and Kennedy (1962), Haas (1976) and Bodnar et al. (1985); (c) H₂O-KCl (20 wt%), T-P data from Bodnar and Sterner (1985); (d) H₂O-CaCl₂ (5.3 wt%), T-P data from Zhang and Frantz (1989) for T > 500 C and estimated from the equation by Khaibullin and Borisov (1966) for T < 500 C (the equation is for 2.0 molal NaCl-H₂O fluid, but it can be used for other salts and other concentrations, because at T < 500 C, the variation of P with composition on the phase boundary is relatively small, see Zhang and Frantz, 1987); (e) H₂O-CO₂ (4 mole%), T-P data from Gehrig et al. (1979); (f) H₂O-CO₂ (9.7 mole%)-NaCl (1.7 mole%), T-P data from Gehrig et al. (1979); (g) H₂O-CO₂ (16 wt%)-CaCl₂ (4.7 wt%), T-P data from Zhang and Frantz (1989). Density = 1.0 g/cm³ for the hydrostatic system; = 2.7 g/cm³ for the lithostatic system.

domain after the pressure system changes from lithostatic to hydrostatic, it will have to move up some distance to reach the two-phase domain.

Therefore, in order to determine whether phase separation takes place at the contact zone or in distal sites, and, in the latter case, the vertical distance between the site of phase separation and the contact of the intrusion, the following factors have to be estimated: (1) the depth of the emplacement of the intrusion; (2) the conditions of pressure: lithostatic or hydrostatic or a condition between the two? (3) the temperature of the fluid; (4) the bulk composition of the fluid.

8.5 Forced Venting vs. Convective Fluid Flow

The above discussions regarding the relationship between ore localization and the depth of magmatic intrusion, fluid migrational capacity and phase separation field, are based on the assumption that the flow of the ore-forming fluid is driven predominantly by the pressure contrast between lithostatic and hydrostatic systems (forced venting), which is supported by the geochemical studies of the ore minerals in the Xinlu ore field. However, the role of fluid convection has not been considered, and will be discussed as follows.

Unlike forced venting, fluid convection is not controlled by the pressure contrast between lithostatic and hydrostatic systems, but by the density difference of the fluid generated by a thermal anomaly. The convective flow can be described by the empirical relationship given by Darcy's Law (Norton and Cathles, 1979):

$$q = -(k/\nu) * (\rho g z + \nabla p)$$

where q is the fluid mass flux ($\text{g}/\text{cm}^2 \cdot \text{sec}$), k is permeability of the medium, ν is the dynamic viscosity of the fluid, ρ is the density of the fluid, z is a unit vector directed vertically ($z=0$ at the surface and negative downward), and ∇ is the gradient operator which gives the magnitude and direction of the most rapid change in hydrostatic pressure (P).

If there is no fluid flow, the mass flux (q) is zero, which requires the hydrostatic condition

$$\rho g z + \nabla p = 0$$

This equation can be written in vector form:

$$\begin{vmatrix} 0 \\ 0 \\ \rho g \end{vmatrix} + \begin{vmatrix} \partial P / \partial x \\ \partial P / \partial y \\ \partial P / \partial z \end{vmatrix} = \begin{vmatrix} 0 \\ 0 \\ 0 \end{vmatrix}$$

A consequence of this expression is that for no fluid flow, $\partial P/\partial x = \partial P/\partial y = 0$, indicating that pressure can only vary with depth and not with horizontal location. Therefore, conditions of no fluid flow require fluid density to be constant on horizontal planes. Then fluid flow is an inevitable consequence of fluid density variation on a horizontal plane at a given elevation, as is the case of magmatic intrusion environments.

The pattern of fluid convection is closely related to the shape of the intrusion. In the case of convex intrusion environment, the fluid flow pattern is characterized by upward flow above the intrusion and lateral flow toward the intrusion on the sides of the intrusion (Fig. 68, see Norton and Cathles, 1979 and Norton and Knight, 1977). In the case of concave intrusion environment, a downward flow in the central part (Fig. 68) can be expected from the thermal patterns (Fig. 59b and 62).

On the other hand, the venting of magmatic fluid is mainly controlled by the pressure contrast between the source of the fluid (\geq lithostatic) and the ground water surrounding the intrusion (\approx hydrostatic), which has been discussed by Whitney (1975) and Westra (1979). Most often the magmatic fluids vent upward (Cathles, 1981). As a consequence, the flow of magmatic fluid is upward even in the central part of a concave intrusion environment, where the convecting flow is downward.

The interaction of magmatic plume with convecting ground water is a subject which is less studied than magmatic forced venting and ground water convection separately (Cathles, 1981). One apparent effect of the convecting ground water on the venting fluid is the dispersion of heat and salinity by fluid mixing at the edges of the venting plume (Henley and McNabb, 1978). This effect may be stronger in the central part of a concave intrusion environment, where the flow direction of the convecting ground water is just opposite to that of the venting fluid. The temperature reduction due to mixing of ground water may influence the phase behaviour of the fluid, depending on the composition of the fluid. On the other hand, the heat released in volatile condensation will tend to offset the thermal losses due to mixing with cool ground water and therefore tends to produce isothermal conditions (Cathles, 1981), which will promote isothermal venting of the forthcoming fluids from the intrusion. Moreover, if the upward flow velocity is so high that the fluid-flow resistance plus the weight of the overlying fluids in the plume equals the hydrostatic pressure in the cold ground water (Cathles, 1981), the extent of ground water mixing will be greatly reduced.

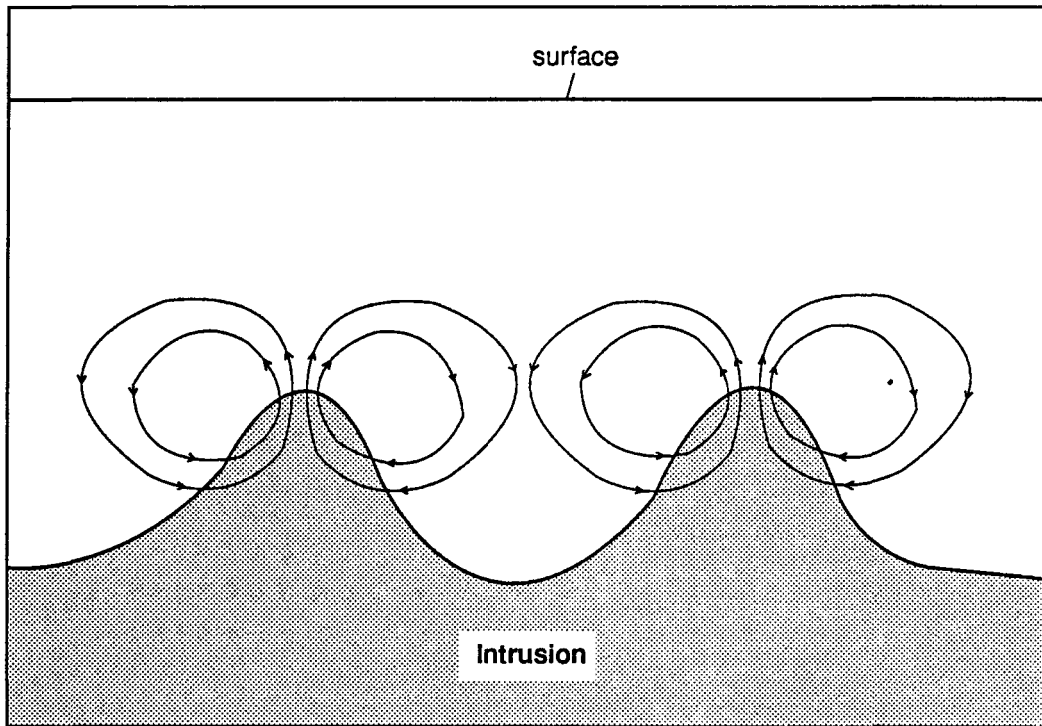


Fig. 68 Schematic diagram showing the fluid convection patterns in convex and concave intrusion environments.

In general, the relative importance of forced venting and convective fluid flow varies with specific cases. Although the mass of magmatic volatiles vented by a source is less than the mass of meteoric water likely to circulate in response to that source (Cathles, 1981), in most cases the ore-forming fluids are initiated as a magmatic fluid, which carries most of the ore-forming components. Even in the case of the Cornwall ore field, where O and H isotope data indicate that the ore-forming fluids were overwhelmingly of meteoric origin and that any magmatic signature has been diluted beyond recognition, it is believed that the ore-forming fluids had a magmatic provenance (Jackson et al., 1989). If the ore-forming fluids originated from melt-fluid segregation, forced venting will be the main mechanism for the release of the fluids. If the ore-forming fluids originated from fluid-rock (intrusive rocks included) interaction, and if this interaction took place after the interior of the intrusion had been connected with the outside hydrostatic condition, fluid convection will be the main form of fluid flow. Since most magmas intruding the earth's crust contain 2 to 9 wt% of water (Burnham, 1979), volatile release seems unavoidable during the crystallization of the magmatic intrusion. The pressure contrast at the departure of the magmatic fluid is generally higher than that generated by heat abnormal-induced density change, which drives the convection of the ground water. Therefore, it is believed that the ore localization models (with respect to the intrusion) in this study established on the basis of forced venting are applicable to most intrusion-associated hydrothermal deposits, although they may be distorted to variable extents, depending on the relative importance of forced venting and convection.

8.6 Possible Application of the Models in Ore Prospecting

It has been pointed out in chapter 1 that the most important element in a metallogenic model for exploration and prospecting geologists is to determine the factors that control the localization of the deposits. For intrusion-associated hydrothermal deposits, the focus of ore localization is the spatial distribution of ore deposits with respect to the intrusion. The models which have been discussed in this study are focused on the localization of proximal vs. distal deposits, which reflect two apparently different prospecting targets. In this section, an attempt will be made to apply these models to problems in ore prospecting. The questions that can be asked are: Under what conditions proximal deposits may be expected? What conditions may favour the formation of distal deposits? If distal deposits are predicted,

what is the probable vertical distance between the deposits and the unexposed intrusion? Apparently, these problems are so complicated that no single models can resolve them. However, the models established in this study do provide some insight toward the solution of the problems.

The models are based on the following presumptions: (1) the ore-forming fluid is derived from the magmatic intrusion; (2) the fluid flow is driven by the pressure contrast between the lithostatic pressure (within the intrusion) and the hydrostatic pressure (in the conduit system in the country rocks); (3) phase separation and/or temperature drop are the major mechanism of ore deposition. If all these presumptions are true, the mineralization will be most likely located in areas illustrated in Fig. 69. Proximal deposits (such as some porphyry copper deposits) will form along the contact zone of the stock which is above the hydrostatic phase-separation boundary. In fact, a model has been proposed by Cunningham (1978) to explain the envelope-like mineralization of porphyry copper deposits by phase separation. If the top of a protruding intrusion intersects with the phase-separation boundary, ore deposition will take place at the top contact (point B in Fig. 69). If the intrusion contact is below the phase-separation boundary, ore deposition will occur in some distance above the intrusion (point C and D in Fig. 69).

However, it is obvious that the presumptions are not likely to be completely satisfied in practical application. Therefore, one major task in applying the models in prospecting is to estimate how much the real situation deviates from the ideal models, which may be inferred from evidence such as petrological, mineralogical and geochemical characteristics of the ores. The various situations are illustrated in Fig. 69.

If the ore deposit is not genetically related to the magmatic intrusion, e.g., sedimentary mineralization (point E in Fig. 69), the localization of mineralization will not be related to any of the factors in the models. If there is a syngenetic enrichment of ore-forming components, and a superimposition of magmatic components is required to make a deposit, a coincidence of the syngenetic ore bed with a favourable deposition site of magmatic ore-forming components (e.g. phase-separation surface, point C in Fig. 69) will be a desirable prospecting target.

If the pressure system in the conduit system outside the intrusion is not completely hydrostatic, i.e., meta-hydrostatic, the phase separation surface will move to a higher level (point F in Fig. 69). However, at the same time, the velocity of fluid flow is reduced, which enhances the opportunity of reacting with the surrounding rocks and probably causes

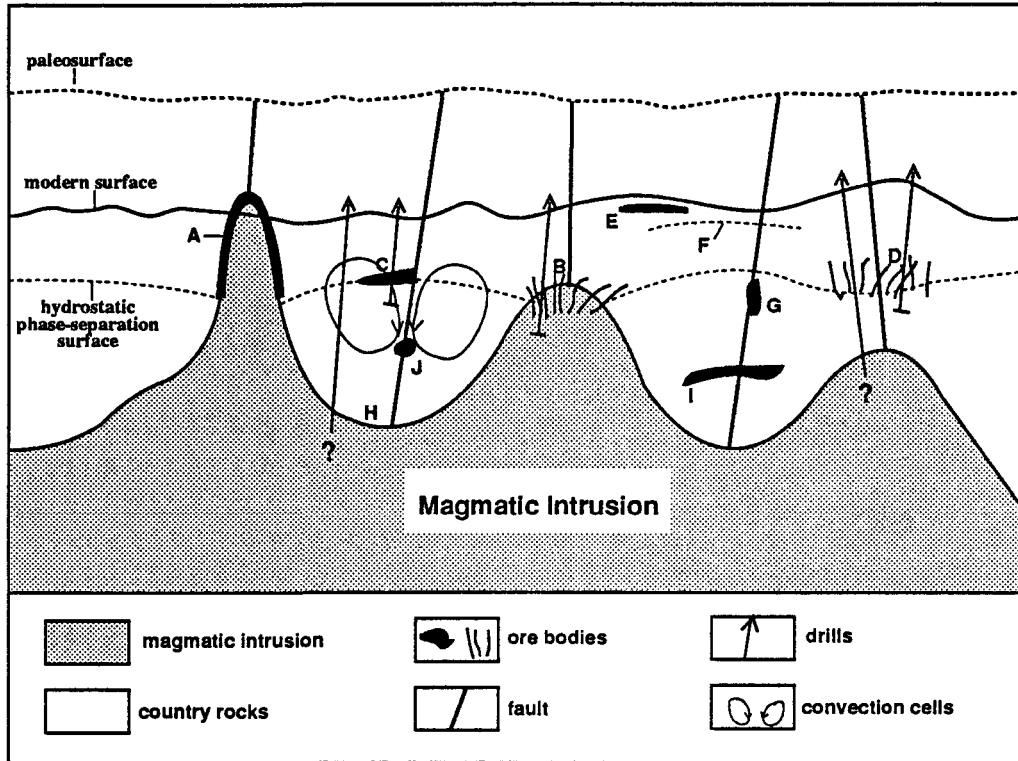


Fig. 69 A schematic diagram showing possible locations (A, B, C,, J) of mineralization with respect to the magmatic intrusion. See the text for explanation.

the deposition (point G in Fig. 69) of ore-forming components before reaching the phase-separation boundary.

If phase separation is not the major mechanism of ore deposition, other forms of ore deposition have to be considered, including temperature drop, chemical reaction with rock and mixing with other fluids (Skinner, 1979). Temperature drop has been considered in the thermal field models as described above. However, the models only show the tendency of temperature gradient in a concave intrusion environment vs. a convex environment. Although they have significance on differentiating proximal and distal prospecting targets as a whole, they cannot indicate a space as fixed as the phase-separation surface. A numeric simulation on real scale will be helpful, but again the temperature of ore deposition is related to the species of the ore components in the fluid and other physicochemical conditions. Since deep intrusion is often related to concave space (point H in Fig. 69), the phase-separation surface is broadly consistent with the high temperature-gradient zone. If chemical reaction is the main mechanism of ore deposition, the localization of mineralization will be related to the lithology of the country rocks; if a mineralization-favourable bed is developed near the conduit of the ore-forming fluid, a deposit may be formed even though the fluid is in the one-phase domain (point I in Fig. 69). If mixing with other fluids, e.g. convecting ground water, is the main mechanism of ore deposition, the site of mineralization may also be below the phase-separation surface (point J in Fig. 69), depending on where intensive mixing takes place.

In summary, real geological conditions are generally more complicated than the models established in this paper, and the application of the models should be based on geological observations, and should make full use of the data from other studies (geochemical, petrological, mineralogical, etc.). However, from the above discussions it is clear that the ore localization features indicated by the models exist in a wide range of geological conditions related to intrusion-associated hydrothermal deposits. Therefore, the models are helpful in selecting prospecting targets and designing the depth of diamond drill holes.

CHAPTER IX

CONCLUSIONS

The objective of this thesis was to study the various factors related to the localization of the proximal and distal tin-polymetallic deposits in the Xinlu ore field, including the geochemistry of host rocks and ore minerals, the sources of the ore-forming fluids, their conduits and migration dynamics, and the depositional conditions. The main conclusions are as follows.

1. The phase III and phase II intrusions of the Guposhan batholith belong to S-type granites, the former being derived from the latter through fractional crystallization. The phase I intrusions of the same batholith was derived from a S-I transitional source. The phase III granites have the highest ore-forming potential, and provided the majority of the ore-forming components in the Xinlu ore field.

2. The dykes are comagmatic with the intrusions of the Guposhan batholith. The compositional deviation of the dykes from corresponding granites may be due to contamination by sediments. The dykes have low capacity of providing ore-forming components.

3. The sedimentary rocks have lower contents of ore-forming elements than the granites except in a few beds. Their capacity of providing ore-forming elements is generally low.

4. Isotopes (S, O, Pb) of ore minerals indicate that the ore-forming fluids for both proximal and distal deposits in the Xinlu ore field were mainly derived from the granitic intrusions. Minor amounts of meteoric water were incorporated into the distal ore-forming fluids.

5. The separation of proximal and distal deposits are not caused by non-magmatic sources of the distal deposits or controlled by specific lithological units, nor an effect of metal zonation can be established.

6. The vertical distance from the sites of ore deposition to the granite intrusion surface is proportional to the depth of emplacement of the intrusions.

7. The orientation of most dyke-controlling structures were consistent with the principal compressive stress generated by granite intrusions, which promoted the extension of the structures, and provided effective conduits for the ore-forming fluids. Pre-existent structures that were reactivated by the force of granitic intrusion also provided conduits for the ore-forming fluids.

8. The fluid inclusions in cassiterite from proximal and distal ores and in quartz from granites indicate that the chemical system of the ore-forming fluids may be circumscribed by $\text{H}_2\text{O}-\text{CO}_2-\text{NaCl}-\text{CaCl}_2$. The common coexistence of relatively CO_2 -rich gas inclusions and relatively saline liquid inclusions indicates that fluid phase separation is probably an important mechanism of the deposition of both proximal and distal deposits. Phase separation was mainly related to pressure drop.

9. Homogenization temperatures of fluid inclusions are similar between proximal and distal deposits, being mainly from 320 to 500 °C for the former and from 280 to 460 °C for the latter, and indicating a rather small temperature gradient in the conduits of the ore-forming fluids and a high flow rate.

10. Fluid pressures estimated from fluid inclusions range from 446 to 792 bars for the distal deposits, from 148 to 404 bars for the proximal deposit, and from 124 to 2303 bars for the granites at Liuhe'ao. At the depth of 3900 m (estimated from stratigraphic data), these pressure values indicate that a pressure contrast may have existed between the interior of the intrusions (approximated by lithostatic system) and the contact zone and fractures in the country rocks (approximated by hydrostatic system), and was the major dynamics driving fluid flow.

11. The migrational capacity of the ore-forming fluids is related to the depth of emplacement of the intrusions. The pressure contrast between hydrostatic and lithostatic systems rapidly increases with depth, so that the flow rate of ore-forming fluids derived from an intrusion increases with increasing depth of emplacement of the intrusion, the effect of temperature drop is reduced, and the ore-forming components can be transported to a longer distance before being deposited.

12. The phase separation fields of the ore-forming fluids are related to the depth of emplacement of the intrusions such that when the intrusion is emplaced at high levels, the ore-forming fluid released from the intrusion changes from the one-phase domain under lithostatic system (within the intrusion) to the two-phase domain under hydrostatic system (at the contact zone), and phase separation takes place at the contact zone; whereas when the

intrusion is emplaced at deeper levels, the ore-forming fluid released from the intrusion remains in the one-phase domain after the pressure system has changed from lithostatic (within the intrusion) to hydrostatic (at the contact zone), and phase separation does not take place until the fluid ascends to a higher level.

13. Numerical modelling indicates that in a concave intrusion environment like the Xinlu ore field, the temperature gradient is lowest at the contact zone, and increases away from the intrusion, which is opposite to a convex intrusion environment. Since hydrothermal deposits tend to occur where the temperature of the ore-forming fluid drops in a localized area, namely in the high-temperature segment of the environment, proximal deposits are more difficult to form in a concave intrusion environment.

14. The separation of proximal and distal deposits in the Xinlu ore field resulted from a combination of several factors including fluid flow dynamics, phase separation, and thermal environment. Proximal deposits were developed when the intrusion was emplaced at relatively high level and had a convex surface; distal deposits were developed when the intrusion was emplaced relatively deeply and had a concave surface.

15. A preliminary survey of the literature indicates that the models established in the Xinlu ore field may be applied to a variety of intrusion-associated hydrothermal deposits in other regions in the world (although specific geological settings may distort the models to variable extents), and may be useful in selecting prospecting targets and establishing the depth of drilling.

REFERENCES

- Anderson, A. J., Clark, A. H., Macarthur, D. J., and Darsono, D. J. 1990. Proton-induced gamma-ray analysis of light elements in individual, unopened fluid inclusions: theory, methods and detection limits (abstract). Abstracts of the Third Biennial Pan-American Conference on Research on Fluid Inclusions (May 20-22, 1990, Toronto), p. 10.
- Ashley, P. M., and Plimer, I. R. 1989. "Stratiform skarns"--A re-evaluation of three eastern Australian deposits. *Mineralium Deposita*, **24**, pp. 289-298.
- Badham, J. P. N. 1975. Mineralogy, paragenesis and origin of the Ag-Ni, Co arsenide mineralization, Camsell River, N. W. T. Canada. *Mineralium Deposita*, **10**, pp. 153-175.
- Balashov, Yu. A., and Krigman, L. D. 1975. The effects of alkalinity and volatiles on rare-earth separation in magmatic systems. *Geochemistry International*, **12**, pp.165-170.
- Bandurkin, G. A. 1961. Behavior of the rare earths in fluorine-bearing media. *Geochemistry*, pp. 159-167.
- Barton, P. B., Bethke, P. M., and Roedder, E. 1977. Environment of ore deposition in the Creede mining district, San Juan Mountains, Colorado: Pt. III. Progress toward interpretation of the chemistry of the ore-forming fluid for the OH vein. *Economic Geology*, **72**, pp. 1-24.
- Bédard, L. P., and Barnes, S. J. 1990. Instrumental neutron activation analysis by collecting only one spectrum: results for international geochemical reference sample. *Geostandards Newsletter*, **14**, pp. 479-484.
- Beus, A. A., and Sitnin, A. A. 1968. Geochemical specialization of magmatic complexes as criteria for the exploration of hidden deposits. Proceedings of the 23th International Geological Congress, Section 6, pp. 101-105.
- Biste, M. 1982. Geochemistry of South Sardinian granites compared with their tin potential. *In Metallization Associated with Acid Magmatism. Edited by A. M. Evans.* John Wiley & Sons, pp. 37-50.
- Blake, D. H., and Smith, J. W. 1970. Mineralogical zoning in the Herberton tinfield, North Queensland, Australia. *Economic Geology*, **65**, pp. 993-997.
- Bodnar, R., and Beane, R. 1980. Temporal and spatial variations in hydrothermal fluid characteristics during vein filling in preore cover overlying deeply buried porphyry

- copper-type mineralization at Red Mountain, Arizona. *Economic Geology*, **75**, pp. 876-893.
- Bodnar, R. J., and Sterner, S. M. 1985. Synthetic fluid inclusions in natural quartz. II. Application to PVT studies. *Geochimica et Cosmochimica Acta*, **49**, 1855-1859.
- Bodnar, R. J., Burnham, C. W., and Sterner, S. M. 1985. Synthetic fluid inclusions in natural quartz. III. Determination of phase equilibrium properties in the system H₂O-NaCl to 1000°C and 1500 bars. *Geochimica et Cosmochimica Acta*, **49**, pp. 1861-1873.
- Bodnar, R. J., Reynolds, T. J., and Kuehn, C. A. 1985. Fluid-inclusion systematics in epithermal systems. *In* *Geology and geochemistry of epithermal systems. Edited by B. R. Berger and P. M. Bethke. Reviews in Economic Geology*, **2**, pp. 73-98.
- Boissavy-Vinau, M., and Roger, G. 1980. The TiO₂/Ta ratio as an indicator of the degree of differentiation of tin granites. *Mineralium Deposita*, **15**, 231-236.
- Borshchevskiy, Yu.A. 1979. Oxygen-isotope features of cassiterites from tin-ore deposits of Central Asia. *International Geological Review*, **21**, pp. 937-944.
- Bottinga, T., and Javoy, M. 1973. Comments on oxygen isotope geothermometry. *Earth and Planetary Science Letter*, **20**, pp. 250-265.
- Bowers, T. S., and Helgeson, H. C. 1983. Calculation of the thermodynamic and geochemical consequences of nonideal mixing in the system H₂O-CO₂-NaCl on phase relations in geologic systems: Equation of state for H₂O-CO₂-NaCl fluids at high pressures and temperatures. *Geochimica et Cosmochimica Acta*, **47**, pp. 1247-1275.
- Brown, P. E. 1989. FLINCOR: A microcomputer program for the reduction and investigation of fluid-inclusion data. *American Mineralogist*, **74**, pp. 1390-1393.
- Brown, P. E., and Lamb, W. M. 1989. P-V-T properties of fluids in the system H₂O-CO₂-NaCl: New graphical presentations and implications for fluid inclusion studies. *Geochimica et Cosmochimica Acta*, **53**, pp. 1209-1221.
- Burnham, C. W. 1967. Hydrothermal fluids at the magmatic stage. *In* *Geochemistry of Hydrothermal Ore Deposits. Edited by H. L. Barnes. Holt, Rinehart and Winston, Inc.*, pp. 34-76.
- Burnham, C. W. 1979. Magmas and hydrothermal fluids. *In* *Geochemistry of Hydrothermal Ore Deposits (2nd edition). Edited by H. L. Barnes. John Wiley & Sons*, pp. 71-136.
- Burnham, C. W., and Nekvasil, H. 1986. Equilibrium properties of granite pegmatite magmas. *American Mineralogist*, **71**, pp. 239-263.

- Burruss, R. C. 1981. Analysis of phase equilibria in C-O-H-S fluid inclusions. *In* Short Course in Fluid Inclusions: applications to petrology. *Edited by* L. S. Hollister and M. L. Crawford. Mineralogical Association of Canada, short course handbook, 6, pp. 39-74.
- Campbell, A. R., and Panter, K.S. 1990. Comparison of fluid inclusions in coexisting (cogenetic?) wolframite, cassiterite, and quartz from St. Michael's Mount and Cligga Head, Cornwall, England. *Geochimica et Cosmochimica Acta*, 54, pp. 673-681.
- Carmichael, I. S. E., Turner, F. J., and Verhoogen, J. 1974. *Igneous Petrology*. McGraw-Hill Book Company, 739 p.
- Cathles, L.M. 1981. Fluid flow and Genesis of hydrothermal ore deposits. *Economic Geology*, 75 Anniversary Volume, pp. 424-457.
- Chappell, B.W. 1984. Source rocks of I- and S-type granites in the Lachlan Fold Belt, southern Australia. *Philosophical Transactions of the Royal Society of London*, A310, pp. 693-707.
- Chappell, B. W., and White, A. J. R. 1974. Two contrasting granite types. *Pacific Geology*, 8, 173-174.
- Charoy, B. 1979. Définition et importance des phénomènes deutériques et des fluides associés dans les granites--Conséquences métallogéniques. Ph.D. thesis, Institut National Polytechnique de Lorraine (Ecole Nationale Supérieure de Géologie Appliquée et de Prospection Minière), France, 364 p.
- Chen, G. -D. 1959. The third tectonic element of the earth's crust--the diwa region (*in Chinese*). *Kexue Tongbao (Science Bulletin)*, 10, pp. 84-95.
- Chen, G. -D. 1965. Diwa region--a new type mobile region of postplatform stage (*in Chinese*). *In* *Geotectonic problems of China*. Science Press, Beijing.
- Chen, G. -D. 1988. *Tectonics of China*. International Academia Publishers, 258 p.
- Chen, Y. -C., Huang, M. -Z., Xu, Y., Ai, Y. -D., Li, X. -M., Tang, S. -H., and Meng, L. -K. 1987. Geological characteristics, mineralization features, models and sequences in the Dachang cassiterite-sulfide polymetallic mineralization belt, Guangxi (*in Chinese*). *In* *Proceedings of the International Conference on Geology of Sn Deposits (1984, China)*. *Edited by* J. -X. Tang. Geology Press, China, pp. 110-122.
- Chi, G. -X. 1989 a. A study of the multi-source characteristics of the diwa-stage granitoids and their tectonic mechanism in the Guposhan region, Guangxi (*in Chinese*). *Geotectonica et Metallogenia*, 12, pp. 69-79.

- Chi, G. -X. 1989 b. The diwa tectonics in western North America and comparison with the diwa regions in eastern China (*in Chinese*). *Geotectonica et Metallogenia*, **12**, pp. 352-363.
- Chi, G. -X. 1989 c. An analysis on the diwa-stage tectonics controlling the formation of magmatic rocks and ore deposits in the Ping-Bao region, South Hunan (*in Chinese*). *Diwa Tectonics and Metallogeny*, **3**, pp. 165-176.
- Chi, G. -X., Guha, J., and Lu, H. -Z. 1991. Correlating the depth of granitic intrusions with the localization of associated hydrothermal deposits--examples, preliminary model and possible application to mineral prospecting. GAC-MAC-SEG Program with Abstracts, **16**, p. A23.
- Chorlton, L. B., and Martin, R. F. 1978. The effect of boron on the granite solidus. *Canadian Mineralogist*, **16**, pp. 239-244.
- Collins, P. L. F. 1979. Gas hydrates in CO₂-bearing fluid inclusions and the use of freezing data for estimation of salinity. *Economic Geology*, **74**, pp. 1435-1444.
- Coulombe, L., and Poitras, A. 1986. Livret guide de l'utilisateur pour la méthode d'analyses par activation neutronique instrumentale. Unpublished.
- Crawford, M. L. 1981. Phase equilibria in aqueous fluid inclusions. *In Short Course in Fluid Inclusions: applications to petrology. Edited by L. S. Hollister and M. L. Crawford. Mineralogical Association of Canada, short course handbook*, **6**, pp. 75-100.
- Cunningham, C. G. 1978. Pressure gradients and boiling as mechanisms for localizing ore in porphyry systems. *Journal of Research of U.S. Geological Survey*, **6**, pp.745-754.
- Demin, U. I., and Zolotarev, V. G. 1980. Isothermal stabilization and gradient zones in granitoid fields and the possibilities of finding mineral deposits (*in Russian*). *Geochemistry*, No.5, pp. 3-17.
- Deng, Q. -P. 1984. A preliminary study on the tin mineralization series associated with the diwa-stage granites in the Xinlu ore field with emphasis on the genesis of the Baimianshan deposit, northeastern Guangxi (*in Chinese*). M.Sc. thesis, Central-South University of Technology, Changsha, China.
- Deng, Q. -P. 1985. A preliminary study on the genesis of the Baimianshan cassiterite-sulfide deposit (*in Chinese*). *Journal of Guilin College of Geology*, **5**, pp. 239-249.
- Dingwell, D. B. 1985. The structure and properties of fluorine-rich silicate melts: implications for granite petrogenesis: *In Granite-related Mineral Deposits Geology*,

- Petrogenesis and Tectonic Setting. *Edited by* R. P. Taylor and D. F. Strong. CIM Conference on Granite-related Mineral Deposits, pp. 72-81.
- Dingwell, D. B. 1988. The structures and properties of fluorine-rich magmas: a review of experimental studies. *In* Recent Advances in Granite-related Mineral Deposits. *Edited by* R. P. Taylor and D. F. Strong. The Canadian Institute of Mining and Metallurgy, special volume 39, pp. 1-12.
- Doe, B. R., and Stacey, J. S. 1974. The application of lead isotopes to the problems of ore genesis and ore prospect evaluation: a review. *Economic Geology*, **69**, pp. 757-776.
- Doe, B. R., and Zartman, R. E. 1979. Plumbotectonics, the Phanerozoic. *In* Geochemistry of Hydrothermal Ore Deposits (2nd edition). *Edited by* H. L. Barnes. John Wiley & Sons, pp. 22-70.
- Donaldson, I. G. 1968. The flow of steam water mixtures through permeable beds: a simple simulation of a natural undisturbed hydrothermal region. *New Zealand Journal of Science*, **5**, pp. 337-357.
- Dong, Z. -C. 1989. The Bojiling granite and its relation to the Liuhe'ao ore deposits, Xinlu, Guangxi (*in Chinese*). *Journal of the Guilin College of Geology*, **9**, pp. 35-43.
- Dostal, J., and Elson, C. 1980. General principles of neutron activation analysis. *In* Short Course in Neutron Activation Analysis in the Geosciences. *Edited by* G. K. Muecke. Mineralogical Association of Canada, Short Course Handbook, **5**, pp. 21-42.
- Drummond, S. E., and Ohmoto, H. 1985. Chemical evolution and mineral deposition in boiling hydrothermal systems. *Economic Geology*, **80**, pp. 126-147.
- Eadington, P. J. 1988. The solubility of cassiterite in hydrothermal solution in relation to some lithological and mineral association of tin ores. *In* Recent Advances in Granite-related Mineral Deposits. *Edited by* R. P. Taylor and D. F. Strong. The Canadian Institute of Mining and Metallurgy, special volume 39, pp. 25-32.
- Flynn, R. T., and Burnham, C. W. 1978. An experimental determination of rare earth partition coefficients between a chloride containing vapour phase and silicate melts. *Geochimica et Cosmochimica Acta*, **42**, pp. 685-701.
- Fournier, R. O. 1969. Depths of intrusion and conditions of hydrothermal alteration in porphyry copper deposits (abstract). *Geological Society of America Special Paper*, **121**, p. 101.

- Fournier, R. O. 1972. The importance of depth of crystallization on the character of magmatic fluids. Proceedings of 24th International Geological Congress, Section 10, p. 214.
- Fu, M. -L. 1984. Geochemistry of the Changpo cassiterite-sulfide deposit, Dachang, Guangxi (*in Chinese*). M.Sc. thesis, Guilin College of Geology, Guilin, China.
- Fyfe, W. S., Price, N. J., and Thompson, A. B. 1978. Fluid in the earth's crust. Development in Geochemistry, 1. Elsevier Scientific Publishing Company, 383 p.
- Gehrig, M., Lentz, H., and Franck, E. U. 1979. Thermodynamic properties of water-carbon dioxide-sodium chloride mixtures at high temperatures and pressures. *In* 6th International conference on high-pressure science and technology, volume 1, Physical properties and material synthesis. Edited by K. D. Timmerhaus and M. S. Barber. Plenum Press, New York, pp. 539-542.
- Ginzburg, A. I., Kupriyanova, I. I., and Feldman, L. G. 1974. A model for the geological-geochemical system "granite intrusive-rare-metal ore mineralization". *In* Metallization associated with acid magmatism, volume 1. Edited by M. Stempok. Publishing House of the Czechoslovak Academy of Sciences, Prague, pp. 95-98.
- Gong, A., Wen, S. -Y., and Wei, Y. -S. 1985. Origin and evolution of the west part of the Guposhan granite batholith (*in Chinese*). Journal of Guilin College of Geology, 5, pp. 21-30.
- Graf, Jr. J. L. 1977. Rare earth elements as hydrothermal tracers during the formation of massive sulfide deposits in volcanic rocks. Economic Geology, 72, pp. 527-548.
- Guha, J., Lu, H. -Z., Gagnon, M. 1990. Gas composition of fluid inclusions using solid probe mass spectrometry and its application to the study of mineralizing processes. Geochimica et Cosmochimica Acta, 54, pp. 553-558.
- Haas, J. L. Jr. 1976. Thermodynamic properties of the coexisting phases and thermodynamic properties of the NaCl component in boiling NaCl solutions. U. S. Geological Survey Bulletin, 1421-B, 71 p.
- Hanson, G. N. 1978. The application of trace elements to the petrogenesis of igneous rocks of granitic composition. Earth and Planetary Science Letters, 38, pp. 26-43.
- Henley, R. W. 1985. The geothermal framework of epithermal deposits. *In* Geology and geochemistry of epithermal systems. Edited by B. R. Berger and P. M. Bethke. Reviews in Economic Geology, 2, pp. 1-24.

- Henley, R. W., and McNabb, A. 1978. Magmatic vapor plumes and ground water interaction in porphyry copper emplacement. *Economic Geology*, **73**, pp. 1-20.
- Hesp, W. R., and Varlamoff, N. 1977. Temporal and spatial relations between the formation of acid magmatic rocks and deposits. *In Metallization associated with acid magmatism, volume 2. Edited by M. Stemprok, L. Burnol and G. Tischendorf. Published by the Geological Survey of Czechoslovakia*, pp. 23-40.
- Hoefs, J. 1973. Stable isotope geochemistry. *Minerals, Rocks and Inorganic Materials*, **9**.
- Holland, H. D. 1972. Granites, solutions, and base metal deposits. *Economic Geology*, **67**, pp. 281-301.
- Hu, H. -Y. 1986. On the mineralization conditions and ore-searching direction of primary tin deposits in the Ping-Gui region, Guangxi (*in Chinese*). Unpublished.
- Hu, H. -Y., Dong, Z. -C., and Qiu, L. -B. 1989. The mineralization features and prediction of hidden ore bodies in the Baimianshan and Liuhe'ao tin-polymetallic deposits, Xinlu, Guangxi (*in Chinese*). Report of the Ping-Gui tin mineralization project of the Changsha Institute of Geotectonics in cooperation with the Ping-Gui Mining Bureau. Unpublished.
- Huang, R. -H., Du, F. -Q., Wang, F. -Q., and Wu, Q.-H. 1985. Tectonochemistry of tin in Southeast Diwa Region (*in Chinese*). Research Report of Changsha Institute of Geotectonics, Academia Sinica, 170 p.
- Hubbert, M. K., and Rubey, W. W. 1959. Role of fluid pressure in mechanics of overthrust faulting. *Geological Society of America Bulletin*, **70**, pp. 115-167.
- Irving, E. 1979. Pole positions and continental drift since the Devonian. *In The Earth: its origin, structure and evolution. Edited by M. W. McElhinny. Academic Press, London*, pp. 567-593.
- Jackson, K. J., and Helgeson, H. C. 1985. Chemical and thermodynamic constraints on the hydrothermal transport and deposition of tin: II. interpretation of phase relations in the Southeast Asian tin belt. *Economic Geology*, **80**, pp. 1365-1378.
- Jackson, N. J., Willis-Richards, J., Manning, D. A. C., and Sams, M. S. 1989. Evolution of the Cornubian ore field, Southwest England: Part II, mineral deposits and ore-forming processes. *Economic Geology*, **84**, pp. 1101-1133.
- Jensen, M. L. 1967. Sulfur isotope and mineral genesis. *In Geochemistry of Hydrothermal Ore Deposits. Edited by H. L. Barnes. Holt, Rinehart and Winston, Inc.*, pp. 143-165.

- Kamilli, R. J., and Ohmoto, H. 1977. Paragenesis, zoning, fluid inclusion, and isotopic studies of the Finlandia vein, Colqui district, central Peru. *Economic Geology*, **72**, pp. 950-982.
- Kelly, Wm. C., and Turneure, F. S. 1970. Mineralogy, paragenesis and geothermometry of the tin and tungsten deposits of the Eastern Andes, Bolivia. *Economic Geology*, **65**, pp. 69-80.
- Khaibullin, K. H., and Borisov, N. M. 1966. Experimental investigation of the thermal properties of aqueous and vapor solutions of sodium and potassium chlorides at phase equilibrium. *High Temperature (U.S.S.R.)*, **7**, pp. 489-494.
- Kirkham, R. V., and Sinclair, W. D. 1988. Comb quartz layers in felsic intrusions and their relationship to porphyry deposits. *In Recent Advances in Granite-related Mineral Deposits. Edited by R. P. Taylor and D. F. Strong. The Canadian Institute of Mining and Metallurgy, special volume 39*, pp. 50-71.
- Kovalenko, V. I. 1978. The genesis of rare metal granitoids and related ore deposits. *In Metallization Associated with Acid Magmatism, volume 3. Edited by M. Stemprok, L. Burnol and G. Tischendorf. Geological Survey of Czechoslovakia*, pp. 235-248.
- Kreith, F., and Bohn, 1986. Principles of heat transfer (fourth edition). Harper & Row, Publishers, New York, 700 p.
- Kwak, T. A. P. 1987. W-Sn skarn deposits and related metamorphic skarns and granitoids. *Developments in Economic Geology*, **24**. Elsevier Scientific Publishing Company.
- Lai, L. -R., and Zen, N. -S. 1985. Geochemistry of tin in skarn mineralization in the Ping-Gui district (*in Chinese*). *Geology and Prospecting*, **21**, pp. 16-21.
- Lawrence, G. 1975. The use of Rubidium/Strontium ratios as a guide to mineralization in the Galway granite, Ireland. *In Geochemical Exploration 1974. Edited by I. L. Elliott and W. K. Fletcher. Development in Economic Geology*, **1**. Elsevier Scientific Publishing Company, pp. 353-370.
- Laznicka, P. 1985. Empirical metallogeny--depositional environments, lithologic association and metallic ores, volume 1: Phanerozoic environments, association and deposits, part B. *Developments in Economic Geology*, **19**. Elsevier Scientific Publishing Company, 1758 p.
- Laznicka, P. 1986. Ensilic activation metallogeny in North America, a counterpart of Chinese diwa metallogeny. *Geotectonica et Metallogenia*, **10**, pp. 1-24.

- Li, J. -S. 1986. The relationship between the tin deposits and the strata in the Ping-Gui mineralization district (*in Chinese*). Base Metal Geology of Guangxi, (1986)-No.1, pp. 17-30.
- Li, Y. -X. 1985. Devonian lithofacies and paleogeography and their relationships with tin deposits in the Fuchuan-Zhongshan-Hexian Area, Guangxi (*in Chinese*). Geology Review, **31**, pp. 429-436.
- Liang, Y. -H., and Lu, L.-S. 1987. Geochemical characteristics of Devonian system in central and eastern Guangxi (*in Chinese*). Collected Reports on Geology and Mineral Resources in the Nanling Region, volume 1. Wuhan College of Geology Publishing House, pp.103-144.
- Liu, G. -Q., and Chang, H. -L. 1987. Thermobarogeochemical study on some Yanshanian granitic intrusions and related vein-type tungsten deposits in the Nanling region (*in Chinese*). Collected Reports on Geology and Mineral Resources in the Nanling Region, volume 1. Wuhan College of Geology Publishing House, pp. 145-196.
- Liu, W. -L., and Yuan, K. -R. 1989. On the source of ore-forming materials and tin enrichment mechanism of the Xinlu-Shuiyanba tin deposits, Guangxi (*in Chinese*). Journal of Guilin College of Geology, **9**, pp. 283-291.
- Liu, Y. -X., Wu, K. -H., Yu, T. -J., and Li, C. -C. 1987. Characteristics of fluid inclusions from tin deposits in Dachang and northern Guangxi (*in Chinese*). In Proceedings of the International Conference on Geology of Sn Deposits (1984, China). Edited by J. -X. Tang. Geology Press, China, pp. 241-246.
- Lu, H. -Z. 1983. Genesis of tungsten ore deposits in south China. Ph.D. thesis, University of Pennsylvania, 251 p.
- Lu, H. -Z., Wang, Z. -F., Xu, S. -J., and Guo, Y. -Q. 1979. Fluid inclusion characteristics and the temperature of formation of the Dachang and Gejiu tin deposits (*in Chinese*). In Fluid inclusion study in minerals. Edited by Guiyang Institute of Geochemistry, Academia Sinica. Science and Technology Literature Publishing House, China, pp. 130-148.
- Macdonald, A. J. 1983. Boss Mountain molybdenite deposit: Fluid geochemistry and hydrodynamic considerations. Ph.D. thesis, University of Toronto.
- Manning, D. A.C. 1981. The effect of fluorine on liquidus relationships in the system Qz-Ab-Or with excess water at 1 kb: Contributions to Mineralogy and Petrology, **76**, pp. 206-215.

- Manning, D. A. C., and Pichavant, W. 1988. Volatiles and their bearing on the behaviour of metals in granitic systems. *In* Recent Advances in Granite-related Mineral Deposits. *Edited by* R. P. Taylor and D. F. Strong. The Canadian Institute of Mining and Metallurgy, special volume 39, pp. 13-24.
- Mason, B. 1966. Principles of Geochemistry. John Wiley & Sons, Inc., 329 p.
- Matsuhisa, Y., Goldsmith, J. R., and Clayton, R.N. 1979. Oxygen isotopic fractionation in the system quartz-albite-anorthite-water. *Geochimica et Cosmochim. Acta*, **43**, pp. 1131-1140.
- Mineyev, D. A., Dikov, Yu. P., Sobolev, B. P., and Borutskaya, V. L. 1966. Differentiation of rare earth elements under supercritical conditions. *Geochemistry International*, **3**, pp. 357-359.
- Moore, J. M. 1975. A mechanical interpretation of the vein and dyke systems of the S.W. England ore field. *Mineralium Deposita*, **10**, pp. 374-388.
- Muecke, G. K., and Clarke, D. B. 1981. Geochemical evolution of the South Mountain batholith, Nova Scotia: rare-earth-element evidence. *Canadian Mineralogist*, **19**, pp. 133-145.
- Neiva, A. M. R. 1984. Geochemistry of tin-bearing granite rocks. *Chemical Geology*, **43**, pp. 241-256.
- Neumann, W., and Huster, H. 1974. The half-life of ^{87}Rb measured as a difference between the isotopes ^{87}Rb and ^{85}Rb . *Z. Physik*, **270**, pp. 121-127.
- No.8 Geologic Team of Guangxi. 1981. Regional geological map of the Xinlu mining district with distribution of mineralization occurrences and geochemical prospecting (*in Chinese*). Unpublished.
- No.204 Geologic Team of Guangxi. 1979. Geological characteristics and ore-controlling factors of the Baimianshan cassiterite-sulfide deposit (*in Chinese*). Unpublished.
- No.204 Geologic Team of Guangxi. 1986. Extent of geological work in the Ping-Gui district and suggestions for further prospecting (*in Chinese*). Unpublished.
- Norton, D. 1978. Sourcelines, source regions, and pathlines for fluids in hydrothermal systems related to cooling plutons. *Economic Geology*, **73**, pp. 21-28.
- Norton, D., and Cathles, L.M. 1979. Thermal aspects of ore deposition. *In* Geochemistry of Hydrothermal Ore Deposits (2nd edition). *Edited by* H. L. Barnes. John Wiley & Sons, pp. 611-631.

- Norton, D. and Knight, J. 1977. Transport phenomena in hydrothermal systems: cooling plutons. *American Journal of Science*, **277**, pp. 937-981.
- Oakes, C. S., Bodnar, R. J., and Simonson, J. M. 1990. The system NaCl-CaCl₂-H₂O: I. The ice liquidus at 1 atm total pressure. *Geochimica et Cosmochimica Acta*, **54**, 603-610.
- Ohmoto, H. 1986. Stable isotope geochemistry of ore deposits. *In Stable Isotopes in High Temperature Geological Processes. Edited by J. W. Valley, H. P. Taylor, Jr. and J. R. O'Neil. Review in Mineralogy*, **16**, pp. 491-559.
- Ohmoto, H., and Rye, R. O. 1979. Isotopes of sulfur and carbon. *In Geochemistry of Hydrothermal Ore Deposits (2nd edition). Edited by H. L. Barnes. John Wiley & Sons*, pp. 509-567.
- Patterson, D. J., Ohmoto, H., and Solomon, M. 1981. Geologic setting and genesis of cassiterite-sulfide mineralization at Renison Bell, Western Tasmania. *Economic Geology*, **76**, pp. 393-438.
- Pichavant, M., and Wyart, J. 1981. Application des données expérimentales aux conditions de genèse et de cristallisation des leucogranites à tourmaline. *Comptes Rendus Académie des Sciences Paris, Série II*, **292**, pp. 851-854.
- Pichavant, M., Ramboz, C. and Weisbrod, A. 1982. Fluid immiscibility in natural processes: use and misuse of the fluid inclusion data, I--phase equilibria analysis--a theoretical and geometrical approach. *Chemical Geology*, **37**, pp. 1-27.
- Ping-Gui Mining Bureau. 1986. A brief description of the exploration extent of the ore deposits and occurrences in the Ping-Gui mining district (*in Chinese*). Unpublished.
- Polya, D. A. 1989. Chemistry of the main-stage ore-forming fluids of the Panasqueira W-Cu (Ag)-Sn deposit, Portugal: implication for models of ore genesis. *Economic Geology*, **84**, pp. 1134-1152.
- Potter II, R. W., Babcock, R. S., and Brown, D. L. 1977. A new method for determining the solubility of salts in aqueous solutions at elevated temperatures. *Journal of Research of U.S. Geological Survey*, **5**, pp. 389-395.
- Pu, L. -P. 1986. Origin of the Guposhan granite batholith and the enclaves (*in Chinese*). M.Sc. thesis, Central-South University of Technology, Changsha, China.
- Qian, J. -P. 1985. Tectonogeochemical evolution of western Guangdong (*in Chinese*). M.Sc. thesis, Changsha Institute of Geotectonics, Academia Sinica, Changsha, China.

- Qin, C. -X. 1985. The temporal-spatial model of mineralization in the Xinlu tin ore field, northeast Guangxi (*in Chinese*). M.Sc. thesis, Wuhan College of Geology, Wuhan, China.
- Qiu, L. -B. 1989. Geological features and ore-controlling role of the favourable layers in the Baimianshan stannolite-sulfide ore deposit, Xinlu, Guangxi (*in Chinese*). M.Sc. thesis, Changsha Institute of Geotectonics, Academia Sinica, Changsha, China, 58 p.
- Ramboz, C., Pichavant, M., and Weisbrod, A. 1982. Fluid immiscibility in natural processes: use and misuse of the fluid inclusion data, II--interpretation of fluid inclusion data in terms of immiscibility. *Chemical Geology*, **37**, pp. 29-48.
- Rankin, A. H., Ramsey, M. H., Coles, B., Langevelde, B., Van, F., and Thomas, C. R. 1990. Ore metal contents of hypersaline iron-rich granitic fluids based on laser-ICP and synchrotron XRF-microprobe analysis of individual fluid inclusions in topaz (abstract). Abstracts of the Third Biennial Pan-American Conference on Research on Fluid Inclusions (May 20-22, 1990, Toronto), p. 73.
- Raznjevic, K. 1975. Handbook of thermodynamic tables and charts. Hemisphere Publishing Corporation, 392 p.
- Reynolds, J. 1988. Instruction manual of the U.S.G.S. gas-flow heating/freezing system. Unpublished.
- Rittman, A. 1973. Stable mineral assemblages of igneous rocks. Springer Verlag, Berlin.
- Rock, N. M. S. 1989. CIPW: A terminal-interactive FORTRAN 77 program for tabulating extended CIPW norms from large batches of analyses. *COGS Computer Contributions*, **5**, pp.17-41.
- Roedder, E. 1984 a. Interpretation and utilization of inclusion measurements--compositional data on liquid and gas inclusions. *In Fluid Inclusions. Edited by P. H. Ribbe. Reviews in Mineralogy*, **12**, pp. 221-250.
- Roedder, E. 1984 b. Interpretation and utilization of inclusion measurements--temperature, pressure and density at trapping. *In Fluid Inclusions. Edited by P. H. Ribbe. Reviews in Mineralogy*, **12**, pp. 251-290.
- Roedder, E. 1990. Fluid inclusion analysis--prologue and epilogue. *Geochimica et Cosmochimica Acta*, **54**, pp. 495-507.
- Roedder, E., and Bodnar, R.J. 1980. Geologic pressure determinations from fluid inclusion studies. *Annual Review of Earth and Planetary Sciences*, **8**, pp. 263-301.

- Rundkvist, D. V., 1977. The distribution of mineral zones associated with granitoid magmatism and rare-metal mineralization in space and time. *In Metallization associated with acid magmatism, volume 2. Edited by L. Burnol and G. Tischendorf. Publishing House of the Czechoslovak Academy of Sciences, Prague, pp. 11-22.*
- Rundkvist, D. V., 1982. Zoning of metallization associated with acid magmatism. *In Metallization Associated with Acid Magmatism. Edited by A. M. Evans. John Wiley & Sons, pp. 279-290.*
- Sams, M. S., and Thomas-Betts, A. 1988. Models of convective fluid flow and mineralization in south-west England. *Journal of the Geological Society, London, 145, pp. 809-817.*
- Schwartz, M. O., and Askury, A. K. 1989. Geologic, geochemical, and fluid inclusion studies of the tin granites from the Bujang Melaka pluton, Kinta Valley, Malaysia. *Economic Geology, 84, pp. 751-779.*
- Seal, R. R., Clark, A. H., and Morrissy, C. J. 1987. Stockwork Tungsten (Scheelite)-molybdenum mineralization, Lake George, Southwest New Brunswick. *Economic Geology, 82, pp. 1259-1282.*
- Seal, R. R., Clark, A. H., and Morrissy, C. J. 1988. Lake George, southwestern New Brunswick: a Silurian, multi-stage, polymetallic (Sb-W-Mo-Au-base metal) hydrothermal centre. *In Recent Advances in Granite-related Mineral Deposits. Edited by R. P. Taylor and D. F. Strong. The Canadian Institute of Mining and Metallurgy, special volume 39, pp. 252-264.*
- Shan, Z. -H. 1987. The geological characteristics, mineralization sequence and models of the Ping-Gui tin mineralization district (*in Chinese*). *Geology of Guangxi, 1987-No.2, pp. 91-96.*
- Sheets, R. W., Oakes, C. S., and Bodnar, R. J. 1990. Metastable and stable phase relationship in the system NaCl-CaCl₂-H₂O. *Abstracts of All GSA Meetings 1990.*
- Sheglov, A. D. 1968. Endogenous deposits of the regions of autonomous activation. *In Proceedings of the International Geological Congress (1968), section 7. pp. 43-55.*
- Sheppard, S. M. F. 1986. Characterization and isotopic variations in natural waters. *In Stable Isotopes in High Temperature Geological Processes. Edited by J. W. Valley, H. P. Taylor, Jr. and J. R. O'Neil. Review in Mineralogy, 16, pp. 165-184.*
- Shong, C.-A. 1984. Compositional features of fluid inclusions from tin deposits in Limu

- and Ping-Gui regions and their significance in ore prediction (*in Chinese*). *Yuannan Geology*, **3**, pp. 229-236.
- Skinner, B. J. 1979. The many origins of hydrothermal mineral deposits. *In Geochemistry of Hydrothermal Ore Deposits* (2nd edition). *Edited by* H. L. Barnes. John Wiley & Sons, pp. 1-12.
- Sourirajan, S., and Kennedy, G. C. 1962. The system H₂O-NaCl at elevated temperatures and pressures. *American Journal of Sciences*, **260**, 115-141.
- Spooner, E. T. C. 1981. Fluid inclusion studies of hydrothermal ore deposits. *In Short Course in Fluid Inclusions: applications to petrology. Edited by* L. S. Hollister and M. L. Crawford. Mineralogical Association of Canada, short course handbook, **6**, pp. 209-240.
- Stewart, D. B. 1978. Petrogenesis of lithium-rich pegmatites. *American Mineralogist*, **63**, pp. 970-980.
- Strecheisen, A. 1976. To each plutonic rock its proper name. *Earth Science Review*, **12**, pp. 1-33.
- Strong, D. F. 1981. A model for granophile mineral deposits. *Geoscience Canada*, **8**, pp. 155-161.
- Strong, D. F. 1988. A review and model for granite-related mineral deposits. *In Recent Advances in Granite-related Mineral Deposits. Edited by* R. P. Taylor and D. F. Strong. The Canadian Institute of Mining and Metallurgy, special volume 39, pp. 424-445.
- Sun, S. S., and Eadington, P.J. 1987. Oxygen isotope evidence for the mixing of magmatic and meteoric waters during tin mineralization in the Mole granite, New South Wales, Australia. *Economic Geology*, **82**, pp. 43-52.
- Sun, N., and Peng, Y. -M. 1985. *Igneous Petrology (in Chinese)*. Geology Press, China, 324 p.
- Tanelli, G. 1982. Geological setting, mineralogy and genesis of tungsten mineralization in Dayu district, Jiangxi (People's Republic of China): an outline. *Mineralium Deposita*, **17**, pp. 279-294.
- Taylor, R. P., and Fryer, B. J. 1982. Rare earth element geochemistry as an aid to interpreting hydrothermal ore deposits. *In Metallization Associated with Acid Magmatism. Edited by* A. M. Evans. John Wiley & Sons, pp.357-366.
- Taylor, R. G., and Steveson, B. G. 1972. An analysis of metal distribution and zoning in

- the Herberton tinfield, North Queensland, Australia. *Economic Geology*, **67**, pp. 1234-1240.
- Tischendorf, G. 1977. Geochemical and petrographic characteristics of silicic magmatic rocks associated with rare-element mineralization. *In Metallization associated with acid magmatism, volume 2. Edited by M. Stempok, L. Burnol and G. Tischendorf. Published by the Geological Survey of Czechoslovakia, pp. 41-98.*
- Tischendorf, G., Lachelt, S., Lange, H., Palchen, W., and Meinel, G. 1972. Geochemical specialization of granitoids in the territory of the German Democratic Republic. *Proceedings of the 24th International Geological Congress, Section 4, pp.266-275.*
- Tu, G. -Z. 1987. Genesis of the Dachang ore deposit with discussion on the formation conditions of cassiterite-sulfide deposits (*in Chinese*). *In Proceedings of the International Conference on Geology of Sn Deposits (1984, China). Edited by J. -X. Tang. Geology Press, China, pp. 105-109.*
- Turcotte, D. L., and Schubert, G. 1982. *Geodynamics--application of continuum physics to geological problems. John Wiley & Sons, 435 p.*
- Urabe, T. 1985. Aluminous granite as a source magma of hydrothermal ore deposits: an experimental study. *Economic Geology*, **80**, pp. 148-157.
- Vanco, D. A., Bodnar, R. J., and Sterner, S. M. 1988. Synthetic fluid inclusions: VIII. Vapor-saturated halite solubility in part of the system NaCl-CaCl₂-H₂O, with application to fluid inclusions from oceanic hydrothermal systems. *Geochimica et Cosmochimica Acta*, **52**, pp. 2451-2456.
- Wall, V. J., Clements, J. D., and Clarke, D. B. 1987. Models for granitoid evolution and source compositions. *The journal of Geology*, **95**, pp. 731-749.
- Weisbrod, A. 1981. Fluid inclusions in shallow intrusives. *In Short Course in Fluid Inclusions: applications to petrology. Edited by L. S. Hollister and M. L. Crawford. Mineralogical Association of Canada, short course handbook, 6, pp. 241-271.*
- Wendlandt, R. F., and Harrison, W. J. 1979. Rare earth partitioning between immiscible carbonate and silicate liquids and CO₂ vapour: results and implications for the formation of light rare earth-enriched rocks. *Contributions to Mineralogy and Petrology*, **69**, pp. 409-419.
- Werre, Jr. R. W., Bodnar, R. J., Bethke, P. M., and Barton, Jr. P. B. 1979. A novel gas-flow fluid inclusion heating/freezing stage (abstract). *Geological Society of America Abstract with Programs*, **11**, p. 539.

- Westra, G. 1979. Porphyry copper genesis at Ely, Nevada. *In* Papers on mineral deposits in western North America. *Edited by* J. Rodge. Nevada Bureau Mines and Geology Report, **33**, pp. 127-140.
- White, A. J. R., and Chappell, B.W. 1977. Ultrametamorphism and granitoid genesis. *Tectonophysics*, **43**, pp.7-22.
- White, A. J. R., and Chappell, B.W. 1983. Granitoid types and their distribution in the Lachlan Fold Belt, southeastern Australia. *Geological Society of America Memoir*, **159**, pp. 21-34.
- Whitney, J. A. 1975. Vapor generation in a quartz monzonite magma: a synthetic model with application to porphyry copper deposits. *Economic Geology*, **70**, pp. 346-358.
- Williams-Jones, A. E., and Samson, I. M. 1990. Theoretical estimation of halite solubility in the system NaCl-CaCl₂-H₂O: Application to fluid inclusions. *Canadian Mineralogist*, **28**, pp. 299-304.
- Willis-Richards, J., and Jackson, N. J. 1989. Evolution of the Cornubian ore field, Southwest England: Part I. Batholith modeling and ore distribution. *Economic Geology*, **84**, pp. 1078-1100.
- Wilson, G. A., and Eugster, H. P. 1990. Cassiterite solubility and tin speciation in supercritical chloride solutions. *In* Fluid-mineral interaction: a tribute to H. P. Eugster. *Edited by* R. J. Spencer and I. -M. Chou. The Geochemical Society, Special Publication No.2, pp. 179-195.
- Wyllie, P. J., and Tuttle, O.F. 1961. Experimental investigation of silicate systems containing two volatile components, Part II: The effects of NH₃ and HF, in addition to H₂O on the melting temperatures of albite and granite. *American Journal of Sciences*, **259**, pp. 128-143.
- Xia, H. -Y., and Liang, S.-Y. 1984. Primary zoning and genetic sequences of W, Sn (Nb, Ta) deposits in Nanling region (*in Chinese*). Research report of Chengdu College of Geology, China.
- Xie, G. -Y. 1989. Metallotectonic study on the Baimianshan tinspar-sulfide ore deposit in the Xinlu ore field, Guangxi (*in Chinese*). M.Sc. thesis, Changsha Institute of Geotectonics, Academia Sinica, Changsha, China, 53 p.
- Xiong, Y. -L. 1986. Classification, evolution and mineralization zoning of the tin deposit at Lantoushan, the Shuiyanba tin ore field, northeast Guangxi (*in Chinese*). M.Sc. thesis, Wuhan College of Geology, Wuhan, China.

- Xu, W. -X. 1987 a. Physicochemical conditions and isotope study of the main tin deposits in Guangxi (*in Chinese*). *Geology of Guangxi*, (1987)-No.2, pp. 55-63.
- Xu, W. -X. 1987 b. Isotope geochemical study on the Dachang tin-polymetallic ore field (*in Chinese*). *In Proceedings of the International Conference on Geology of Sn Deposits (1984, China)*. Edited by J. -X. Tang. Geology Press, China, pp. 156-164.
- Yang, Z. -W. 1986. Factors controlling the W-Sn deposits and ore-searching direction in the Fu-He-Zhong region (*in Chinese*). *Journal of Guilin College of Geology*, 6, pp. 119-130.
- Yardley, B. W. D., and Banks, D. A. 1990. Simple chemical analysis methods for fluid inclusions, and their application in geochemical modelling (abstract). Abstracts of the Third Biennial Pan-American Conference on Research on Fluid Inclusions (May 20-22, 1990, Toronto), p. 96.
- Yichang Institute of Geology. 1985. Intrusion- and ore-controlling structures in Huashan-Guposhan region (*in Chinese*). Unpublished.
- You, J. -S. 1990. Geological features and mineralization regularities in the Xinlu ore field (*in Chinese*). M.Sc. thesis, Changsha Institute of Geotectonics, Academia Sinica, Changsha, China, 47 p.
- Yu, C. -W., Lo, T. -C., and Bao, Z. -Y. 1987. Regional geochemistry of Nanling region (*in Chinese*). Geology Press, China, 543 p.
- Yu, Z. -P. 1979. Heat transfer (*in Chinese*). Superior Education Press, China.
- Yuan, K. -R. 1981. Reconstruction of the original shape and emplacement mechanism of the Guposhan-Lishong granite (*in Chinese*). *Journal of Guilin College of Geology*, 1, pp. 1-13.
- Yuan, K. -R., and Yang, X. -Y. 1988. Accretion of continental margin terrane and the granites in Guangxi with relation to metallogenesis (*in Chinese*). *Journal of Guilin College of Geology*, 8, pp. 205-224.
- Zen, Y. -F., Shen, D.-Q., and Zhang, J.-Q. 1987. Strata-bound ore deposits in Devonian of Nanling district, southern China (*in Chinese*). Geology Press, China, 213 p.
- Zhang, Y. -G., and Frantz, J. D. 1987. Determination of the homogenization temperatures and densities of supercritical fluids in the system NaCl-KCl-CaCl₂-H₂O using synthetic fluid inclusions. *Chemical Geology*, 64, pp. 289-308.

- Zhang, Y. -G., and Frantz, J. D. 1989. Experimental determination of the compositional limits of immiscibility in the system $\text{CaCl}_2\text{-H}_2\text{O-CO}_2$ at high temperatures and pressures using synthetic fluid inclusions. *Chemical Geology*, **74**, pp. 335-350.
- Zhang, D. -Q., Wang, X. -Y., and Sun, G.-Y. 1985. Cooling history and emplacement ages of the Guposhan-Lishong granite masses, Guangxi (*in Chinese*). *Geology Review*, **31**, pp. 232-239.
- Zhao, Z. -J., Ma, D. -Q., and Lin, H. -K. 1987. Geochemical characteristics and geological setting of the formation of the Longwo and Fugang granitoid batholiths, Guangdong Province (*in Chinese*). *Collected Reports on Geology and Mineral Resources in the Nanling Region*, volume 1. Wuhan College of Geology Publishing House, pp. 28-68
- Zheng, C. -L. 1987. A discussion on the mineralization model of the Sn deposits in Dachang and Ping-Gui, Guangxi (*in Chinese*). *In Proceedings of the International Conference on Geology of Sn Deposits (1984, China)*. Edited by J. -X. Tang. Geology Press, China, pp. 211-218.

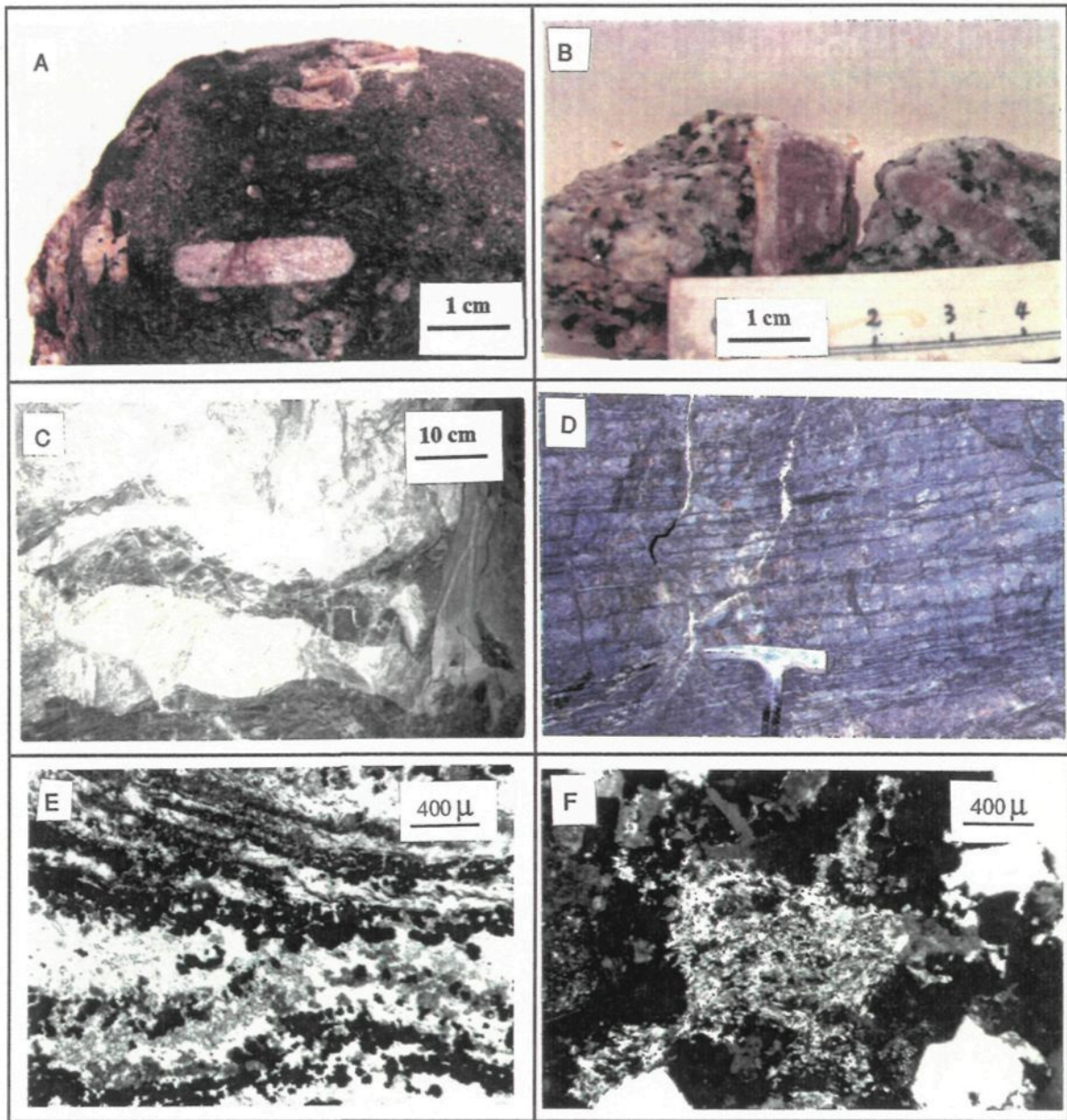


Plate 1 A--"Dark enclaves" of intermediate composition developed in the central part of the phase I granite of the Guposhan batholith; B--Oligoclase "envelope" around K-feldspar megacrysts in the central part of the phase I granite of the Guposhan batholith; C--Branches of an intermediate dyke intruding phase III granite at Liuhe'ao, also showing a xenolith of the dyke in the granite; D--Stratiform skarns developed near the contact zone at Liuhe'ao; E--Wrigglite skarn composed of rhythmic opaque mineral and fluorite layers from Liuhe'ao; F--Biotite replaced by muscovite in granite from Liuhe'ao.

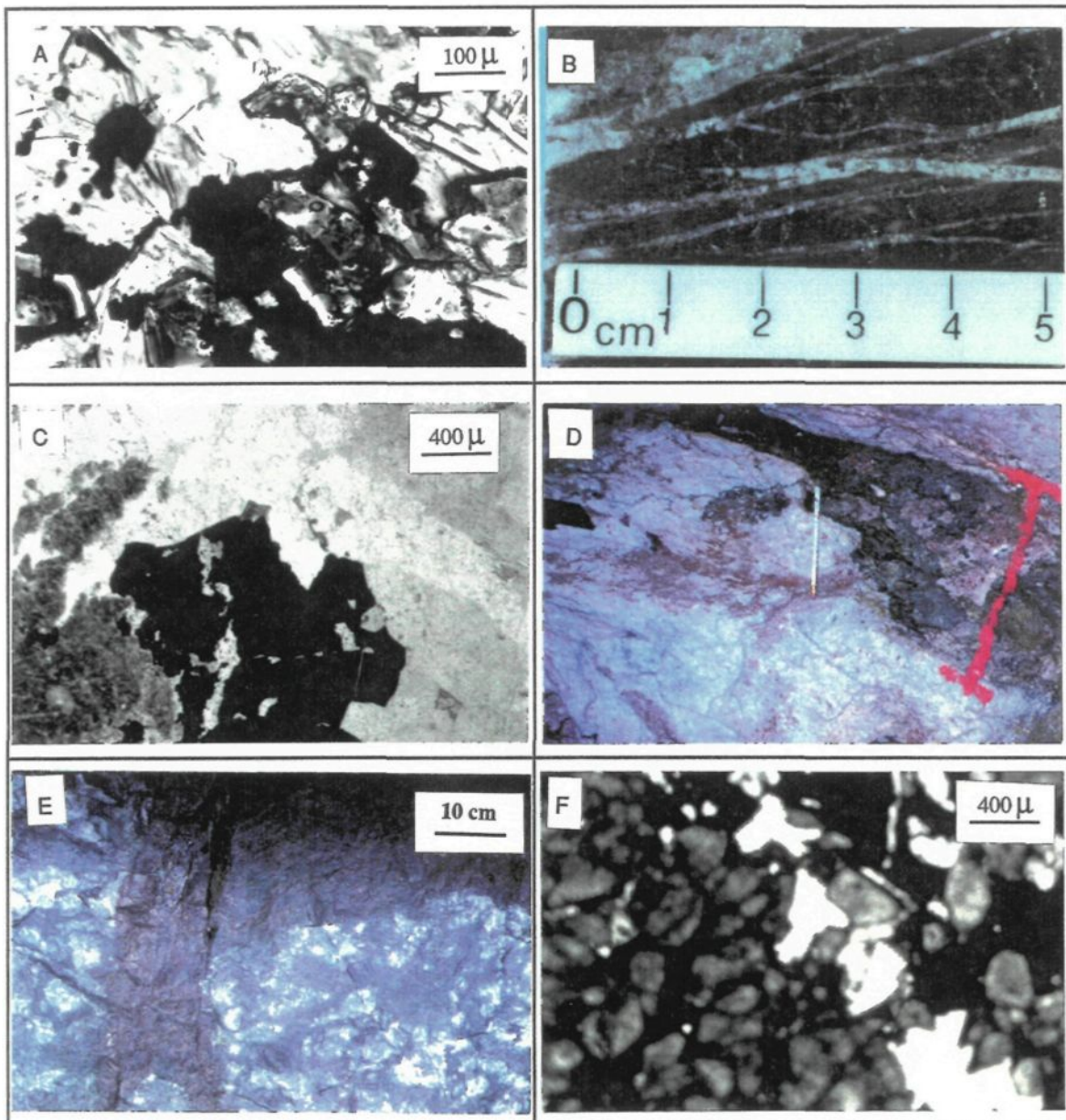


Plate 2 A- Proximal ore composed of sulfides, cassiterite, chlorite and actinolite from Liuhe'ao; B- Cassiterite-bearing quartz-fluorite veinlets superimposed on skarns at Liuhe'ao; C- Cassiterite-quartz veinlets developed at the margin of the granite intrusion at Liuhe'ao; D- A cassiterite-bearing sulfide vein developed in the marble at the Muqiaomian deposit; E- A branch of a stratiform ore body cutting the sedimentary beds at the Baimianshan deposit; F- A distal ore composed mainly of cassiterite and some sulfides, calcite and quartz at Baimianshan.

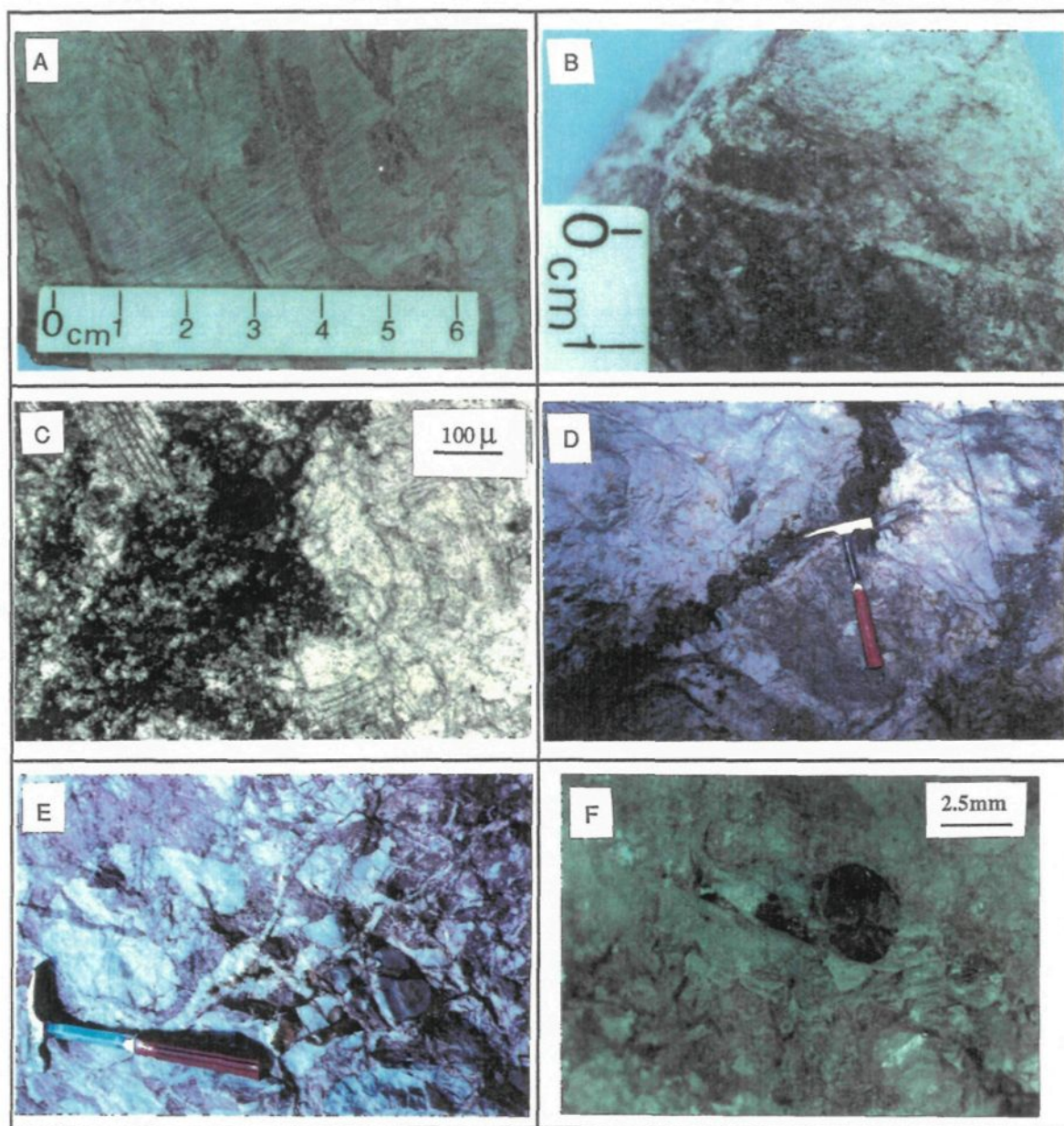


Plate 3 A--Lens-like bedding structures developed in a stratiform ore body at Baimianshan; B--Bleached (white) and unbleached limestone near an ore body at Baimianshan; C--Bleached (white) and unbleached limestone near an ore body at Baimianshan; D--Cassiterite-bearing sulfide veins developed in the marble at the Shimen deposit; E--Dolomite breccia pipe which hosts the cassiterite mineralization at Dongjia'ao deposit; F--Cassiterite occurring in the dolomite near the breccia pipe at the Donjia'ao deposit.

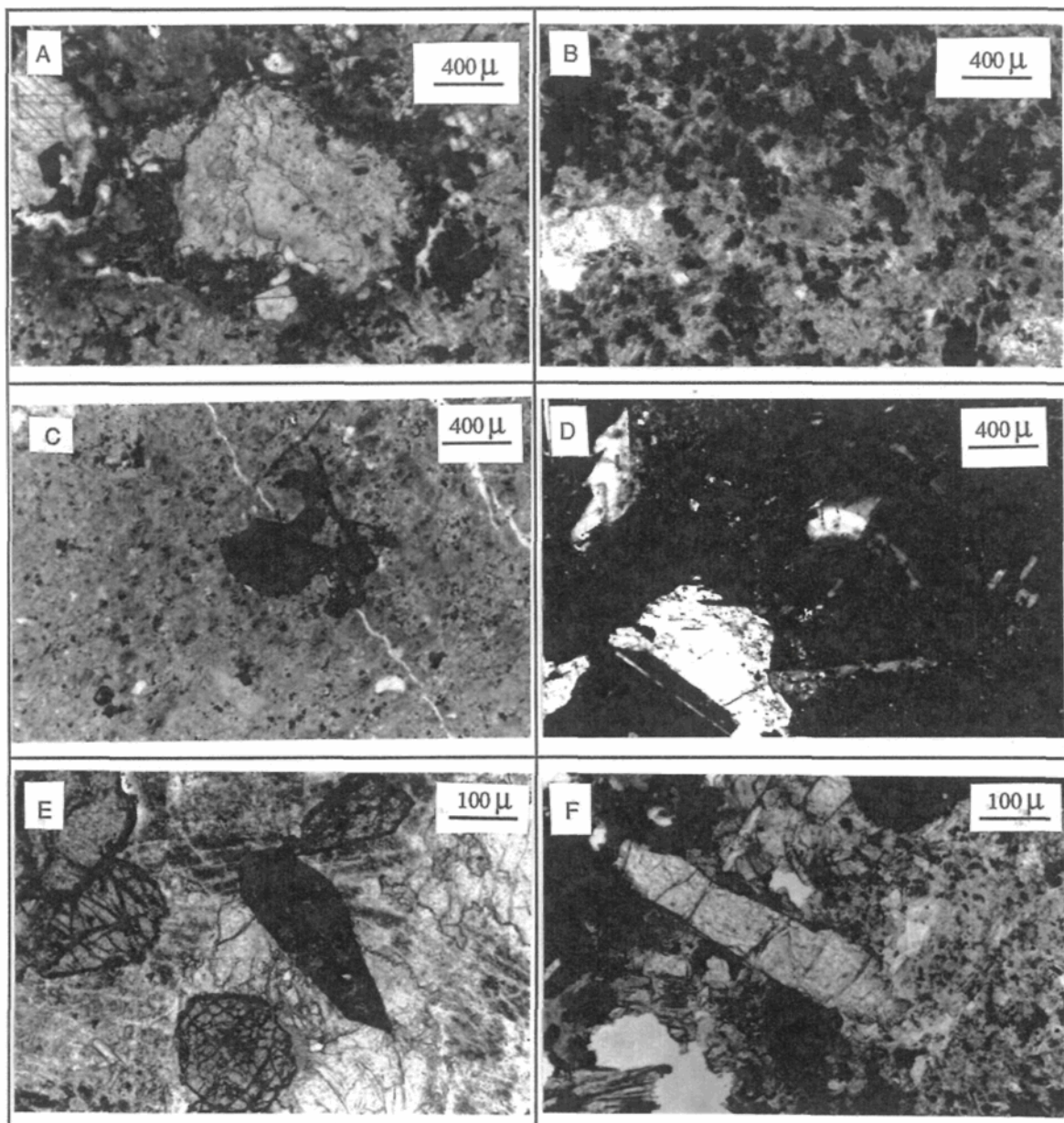


Plate 4 A--Calcite in an intermediate dyke; B--Carbonate in an intermediate dyke; C--An argillaceous fragment in an intermediate dyke; D--Oscillatory zoning in plagioclase from an intermediate dyke; E--Titanite in an intermediate dyke; F--Apatite in an intermediate dyke.

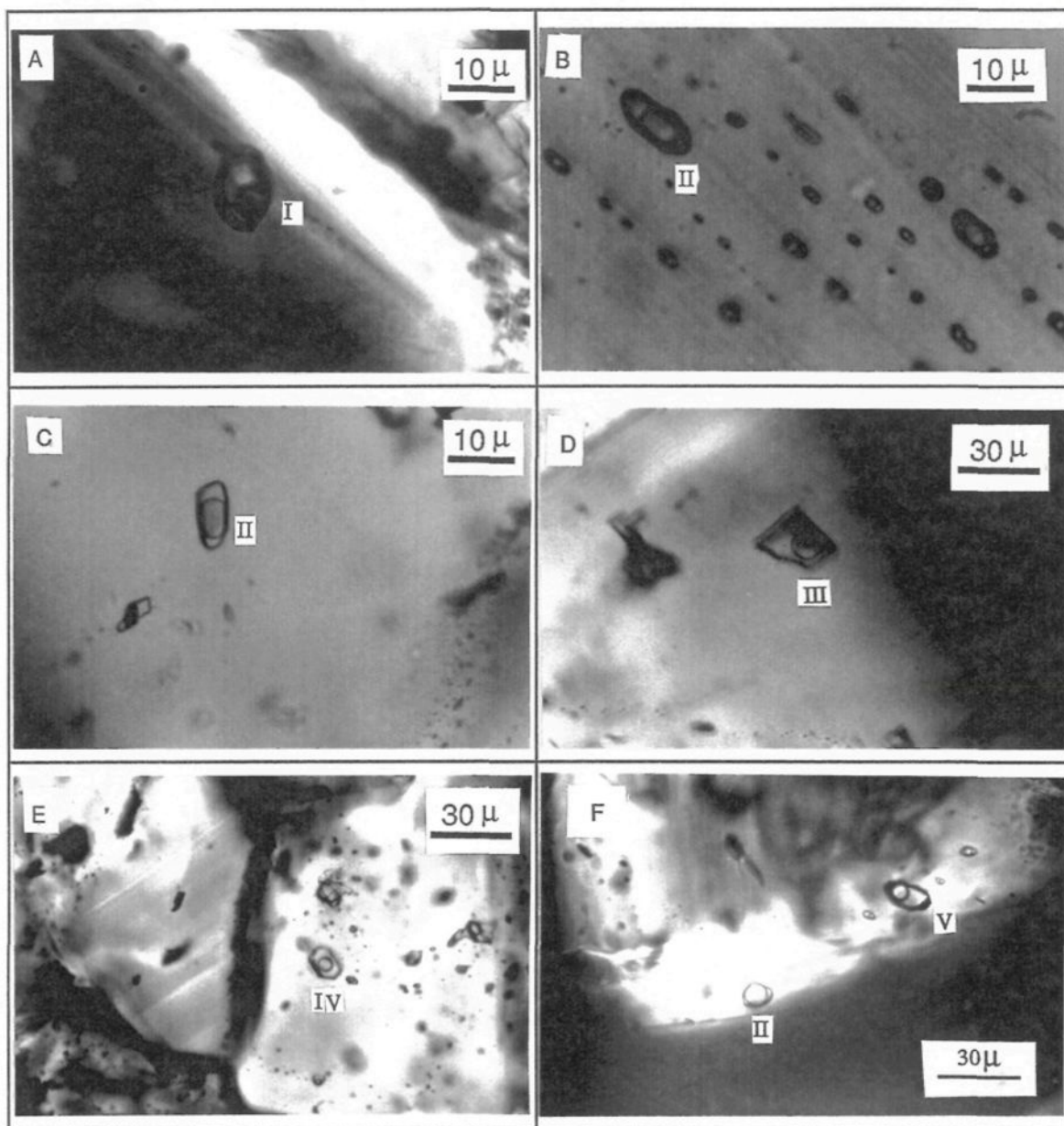


Plate 5 A--Type-I fluid inclusion in cassiterite from the Liuhe'ao deposit; B--Type-II fluid inclusions in cassiterite from the Dongjia'ao deposit; C--Type-II fluid inclusion in cassiterite from the Baimianshan deposit; D--Type-III fluid inclusion in cassiterite from the Liuhe'ao deposit; E--Type-IV fluid inclusion in cassiterite from the Liuhe'ao deposit; F--Type-V fluid inclusion in cassiterite from the Shimen deposit.

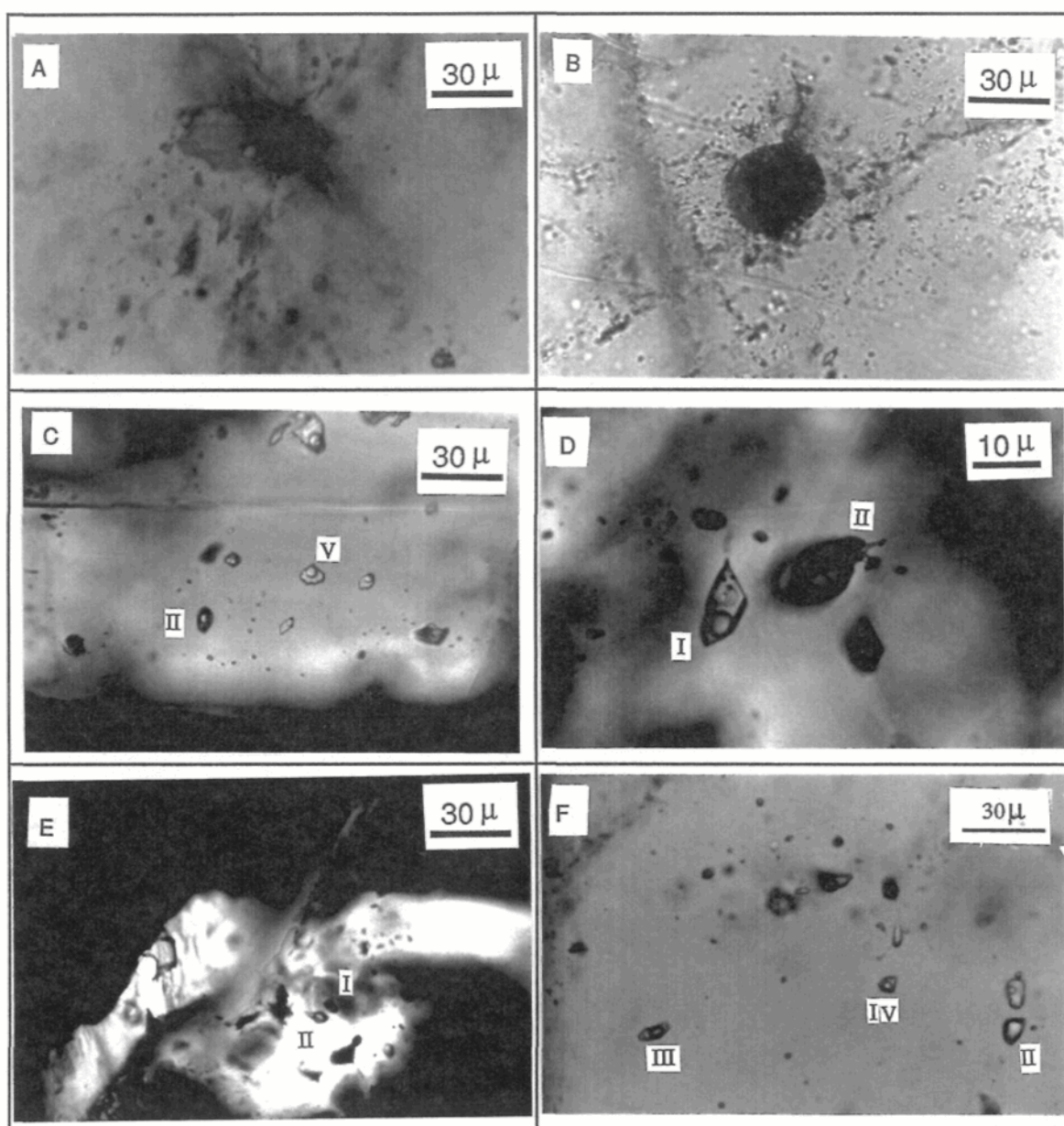


Plate 6 A--A melt inclusion with associated fluid inclusions in the granite at the Liuhe'ao deposit; B--A melt inclusion with associated fluid inclusions in the granite at the Liuhe'ao deposit; C--Co-existence of type-II and -V fluid inclusions in the same growth zone in cassiterite from the Shimen deposit; D--Co-existence of type-I and -II fluid inclusions in close proximity in cassiterite from the Liuhe'ao deposit; E--Co-existence of type-I and -II fluid inclusions in cassiterite from the Liuhe'ao deposit; F--Co-existence of type-II, -III and -IV fluid inclusions in quartz in the granite from the Liuhe'ao deposit.

APPENDIX A

**PETROGRAPHIC CHARACTERISTICS OF SAMPLES OF
GRANITES, DYKES, SEDIMENTARY ROCKS AND ORES**

Abbreviations:

Act-actinolite	Di-diopside	Ms-muscovite	Ser-sericite
Ap-apatite	Dol-dolomite	Ti-titanite	Sep-serpentine
As-arsenopyrite	Epd-epidote	Opq-opaque minerals	Sp-sphalerite
Aug-augite	FI-fluid inclusion	Or-orthoclase	TE-trace elements
Bi-biotite	Flu-fluorite	Ort-orthite	Trm-Tremolite
Cab-carbonate	Ga-garnet	Peth-perthite	Tur-tourmaline
Cal-calcite	Hbl-hornblende	Pl-plagioclase	Wol-wollastonite
Cas-cassiterite	Jam-jamesonite	Py-pyrite	Zir-zircon
Chal-chalcopyrite	Mac-marcasite	Pyr-pyrrhotite	Zo-zoisite
Cham-chamosite	ME-major elements	Q-quartz	Zon-zonochlorite
Chl-chlorite	Mic-microcline	REE-rare earth elements	

1. GRANITES**No. 43**

Rock type: fine-grained porphyritic quartz diorite

Locality: 600 metres south of Lishong village;

Occurrence: " dark enclaves" (E) in the central part of phase I of the Guposhan batholith;

Mineral components: Phenocrysts 10%: including Peth 4%, Pl 3% (An=20), slightly sericitized, Q 3%;

Groundmass 90%: including Pl 45% (An=20-33), Bi 3%, Q 10%, Or 15%, Hbl 10%, Ap 1.5%, Ti 1.5%, Opq 2%, Zo 2%.

Textures and structures: (1) porphyritic texture; (2) fine-grained texture in groundmass (0.1-0.3mm); (3) ring distribution of solids in the margin of Pl; (4) Per cut by Bi veinlets; (5) Zo replacing Bi and Hbl.

Chemical analyses: REE, TE.

CX055-1

Rock type: fine- to medium-grained quartz monzonite

Locality: near the old bridge of Shankou village, Lishong

Occurrence: "dark enclaves" (E) in the central part of phase I of the Guposhan batholith

Mineral components: Pl 40% (An=20-28), slightly sericitized, Q 10%, Or and Peth 35%, Bi 10%, Hbl 3%, Ti <0.5%, Ap <0.5%, Opq <1%.

Textures and structures: fine- to medium-grained texture (0.5-3 mm).

Chemical analyses: REE, TE

CX055-2

Rock type: medium-grained hornblende biotite granite

Locality: near the old bridge of Shankou village, Lishong

Occurrence: the central part of phase I of the Guposhan batholith (Ic)

Mineral components: Pl 40% (An=25), slightly sericitized, Or and Peth 20%, Q 30%, Bi 9%; Hbl 1%, Ap <0.1%, Ti <0.1%.

Textures and structures: (1) medium-grained texture (0.5-4 mm); (2) zoned distribution of solids in the margin of Pl.

Chemical analyses: REE, TE

CX058

Rock type: medium-grained hornblende biotite granite

Locality: near the small bridge in the south of Lishong Village

Occurrence: the central part of phase I of the Guposhan batholith (Ic)

Mineral components: Pl 35% (An=23-32), Peth 25%, Q 30%, Bi 5%, Hbl 3%, Ap <0.5%, Zo 1%, Opq 1%.

Textures and structures: (1) medium-grained texture; (2) polysynthetic twin and rhythmic ring in Pl; (3) Pl replacing Per and producing myrmekitic Q; (4) Zo replacing Bi.

Chemical analyses: REE, TE.

No.17

Rock type: medium-grained porphyritic biotite granite

Locality: near the Xinlu hydroelectric reservoir

Occurrence: the transitional part of phase I of the Guposhan batholith (It)

Mineral components: Pl 14% (An=23), Peth 45%, Q 30%, Bi 10%, Ap <0.5%, Opq 0.5%.

Textures and structures: (1) porphyritic texture; (2) medium-grained texture in the groundmass; (3) polysynthetic twin developed in Pl; (4) a few reverse ring texture in Pl.

Chemical analyses: REE, TE.

No.19

Rock type: fine-grained biotite granite

Locality: at the road side opposite to the the Xinlu hydroelectric plant

Occurrence: the marginal part of phase I of the Guposhan batholith (Im)

Mineral components: Pl 20% (An=25), Or and Peth 35%, Q 40%, Bi 5%, Flu <0.2

Textures and structures: (1) fine-grained texture; (2) Pl replacing Or and producing myrmekitic Q

Chemical analyses: REE, TE.

CX069

Rock type: fine-grained biotite granite (slightly altered)

Locality: Level 230, Liuhe'ao deposit

Occurrence: marginal part of Bojiling granite which is a part of phase III of the Guposhan batholith (II)

Mineral components: Pl 25% (An=23-30), Or 35%, Q 33%, Bi 3%, Ms 2%, Chl 2%, Flu <0.1%, black Tur <0.1%.

Textures and structures: (1) fine-grained texture; (2) Ms, Ser and Chl replacing Bi; (3) Ms and Ser replacing Pl and Or.

Chemical analyses: REE, TE.

CX082

Rock type: zoisite anorthosite

Locality: Level 230, Liuhe'ao deposit

Occurrence: contaminated rock at the contact zone

Mineral components: Pl 60% (An=20-45), Or 15%, Q 2%, Zo and Zon 15%, Cab 8%, Ort a little, Zir a little.

Textures and structures: (1) polysynthetic and patch-like twin developed in Pl; (2) Zo and Car replacing Pl in the form of network.

Chemical analyses: TE, ME

CX085

Rock type: hornblende anorthosite

Locality: Level 230, Liuhe'ao deposit

Occurrence: contaminated rock at the contact zone

Mineral components: Hbl 45%, Pl 54% (An=20-27), slightly sericitized, Cab 1%.

Textures and structures: (1) medium-grained texture; (2) Cab veinlets cutting Pl and Hbl.

Chemical analyses: REE, TE, ME

CX004

Rock type: altered potassic fine-grained granite

Locality: Level 208, Liuhe'ao deposit

Occurrence: marginal part of the Bojiling granite body which is a part of phase III of the Guposhan batholith and is very close to a cassiterite-quartz vein

Mineral components: Or 60%, Q 35%, Ms 3%, Cab 2%, Cas a few

Textures and structures: (1) fine-grained texture; (2) Ser veinlets cutting Or and Q; (3) Cab veinlets cutting Or

Chemical analyses: FI

CX071

Rock type: slightly altered fine-grained granite

Locality: Level 230, Liuhe'ao deposit

Occurrence: Marginal part of the Bojiling granite body (phase III)

Mineral components: Pl 29% (An=23-30), Or 35%, Q 35%, Bi 0.2%, Ms 1%, Flu 0.2%

Textures and structures: (1) fine-grained texture; (2) Pl replacing Or; (3) Flu replacing Q and Or; (4) Or replacing Pl; (5) Ms replacing Bi.

Chemical analyses: FI

CX072

Rock type: altered fine-grained granite

Locality: Level 230, Liuhe'ao deposit

Occurrence: marginal part of Bojiling granite body (phase III)

Mineral components: Pl 35% (An=27-29), Or 15%, Mic 10%, Q 35%, Bi 0.5%, black Tur 2%, Mg Tur .0.1%; Cab 2%, Flu a few

Textures and structures: (1) fine-grained texture; (2) Tur replacing Or and Pl; (3) Cab replacing Or; (4) Cab+Q+Ser veinlets cutting the other mineral assemblages; (5) early-generation Or replaced by late Q, Mic and Pl.

Chemical analyses: FI

No.305-2

Rock type: fine-grained biotite granite

Locality: Level 208, Liuhe'ao deposit

Occurrence: marginal part of Bojiling granite body (phase III)

Mineral components: Pl 10%, Or and Mic 50%, Q 39%, Bi 1%. (all minerals with fresh surface).

Textures and structures: (1) fine-grained texture; (2) Bi replacing Q; (3) Mic replacing Or.

Chemical analyses: REE, TE.

No.306

Rock type: altered fine-grained granite

Locality: Level 208, Liuhe'ao deposit, very close to No.305-2

Occurrence: marginal part of Bojiling granite body (phase III), close to the major ore body at the contact zone.

Mineral components: Pl 13% (An=23-27), Or and Mic 50%; Q 35%, Cab 0.5%; Ser 1.5%

Textures and structures: (1) fine-grained texture; (2) Pl replacing Or and Mic; (3) Cab replacing Pl and Or; (4) Ser replacing Pl and Or.

Chemical analyses: REE, TE

No.38

Rock type: fine-grained biotite granite

Locality: southern Fuchuanling Mount, near the main road

Occurrence: small stock in the middle of the Xinlu ore field (phase III)

Mineral components: Pl 30% (An=23-29), Or and Per 30%, Q 36%, Bi 3%, Ser 1%, Zir a few.

Textures and structures: (1) fine-grained texture; (2) polysynthetic twin developed in Pl; (3) Ser replacing Pl, Or and Bi.

Chemical analyses: REE, TE.

2. DYKES

V12-1-4

Rock type: fine-grained granite

Locality: western Shimen

Occurrence: dyke

Mineral components: Pl 22% (An=30), Or 40%, Q 35%, Bi <0.5%, Flu <0.5%, Opq <0.5%, Chl < 0.5%, Epd <0.5%.

Textures and structures: (1) fine-grained texture; (2) myrmekitic Q replacing Or; (3) Flu+ Chl+Epd irregular veinlets replacing the other minerals.

Chemical analyses: REE, TE, ME.

V14-1-1

Rock type: quartz porphyry

Locality: western Shimen

Occurrence: dyke

Mineral components: Phenocrysts 25%: including Q 10%, Or 10% and Opq a few; Groundmass 80%: including Q 33%, Or 32%, Pl 10%, Ms 1%, Opq 3%, Trm <0.1%, Flu <0.1%, Epd <0.5%, Zir <0.1%.

Textures and structures: (1) porphyritic texture; (2) micro- to fine-grained texture in the groundmass (<0.1 mm); (3) melt concave texture in Q phenocrysts; (4) Ms replacing Or phenocrysts; (5) Trm+Epd+Ms+Opq+Flu veinlets cutting the other minerals.

Chemical analyses: REE, TE, ME, K-Ar age, Sr isotopes.

V11-3

Rock type: biotite quartz dioritic porphyry

Locality: southern bank of the Shanba river at Baimianshan

Occurrence: dyke

Mineral components: Phenocrysts 10%: including Pl 5%, Q 1%, Bi 3%, Cal 0.5%, Ort 0.5%; Groundmass 90%: including Pl 40% (An=20-28), Q 30%, Bi 15%, Opq 2%, Epd <1%, Cab 1%, Ap <0.5%, Ti <0.1%.

Textures and structures: (1) porphyritic texture; (2) Pl and Bi comprise pilotaxitic texture in the ground mass; (3) Q enclave several Pl in the groundmass; (4) Cab replacing Pl phenocrysts.

Chemical analyses: REE, TE, ME, K-Ar age, Sr isotopes.

V22-1

Rock type: fine-grained monzonite

Locality: Maobeiling, Shimen

Occurrence: Small stock close to the Shimen deposit

Mineral components: Pl 40% (An=37), Or 35%, Q 3%, Hbl 15%, Aug 1%, Ti 2%, Ap 1%, Ort <0.5%, Opq <0.1%, Trm 2%.

Textures and structures: (1) fine-grained texture; (2) Bi replacing Hbl; (3) Trm veinlets cutting the other minerals.

Chemical analyses: REE, TE, K-Ar age, Sr isotope.

V22-2

Rock type: fine-grained biotite granodiorite

Locality: Maobeiling, Shimen

Occurrence: small stock close to the Shimen deposit

Mineral components: Pl 40% (An=23-47), Or 15%, Q 20%, Bi 11%, Hbl 8%, Opq 5%, Ap <0.5%, Cal <0.5%.

Textures and structures: (1) fine-grained texture; (2) oscillatory zoning developed in Pl; (3) Cal replacing Or; (4) Ser replacing Pl.

Chemical analyses: REE, TE, ME.

V44-1

Rock type: quartz dioritic porphyry

Locality: Nanzhudou, south of Xinlu ore field

Occurrence: dyke

Mineral components: Phenocrysts 5%: including Pl 2.5% (An=45), Cal 2%, Q 0.5%; Groundmass 95%: including Pl 54%, Q 10%, Cab 20%, Opq 5%, Ms 5%, Ap 1%, Flu a trace, Trm a trace.

Textures and structures: (1) porphyritic texture; (2) pilotaxitic texture in the groundmass; (3) melt concave texture in Q phenocrysts; (4) wavy extinction in Cal phenocrysts.

Chemical analyses: REE, TE, ME

BK193-1-1

Rock type: dioritic porphyry

Locality: southern segment of Level 193, Baimianshan deposit

Occurrence: dyke

Mineral components: Phenocrysts 20%: including Pl 13% (An=33-47), with very fresh surface (very slightly sericitized), Q 0.5%, Cal 2%; Bi 2%, Opq 2%, Ap 0.5%; Groundmass 80%, cryptocrystalline.

Textures and structures: (1) porphyritic texture and cluster porphyritic texture; (2) cryptocrystalline texture in the groundmass; (3) oscillatory zoning very developed in PL; (4) Cal+Bi+Ap+Opq form glomerophytic.

Chemical analyses: REE, TE, ME.

No.314

Rock type: strongly sericitized quartz dioritic porphyry

Locality: central-south segment of Level 193, Baimianshan deposit

Occurrence: dyke filled in F2 and close to the main ore body of Baimianshan deposit

Mineral components: Phenocrysts 7%: including Pl 6.5%, strongly sericitized and some chloritized ,Opq 0.5%; Groundmass 93%: including Q 23%, Pl 50%, mostly sericitized, Opq 5%, Cab 15%, Ap <0.1%, Ort <0.1%, Epd a few.

Textures and structures: (1) porphyritic texture; (2) Ser and Chl replacing Pl; (3) Ser+Opq veinlets cutting the groundmass.

Chemical analyses: REE, TE.

CX086

Rock type: biotite quartz dioritic porphyry

Locality: Level 230, Liuhe'ao deposit

Occurrence: dyke situated at the contact zone, also close to the contaminated rocks (CX082, CX085)

Mineral components: Phenocrysts 10%: all Pl (An=45), with little zoning texture; Groundmass 90%: including Pl 50% , Q 15%, Or a few, Bi 15%, Chl 5%, Opq 2%, Cal 2.5%, Ap 0.5%.

Textures and structures: (1) porphyritic texture; (2) pilotaxitic texture in the groundmass; (3) Bi and Chl have gradually transitional boundaries; (4) Cal usually coexist with Opq and Chl, but they do occur in the form of veins.

Chemical analyses: REE, TE

No.305-1

Rock type: biotite quartz dioritic porphyry

Locality: Level 208, Liuhe'ao deposit

Occurrence: xenolith in the granite, close to the dyke at the contact zone

Mineral components: Phenocrysts 10%, all Pl (An=24-63), only very slightly sericitized; Groundmass 90%: including Pl 60% (An=30-57), Q 15%, Bi 10%, Opq 3%, Cal 1.5%, Ap 0.5%.

Textures and structures: (1) porphyritic texture; (2) pilotaxitic and microlitic texture in the ground mass; (3) a few Bi+Opq veinlets cutting through the groundmass.

Chemical analyses: REE, TE

No.304

Rock type: sericitized biotite quartz dioritic porphyry

Locality: Level 208, Liuhe'ao deposit

Occurrence: dyke at the contact zone, very close to No.305-1 and to the major ore body at the contact zone.

Mineral components: Phenocrysts 15%: including Pl 10%, strongly sericitized, Bi+Opq 5%; Groundmass 85%: including Pl 50%, strongly sericitized, Q 15%, Bi 10%, Opq 5%, Ap 0.5%, Cab 3%, Chl 1.5%.

Textures and structures: (1) porphyritic texture; (2) pilotaxitic and microlitic texture in the ground mass; (3) Q+Ms+Opq veinlet cutting the groundmass, and cut by Cal vein; (4) Bi+Opq comprise taxite structures.

Chemical analyses: REE, TE

3. SEDIMENTARY ROCKS

No.57

Rock type: silty phyllite

Locality: Huangjinchong

Occurrence: Shuikou Group (Cambrian)

Mineral components: Q 38% (<0.1mm), Ser 40%, Chl 10%, cab 3%, Epd 2%, Opq 7%.

Textures and structures: bedding

Chemical analyses: REE, TE

No.11

Rock type: weakly metamorphic feldspar-quartz siltstone

Locality: at road side 18 km southwest of Danin village

Occurrence: Shikou Group (Cambrian)

Mineral components: Q 70% (<0.1mm), Pl 10%, Ser 10%, Cab 4%, Opq 2%, Chl 4%, Peth and Zir a few.

Textures and structures: (1) clastic texture; (2) Chl replacing Q.

Chemical analyses: REE, TE.

D1L-1

Rock type: argillaceous siltstone

Locality: Qiling, west of Shanhu ore field

Occurrence: Lianhushan Formation (D1L)

Mineral components: Q 80%, Ser 16%, Opq 4%.

Textures and structures: clastic-argillaceous texture.

Chemical analyses: REE, TE.

D1N-1

Rock type: silty mudstone

Locality: Qiling, west of Shanhu ore field

Occurrence: Nagaoling Formation (D1n)

Mineral components: Ser and clay minerals 80%, Q 8%, Cab 7%, Py 5%.

Textures and structures: (1) clastic-argillaceous texture; (2) a few veinlets Cab.

Chemical analyses: REE, TE.

CX046

Rock type: lens-like bioclastic limestone

Locality: Haodong, east of Xinlu ore field

Occurrence: Yujiang Formation (D2y₂⁴)

Mineral components: Cab 97%, Opq 3%.

Textures and structures: (1) lens-like structure; (2) micritic texture in the matrix

Chemical analyses: REE, TE.

CX044

Rock type: fine-grained quartz sandstone

Locality: east Baimianshan

Occurrence: Yujiang Formation (D2y₂³)

Mineral components: Q 90%, Ser 5%, Chl 3%, Opq 2%, Zir a trace.

Textures and structures: fine-grained clastic texture

Chemical analyses: REE, TE

CX045

Rock type: silty shale

Locality: east Baimianshan

Occurrence: Yujiang Formation (D2y2³)

Mineral components: Q 37%, Ser and clay minerals 60%, Opq 3%, Zir a few.

Textures and structures: (1) silty pelitic texture; (2) clear bedding.

Chemical analyses: REE, TE.

CX050

Rock type: fossiliferous limestone

Locality: Haodong

Occurrence: Donggangling Formation (D2d2²)

Mineral components: Fossil 10%: including chalcedony 2% and micritic limestone 8%; Groundmass 90%: including micritic limestone 40% and sparry limestone 50%.

Textures and structures: micritic and sparry texture.

Chemical analyses: REE, TE.

CX053

Rock type: oolitic limestone

Locality: south of Shimen

Occurrence: Kuiling Formation (D3k)

Mineral components: Oolite 80%, composed of micritic calcite; Matrix 20%, composed of sparry limestone.

Textures and structures: oolitic structure

Chemical analyses: REE, TE.

No.12

Rock type: sparry limestone

Locality: road side 4 km east of Liantang village

Occurrence: Early Carboniferous

Mineral components: micritic limestone 70%, sparry limestone 25%, Opq 5%.

Textures and structures: micritic and sparry texture.

Chemical analyses: REE, TE.

No.315-1

Rock type: sparry limestone

Locality: Level 193, Baimianshan deposit

Occurrence: Donggangling Formation (D2d), leached, with light colour.

Mineral components: Cal 99%, Q 1%.

Textures and structures: sparry texture

Chemical analyses: REE, TE.

No.315-2

Rock type: micritic limestone

Locality: Level 193, Baimianshan deposit

Occurrence: Donggangling Formation (D2d), unaltered, with dark colour.

Mineral components: Opq 20%, bioclasts 20% (composed of sparry Cal), groundmass 60% (composed of micritic limestone).

Textures and structures:

Chemical analyses: REE, TE.

No.317-1

Rock type: sparry limestone

Locality: Level 193, Baimianshan deposit

Occurrence: Donggangling Formation (D2d), leached, with light colour.

Mineral components: Opq 1%, Q 1%, Cal 98%, a few Wol and Trm.

Textures and structures:

Chemical analyses: REE, TE.

No.317-2

Rock type: sparry limestone

Locality: Level 193, Baimianshan deposit

Occurrence: Devonian Donggangling Formation (D2d), unaltered, with dark colour.

Mineral components: Opq 5%, Cal 95%.

Textures and structures:

Chemical analyses: REE, TE

4. ORES

No.21

Rock type: mineralized skarn

Locality: Level 208, Liuhe'ao deposit

Occurrence: stratiform skarn near the contact zone

Mineral components: three mineral assemblages: (a) Q+Cas vein 20%, including Q 15%, Cas 1%, Or 0.2%, Flu 1%, Pyr 2%, Chal 0.8%; (b) green assemblage 40%, including Act 15%, Epd 15%, Q 7%, Pyr 2%, Chal 1%; (c) light-coloured assemblage 40%, including Q 20%, Di 18%, Ga 2%.

Textures and structures: (1) bedding structure; (2) assemblage b is distributed beside assemblage a and cuts assemblage c; (3) homogeneous fine-grained texture in assemblage c.

Chemical analyses: REE, TE

No.24

Rock type: cassiterite-rich sulfide skarn

Locality: Level 208, Liuhe'ao deposit

Occurrence: major skarn ore body at the contact zone

Mineral components: Cas 35%, Sp 20%, As 5%, Chl 40%.

Textures and structures: (1) massive structure; (2) brown coloured Cas with well developed zoning texture and elbow twins; (3) Chl has clear crystal.

Chemical analyses: FI

No.25

Rock type: cassiterite-rich sulfide skarn

Locality: Level 208, Liuhe'ao deposit

Occurrence: major skarn ore body at the contact zone

Mineral components: Cas 30%, Sp 15%, As 15%, Chl 40%.

Textures and structures: same as No.24

Chemical analyses: REE, TE, FI.

No.311

Rock type: banded sulfide ore

Locality: Level 180, Baimianshan deposit

Occurrence: stratiform ore body, parallel to the lens-like limestone on top of the Yujiang Formation (D2y)

Mineral components: three mineral assemblages: (1) Pyr 20%+Sp 12%+Jam 5% +Q 3%; (2) Ser 10%+Pyr 3%+Sp 2%; (3) Ser 40%+Cham 1%+Q4%+a few Flu.

Textures and structures: (1) Banded and lens-like structure; (2) the bands are parallel to the bedding of the limestone.

Chemical analyses: REE, TE

XQ132

Rock type: sulfide-bearing cassiterite ore

Locality: south segment of Level 193, Baimianshan deposit

Occurrence: ore vein filled in a fracture

Mineral components: Sp 15%, As 3%, Chal 1%, Py 1%, Cas 75%, Cal 4%, Q 0.5%, Sep 0.5%.

Textures and structures: (1) massive structure; (2) Chal and Cal veinlets cutting Cas; (3) Cal and Q filling in the intergranular space.

Chemical analyses: REE, TE, FI

No.28

Rock type: Cassiterite-bearing sulfide ore

Locality: Dalongshan, Shimen

Occurrence: ore vein filled in fissures in the marble

Mineral components: Sp 40%, Pyr 5%, As 10%, Cas 5%, Cal and Dol 25%, Q 15%.

Textures and structures: (1) massive structure; (2) there two generations of Q and Cal; (3) Pyr cutting As.

Chemical analyses: REE, TE, FI

No.333

Rock type: cassiterite-bearing sulfide ore

Locality: Level 170, Muqiaomian deposit

Occurrence: ore vein filling fracture in marble

Mineral components: Pyr 30%, Sp 20%, Mac 2%, Cas 1%, Cal 47%.

Textures and structures: Cas usually coexists with Cal and occurs as inclusions in Cal.

Chemical analyses: REE, TE

No.330

Rock type: cassiterite-bearing dolomite

Locality: Dongjia'ao deposit

Occurrence: dolomite near breccia pipe

Mineral components: Dol and Cal 98%, Q 1%, Cas 1%.

Textures and structures: Cas occurs in veinlets or separate grains in dolomite.

Chemical analyses: REE, TE (Cas).

CX035

Rock type: cassiterite-bearing dolomite

Locality: Dongjia'ao deposit

Occurrence: dolomite near the breccia pipe

Mineral components: Cal and Dol 98%, Cas 1%, Flu 1%.

Textures and structures: (1) Cas occurs in veinlets or separate grains in dolomite; (2) Flu occur in veinlets in dolomite; (3) vug structures developed and Cas often occurs in the vugs.

Chemical analyses: REE, TE, FI

Appendix B

Calculation of REE Parameters for Analysis by INAA

Since only the results of seven rare earth elements: La, Ce, Sm, Eu, Tb, Yb and Lu, are receivable from the instrumental neutron activation analysis, three important parameters, i.e. ΣREE , δEu , and $\Sigma\text{LREE}/\Sigma\text{HREE}$, cannot be calculated. Some authors (e.g. Graf, Jr, 1977) use Eu/Sm to reflect the extent of Eu depletion and La/Lu to reflect the relative enrichment of LREE vs. HREE. However, these parameters are not comparable with δEu and $\Sigma\text{LREE}/\Sigma\text{HREE}$; for example, when there is no Eu depletion, $\delta\text{Eu}=1$, but Eu/Sm is not necessarily equal to 1. In order to make the data of complete REE analyses comparable with those of incomplete REE analyses, the following parameters, $\Sigma\text{REE}'$, $\delta\text{Eu}'$, and $\Sigma\text{LREE}'/\Sigma\text{HREE}'$, are calculated.

First, the data of analysed REEs are converted into logarithmic chondrite-normalized values:

$$La = \log (La/\text{chondrite})$$

$$Ce = \log (Ce/\text{chondrite})$$

$$Sm = \log (Sm/\text{chondrite})$$

$$Eu = \log (Eu/\text{chondrite})$$

$$Tb = \log (Tb/\text{chondrite})$$

$$Yb = \log (Yb/\text{chondrite})$$

$$Lu = \log (Lu/\text{chondrite})$$

These values (except Eu) are, theoretically, arranged linearly in the diagram illustrated in Fig. 70. The contents of unanalysed elements can be inferred from those of the analysed ones:

$$Pr' = 0.12 * 10^{(3La + 2Sm)/5}$$

$$Nd' = 0.60 * 10^{(2La + 3Sm)/5}$$

$$Gd' = 0.31 * 10^{(2Tb + Sm)/3}$$

$$Dy' = 0.31 * 10^{(Yb + 4Tb)/5}$$

$$Ho' = 0.073 * 10^{(2Yb + 3Tb)/5}$$

$$Er' = 0.21 * 10^{(3Yb + 2Tb)/5}$$

$$Tm' = 0.033 * 10^{(Yb + 4Tb)/5}$$

Then, $\Sigma\text{REE}'$ and $\Sigma\text{LREE}'/\Sigma\text{HREE}'$ can be calculated as follows:

$$\Sigma\text{REE}' = La + Ce + Pr' + Nd' + Sm + Eu + Gd' + Tb + Dy' + Ho' + Er' + Tm' + Yb + Lu + Y$$

$$\Sigma\text{LREE}'/\Sigma\text{HREE}' = (La + Ce + Pr' + Nd' + Sm + Eu) / (Gd' + Tb + Dy' + Ho' + Er' + Tm' + Yb + Lu + Y)$$

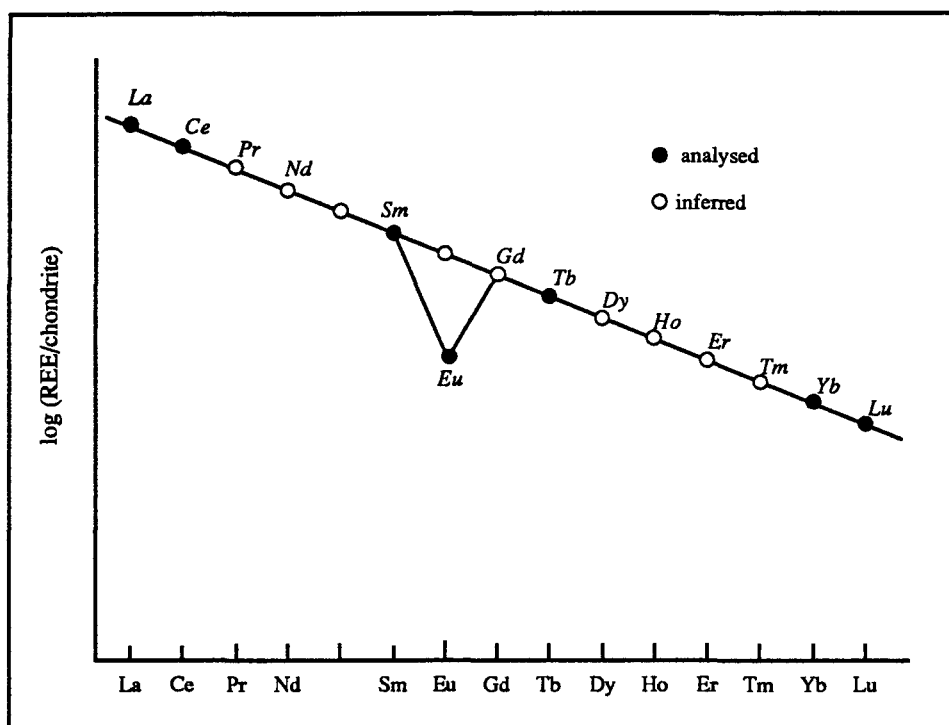


Fig. 70 A diagram showing the method of calculation of unanalysed REEs from analysed ones.

and $\delta Eu'$ can be calculated as follows:

$$\delta Eu' = Eu/Eu'$$

$$\text{where } Eu' = 0.073 \cdot 10^{(2Sm+Tb)/3}$$

A comparison is made between $\Sigma REE'$, $\delta Eu'$, $\Sigma LREE'/\Sigma HREE'$ and ΣREE , δEu and $\Sigma LREE/\Sigma HREE$ for two samples of granite and dyke as follows:

Parameters	f-3(granite)	L15-3 (granite)	V22-2 (dyke)	CX086 (dyke)
ΣREE	169.74	268.78	213.1	264.2
$\Sigma REE'$	174.44	274.22	211.2	262.0
δEu	0.093	0.56	0.90	0.99
$\delta Eu'$	0.086	0.49	0.81	0.88
$\Sigma LREE/\Sigma HREE$	3.05	9.98	10.44	10.87
$\Sigma LREE'/\Sigma HREE'$	3.12	8.58	9.05	9.20

From the comparison it is shown that $\Sigma REE'$, $\delta Eu'$ and $\Sigma LREE'/\Sigma HREE'$ are similar to ΣREE , δEu and $\Sigma LREE/\Sigma HREE$ respectively for the samples of granites and dykes. This may be extended to the samples of sedimentary rocks which have regular REE patterns.

APPENDIX C

DESCRIPTION OF THE METHODS USED IN CHEMICAL ANALYSES

1. General Description

The chemical analyses used in this study include: (1) analyses of major elements by chemical methods at Changsha Institute of Geotectonics of the Chinese Academy of Sciences (CIGCAS), (2) analyses of trace elements (including some rare earth elements) by INAA at l'Université du Québec à Chicoutimi (UQAC), (3) analyses of REE by plasma spectrometry at the Hubei Institute of Geology (HIG), (4) analyses of trace elements by various methods at the Hunan Institute of Analysis and Utilization of Minerals (HIAUM), (5) analyses of trace elements by direct-reading spectrometry at the Hunan Institute of Metallurgical Geology (HIMG), (6) analyses of K-Ar ages by dilution method at the Third Institute of Uranium at Beijing (TIUB), and (7) analyses of Sr isotopes at the TIUB.

The analysis procedures of INAA at UQAC will be briefly described in the following. The other analyses have been carried out by the units mentioned above without the participation of the author, so that only the names of the methods are listed. Some comparisons of results obtained by different methods will be listed.

2. Instrumental Neutron Activation Analysis (INAA)

2.1 Principles of the Method

In neutron activation analysis, low energy neutrons are used to activate the sample, which produces γ -rays and radionuclides. The radionuclides emit beta particles or γ -rays during decay, which are used to characterize and quantify the elements present in the sample (Dostal and Elson, 1980). The concentration of an element in the sample is calculated by comparing the peak area of the element with that of a standard sample with known content of the element and irradiated and counted under similar conditions. The formula is as follows:

$$C = A\lambda / (BW\phi * (1 - e^{-\lambda t_i}) * (e^{-\lambda t_d}) * (1 - e^{-\lambda t_c})),$$

where

C=concentration of the element in the sample (ppm),

A=surface of the peak of energy characteristic of the element (number of counts),

λ =decay constant,

B=activation constant,

W= weight of the sample (gram),

ϕ =the neutron flux (neutrons/cm².second),

t_i=the irradiation time (minute),

t_d=the decay time (hour),

t_c=the counting time (second).

2.2 Sample Preparation

First, cut or break the sample into fragments of less 10 cm³; secondly, rough-hew the fragments in a steel jaw crusher; thirdly, put the crushed sample into a alumina shatter-box to make powder. Make sure that the container be cleaned in every step. Quartz grains are used to clean the shatter box after crushing each sample in the last step. The powder is held in a sterile plastic bottle. Finally, put the powder (1 to 2 grams) into a plastic capsule, weight the sample, then cover the capsule tightly (using flame).

2.3 Operation Procedure

The neutron activation analysis at UQAC includes the following steps:

- (1) Send the samples to be irradiated (at l'Ecole Polytechnique, Université de Montréal);
- (2) The samples are ready for detection about one week after the irradiation;
- (3) Examine the detector, high voltage power supply, amplifier and analyser;
- (4) Put the capsules of samples in the capsule support;
- (5) Turn on the computer, then the arm manipulator, and then enter the instructions for the operation of the instrument (details see the manual of instrumental neutron activation analysis by Coulombe and Poitras, 1986).
- (6) Calculate the concentrations of the elements with computer.

2.4 Results of Standard Sample (Sh-18)

Elements	Run-1	Run-2	Run-3	official values
La	34.66	34.50	34.81	33
Ce	67.51	64.85	65.21	65
Nd	33.82	33.57	25.92	33
Sm	5.29	5.44	5.57	5.28
Eu	1.35	1.18	1.22	1.19
Tb	0.79	0.84	0.86	0.74
Yb	2.83	2.86	2.72	2.8
Lu	0.57	0.57	0.51	0.41
As	19.61	20.29	20.50	19
Ba	595.54	636.96	598.82	586
Co	30.26	29.15	28.70	28
Cr	123.00	127.31	120.70	119
Cs	3.64	4.11	3.54	3.3
Fe ₂ O ₃ %	3.56	3.65	3.58	3.53
Hf	4.37	4.03	4.19	4
Na ₂ O%	0.93	0.93	0.92	0.94
Ni	84.07	73.69	37.52	51
Rb	133.64	135.49	134.31	127
Sb	1.53	1.58	1.55	1.47
Sc	20.91	21.18	20.77	21
Ta	1.48	1.75	1.26	1.3
Th	9.37	9.66	8.87	9
U	5.14	5.47	4.14	4.8
Zn	37.90	18.02	26.18	17
Zr	185.57	225.12	159.57	149

Notes: The official values are from Bédard and Barnes (1990).

3. Methods Used by the HIAUM for Analyses of Trace Elements

3.1 List of Methods Used for Different Elements

The following methods are used to analyse different elements:

- (1) X-ray fluorescence spectrometry: Cl, Sr, Ba, Nb, Rb.
- (2) electrode emission spectrometry: Sn, Be, B.
- (3) ion selective electrode: F.
- (4) flame emission atomic absorption: Li, Cs.
- (5) hydrogenide atomic fluorescence: Bi, Sb.
- (6) catalytic polarography: W.
- (7) extraction colorimetry: Ta.

3.2 The Results of Analyses of Some Elements in Standard Samples

Sn, F, Cl and Sr are analysed for four standard samples with known concentrations of these elements. The results are listed in the following:

Sample	Rock type	Data type	F	Sn	Sr	Cl (ppm)
GSR-1*	granite	official values	2350	12.5	106	
		measured val.	2560	14.0	106	
GSR-6*	limestone	official values	414	0.98	913	
		measured val.	400	-----	897	
DZ-1		official values			2.3	5700
		measured val.			2.0	5843
DZ-2		official values			33.2	220
		measured val.			38	225

* Ministry standard of China.

4. Comparisons of the Results Obtained by Different Methods and/or Analysers

4.1 Rare Earth Elements (sample: BK193-1-1)

Element	INAA at UQAC	Plasma Spectrometry at HIG
La	53.73	48.81
Ce	103.5	98.75
Sm	7.59	7.84
Eu	1.85	1.85
Tb	1.02	0.98
Yb	2.55	2.50
Lu	0.44	0.36

4.2 Trace Elements

	BK193-1-1			V11-3		
	(1)	(2)	(3)	(1)	(2)	(3)
Sb	6.9	8.2		8.6	8.6	
Rb	445.0	448.0		239.9	253.0	
Cs	110.0	77.9		19.4	15.5	
W	11.5	1.5		6.0	1.74	
Ta	2.2	16.0		3.0	16.0	
Ba	364.8	392.0	421.0	1094.0	1021.0	1400.0
Cr	68.8		65.6	19.0		11.0
Ni	57.0		17.6	50.1		7.81
Co	17.7		23.5	3.0		7.88
Zn	872.0		997.0	32.3		53.0
Sr		314.0	303.0		359.0	362.0

(1): INAA at UQAC; (2) various methods used at HIAUM; (3) direct-reading spectrometry at HIMG.

APPENDIX D

DESCRIPTION OF THE METHODS USED IN FLUID INCLUSION STUDY

1. General Description of the Methods Used in Fluid Inclusion Studies

There are two general categories of methods of studying fluid inclusions: nondestructive methods and destructive methods (Roedder, 1990). The former includes: (1) observation of the optical features of the fluid inclusions and the phase change during freezing and heating under microscope, (2) infrared absorption and Fourier transform infrared spectroscopy, (3) ultraviolet absorption, (4) Raman spectroscopy, (5) Fedorov (universal) stage and reflection measurement (to estimate the index of refraction of the fluids in the inclusions), (6) electron microscope, (7) electron microprobe, (8) ion microprobe, (9) X-ray diffraction, (10) Laser-ICP and Synchrotron XRF-microprobe (Rankin et al., 1990), (11) Proton-induced gamma-ray analysis (Anderson et al., 1990). The latter includes: (1) chemical analysis (e.g. Yardley and Banks, 1990), (2) gas chromatography, (3) mass spectrometry, (4) solid-probe mass spectrometry (Guha et al., 1990), (5) decrepitation, (6) most of the nondestructive methods.

The method of observation of the optical features of the fluid inclusions and the phase change during freezing and heating under microscope is used in the fluid inclusion study in this paper. This is the method that produced most fluid inclusion data in the current literature (Roedder, 1990). The fluid inclusion study is based on the geological and petrological studies of the ores and the host rocks.

2. Sample Preparation

2.1 Field Sampling

Since the purpose of fluid inclusion study in this paper is to evaluate the origins and evolution of the ore-forming fluids and associated temperature-pressure conditions, the samples selected to study are mainly ores from various occurrences and environments and granites associated with deposits.

2.2 Cutting and Polishing

The samples selected were cut in Changsha Institute of Geotectonics of Chinese Academy of Sciences and Hunan Institute of Analysis and Utilization of Minerals. Doubly polished thin sections were made in UQAC.

3. Experimental Procedures

3.1 Selection of Studying Objects

3.1.1 Host Minerals

The host minerals of fluid inclusions selected to study are cassiterite in ores and quartz in granites. Since cassiterite is the major ore mineral, the primary fluid inclusions in cassiterite can best represent the ore-forming fluids, although quartz has been the major host mineral of fluid inclusion studies of most authors. The study of fluid inclusions in quartz associated with ore minerals is based on the assumption that the quartz and the ore minerals were precipitated from the same ore-forming fluids at the same time. This assumption can be ascertained by careful petrographical studies, but examples have been reported that the primary fluid inclusions in cassiterite and associated quartz which seems to have been formed at the same time as the cassiterite have quite different composition (Schwartz and Askury, 1989) and that coexisting wolframite, cassiterite and quartz have systematically different Th and salinities (Campbell and Panter, 1990). In these cases, the primary fluid inclusions in the quartz do not well represent the ore-forming fluid. Therefore, the study of fluid inclusions in the ore minerals (if transparent, e.g. cassiterite) is the best way to avoid false representation of ore-forming fluids by fluid inclusions.

Fluid inclusions in granites are studied in both primary and secondary quartz. Primary fluid inclusions in primary quartz represent the initial fluid derived from the granite magma; those in secondary quartz represent the fluid evolved from the initial fluid through water-rock interaction and phase separation.

3.1.2 Origins of Fluid Inclusions

All the fluid inclusions from ore mineral (cassiterite) selected to study are primary inclusions. This is to ascertain the genetic and temporal relationship between the host minerals and the fluid inclusions, although secondary fluid inclusions can give much information about the evolution of the fluid system if the generations of

inclusions can be clearly identified and associated to certain geological events. Some secondary inclusions in quartz from granites are also studied; they are believed to be related to the ore-forming fluids through comparison with other inclusions.

3.1.3 Size of Inclusions

The size of fluid inclusions in cassiterite and in quartz from granites varies mainly from $<1\mu$ to 50μ . The inclusions selected for heating are $>4\mu$, although it has been shown by Reynolds (1989, personal communication) that inclusions as small as 1μ is good enough for heating using the U.S.G.S. Gas-Flow Heating/Freezing System. The inclusions selected for freezing are $>7\mu$. This ensures that the eutectic points (generally $<-50^{\circ}\text{C}$) can be measured in most cases.

3.2 Photographing

Before doing runs, photographs were taken of the fluid inclusions which are representative of a type or a relationship. The orientation of the sample, the shape of the grain that holds the inclusions and the surrounding mineral features are marked on the paper in order to relocate them on the freezing-heating stage.

3.3 Examination of the Instrument

3.3.1 Adjustment of the U.S.G.S. Gas-Flow Heating/Freezing System

The U.S.G.S. Gas-Flow Heating/Freezing System was designed by Werre et al. (1979) at the U.S. Geological Survey. The cooling and heating of the sample is done by passing preheated or cooled N_2 gas (or ordinary compressed air from above room temperature to 500°C) directly over the sample which is held in a chamber, with the thermocouple rested directly on the sample.

The system consists of seven basic parts: (1) N_2 gas cylinder, (2) liquid N_2 dewar, (3) microscope, (4) freezing/heating stage, (5) variable transformer, (6) trendicator, (7) foot switch.

In installing and adjusting the system, the following things, among others, should be paid attention to: (1) the parts should be arranged in a way that ensures the operator carry out the cooling/heating operations without moving from the seat; the liquid N_2 dewar and transformer should be near enough to the microscope to be reached by hand sitting at the microscope; the trendicator should be put in the direction so that the operator can see the temperature without moving the head; (2) the pipe that connects the liquid N_2 dewar to the electric gas heating

element should be twisted in a way that ensures the front part of the pipe be parallel and fit to the electric gas heating element in order not to destroy the cylindrical slot surrounding the electric gas heating element; (3) wrap the joints of the pipe connecting the liquid N₂ dewar and the electric gas heating element with teflon tape in order to avoid leakage. Details of the assembly of the U.S.G.S. Gas-Flow Heating/Freezing System are described in the instruction manual (Reynolds, 1988).

3.3.2 Calibration of the Trendicator and Thermocouple

Calibration of the trendicator and thermocouple was carried out by measuring the phase-change temperatures of chemical materials and synthetic fluid inclusions with the freezing/heating stage over a fairly wide range. The results are listed as follows and illustrated in Fig. 71:

Substances	Standard temperatures(°C)	Measured temperature(°C)
n-hexane	-95.0	-92.8
CO ₂	-56.5	-55.3
CCl ₄	-23.0	-22.5
H ₂ O	0.0	-0.8
Merck (9135)	135.0	137.2
Merck (9800)	200.0	203.0
K ₂ Cr ₂ O ₇	388.0	390.0

The measured temperature and the standard temperature are related in the following least-square equation: $T_{\text{standard}} = -0.79985 + 0.99493 * T_{\text{measured}}$. From the equation and the correlation coefficient (=1), it is shown that the accuracy of the trendicator and thermocouple is fairly good. By comparing the calibration results of this paper with those of other operators in the same lab and through repetition of temperature measurements for the same sample and under the same condition, it is shown that the trendicator and thermocouple have good precision and replicability. For these reasons, the measured temperatures are adopted without calibration except for T_{mCO_2} . In the later case, a simple equation ($T_{\text{calibrated}} = T_{\text{measured}} - 1.2$) is used according to the calibration result of the melting temperature of synthetic CO₂ inclusions (see the above table), in order to eliminate unreasonable values of $T_{\text{mCO}_2} < 56.5$ °C.

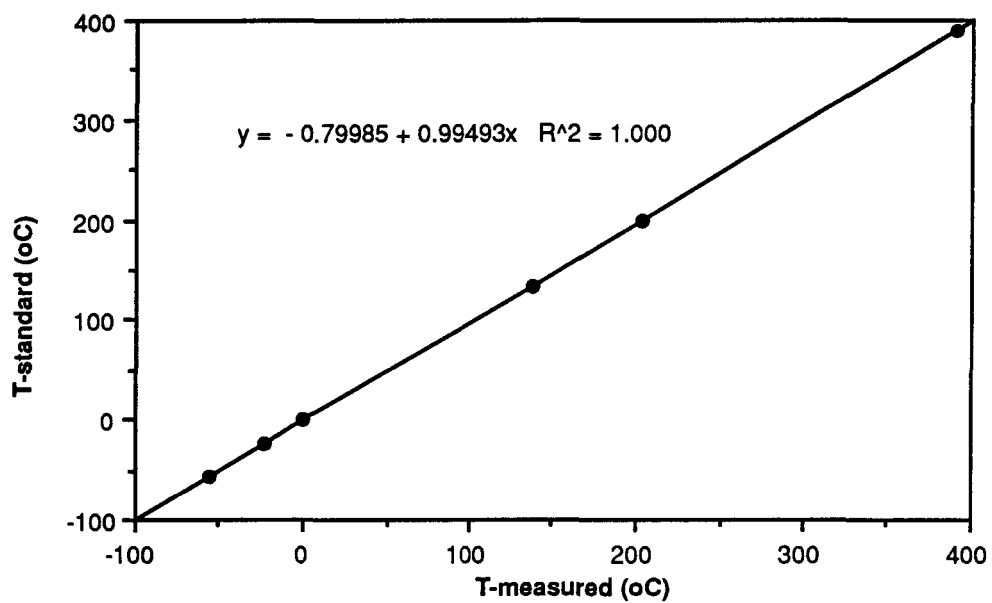


Fig. 71 Correlation between measured and standard temperatures for the U.S.G.S. Gas-Flow Heating-Freezing System.

3.4 Freezing

Freezing runs were done before heating. Since most of the fluid inclusions in this study either contain Ca which causes low eutectic temperature ($<-50\text{ }^{\circ}\text{C}$) or contain liquid CO_2 which has melting temperature of $-56.5\text{ }^{\circ}\text{C}$, the temperature is first lowered to around $-90\text{ }^{\circ}\text{C}$ by turning on the liquid N_2 . In the case of the existence of CO_2 , temperature is often lowered to $-186\text{ }^{\circ}\text{C}$ in order to determine if there is CH_4 . The sample is then warmed by turning on the electric gas heating element through the control of the transformer (according to Reynolds, it is preferred to keep the valve of liquid N_2 open instead of turning on the gas N_2 , since the combination of the electric gas heating element with cooled N_2 can best control the temperature).

3.5 Heating

Before turning on the electric gas heating element, the ordinary compressed air is turned on. When temperature exceeds $500\text{ }^{\circ}\text{C}$, N_2 gas must be used. Cooling coils should be put on the objective. The temperature is controlled by the transformer and the flux of the compressed air.

3.6 Recording

The following items are recorded before freezing and heating: the shape, size, color, phases, volume ratios of each phases, origins (primary or secondary). In freezing and heating, the following temperatures are recorded where observable: melting temperature of solid CO_2 , the homogenization temperature of liquid CO_2 and gas CO_2 (marking homogenized to liquid or gas), first melting temperature in the aqueous phase, melting temperatures of NaCl , H_2O and $\text{NaCl}\cdot 2\text{H}_2\text{O}$, the filling temperature of the fluid inclusions (marking homogenized to liquid or to gas or critical).

4. Treatment of the data

The FLINCOR program (Brown, 1989) is used to calculate the bulk density, CO_2 (mole%) and isochores. These are the most basic and useful data of fluid inclusions.

Appendix E

Computer Programs of Modelling of Temperature Gradient Patterns

(1)

Two-dimensional Steady-state Heat Conduction in Concave Magma Intrusion Environment

```

DIMENSION T(-1:22,1:21),Q(-1:22, 1:21)
C TWO-DIMENSIONAL STEADY-STATE MODEL OF CONCAVE HEAT CONDUCTION
OPEN (13,FILE='CHI-2.RES',STATUS='NEW')
DO 10 I=-1,1
DO 10 J=1,21
10 T(I,J)=25+38.16*(J-1)
DO 20 I=2,4
DO 20 J=1,20
20 T(I,J)=25+38.16*(J-1)
DO 30 I=5,6
DO 30 J=1,19
30 T(I,J)=25+40.28*(J-1)
DO 40 J=1,18
40 T(7,J)=25+42.65*(J-1)
DO 50 J=1,17
50 T(8,J)=25+45.31*(J-1)
DO 60 J=1,15
60 T(9,J)=25+51.79*(J-1)
DO 70 J=1,13
70 T(10,J)=25+60.42*(J-1)
DO 80 J=1,11
80 T(11,J)=25+72.5*(J-1)

```

```

DO 90 I=12,22
DO 90 J=1,9
90  T(I,J)=25+90.63*(J-1)
    T(2,21)=750
    T(5,20)=750
    T(7,19)=750
    T(8,18)=750
    T(9,17)=750
    T(9,16)=750
    T(10,15)=750
    T(10,14)=750
    T(11,13)=750
    T(11,12)=750
    T(12,11)=750
    T(12,10)=750
95  S=0
    DO 100 I=0,21
    DO 100 J=2,8
        Q(I,J)=(T(I,J-1)+T(I+1,J)+T(I,J+1)+T(I-1,J)-4*T(I,J))/4
100  S=S+ABS(Q(I,J))
    DO 110 I=0,11
    DO 110 J=9,10
        Q(I,J)=(T(I,J-1)+T(I+1,J)+T(I,J+1)+T(I-1,J)-4*T(I,J))/4
110  S=S+ABS(Q(I,J))
    DO 120 I=0,10
    DO 120 J=11,12
        Q(I,J)=(T(I,J-1)+T(I+1,J)+T(I,J+1)+T(I-1,J)-4*T(I,J))/4
120  S=S+ABS(Q(I,J))
    DO 130 I=0,9
    DO 130 J=13,14
        Q(I,J)=(T(I,J-1)+T(I+1,J)+T(I,J+1)+T(I-1,J)-4*T(I,J))/4
130  S=S+ABS(Q(I,J))
    DO 140 I=0,8

```

```

DO 140 J=15,16
Q(I,J)=(T(I,J-1)+T(I+1,J)+T(I,J+1)+T(I-1,J)-4*T(I,J))/4
140 S=S+ABS(Q(I,J))
DO 150 I=0,7
Q(I,17)=(T(I,16)+T(I+1,17)+T(I,18)+T(I-1,17)-4*T(I,17))/4
150 S=S+ABS(Q(I,17))
DO 160 I=0,6
Q(I,18)=(T(I,17)+T(I+1,18)+T(I,19)+T(I-1,18)-4*T(I,18))/4
160 S=S+ABS(Q(I,18))
DO 170 I=0,4
Q(I,19)=(T(I,18)+T(I+1,19)+T(I,20)+T(I-1,19)-4*T(I,19))/4
170 S=S+ABS(Q(I,19))
DO 180 I=0,1
Q(I,20)=(T(I,19)+T(I+1,20)+T(I,21)+T(I-1,20)-4*T(I,20))/4
180 S=S+ABS(Q(I,20))
DO 190 J=2,8
Q(22,J)=(T(22,J-1)+T(22,J+1)+T(21,J)-3*T(22,J))/4
190 S=S+ABS(Q(22,J))
DO 200 I=0,22
DO 200 J=2,8
200 T(I,J)=T(I,J)+Q(I,J)
DO 210 I=0,11
DO 210 J=9,10
210 T(I,J)=T(I,J)+Q(I,J)
DO 220 I=0,10
DO 220 J=11,12
220 T(I,J)=T(I,J)+Q(I,J)
DO 230 I=0,9
DO 230 J=13,14
230 T(I,J)=T(I,J)+Q(I,J)
DO 240 I=0,8
DO 240 J=15,16
240 T(I,J)=T(I,J)+Q(I,J)

```



```
DO 250 I=0,7
250 T(I,17)=T(I,17)+Q(I,17)
DO 260 I=0,6
260 T(I,18)=T(I,18)+Q(I,18)
DO 270 I=0,4
270 T(I,19)=T(I,19)+Q(I,19)
DO 280 I=0,1
280 T(I,20)=T(I,20)+Q(I,20)
DO 290 J=2,20
290 T(-1,J)=T(1,J)
IF(S-0.001)310,310,300
300 GOTO 95
310 WRITE(13,320)((T(I,J),I=0,22),J=1,9)
320 FORMAT(1X,23F4.0)
WRITE(13,330)((T(I,J),I=0,12),J=10,11)
330 FORMAT(1X,13F4.0)
WRITE(13,340)((T(I,J),I=0,11),J=12,13)
340 FORMAT(1X,12F4.0)
WRITE(13,350)((T(I,J),I=0,10),J=14,15)
350 FORMAT(1X,11F4.0)
WRITE(13,360)((T(I,J),I=0,9),J=16,17)
360 FORMAT(1X,10F4.0)
WRITE(13,370)(T(I,18),I=0,8)
370 FORMAT(1X,9F4.0)
WRITE(13,380)(T(I,19),I=0,7)
380 FORMAT(1X,8F4.0)
WRITE(13,390)(T(I,20),I=0,5)
390 FORMAT(1X,6F4.0)
WRITE(13,400)(T(I,21),I=0,2)
400 FORMAT(1X,3F4.0)
END
```

(2)

**Two-dimensional Steady-state Heat Conduction in
Convex Magma Intrusion Environment**

```

DIMENSION T(-1:22,1:21),Q(-1:22,1:21)
C   TWO-DIMENSIONAL MODEL OF HEAT CONDUCTION AROUND A
C   DOME-LIKE INTRUSION
OPEN(16,FILE='CHI-5.RES',STATUS='NEW')
DO 10 I=-1,2
DO 10 J=1,9
10  T(I,J)=25+90.63*(J-1)
DO 20 I=3,5
DO 20 J=1,10
20  T(I,J)=25+80.56*(J-1)
DO 30 I=6,7
DO 30 J=1,11
30  T(I,J)=25+72.5*(J-1)
DO 40 J=1,12
40  T(8,J)=25+65.91*(J-1)
DO 50 J=1,13
50  T(9,J)=25+60.4*(J-1)
DO 60 J=1,15
60  T(10,J)=25+51.79*(J-1)
DO 70 J=1,17
70  T(11,J)=25+45.31*(J-1)
DO 80 J=1,19
80  T(12,J)=25+40.28*(J-1)
DO 90 I=13,22
DO 90 J=1,21
90  T(I,J)=25+36.25*(J-1)
T(2,10)=750
T(5,11)=750
T(7,12)=750

```

```

T(8,13)=750
T(9,14)=750
T(9,15)=750
T(10,16)=750
T(10,17)=750
T(11,18)=750
T(11,19)=750
T(12,20)=750
T(12,21)=750
95  S=0
    DO 100 I=0,2
    DO 100 J=2,8
      Q(I,J)=(T(I,J-1)+T(I+1,J)+T(I,J+1)+T(I-1,J)-4*T(I,J))/4
100  S=S+ABS(Q(I,J))
    DO 110 I=3,5
    DO 110 J=2,9
      Q(I,J)=(T(I,J-1)+T(I+1,J)+T(I,J+1)+T(I-1,J)-4*T(I,J))/4
110  S=S+ABS(Q(I,J))
    DO 120 I=6,7
    DO 120 J=2,10
      Q(I,J)=(T(I,J-1)+T(I+1,J)+T(I,J+1)+T(I-1,J)-4*T(I,J))/4
120  S=S+ABS(Q(I,J))
    DO 130 J=2,11
      Q(8,J)=(T(8,J-1)+T(9,J)+T(8,J+1)+T(7,J)-4*T(8,J))/4
130  S=S+ABS(Q(8,J))
    DO 140 J=2,12
      Q(9,J)=(T(9,J-1)+T(10,J)+T(9,J+1)+T(8,J)-4*T(9,J))/4
140  S=S+ABS(Q(9,J))
    DO 150 J=2,14
      Q(10,J)=(T(10,J-1)+T(11,J)+T(10,J+1)+T(9,J)-4*T(10,J))/4
150  S=S+ABS(Q(10,J))
    DO 160 J=2,16
      Q(11,J)=(T(11,J-1)+T(12,J)+T(11,J+1)+T(10,J)-4*T(11,J))/4

```

```
160  S=S+ABS(Q(11,J))
      DO 170 J=2,18
      Q(12,J)=(T(12,J-1)+T(13,J)+T(12,J+1)+T(11,J)-4*T(12,J))/4
170  S=S+ABS(Q(12,J))
      DO 180 I=13,21
      DO 180 J=2,20
      Q(I,J)=(T(I,J-1)+T(I+1,J)+T(I,J+1)+T(I-1,J)-4*T(I,J))/4
180  S=ABS(Q(I,J))
      DO 190 J=2,20
      Q(22,J)=(T(22,J-1)+T(22,J+1)+T(21,J)-3*T(22,J))/4
190  S=S+ABS(Q(22,J))
      DO 200 I=0,2
      DO 200 J=2,8
200  T(I,J)=T(I,J)+Q(I,J)
      DO 210 I=3,5
      DO 210 J=2,9
210  T(I,J)=T(I,J)+Q(I,J)
      DO 220 I=6,7
      DO 220 J=2,10
220  T(I,J)=T(I,J)+Q(I,J)
      DO 230 J=2,11
230  T(8,J)=T(8,J)+Q(8,J)
      DO 240 J=2,12
240  T(9,J)=T(9,J)+Q(9,J)
      DO 250 J=2,14
250  T(10,J)=T(10,J)+Q(10,J)
      DO 260 J=2,16
260  T(11,J)=T(11,J)+Q(11,J)
      DO 270 J=2,18
270  T(12,J)=T(12,J)+Q(12,J)
      DO 280 I=13,22
      DO 280 J=2,20
280  T(I,J)=T(I,J)+Q(I,J)
```

```

DO 290 J=2,8
290  T(-1,J)=T(1,J)
      IF(S-0.001)310,310,95
310  WRITE(16,320)((T(I,J),I=0,22),J=1,9)
320  FORMAT(1X,23F4.0)
      WRITE(16,330)(T(I,10),I=2,22)
330  FORMAT(9X,21F4.0)
      WRITE(16,340)(T(I,11),I=5,22)
340  FORMAT(21X,18F4.0)
      WRITE(16,350)((T(I,12),I=7,22)
350  FORMAT(29X,16F4.0)
      WRITE(16,360)(T(I,13),I=8,22)
360  FORMAT(33X,15F4.0)
      WRITE(16,370)((T(I,J),I=9,22),J=14,15)
370  FORMAT(37X,14F4.0)
      WRITE(16,380)((T(I,J),I=10,22),J=16,17)
380  FORMAT(41X,13F4.0)
      WRITE(16,390)((T(I,J),I=11,22),J=18,19)
390  FORMAT(45X,12F4.0)
      WRITE(16,400)((T(I,J),I=12,22),J=20,21)
400  FORMAT(49X,11F4.0)
      END

```

(3)

**Two-dimensional Transient Heat Conduction in
Concave Magma Intrusion Environment**

```

DIMENSION T(-1:22,1:21)
C TWO-DIMENSIONAL MODEL OF UNSTEADY-STATE CONCAVE HEAT CONDUCTION
C FOR XINLU ORE FIELD
OPEN(14, FILE='CHI-4.RES', STATUS='NEW')
DO 10 I=-1,22

```

```
DO 10 J=1,8
10  T(I,J)=25+1.5*(J-1)
    DO 20 I=-1,11
      DO 20 J=9,10
20  T(I,J)=25+1.5*(J-1)
    DO 30 I=-1,10
      DO 30 J=11, 12
30  T(I,J)=25+1.5*(J-1)
    DO 40 I=-1,9
      DO 40 J=13, 14
40  T(I,J)=25+1.5*(J-1)
    DO 50 I=-1,8
      DO 50 J=15,16
50  T(I,J)=25+1.5*(J-1)
    DO 60 I=-1,7
60  T(I,17)=49
    DO 70 I=-1,6
70  T(I,18)=50.5
    DO 80 I=-1,4
80  T(I,19)=52
    DO 90 I=-1,1
90  T(I,20)=53.5
    DO 500 Q=1,86444
      X=149500000-45*Q
      Y=300+450*((X-145600000)/3900000)
    DO 100 I=12,22
100 T(I,9)=Y
    DO 110 J=10,11
110 T(12,J)=Y
    DO 120 J=11,13
120 T(11,J)=Y
    DO 130 J=13,15
130 T(10,J)=Y
```

```

DO 140 J=15,17
140 T(9,J)=Y
DO 150 J=17,18
150 T(8,J)=Y
DO 160 J=18,19
160 T(7,J)=Y
DO 170 I=5,6
170 T(I,19)=Y
DO 180 I=2,5
180 T(I,20)=Y
DO 190 I=-1,2
190 T(I,21)=Y
DO 200 I=0,21
DO 200 J=2,8
200 T(I,J)=(T(I,J-1)+T(I+1,J)+T(I,J+1)+T(I-1,J))/4
DO 210 I=0,11
DO 210 J=9,10
210 T(I,J)=(T(I,J-1)+T(I+1,J)+T(I,J+1)+T(I-1,J))/4
DO 220 I=0,10
DO 220 J=11,12
220 T(I,J)=(T(I,J-1)+T(I+1,J)+T(I,J+1)+T(I-1,J))/4
DO 230 I=0,9
DO 230 J=13,14
230 T(I,J)=(T(I,J-1)+T(I+1,J)+T(I,J+1)+T(I-1,J))/4
DO 240 I=0,8
DO 240 J=15,16
240 T(I,J)=(T(I,J-1)+T(I+1,J)+T(I,J+1)+T(I-1,J))/4
DO 250 I=0,7
250 T(I,17)=(T(I,16)+T(I+1,17)+T(I,18)+T(I-1,17))/4
DO 260 I=0,6
260 T(I,18)=(T(I,17)+T(I+1,18)+T(I,19)+T(I-1,18))/4
DO 270 I=0,4
270 T(I,19)=(T(I,18)+T(I+1,19)+T(I,20)+T(I-1,19))/4

```

```

DO 280 I=0,1
280  T(I,20)=(T(I,19)+T(I+1,20)+T(I,21)+T(I-1,20))/4
      DO 290 J=2,8
290  T(22,J)=(T(22,J-1)+T(22,J)+T(22,J+1)+T(21,J))/4
      DO 300 J=2,20
300  T(-1,J)=T(1,J)
      IF (Q-100)310, 400, 310
310  IF (Q-500)320, 400, 320
320  IF (Q-2000)330, 400, 330
330  IF (Q-6000)340, 400, 340
340  IF (Q-10000)350, 400, 350
350  IF (Q-20000)360, 400, 360
360  IF (Q-40000)370, 400, 370
370  IF (Q-60000)380, 400, 380
380  IF (Q-86444)500, 400, 500
400  WRITE (14, *) 'AGE=', X
      WRITE (14, 405)
405  FORMAT ('-----')
      WRITE (14,410)((T(I,J), I=0,22), J=1,9)
410  FORMAT (1X, 23F4.0)
      WRITE (14, 420)((T(I,J), I=0, 12), J=10,11)
420  FORMAT (1X, 13F4.0)
      WRITE (14, 430)((T(I,J), I=0, 11), J=12,13)
430  FORMAT (1X, 12F4.0)
      WRITE (14, 440)((T(I,J), I=0, 10), J=14,15)
440  FORMAT (1X, 11F4.0)
      WRITE (14, 450)((T(I,J), I=0, 9), J=16,17)
450  FORMAT (1X, 10F4.0)
      WRITE (14, 460)((T(I,18), I=0, 8)
460  FORMAT (1X, 9F4.0)
      WRITE (14, 470)((T(I,19), I=0, 7)
470  FORMAT (1X, 8F4.0)
      WRITE (14, 480)((T(I,20), I=0, 5)

```



```
480  FORMAT (1X, 6F4.0)
      WRITE (14, 490)((T(I,21), I=0, 2)
490  FORMAT (1X, 3F4.0)
      WRITE (14, 495)
495  FORMAT ( '  ')
500  CONTINUE
      END
```